



**HAL**  
open science

# Magnetosomes used as biogenic MRI contrast agent for molecular imaging of glioblastoma model

Marianne Boucher

► **To cite this version:**

Marianne Boucher. Magnetosomes used as biogenic MRI contrast agent for molecular imaging of glioblastoma model. Medical Physics [physics.med-ph]. Université Paris Saclay (COMUE), 2016. English. NNT : 2016SACLS234 . tel-01397186

**HAL Id: tel-01397186**

**<https://theses.hal.science/tel-01397186>**

Submitted on 15 Nov 2016

**HAL** is a multi-disciplinary open access archive for the deposit and dissemination of scientific research documents, whether they are published or not. The documents may come from teaching and research institutions in France or abroad, or from public or private research centers.

L'archive ouverte pluridisciplinaire **HAL**, est destinée au dépôt et à la diffusion de documents scientifiques de niveau recherche, publiés ou non, émanant des établissements d'enseignement et de recherche français ou étrangers, des laboratoires publics ou privés.



Université Paris Saclay Ph.D. thesis in Physics and Medical Imaging  
NTT: 2016SACLS234

Electrical Optical Bio-physics and Engineering Doctoral School, ED575

Unité d'Imagerie par Résonance Magnétique et de Spectroscopie  
(NeuroSpin, I<sup>2</sup>BM, CEA Saclay)

# **Magnetosomes used as biogenic MRI contrast agent for molecular imaging of glioblastoma model**

**Marianne Boucher**

Ph.D. thesis defended at Gif-sur-Yvette the 30<sup>th</sup> of September, 2016,  
in front of the following jury:

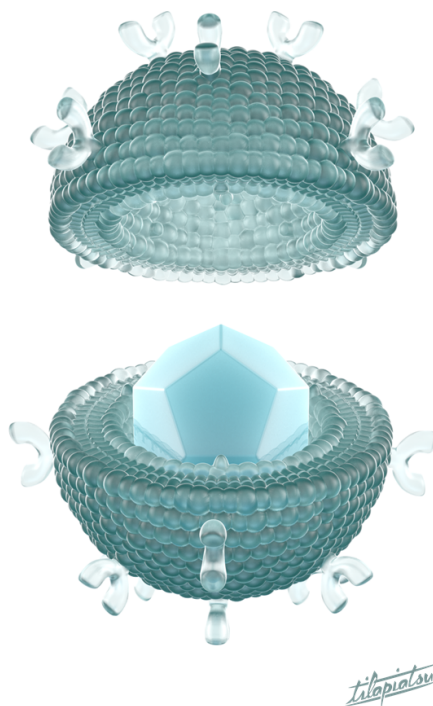
Dr. Florence Gazeau	DR, Paris Diderot	Referee
Dr. Damien Faivre	Group Leader, Max Plank Institute <i>missing</i>	Referee
Dr. Nicolas Ginet	CR1, Université Aix Marseille	Examiner
Dr. Nicolas Tsapis	DR, Université Paris Saclay - Paris Sud	Examiner
Dr. Olivier Clément	Pr, Hopital Européen Georges Pompidou PARCC	President
Dr. Sébastien Mériaux	Ingénieur Chercheur, Université Paris Saclay - CEA	Supervisor
Dr. Michel Bottlaender	Ingénieur Chercheur, Université Paris Saclay - CEA	PhD Director





Université Paris Saclay Ph.D. thesis in Physics and Medical Imaging

**Magnetosomes used as biogenic MRI contrast agent for  
molecular imaging of glioblastoma model**



**Marianne Boucher**



”Qu’importe chemin douloureux à qui trouve logis accueillant !”

Benoît Desforêt



*À Bastien, mon compagnon.*



# Remerciements

Je voudrais tout d'abord remercier les membres de mon jury, rapporteurs et examinateurs, pour m'avoir fait l'honneur d'accepter d'évaluer mon travail de thèse. Merci pour leur retours constructifs et pour m'avoir permis de défendre ce travail.

Je souhaiterais ensuite remercier Sébastien Mériaux, mon encadrant de thèse, pour m'avoir prise en stage de Master 2 et pour m'avoir gardé en thèse, sans qui cette expérience n'aurait pas été possible. Merci pour m'avoir mis le pied à l'étrier au début et pour l'indépendance laissée à la fin.

Je remercie également Michel Bottlaender pour avoir accepté d'être mon directeur de thèse jusqu'au bout.

Ce manuscrit n'aurait pu être si fourni sans le travail de Françoise Geffroy et Erwan Selingue ! Pour toute votre aide et votre bonne humeur merci ! Françoise, chaque hiver, je penserai à toi aux premières chutes de température en reniflant le fameux mélange Menthe/Ravinstara/Niaouli/Eucalyptus ! Erwan je n'oublierai pas nos interminables discussions à l'aimant, ni tes mythiques blagues !

Le projet collaboratif MEFISTO m'a également permis de découvrir un autre labo : le LBC ! Un immense merci à David Pignol, Nicolas Ginet, Christopher Lefèvre, Sandra Préveral, Géraldine Adryanczyk et Michel Péan pour m'avoir fait découvrir le monde magique des bactéries magnétotactiques ! Désolée de vous avoir fait avoir des sueurs froides à l'annonce des quantités de magnétosomes nécessaires à mes manips ! J'espère en avoir fait bon usage. Merci pour m'avoir permis d'aller au congrès MTB, où j'ai appris énormément de choses passionnantes sur les bactéries magnétotactiques et les magnétosomes.

Merci à Alice Gaudin pour m'avoir aidé à mettre en place mes manips au tout début de cette thèse.

Merci à Laurent Bellanger du LI2D pour la production de l'anticorps qui a permis de débloquer pas mal de manips.

Merci à Fabrice Richard pour les superbes images de microscopie électronique à transmission sur cellules et tissus biologiques.

J'ai aussi eu l'occasion de participer à d'autres projets, notamment le projet TROPICA. Je

souhaiterai remercier Didier Boquet et Amaury Herbert pour m'avoir fait découvrir un autre modèle tumoral. Merci à Laurence Motte, Yoann Lalatonne et Sophie Richard pour m'avoir permis de travailler sur des nanoparticules, synthétisées par voie chimique, de tailles, de coatings et de fonctionnalisations différentes. Merci pour les caractérisations physico-chimique des magnétosomes. J'ai beaucoup appris lors de nos discussions et j'ai pu ainsi diversifier mon travail. Sophie, belle rencontre au détour d'une paillasse... qui se poursuit maintenant régulièrement autour d'une bonne table, je voudrais te remercier pour ton soutien, en particulier pendant ma dernière année de thèse.

Cette thèse s'est déroulée à NeuroSpin, au laboratoire UNIRS. Merci à Benoît Larrat (pour m'avoir présenté à Sébastien, et pour mettre une bonne ambiance au labo) à Fawzi Boumezbear, Luisa Ciobanu et Cyril Poupon pour d'intéressantes discussions. Merci aux post-doc que j'ai eu la chance de rencontrer : Elodie P. (pour m'avoir chaperonné au 11,7, entre autres), David (pour nos discussions animées), Allegra (for your unfailing joy of life), Hermes (for your comment on the defense) et Elodie G. (pour nos interminables discussions).

J'ai eu la chance de prendre part à l'animation des NeuroBreakfast puis du SpinDating, évènements permettant des échanges scientifiques informels au sein du labo. Merci Benoît (Larrat) pour m'avoir incité y prendre part. Thanks Valentina for your amazing energy. Merci Gabrielle pour cette aventure et pour m'avoir soutenu, surtout lors de la rédaction. Merci Benoît M. et Carole pour cette superbe organisation. Enfin, un grand merci à Arthur, pour cette aventure et pour avoir rêvé avec moi d'un autre monde de la recherche ! Courage pour la suite !

Enfin, merci à tous ceux qui ont également partagé l'openspace 1025A ou le premier étage! Merci à Rémi (pour détester le RER autant que moi et pour avoir fait passer le temps en parlant gastronomie et campagne, entre autre), Alfredo (pour ton optimisme), Guillaume (pour nos discussions photos), Solenne (tu me tiendra au courant ?), Justine (pour ton enthousiasme), Matthieu (pour ta bonne humeur), Andrea, Pavel, Jacques et Khieu.

Malgré le temps passé au labo et dans les transports... j'ai quand même pu profiter du soutien de mes amis ! Merci à tous mes amis de l'ESPCI (7 ans déjà), en thèse comme moi (ou pas), avec qui j'ai pu partager les bons et les mauvais moments ! Merci à Benoît G., Marine, Joachim, Antoine, Nicolas et Rémi. Merci aux PICMiens, Jean-Christophe, Romain et Marion, et Paul N. pour m'avoir accueilli parmi vous et pour m'avoir montré une autre vision de la thèse. Merci à mes amies et témoins : Bénédicte, Celia, Claire, Fanny et Pascaline pour votre soutien sans faille et pour tous ces supers moments passés et futurs.

Pour finir, je souhaiterai remercier le plus chaleureusement possible ma famille ! Merci à mes beaux-frères Basile et Benoît, ma belle-sœur Fanny et mes beau parents Laurent et Evelyne, pour tous les diners/ week-end/ vacances passé(e)s ensemble qui m'ont permis de m'échapper du quotidien. Merci aussi pour votre écoute et votre soutien. Merci à mes frères, Paul et Laurent, et mes belles-sœurs, Liliane et Laurence, pour avoir été ma famille « métropolitaine » pendant ces 10 dernières années loin de maman ! Merci pour m'avoir épaulé dans toutes les étapes de mes études, prépa, école et thèse ! Merci pour m'avoir offert votre présence à la soutenance ainsi que le super week-end qui a suivi. Merci pour avoir imaginé ce petit magnétosome en 3D. Merci à mes neveux Marius et Isaac, qui sont nés pendant cette thèse et qui m'ont apporté tant de joie ! Recevoir vos adorables petites bouilles en photo ou vidéo sur

WhatsApp suffisait à effacer les problèmes de ma journée. Merci à mes grands-parents, Suzie et Georges, cette thèse m'a tenue éloignée de la Réunion, et je compte bien rapidement reprendre le rythme de mes retours annuels « à la maison ». Un immense merci maman, pour être une source infinie d'inspiration ! Merci pour m'avoir permis de rêver et pour avoir tout fait pour me donner les outils pour les réaliser. Merci aussi pour avoir fait le déplacement depuis la Réunion pour m'épauler pendant la soutenance.

Je clôture ces remerciements, et par la même occasion la rédaction de ce manuscrit, en remerciant mon meilleur ami et mon plus grand soutien. Bastien, depuis ces 7 dernières années, on en a vécu des aventures ! Et cette thèse en fait partie ! Comme toujours tu m'as donné l'audace d'oser, la folie d'essayer, la force de tenir bon, les raisons de ne pas abandonner et le recul de voir ce qui est beau en chaque chose. Merci Bastien, pour être mon amour et maintenant mon mari.



# Abstract

This work takes place in the context of molecular imaging, which aims at tailoring new diagnostic and therapeutic tools to the needs of the individual patient, by revealing molecular or cellular biomarkers of interest in the less invasive manner. Among the several areas of research conducted in this field, the emphasis is here on MR-based molecular imaging using engineered iron-oxide contrast agent.

This PhD thesis focuses on the study of a new class of contrast agent for MRI, the magnetosomes, which are natural iron-oxide vesicles produced by magnetotactic bacteria. These bacteria synthesize such magnetic vesicles and order them like a nano-compass in order to facilitate their navigation in sediments. Magnetosomes are thus awarded with interesting magnetic properties: iron-oxide core around 50 *nm*, mono-crystalline, single magnetic domain and high saturation magnetization. Furthermore, several bacterial strains exist in nature, each of them producing magnetosomes with specific size, shape and chemical composition. Finally, magnetosomes are naturally coated with a lipid bilayer which content is genetically determined. Lately, researchers have unraveled the proteins content of magnetosome membranes, opening the way to produce functionalized magnetosomes thanks to a fusion between the gene coding for a protein of interest and the gene coding for an abundant protein at magnetosome membrane.

This PhD work aims at investigating a new alternative path using magnetotactic bacteria to tackle the production of high efficiency MR-based molecular imaging probes. The engineering and production of magnetosomes, carried out by our collaborators from the LBC, the *Laboratoire de Bioénergétique Cellulaire* (LBC, CEA Cadarache), are presented and discussed. We firstly characterize wild type magnetosomes as contrast agent for high field MRI, and compare them with chemically produced iron-oxide nanoparticles. Our results confirm that these magnetosomes present very promising contrasting properties *in vitro*, and therefore they can be used *in vivo* as efficient blood pool agent, for vasculature imaging of mouse brain after intravenous injection. Afterward, engineered magnetosomes are tested in a molecular imaging study of a U87 mouse model of glioblastoma. Knowing that  $\alpha_v\beta_3$  integrins over-expressed by tumor cells can be actively targeted by RGD peptide, AMB-1 magnetotactic bacteria are genetically modified to produce RGD functionalized magnetosomes. After verifying their good affinity properties for U87 tumor cells *in vitro*, we demonstrate *in vivo* this specific affinity with MRI acquisitions on a U87 mouse model. Finally, these *in vivo* results are cross-validated with *post mortem* acquisition of histological data.

**Keywords:** Molecular imaging, MRI, iron-oxide nanoparticle, contrast agent, magnetosomes, glioblastoma.



# Résumé court en Français

Ces travaux de thèse s'inscrivent dans le contexte de l'imagerie moléculaire, qui vise à développer de nouveaux outils diagnostiques et thérapeutiques adaptés aux besoins de chaque patient, grâce à l'imagerie non invasive de biomarqueurs cellulaires ou moléculaires. Parmi les nombreuses disciplines contribuant à ce domaine de recherche, l'accent est mis ici sur l'imagerie par résonance magnétique (IRM) moléculaire à l'aide de nanoparticules d'oxyde de fer innovantes.

Cette thèse porte sur l'étude d'une nouvelle classe d'agent de contraste pour l'IRM, les magnétosomes, qui sont des vésicules d'oxyde de fer produites naturellement par des bactéries magnétotactiques. Ces bactéries les synthétisent et les alignent pour qu'elles agissent comme une boussole afin de faciliter leurs déplacements dans les sédiments. Les magnétosomes présentent des propriétés magnétiques très intéressantes : un cœur d'oxyde de fer d'environ 50 nm de diamètre, mono-cristallin, mono-domaine magnétique et avec une forte magnétisation à saturation. De plus, de nombreuses souches bactériennes existent dans la nature, chacune d'entre elles produisant des magnétosomes de taille, forme et composition chimique spécifiques. Enfin, les magnétosomes sont naturellement entourés par une membrane bilipidique dont la composition est déterminée génétiquement. Récemment, le contenu protéique de la membrane des magnétosomes a été mis à jour, ouvrant la voie à la production de magnétosomes fonctionnalisés par ingénierie génétique.

L'ingénierie et la production des magnétosomes, réalisées au *Laboratoire de Bioénergétique Cellulaire* (LBC, CEA Cadarache), sont présentées et discutées. Des magnétosomes sauvages sont caractérisés en tant qu'agents de contraste pour l'IRM, et nos résultats confirment qu'ils présentent des propriétés contrastantes intéressantes pour l'IRM et qu'ils permettent de réaliser l'imagerie de la vascularisation cérébrale chez la souris après une injection intraveineuse. Ensuite, l'étude de faisabilité de la production d'un agent de contraste IRM fonctionnalisé en une seule étape, à l'aide de bactéries magnétotactiques, est réalisée grâce des expériences d'imagerie moléculaire sur un modèle U87 de souris porteuse de glioblastome. Sachant que les cellules tumorales sur-expriment les intégrines  $\alpha_v\beta_3$ , et que ces dernières peuvent être ciblées activement par le peptide RGD, des bactéries magnétotactiques sont génétiquement modifiées pour produire des magnétosomes exprimant le peptide RGD à leur membrane. Après avoir vérifié *in vitro* leur propriétés d'affinité pour les cellules tumorales U87, nous démontrons *in vivo* cette affinité spécifique à l'aide d'acquisitions IRM sur un modèle souris U87. Finalement, ces résultats *in vivo* sont cross-validés par l'acquisition *post mortem* de données histologiques.

**Mots clés** : Imagerie moléculaire, IRM, nanoparticule d'oxyde de fer, agent de contraste, magnétosomes, glioblastome.



# Résumé en français

## Contexte de la thèse

### Les magnétosomes

Cette thèse s'inscrit dans le cadre du projet MEFISTO, portant sur l'étude d'agents de contraste originaux et novateurs : les magnétosomes. Il s'agit de cristaux d'oxyde de fer entourés d'une membrane bilipidique, synthétisés par des bactéries magnétotactiques. Le travail d'optimisation de la production des magnétosomes est mené par le Laboratoire de Bioénergétique Cellulaire (CEA Cadarache), partenaire du projet MEFISTO, tandis que l'étude de leur utilisation comme agent de contraste pour l'Imagerie par Résonance Magnétique (IRM) est menée dans le cadre de cette thèse. Dans le domaine de l'IRM, les suspensions de nanocristaux d'oxyde de fer sont principalement utilisées comme agents de contraste "négatifs", car leur présence se manifeste par des hypo-signaux sur les images pondérées  $T_2$  et  $T_2^*$ . L'effet de tels agents est souvent d'autant plus fort que le champ magnétique est élevé, c'est pourquoi il a été choisi de les étudier avec des scanners précliniques à haut champ magnétique (7 T, 11,7 T et 17,2 T).

Les magnétosomes présentent comme intérêt d'être intégralement produits biologiquement, ce qui induit un contrôle optimisé sur la minéralisation du fer, ainsi qu'une forme, une taille et une composition chimique du cristal propres à la souche bactérienne choisie. De plus, une fois extraits des bactéries, les magnétosomes sont directement utilisables *in vivo* car la membrane lipidique qui entoure leur cœur d'oxyde de fer assure leur biocompatibilité. Cette voie de production de nanocristaux d'oxyde de fer pour des applications biomédicales semble donc particulièrement intéressante pour pallier la multiplication d'étapes nécessaires à la réalisation de tels objets par voie de synthèse chimique.

### Les agents de contraste pour l'imagerie moléculaire par IRM

Les magnétosomes sont pressentis pour être d'excellents agents de contraste pour l'imagerie moléculaire par IRM. En effet, l'imagerie moléculaire vise à fournir de nouveaux outils aux techniques conventionnelles d'imagerie médicale, afin de permettre l'acquisition d'images de marqueurs moléculaires ou cellulaires, en plus des données anatomiques et fonctionnelles déjà disponibles en routine clinique. De telles informations pourraient permettre de développer une médecine dite "personnalisée" où le traitement s'adapte aux biomarqueurs exprimés par chaque patient. Pour cela, il est nécessaire de mettre en place de nouveaux agents de contraste possédant la particularité d'être affins pour le biomarqueur d'intérêt, tout en offrant une excellente sensibilité de détection. L'ajout d'une fonctionnalisation aux agents de contraste déjà existants

requiert habituellement une étape de plus dans le processus de fabrication, qui est déjà constitué de la synthèse du cœur d'oxyde de fer contrastant et de la couche de matériaux biocompatibles qui l'entoure.

Les magnétosomes présentent l'avantage de pouvoir être fonctionnalisés en modifiant le génome de la bactérie magnétotactique qui les produit, afin d'induire l'expression d'un peptide d'intérêt directement à leur membrane. Ces nano-objets biologiques peuvent donc être produits en une étape unique, la culture des bactéries. Par ailleurs, les magnétosomes présentent une excellente cristallinité et une taille plus grande comparativement aux autres agents de contraste à base d'oxyde de fer. Ces caractéristiques pourraient conférer aux magnétosomes des propriétés contrastantes très élevées, et donc une très bonne sensibilité de détection, confirmant leur intérêt en imagerie moléculaire par IRM.

## **Caractérisation des magnétosomes et de nanoparticules d'oxyde fer synthétisées par voie chimique pour l'IRM**

### **Caractérisation de la relaxivité transverse**

L'efficacité contrastante en IRM de ces nanocristaux biogéniques a été caractérisée par la mesure des relaxivités, paramètres qui quantifient l'influence d'un composé sur les temps de relaxation des protons environnants en fonction de sa concentration. Les nanoparticules d'oxyde de fer ont principalement une influence sur les temps de relaxation transversale  $T_2$ , comparativement à leur influence sur les temps de relaxation longitudinale  $T_1$ . Il a donc été entrepris de mesurer principalement la relaxivité transverse pour caractériser l'efficacité contrastante des nanoparticules d'oxyde de fer. Les résultats de cette étude de relaxométrie ont montré que les magnétosomes présentent une excellente relaxivité transverse, autour de  $500 \text{ mM}^{-1}\text{s}^{-1}$  à  $7 T$ , alors que des agents commerciaux ont une relaxivité transverse environ 3 à 5 fois plus faible.

### **Caractérisation des propriétés contrastantes *in vivo***

Ces résultats prometteurs nous ont amené à tester les suspensions de magnétosomes *in vivo* comme agents de contraste capables de révéler la vascularisation cérébrale de la souris, grâce au réhaussement du signal vasculaire après leur injection intra-veineuse. En effet, les magnétosomes circulent uniquement dans les vaisseaux cérébraux car ils ne peuvent pas accéder au parenchyme cérébral à cause de la barrière hémato-encéphalique, ce qui en fait de bons agents de contraste pour l'imagerie du compartiment vasculaire cérébral. Les angiogrammes cérébraux ainsi acquis constituent un bon complément de la mesure de relaxivité, qui caractérise l'efficacité de l'agent *in vitro*, par la mesure du contraste induit par les magnétosomes dans un environnement biologique *in vivo*.

Cette étude a démontré que les magnétosomes induisent un contraste significatif entre les vaisseaux et le parenchyme cérébral, même si les produits commerciaux semblent plus efficaces dans les conditions expérimentales utilisées (voir Figure 1). Ce résultat illustre l'importance de tester *in vivo* les agents de contraste afin de tenir compte, dans leur évaluation, de leur comportement en milieu biologique et pas uniquement de leur potentiel contrastant. En effet,

la différence entre les propriétés contrastantes *in vivo* des magnétosomes et du produit commercial peut être expliquée par une moins bonne biocompatibilité des magnétosomes. La couche biocompatible présente autour du cœur d'oxyde de fer démontre ici toute son importance. En effet, étant plus épaisse dans les particules commerciales, elle peut conduire à écranter les perturbations locales du champ magnétique induites par les nanoparticules sur les protons environnants, ce qui a pour effet de diminuer l'effet contrastant. Cependant, cette couche biocompatible permet aussi de diminuer la clairance et ainsi allonger les temps de circulation dans la vascularisation, ce qui peut induire un meilleur contraste *in vivo*. Par ailleurs, les méthodes développées pour étudier les magnétosomes en tant qu'agent de contraste IRM ont été également utilisées afin de caractériser des agents de contraste synthétisés par voie chimique par des collaborateurs du laboratoire CSPBAT. Cela a permis notamment d'étudier plus finement l'impact de la taille du cœur d'oxyde de fer sur le potentiel contrastant *in vitro*, ainsi que l'influence de la nature la couche biocompatible sur le contraste *in vivo*.

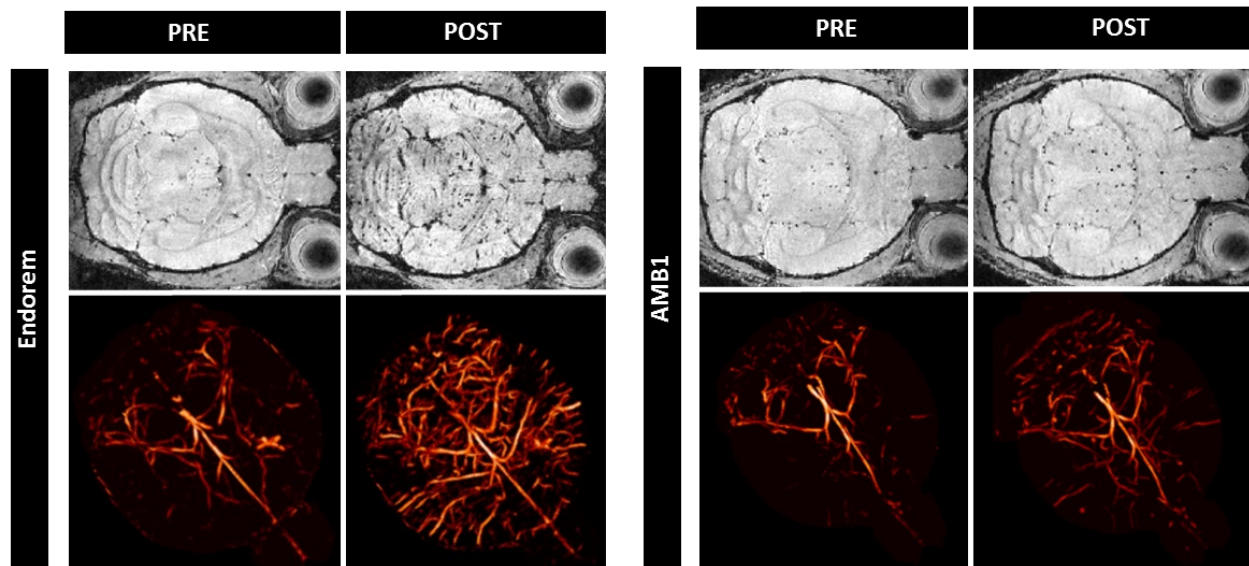


Fig. 1 – Comparaison des propriétés contrastantes *in vivo* de l'Endorem<sup>®</sup> (gauche, 17 T) et des magnétosomes AMB1 (droite, 11.7 T). La première et la troisième colonnes présentent les images avant l'injection alors que la deuxième et quatrième, celles après l'injection. Les images FLASH (première ligne) permettent d'apprécier le contraste entre le parenchyme cérébral et les vaisseaux, à partir duquel les angiogrammes 3D (deuxième ligne) sont calculés.

## Imagerie moléculaire d'un biomarqueur de tumeur cérébrale avec des magnétosomes fonctionnalisés génétiquement

### Choix du biomarqueur : les intégrines $\alpha_v\beta_3$

Un modèle de tumeur cérébrale a été choisi afin d'étudier la possibilité d'utiliser des magnétosomes fonctionnalisés génétiquement pour des applications d'imagerie moléculaire par IRM. Le développement anarchique des cellules tumorales nécessite un apport croissant en oxygène et en

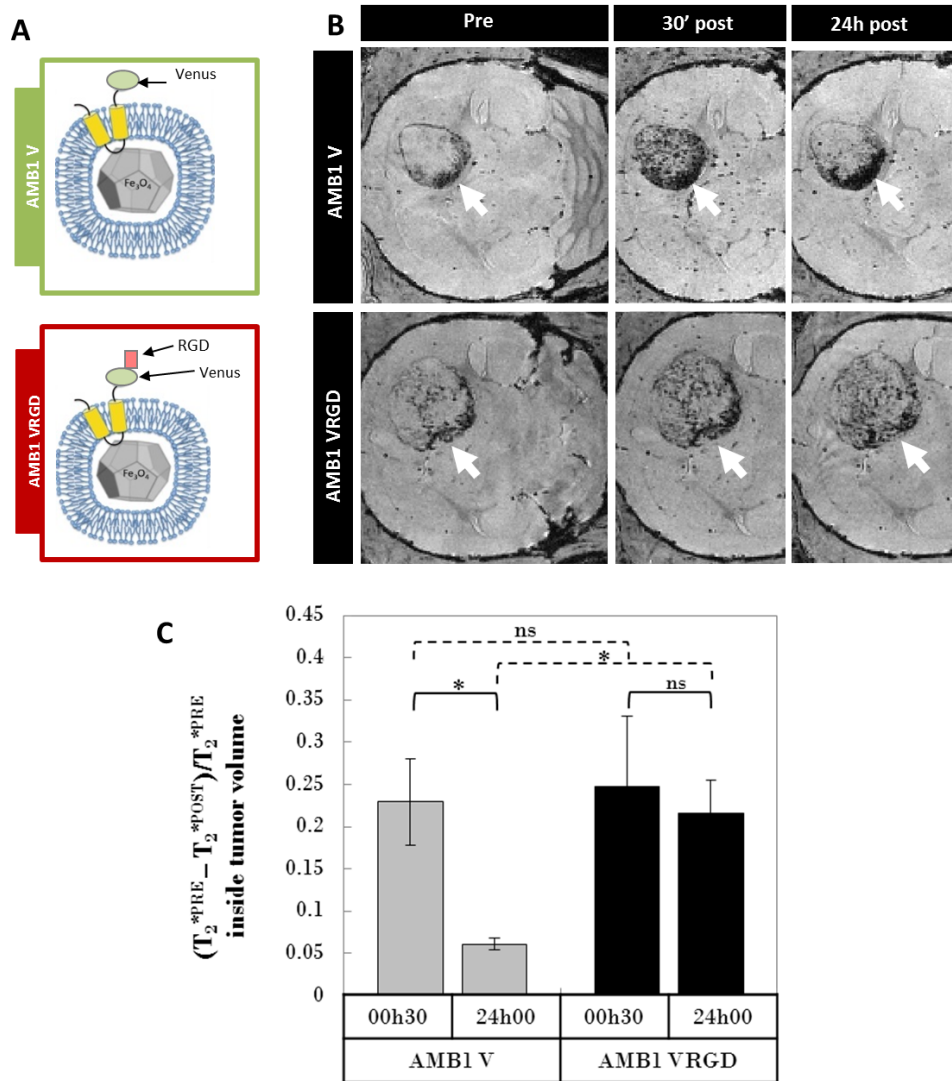


Fig. 2 – Démonstration *in vivo* de l'affinité des magnétosomes RGD pour le modèle animal de tumeur cérébrale U87. A/ Schéma des deux magnétosomes, fonctionnalisés RGD (AMB1 VRGD) et contrôle (AMB1 V), produits pour l'expérience. B/ Images FLASH représentatives du contraste induit dans les tumeurs par l'injection des magnétosomes fonctionnalisés RGD ou contrôles à différents temps après l'administration. C/ Quantification de l'augmentation du contraste dans la tumeur induit par l'injection des magnétosomes.

nutriments : lorsque la tumeur atteint une certaine taille, elle va former son propre réseau vasculaire pour poursuivre sa croissance. Ce phénomène, appelé néo-angiogénèse, est souvent utilisé comme biomarqueur pour le diagnostic tumoral, mais aussi comme cible pour des stratégies thérapeutiques anti-tumorales, puisque sans ces néo-vaisseaux, la tumeur ne peut pas continuer sa progression. Il a été démontré que les cellules néo-angiogéniques tumorales sur-expriment l'intégrine  $\alpha_v\beta_3$  et qu'il était possible de cibler ces intégrines avec le peptide RGD (Arginine - Glycine - Acide aspartique), notamment avec un peptide RGD lié à une nanoparticule d'oxyde de fer. Des magnétosomes porteurs du peptide RGD à leur membrane ont été produits afin de réaliser une première preuve de concept de l'utilisation de magnétosomes fonctionnalisés

génétiqnement pour l'imagerie moléculaire par IRM d'un biomarqueur tumoral (voir Figure 2 A).

## **Études *in vitro* et *in vivo* d'affinité des magnétosomes fonctionnalisés pour les cellules tumorales U87**

Une première étude a permis de montrer *in vitro* que les magnétosomes fonctionnalisés RGD se fixent spécifiquement sur la lignée cellulaire tumorale U87 en culture, cellules de glioblastome humain connues pour sur-exprimer les intégrines  $\alpha_v\beta_3$ . De plus, il a été démontré que cette fixation spécifique induit une internalisation des magnétosomes au sein des cellules tumorales en culture. La deuxième étude s'est intéressée à l'affinité *in vivo* de ces magnétosomes fonctionnalisés pour leur cible sur un modèle souris de tumeur cérébrale. Pour cela, des souris nudes (immunodéprimées) ont reçu une injection intra-cérébrale de cellules U87. Au bout d'une quinzaine de jours, elles étaient porteuses de tumeurs de quelques millimètres de diamètre (autour de 3 mm) à l'emplacement de l'implantation. Une injection intra-veineuse de magnétosomes, fonctionnalisés ou contrôles, a alors été administrée à ces souris, avant de les imager par une série de séquences IRM sensibles au fer, à différents temps avant et après l'injection (séquences  $T_2^*$ , pondérée et paramétrique). Cette étude a permis de démontrer que les magnétosomes fonctionnalisés avec le peptide RGD sont toujours présents en quantité significative dans la tumeur 24 h après l'injection intra-veineuse, contrairement aux magnétosomes contrôles qui semblent être éliminés plus vite (voir Figure 2 B et C). De plus, ces résultats IRM ont été validés par histologie, grâce à des marquages immunohistochimiques sur des coupes de cerveaux de souris, permettant de révéler la présence des magnétosomes dans les vaisseaux tumoraux *post mortem*.

Ainsi, un des objectifs principaux du projet MEFISTO est atteint : il est possible de faire fabriquer à une bactérie un agent de contraste fonctionnalisé pour réaliser de l'imagerie moléculaire *in vivo* par IRM de tumeurs cérébrales.

## **Optimisation de l'administration d'agents de contraste fonctionnalisés pour améliorer leur accumulation dans une tumeur cérébrale**

### **Étude de l'accumulation des magnétosomes RGD dans les cellules U87 *in vitro***

Partant de l'hypothèse que la clairance observée *in vivo* est le facteur limitant de l'accumulation des magnétosomes RGD dans les tumeurs cérébrales, il a été entrepris d'optimiser le protocole d'administration des magnétosomes fonctionnalisés, afin de maximiser la dose de fer restant dans la tumeur après leur administration intra-veineuse. Tout d'abord, il a été vérifié *in vitro*, sur les cellules tumorales U87 en culture, que l'augmentation du temps d'incubation ou de la dose de magnétosomes RGD induit une augmentation de la quantité de magnétosomes accumulés dans les cellules. L'accumulation de nanoparticules fonctionnalisées par un peptide RGD dans une cellule tumorale exprimant des intégrines  $\alpha_v\beta_3$  peut s'expliquer par le recyclage des intégrines : en effet, ces protéines transmembranaires, en se liant aux magnétosomes RGD, permettent leur internalisation dans les cellules U87, puis elles sont à nouveau présentées à la

membrane cellulaire et peuvent donc interagir avec de nouveaux magnétosomes RGD.

## **Multi-injection intra-veineuse de magnétosomes RGD *in vivo***

Le parallèle *in vivo* de l'expérience précédente implique de ralentir la clairance effectuée par le système réticulo-endothélial de l'animal, pour allonger le temps de circulation des magnétosomes dans les vaisseaux tumoraux. Il a donc été proposé de réaliser plusieurs injections de doses plus faibles, afin de déterminer si cette augmentation du temps de contact entre l'agent de contraste et sa cible menait également *in vivo* à l'augmentation de la charge en fer dans la tumeur. Les résultats des expériences, comparant une injection de  $200 \mu\text{mol}_{[\text{Fe}]} / \text{kg}_{\text{BW}}$  à deux injections de  $100 \mu\text{mol}_{[\text{Fe}]} / \text{kg}_{\text{BW}}$  espacées de 6 h, semblent montrer une accumulation un peu plus importante des magnétosomes RGD dans la tumeur pour l'injection double. Toutefois, la variabilité de la mesure ne permet pas d'extraire une différence significative entre les groupes, ce qui peut être expliqué par l'inclusion d'animaux porteurs de tumeurs de taille assez différente (entre 2 et 3 mm). Cependant, cette expérience illustre l'importance du choix du protocole d'administration de l'agent de contraste, et ouvre la discussion sur des méthodes plus proches de l'infusion intra-veineuse par exemple, afin d'optimiser le contraste obtenu.

## **Conclusion**

Ce travail de thèse, aux frontières de la physique, de la biologie et de l'imagerie médicale, a permis de mettre en évidence qu'un nouveau moyen de produire des agents de contraste pour l'IRM était possible, tirant profit de bactéries présentes dans la nature. De plus, ces nouveaux agents de contraste peuvent être fonctionnalisés pour des applications d'imagerie moléculaire, ce qui a été démontré ici sur un modèle de tumeur cérébrale. Ces travaux pourraient également ouvrir la voie vers une nouvelle méthode d'hyperthermie magnétique pour induire une régression tumorale, consistant à injecter des magnétosomes affins pour la zone tumorale par voie intra-veineuse, ce qui ferait des magnétosomes fonctionnalisés un potentiel agent théranostique contre les tumeurs cérébrales.

Par ailleurs, les méthodes développées au cours de cette thèse, de la standardisation de la mesure des relaxivités, à l'acquisition d'angiogrammes cérébraux par injection d'agent de contraste, ou encore la recherche de co-localisation de marquages sur les images d'histologie, sont des outils qui seront à nouveau utilisés par de futurs projets d'imagerie moléculaire.





# Contents

<b>1</b>	<b>Introduction</b>	<b>1</b>
1.1	Molecular imaging combining iron-oxide nanoparticles with MRI acquisitions . . .	2
1.2	Targeting $\alpha_v\beta_3$ integrins for brain tumor molecular imaging . . . . .	3
1.3	The MEFISTO project . . . . .	5
1.4	Outline of this manuscript . . . . .	6
	References . . . . .	9
<b>2</b>	<b>Iron-oxide nanoparticles for diagnostic and therapeutic applications</b>	<b>15</b>
2.1	Why iron nanoparticles? . . . . .	16
2.1.1	Physical origin of magnetism . . . . .	16
2.1.2	Magnetism of nanoparticles . . . . .	18
2.1.3	The interest of IONP in MRI . . . . .	20
2.1.4	Relaxation models for IONP . . . . .	22
2.2	How to optimize IONPs contrasting properties? . . . . .	25
2.2.1	Superparamagnetic iron core optimization . . . . .	26
2.2.2	Coating optimization . . . . .	29
2.3	Interest of magnetosomes as MRI contrast agent . . . . .	31
2.3.1	Magnetotactic bacteria and magnetosomes . . . . .	31
2.3.2	Magnetosomes physico-chemical properties . . . . .	34
2.4	Other biomedical applications of IONP . . . . .	36
2.4.1	IONP labeled cells . . . . .	37
2.4.2	Magnetic hyperthermia . . . . .	40
	References . . . . .	42
<b>3</b>	<b>Magnetosomes and other chemical IONPs used as MRI blood pool contrast agents</b>	<b>49</b>
3.1	Physico-chemical properties of magnetosomes . . . . .	50
3.1.1	Iron core characterization . . . . .	50
3.1.2	Membrane characterization . . . . .	52
3.1.3	Benefits and drawbacks of magnetosomes . . . . .	54
3.2	MRI contrasting properties of magnetosomes and chemical IONPs . . . . .	55
3.2.1	Chemical IONPs transverse relaxivities . . . . .	56
3.2.2	Size effect in chemical IONPs transverse relaxivities . . . . .	58
3.2.3	Magnetosomes transverse relaxivities . . . . .	60
3.3	Brain angiography of healthy mouse with contrast-enhanced MRI . . . . .	63
3.3.1	<i>In vivo</i> contrasting properties of chemical IONPs . . . . .	64
3.3.2	<i>In vivo</i> contrasting properties of magnetosomes . . . . .	66

3.4	Brain tumor contrast-enhanced MRI in a mouse model of glioblastoma . . . . .	68
3.4.1	Tumor growth follow-up in diameter and volume . . . . .	68
3.4.2	Tumor vessels follow-up . . . . .	69
3.4.3	Tumor iron uptake measurements . . . . .	72
3.5	Summary and perspectives . . . . .	75
	References . . . . .	77
<b>4</b>	<b>Magnetosomes for molecular imaging of a mouse glioblastoma model</b>	<b>83</b>
4.1	Genetic functionalization of AMB1 magnetosomes . . . . .	84
4.1.1	Genetic modification of AMB1 strain . . . . .	85
4.1.2	Assessment of successful genetic modification . . . . .	85
4.2	<i>In vitro</i> characterization of functionalized magnetosomes . . . . .	86
4.2.1	MR contrasting properties of functionalized magnetosomes . . . . .	86
4.2.2	Affinity study on U87 cells culture . . . . .	88
4.2.3	Study of RGD functionalized magnetosomes internalization into U87 cells . . . . .	89
4.2.4	Affinity study on spheroid culture of U87 cells . . . . .	91
4.3	<i>In vivo</i> molecular imaging of a mouse glioblastoma model with RGD functionalized magnetosomes . . . . .	94
4.3.1	Dynamic continuous follow-up: assessment of magnetosomes circulation in tumor vessels . . . . .	95
4.3.2	24 h follow-up: <i>in vivo</i> assessment of RGD magnetosomes affinity for U87 tumor . . . . .	96
4.3.3	Cross-validation of MRI results with <i>post mortem</i> histology . . . . .	99
4.3.4	<i>Post-mortem</i> MRI acquisitions: toward histology-like MRI? . . . . .	100
4.4	In which cells can magnetosomes be found after intravenous injection? . . . . .	103
4.4.1	Interaction between liver macrophages and magnetosomes . . . . .	104
4.4.2	Interaction between microglia and magnetosomes . . . . .	104
4.5	Summary and perspectives . . . . .	107
	References . . . . .	108
<b>5</b>	<b>Multi-injections protocol to enhance iron uptake in U87 tumor</b>	<b>111</b>
5.1	<i>In vitro</i> enhancement of magnetosomes uptake by U87 tumor cells . . . . .	112
5.1.1	<i>In vitro</i> kinetics of RGD magnetosomes uptake . . . . .	113
5.1.2	Dose effect on <i>in vitro</i> RGD magnetosomes uptake . . . . .	115
5.2	<i>In vivo</i> comparative study of tumor iron uptake for single versus multiple injections of magnetosomes . . . . .	118
5.2.1	Two injections of half dose . . . . .	118
5.2.2	Toward the injection of smaller doses? . . . . .	120
5.3	Summary . . . . .	122
	References . . . . .	123
	<b>Conclusion and perspectives</b>	<b>125</b>
	References . . . . .	128
	<b>PhD student role within the different collaborations</b>	<b>131</b>
	<b>Appendices</b>	<b>135</b>

---

<b>A</b>	<b>Protocols for <i>in vitro</i> experiments</b>	<b>137</b>
A.1	Relaxometry . . . . .	137
A.2	U87 cells culture . . . . .	140
A.3	U87 cells spheroid culture . . . . .	140
A.4	Immunohistochemical stainings performed on U87 cells . . . . .	141
A.5	Perl's blue staining of U87 cells . . . . .	142
A.6	TEM images of magnetosomes into U87 cells . . . . .	142
<b>B</b>	<b>Protocols for <i>in vivo</i> experiments</b>	<b>145</b>
B.1	<i>In vivo</i> mouse brain imaging . . . . .	145
B.2	Mouse brain MRI scans . . . . .	145
B.3	Induction of U87 mouse model of human glioblastoma . . . . .	146
B.4	Histology . . . . .	146
B.5	Immunochemical staining . . . . .	147
<b>C</b>	<b>Data processing protocols</b>	<b>149</b>
C.1	Brain angiography using Frangi filter . . . . .	149
C.2	Brain angiogram skeletonization and quantification . . . . .	150
C.3	Analysis of immunohistochemical stainings co-localization . . . . .	151
	<b>List of Figures</b>	<b>154</b>
	<b>List of Tables</b>	<b>159</b>
	<b>List of Acronyms</b>	<b>161</b>
	<b>List of Publications</b>	<b>165</b>



# Chapter 1

## Introduction

### Contents

---

1.1	Molecular imaging combining iron-oxide nanoparticles with MRI acquisitions . .	2
1.2	Targeting $\alpha_v\beta_3$ integrins for brain tumor molecular imaging . . . . .	3
1.3	The MEFISTO project . . . . .	5
1.4	Outline of this manuscript . . . . .	6
	References . . . . .	9

---

## 1.1 Molecular imaging combining iron-oxide nanoparticles with MRI acquisitions

This PhD work takes place in the general context of molecular imaging, and more particularly the development of new iron-oxide contrast agents dedicated to MRI applications. The rise of molecular medicine, which aims at tailoring personal medical diagnostics and therapies but also human well-being monitoring, is highly supported worldwide by public research policies. However, while medical imaging, such as X rays, echography, Positron Emission Tomography (PET) and MRI (Magnetic Resonance Imaging), is widely and daily used to get anatomical and functional information, subcellular and even molecular detection of prognostic and diagnostic physiological markers is striving to reach the patient's bed. In this context, molecular imaging is a growing field that aims at overcoming the lack of specificity and sensibility of conventional imaging strategies, to reveal molecular or cellular phenomenon of medical interest in the less invasive manner.

Unraveling molecular information *in vivo* enables to diagnose diseases at earlier stage and to tailor therapeutic strategies to individual patient variability. Molecular imaging thus requires the development of specific functionalized contrast agent to reveal molecular or cellular biomarkers with dedicated imaging modality.

Currently, the most advanced modality for this purpose is PET imaging<sup>1</sup>, with a high sensitivity for biomarkers detection, but a low spatial resolution coupled with the use of radioactive compounds as the main drawbacks. Fluorescence imaging is also very promising since it exhibits a very good sensitivity. However, the poor penetration and complex diffusion of photons in living tissues currently restrain its use mainly to intraoperative applications. On the contrary, MRI suffers from poor sensitivity but offers high spatial resolution<sup>2</sup>, does not rely on radionuclides and can non-invasively provide in-depth information. Its sensitivity can yet be enhanced firstly by increasing the intensity of static magnetic field, secondly by improving detection sensitivity of radiofrequency coils, and thirdly by optimizing the contrasting part of molecular imaging probes. Advantages and drawbacks of widely used imaging modalities are listed in Table 1.1 adapted from Mahmoudi *et al*<sup>2</sup>: this table exhibits that the main disadvantage of MRI compared to other techniques regarding molecular imaging applications is its lack of sensitivity, which therefore needs to be overcome.

One active field of research for improving MRI sensitivity is the design of new types of probes exhibiting very efficient contrasting properties, and in particular, iron-oxide nanoparticles are well studied MRI contrast agents<sup>3</sup>. Some Ultrasmall Superparamagnetic Iron-Oxide nanoparticles (USPIO) have been already tested as MRI contrast agents (Sinerem<sup>®</sup>, Combidex<sup>®</sup>, Clariscan<sup>™</sup>) for clinical applications, *e.g.* to differentiate metastatic from inflammatory lymph nodes<sup>4</sup>. USPIO nanoparticles also showed their potential for providing important information about angiogenesis in tumors<sup>5</sup>, and for helping physicians to identify vulnerable atherosclerotic plaques<sup>6</sup>.

<sup>1</sup>F. Reynolds et al., *Molecular Imaging*, **10**: 407–419, 2011.

<sup>2</sup>M. Mahmoudi et al., *Nanoscale*, **3**: 3007–3026, 2011.

<sup>3</sup>C. Corot et al., *Advanced Drug Delivery Reviews*, **58**: 1471–1504, 2006.

<sup>4</sup>M.-F. Bellin et al., *European Journal of Radiology*, **34**: 257–264, 2000.

<sup>5</sup>Jill Fredrickson et al., *Magnetic Resonance in Medicine*, , 2016.

<sup>6</sup>T. Y. Tang et al., *European Journal of Vascular and Endovascular Surgery*, **35**: 392–398, 2008.

Imaging techniques	Disadvantages	Advantages
PET - SPECT	Low spatial resolution, radiation risks, high cost	High sensitivity, quantitative, no penetration limit
CT	Not quantitative, radiation risks, limited soft tissue resolution, limited molecular applications	Anatomical imaging, bone and tumor imaging
MRI	Low sensitivity, high cost, time consuming scan and processing	Morphological and functional imaging, no penetration limit, high spatial resolution
Optical imaging	Photobleaching, limited penetration, low spatial resolution; autofluorescence disturbing	Low cost, easy manipulation, high sensitivity, detection of fluorochrome in live and dead cells
US	Limited resolution and sensitivity, low data reproducibility	Safety, low cost, wide availability, real time

Tab. 1.1 – Different non-invasive imaging modalities, with their main advantages and disadvantages, adapted from Mahmoudi *et al*<sup>2</sup>.

The last advances in engineering such particles have paved the way for designing more sensitive probes that could be suitable for molecular imaging. It is actually possible to tune their contrasting properties by changing their size and/or shape, or even by doping them with other atoms<sup>7-9</sup>. In addition, functionalization of the probe surface by suitable ligands can confer selectivity for the targeted biomarker, tissue or organ. Additional probe engineering for drug delivery and other therapeutic effects can convert these vectors into theranostic agents. In this context, functionalization of iron-oxide nanoparticles represents a dynamic field of research, investigating different strategies such as antibodies, aptamers, cell penetrating peptides or drugs, for a variety of applications in cancer or inflammation diagnosis for example<sup>7,8</sup>. Thanks to their metallic cores, such agents can also play a key role in cell tracking after transplantation<sup>9</sup>, and can also deliver thermal energy locally for thermoablation therapies<sup>10</sup>.

## 1.2 Targeting $\alpha_v\beta_3$ integrins for brain tumor molecular imaging

Molecular imaging of brain tumor is particularly valuable since it could help performing early diagnosis as well as monitoring treatment efficiency, and might even be coupled with therapy<sup>7,11,12</sup>. To date, brain tumor targeting has been successfully achieved through the EPR (Enhanced

<sup>7</sup>Z. Bakhtiary et al., *Nanomedicine: Nanotechnology, Biology and Medicine*, **12**: 287–307, 2015.

<sup>8</sup>S. Sharifi et al., *Contrast Media and Molecular Imaging*, **10**: 329–355, 2015.

<sup>9</sup>C. A. Pacak et al., *PLoS ONE*, **9**: e108695, 2014.

<sup>10</sup>P. Soares et al., *Recent patents on anti-cancer drug discovery*, **7**: 64–73, 2012.

<sup>7</sup>Z. Bakhtiary et al., *Nanomedicine: Nanotechnology, Biology and Medicine*, **12**: 287–307, 2015.

<sup>11</sup>S. C. Baetke et al., *The British Journal of Radiology*, **88**: 20150207, 2015.

<sup>12</sup>F. Zhang et al., *Biomaterials*, **33**: 5414–5422, 2012.

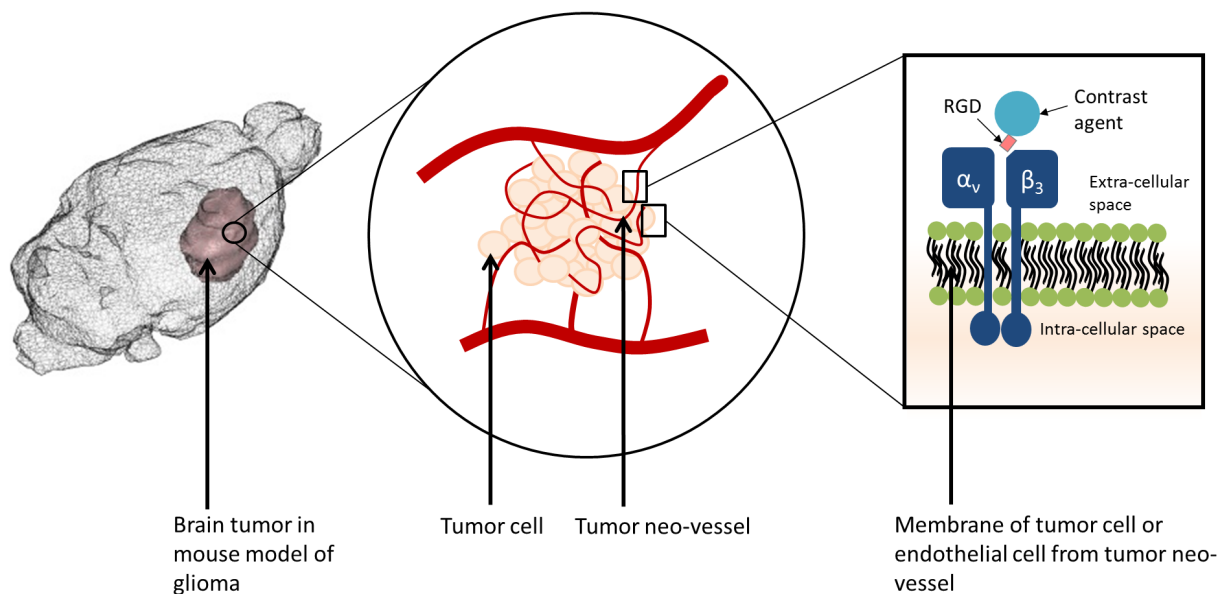


Fig. 1.1 – Principle of targeting  $\alpha_v\beta_3$  integrin *in vivo* with RGD peptide.

Permeability and Retention) effect<sup>13</sup> (a passive targeting due to the leakiness of tumor blood vessels), or by active targeting of molecular biomarkers of tumor angiogenesis<sup>11</sup>, such as  $\alpha_v\beta_3$  integrins over-expressed by tumor cells and endothelial cells of tumor neo-vessels<sup>14</sup>, and involved in development of new blood vessels and cell motility<sup>15,16</sup>.

$\alpha_v\beta_3$  integrin can be targeted *in vivo* by RGD peptide (Arginine-Glycine-Aspartic Acid), which binding efficiency has already been demonstrated by several studies<sup>12,14,17</sup>.

To develop new RGD functionalized probes dedicated to brain tumor molecular imaging, preclinical studies are usually performed on rodent model of glioma. Indeed, glioma has already been deeply studied, and several cellular and animal models are now available for research<sup>18</sup>. In particular, orthotopic xenografts of cultured tumor cells originated from human biopsies lead to reproducible tumors, which explains why they are widely used in preclinical research. Advantages of such glioma models are their very good reproducibility and a good characterization of their biomarkers expression. On the other hand, these xenografts models do not induce brain tumors exhibiting all characteristics of human gliomas, mainly because of the drift during sequential passage of cell culture, but also because of the implantation method. Highly concentrated cells suspension is usually implanted through the skull inside rodent brain, creating a wound on needle path. Therefore, the brain tumor is growing from an environment very rich in tumor cells and in a wounded brain, which is very different from the original human disease where the tumor is supposed to grow from few tumor cells in a healthy brain. Finally, one consequence of this protocol is a rapid tumor growth in rodent brain (only few weeks), which is a drawback in terms of likeness with human glioma, but an advantage for shortening induction time in preclinical research.

<sup>13</sup>J. Fang et al., *Advanced Drug Delivery Reviews*, **63**: 136–151, 2011.

<sup>14</sup>F. Danhier et al., *Molecular Pharmaceutics*, **9**: 2961–2973, 2012.

<sup>15</sup>P. T. Caswell et al., *Traffic*, **7**: 14–21, 2006.

<sup>16</sup>P. C. Brooks et al., *Science*, **264**: 569–571, 1994.

<sup>17</sup>C. Zhang et al., *Cancer Research*, **67**: 1555–1562, 2007.

<sup>18</sup>S. S. Stylli et al., *Journal of Clinical Neuroscience*, **22**: 619–626, 2015.

For the molecular imaging studies performed during this PhD, we chosen the U87 mouse model, consisting in the orthotopic xenograft of U87 human glioblastoma cells, this model being especially used for assessing tumor angiogenesis<sup>19</sup>. Thus, the RGD functionalized probes tested *in vivo* on this model could actively target brain tumors, through the over-expression of  $\alpha_v\beta_3$  integrins by tumor cells and endothelial cells from tumor neo-vessels, as presented in Figure 1.1.

### 1.3 The MEFISTO project

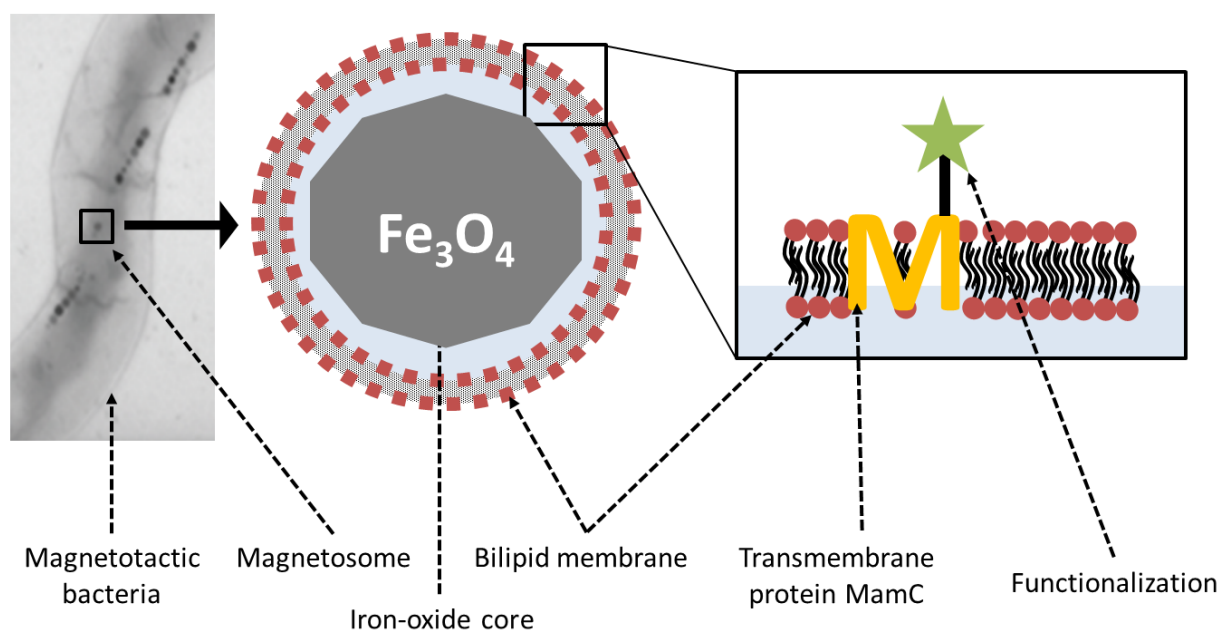


Fig. 1.2 – Principle of using magnetotactic bacteria to produce magnetosomes used as functionalized contrast agent for MRI.

This PhD work was conducted in the framework of the MEFISTO project, funded by an ANR grant in 2012 for 4 years, which aims at developing strategies, based on the use of magnetosomes, for *in vivo* molecular imaging applications dedicated to brain tumor diagnosis and therapy. Magnetosomes are magnetic nanoparticles naturally encapsulated in a lipid vesicle, produced by magnetotactic bacteria. They offer in a single nano-object many of the characteristics that one seeks for multifunctional agent used as theranostic agent: a solid mineral iron-oxide core with contrasting properties for MRI, a therapeutic effect induced by magnetic hyperthermia, a lipid coating for solubilization and biocompatibility, and the possibility to use genetic tools for functionalizing the surface with bioactive ligands.

The production of functionalized synthetic nanoparticles usually requires several chemical procedures, including iron-oxide core synthesis, surface activation, chemical grafting of ligands and coating for solubilization. Each step is performed separately, using dedicated protocols subjected to duration, yield and cost parameters. In the MEFISTO project, we propose a

<sup>19</sup>Nienke A. de Vries et al., *Cancer Treatment Reviews*, **35**: 714–723, 2009.

methodology that gathers all these steps in one, letting the magnetotactic bacteria do the job. After a suitable genetic modification, bacteria are cultivated, and then broken to harvest functionalized magnetosomes by magnetic separation taking advantage of their magnetic properties, leading to a low cost and easy fabrication process.

The principle of magnetosome genetic functionalization is based on the transformation of magnetotactic bacteria with a translational fusion between the gene coding for an abundant transmembrane protein specific to the magnetosome membrane, like MamC<sup>20</sup>, and the gene encoding the targeting ligand. The decoration is thus naturally sorted to the membrane leading to a functionalized magnetosome<sup>21,22</sup>.

The Figure 1.2 briefly illustrates the principle of using magnetotactic bacteria to produce functionalized MRI contrast agents for molecular imaging applications.

## 1.4 Outline of this manuscript

This manuscript is divided into five chapters, this introduction being the first one.

The second chapter draws a non-exhaustive state of the art regarding the use of iron-oxide nanoparticles in biomedical applications, starting from the physical origin of their contrasting properties, to the different strategies to optimize these properties, before focusing on their potential as MRI contrast agent. Besides, magnetotactic bacteria and magnetosomes specificity are also presented.

The third chapter is dedicated to the use of non-functionalized iron-oxide nanoparticles for MRI applications. Both chemically synthesized nanoparticles and magnetosomes are studied in terms of contrast enhancement efficiency *in vitro* and *in vivo*. Transverse relaxivities are measured by suspending iron-oxide nanoparticles in agar to characterize their *in vitro* contrasting properties. Then, the contrast enhancement between brain parenchyma and blood vessels, induced by the intravenous injection of iron-oxide nanoparticles to mouse, is used to evaluate their *in vivo* contrasting properties. Besides, intravenous injections of iron-oxide nanoparticles are also performed on U87 mouse model of glioblastoma, in order to investigate vascular changes inside the tumor in terms of vessels geometric parameters and contrast agent retention. The results presented in this chapter, that focus on magnetosomes, have led to one publication in a peer-reviewed journal<sup>23</sup> and several communications in scientific conferences: one poster for WMIC<sup>24</sup> (Savannah, USA, September 2013) and five oral presentations for GTRV<sup>25</sup> (Orléans, France, December 2013), NeWS Workshop<sup>26</sup> (Gif-sur-Yvette, France, December 2014), MTB congress<sup>27</sup> (Rio de Janeiro, Brazil, September 2014), SFRMRM Congress<sup>28</sup> (Grenoble,

---

<sup>20</sup>K. Grünberg et al., *Applied and Environmental Microbiology*, **70**: 1040–1050, 2004.

<sup>21</sup>J. Xie et al., *Nano Research*, **2**: 261–278, 2009.

<sup>22</sup>N. Ginet et al., *PLoS ONE*, **6**: e21442, 2011.

<sup>23</sup>S. Mériaux et al., *Advanced Healthcare Materials*, **4**: 1076–1083, 2015.

<sup>24</sup>M. Boucher et al., *World Molecular Imaging Congress*, Poster, Savannah –USA, 2013.

<sup>25</sup>M. Boucher et al., *Groupe Thématique de Recherche sur la Vectorisation (now Société Française de Nanomédecine)*, Oral, Orléans –France, 2013.

<sup>26</sup>M. Boucher et al., *Neuroscience Workshop of Saclay*, Oral, Saclay –France, 2014.

<sup>27</sup>N. Ginet et al., *MagnetoTactic Bacteria*, Oral, Rio de Janeiro –Brazil, 2014.

<sup>28</sup>M. Boucher et al., *Société Française de Résonance Magnétique en Biologie et Médecine*, Oral, Grenoble –France, 2015.

France, March 2015) and ISMRM Congress<sup>29</sup> (Toronto, Canada, May 2015). And the results presented in this chapter, that focus on iron-oxide nanoparticles produced by our collaborators from CSPBAT laboratory, have led to one publication in a peer-reviewed journal<sup>30</sup>, two other papers recently submitted to peer-reviewed journals<sup>31,32</sup> and several communications in scientific conferences: three posters for Nanotech Meeting<sup>33</sup> (Washington, USA, May 2013), Nanobio Europe Meeting<sup>34</sup> (Toulouse, France, June 2013) and EMRS Spring Meeting<sup>35</sup> (Lille, France, May 2014), and three oral presentations for Zing Biomaterials Conference<sup>36</sup> (Nerja, Spain, April 2014) and EMRS Spring Meeting<sup>37,38</sup> (Lille, France, May 2014). The results on brain angiography have also been used to evaluate a method of compressed sensing and have led to one poster for ISBI<sup>39</sup> (New-York, USA, April 2015).

The fourth chapter presents the production and the use of RGD functionalized magnetosomes *in vitro* and *in vivo*. The specific affinity and the consecutive internalization of RGD functionalized magnetosomes by U87 human glioblastoma cell cultures are assessed *in vitro*, as well as the MRI contrasting properties of magnetosomes. Then, RGD-labeled and unlabeled magnetosomes are injected at the tail vein of glioblastoma bearing mice to establish *in vivo* the proof of concept that biogenic functionalized contrast agents can be used for MR-based molecular imaging of brain tumors. The results presented in this chapter have led to several communications in scientific conferences: four poster presentations for WMIC<sup>40</sup> (Seoul, South Korea, September 2014), MTB congress<sup>41</sup> (Rio de Janeiro, Brazil, September 2014), SFNANO-ENM Congress<sup>42</sup> (Grenoble, France, December 2015) which received the British Society prize for the best poster presentation, WMIC<sup>43</sup> (Honolulu, USA September 2015), and three oral presentations for SFRMRM Congress<sup>28</sup> (Grenoble, France, March 2015), ISMRM Congress (Toronto, Canada, May 2015)<sup>29</sup> and MTB Congress<sup>44</sup> (Marseille, France September 2016). Finally, a publication is currently on preparation based on the results of this chapter<sup>45</sup>.

The fifth chapter describes a preliminary study dealing with the administration technique of RGD magnetosomes to mice, in order to maximize their accumulation inside brain tumor *in vivo*. The hypothesis whereby magnetosomes are better taken up by targeted tumor cells when the contact duration is lengthened is investigated *in vitro*, and *in vivo* with an intravenous multi-injections protocol. The results of the multi-administration study have led to three poster

---

<sup>29</sup>M. Boucher et al., International Society of Magnetic Resonance in Medicine, Oral, Toronto –Canada, 2015.

<sup>30</sup>S. Richard et al., Journal of Materials Chemistry B, **3**: 2939–2942, 2015.

<sup>31</sup>S. Richard et al., Submitted to ACS Applied Materials & Interfaces, , 2016.

<sup>32</sup>S. Richard et al., Submitted to ACS Chemical Biology, , 2016.

<sup>33</sup>S. Richard et al., Nanotech, Poster, Washington –USA, 2013.

<sup>34</sup>S. Richard et al., Nano Bio Europe, Poster, Toulouse –France, 2013.

<sup>35</sup>S. Richard et al., European Materials Research Society Spring Meeting, Poster, Lille –France, 2013.

<sup>36</sup>S. Richard et al., Zing Bionanomaterials Conference, Oral, Nerja –Spain, 2014.

<sup>37</sup>S. Richard et al., European Materials Research Society Spring Meeting, Oral, Lille –France, 2014.

<sup>38</sup>J. Bolley et al., European Materials Research Society Spring Meeting, Oral, Lille –France, 2014.

<sup>39</sup>N. Chauffert et al., International Symposium on Biomedical Imaging, Poster, New–York –USA, 2015.

<sup>40</sup>M. Boucher et al., World Molecular Imaging Congress, Poster, Seoul –Korea, 2014.

<sup>41</sup>S. Prévéral et al., MagnetoTactic Bacteria, Poster, Rio de Janeiro –Brazil, 2014.

<sup>42</sup>M. Boucher et al., European Nanomedicine Meeting and Société Française de Nanomédecine, Poster, Grenoble –France, 2015.

<sup>43</sup>F. Geffroy et al., World Molecular Imaging Congress, Poster, Honolulu –USA, 2015.

<sup>44</sup>M. Boucher et al., MagnetoTactic Bacteria, Oral, Marseille –France, 2016.

<sup>45</sup>M. Boucher et al., In preparation, , 2016.

presentations for WMIC<sup>46,47</sup> (New York, USA, September 2016) and MTB Congress<sup>48</sup> (Marseille, France, September 2016).

Finally this manuscript ends with a brief conclusion, followed by a summary of the PhD student role within the different collaborations that made this work possible.

---

<sup>46</sup>M. Boucher et al., World Molecular Imaging Congress, Poster, New-York –USA, 2016.

<sup>47</sup>F. Geffroy et al., World Molecular Imaging Congress, Poster, New-York –USA, 2016.

<sup>48</sup>F. Geffroy et al., MagnetoTactic Bacteria, Poster, Marseille –France, 2016.

## References

- [1] F. Reynolds and K. A. Kelly. Techniques for molecular imaging probe design. *Molecular Imaging*, **10**: 407–419, 2011. (see p. 2)
- [2] M. Mahmoudi, V. Serpooshan, and S. Laurent. Engineered nanoparticles for biomolecular imaging. *Nanoscale*, **3**: 3007–3026, 2011. DOI: [10.1039/c1nr10326a](https://doi.org/10.1039/c1nr10326a) (see pp. 2, 3)
- [3] C. Corot, P. Robert, J. Idee, and M. Port. Recent advances in iron oxide nanocrystal technology for medical imaging. *Advanced Drug Delivery Reviews*, **58**: 1471–1504, 2006. DOI: [10.1016/j.addr.2006.09.013](https://doi.org/10.1016/j.addr.2006.09.013) (see p. 2)
- [4] M.-F. Bellin, C. Beigelman, and S. Precetti-Morel. Iron oxide-enhanced MR lymphography: initial experience. *European Journal of Radiology*, **34**: 257–264, 2000. DOI: [10.1016/S0720-048X\(00\)00204-7](https://doi.org/10.1016/S0720-048X(00)00204-7) (see p. 2)
- [5] Jill Fredrickson, Natalie J. Serkova, Shelby K. Wyatt, Richard A. D. Carano, Andrea Pirzkall, Ina Rhee, Lee S. Rosen, Alberto Bessudo, Colin Weekes, and Alex DE Crespigny. Clinical translation of ferumoxytol-based vessel size imaging (VSI): Feasibility in a phase I oncology clinical trial population. *Magnetic Resonance in Medicine*, 2016. DOI: [10.1002/mrm.26167](https://doi.org/10.1002/mrm.26167) (see p. 2)
- [6] T. Y. Tang, S. P. S. Howarth, S. R. Miller, M. J. Graves, J. M. U-King-Im, Z. Y. Li, S. R. Walsh, P. D. Hayes, K. Varty, and J. H. Gillard. Comparison of the Inflammatory Burden of Truly Asymptomatic Carotid Atheroma with Atherosclerotic Plaques in Patients with Asymptomatic Carotid Stenosis Undergoing Coronary Artery Bypass Grafting: An Ultras-small Superparamagnetic Iron Oxide Enhanced Magnetic Resonance Study. *European Journal of Vascular and Endovascular Surgery*, **35**: 392–398, 2008. DOI: [10.1016/j.ejvs.2007.10.019](https://doi.org/10.1016/j.ejvs.2007.10.019) (see p. 2)
- [7] Z. Bakhtiary, A. A. Saei, M. J. Hajipour, M. Raoufi, O. Vermesh, and M. Mahmoudi. Targeted superparamagnetic iron oxide nanoparticles for early detection of cancer: Possibilities and challenges. *Nanomedicine: Nanotechnology, Biology and Medicine*, **12**: 287–307, 2015. DOI: [10.1016/j.nano.2015.10.019](https://doi.org/10.1016/j.nano.2015.10.019) (see p. 3)
- [8] S. Sharifi, H. Seyednejad, S. Laurent, F. Atyabi, A. A. Saei, and M. Mahmoudi. Superparamagnetic iron oxide nanoparticles for *in vivo* molecular and cellular imaging: SPIONs for Molecular and Cellular Imaging. *Contrast Media and Molecular Imaging*, **10**: 329–355, 2015. DOI: [10.1002/cmami.1638](https://doi.org/10.1002/cmami.1638) (see p. 3)
- [9] C. A. Pacak, P. E. Hammer, A. A. MacKay, Rory P. Dowd, K. R. Wang, A. Masuzawa, B. Sill, J. D. McCully, and D. B. Cowan. Superparamagnetic Iron Oxide Nanoparticles Function as a Long-Term, Multi-Modal Imaging Label for Non-Invasive Tracking of Implanted Progenitor Cells. *PLoS ONE*, **9**: e108695, 2014. DOI: [10.1371/journal.pone.0108695](https://doi.org/10.1371/journal.pone.0108695) (see p. 3)
- [10] P. Soares, I. Ferreira, R. Igreja, C. Novo, and J. Borges. Application of hyperthermia for cancer treatment: recent patents review. *Recent patents on anti-cancer drug discovery*, **7**: 64–73, 2012. (see p. 3)
- [11] S. C. Baetke, T. Lammers, and F. Kiessling. Applications of nanoparticles for diagnosis and therapy of cancer. *The British Journal of Radiology*, **88**: 20150207, 2015. DOI: [10.1259/bjr.20150207](https://doi.org/10.1259/bjr.20150207) (see pp. 3, 4)

- [12] F. Zhang, X. Huang, L. Zhu, N. Guo, G. Niu, M. Swierczewska, S. Lee, H. Xu, A. Y. Wang, K. A. Mohamedali, M. G. Rosenblum, G. Lu, and X. Chen. Noninvasive monitoring of orthotopic glioblastoma therapy response using RGD-conjugated iron oxide nanoparticles. *Biomaterials*, **33**: 5414–5422, 2012. DOI: [10.1016/j.biomaterials.2012.04.032](https://doi.org/10.1016/j.biomaterials.2012.04.032) (see pp. 3, 4)
- [13] J. Fang, H. Nakamura, and H. Maeda. The EPR effect: Unique features of tumor blood vessels for drug delivery, factors involved, and limitations and augmentation of the effect. *Advanced Drug Delivery Reviews*, **63**: 136–151, 2011. DOI: [10.1016/j.addr.2010.04.009](https://doi.org/10.1016/j.addr.2010.04.009) (see p. 4)
- [14] F. Danhier, A. Le Breton, and V. Pr at. RGD-Based Strategies To Target Alpha(v) Beta(3) Integrin in Cancer Therapy and Diagnosis. *Molecular Pharmaceutics*, **9**: 2961–2973, 2012. DOI: [10.1021/mp3002733](https://doi.org/10.1021/mp3002733) (see p. 4)
- [15] P. T. Caswell and J. C. Norman. Integrin Trafficking and the Control of Cell Migration: Integrin Trafficking and Cell Migration. *Traffic*, **7**: 14–21, 2006. DOI: [10.1111/j.1600-0854.2005.00362.x](https://doi.org/10.1111/j.1600-0854.2005.00362.x) (see p. 4)
- [16] P. C. Brooks, R. A. Clark, and D. A. Cheresch. Requirement of vascular integrin alpha v beta 3 for angiogenesis. *Science*, **264**: 569–571, 1994. DOI: [10.1126/science.7512751](https://doi.org/10.1126/science.7512751) (see p. 4)
- [17] C. Zhang, M. Jugold, E. C. Woenne, T. Lammers, B. Morgenstern, M. M. Mueller, H. Zentgraf, M. Bock, M. Eisenhut, W. Semmler, and F. Kiessling. Specific Targeting of Tumor Angiogenesis by RGD-Conjugated Ultrasmall Superparamagnetic Iron Oxide Particles Using a Clinical 1.5-T Magnetic Resonance Scanner. *Cancer Research*, **67**: 1555–1562, 2007. DOI: [10.1158/0008-5472.CAN-06-1668](https://doi.org/10.1158/0008-5472.CAN-06-1668) (see p. 4)
- [18] S. S. Stylli, R. B. Luwor, T. M.B. Ware, F. Tan, and A. H. Kaye. Mouse models of glioma. *Journal of Clinical Neuroscience*, **22**: 619–626, 2015. DOI: [10.1016/j.jocn.2014.10.013](https://doi.org/10.1016/j.jocn.2014.10.013) (see p. 4)
- [19] Nienke A. DE Vries, Jos H. Beijnen, and Olaf VAN Tellinghen. High-grade glioma mouse models and their applicability for preclinical testing. *Cancer Treatment Reviews*, **35**: 714–723, 2009. DOI: [10.1016/j.ctrv.2009.08.011](https://doi.org/10.1016/j.ctrv.2009.08.011) (see p. 5)
- [20] K. Gr nberg, E.-C. Muller, A. Otto, R. Reszka, D. Linder, M. Kube, R. Reinhardt, and D. Schuler. Biochemical and Proteomic Analysis of the Magnetosome Membrane in *Magnetospirillum gryphiswaldense*. *Applied and Environmental Microbiology*, **70**: 1040–1050, 2004. DOI: [10.1128/AEM.70.2.1040-1050.2004](https://doi.org/10.1128/AEM.70.2.1040-1050.2004) (see p. 6)
- [21] J. Xie, K. Chen, and X. Chen. Production, modification and bio-applications of magnetic nanoparticles gestated by magnetotactic bacteria. *Nano Research*, **2**: 261–278, 2009. DOI: [10.1007/s12274-009-9025-8](https://doi.org/10.1007/s12274-009-9025-8) (see p. 6)
- [22] N. Ginet, R. Pardoux, G. Adryanczyk, D. Garcia, C. Brutesco, and D. Pignol. Single-Step Production of a Recyclable Nanobiocatalyst for Organophosphate Pesticides Biodegradation Using Functionalized Bacterial Magnetosomes. *PLoS ONE*, **6**: e21442, 2011. DOI: [10.1371/journal.pone.0021442](https://doi.org/10.1371/journal.pone.0021442) (see p. 6)
- [23] S. M riaux, M. Boucher, B. Marty, Y. Lalatonne, S. Pr v ral, L. Motte, C. T. Lef vre, F. Geffroy, F. Lethimonnier, M. P an, D. Garcia, G. Adryanczyk-Perrier, D. Pignol, and N. Ginet. Magnetosomes, Biogenic Magnetic Nanomaterials for Brain Molecular Imaging with 17.2 T MRI Scanner. *Advanced Healthcare Materials*, **4**: 1076–1083, 2015. DOI: [10.1002/adhm.201400756](https://doi.org/10.1002/adhm.201400756) (see p. 6)

- [24] M. Boucher, N. Ginet, B. Marty, C. T. Lefèvre, D. Garcia, D. Pignol, and S. Mériaux. *In Vivo* characterization of MV1-magnetosomes as biogenic contrast agents dedicated to high field MRI: a dose study. *World Molecular Imaging Congress*, Poster, Savannah –USA, 2013. (see p. 6)
- [25] M. Boucher, N. Ginet, B. Marty, C. T. Lefèvre, D. Garcia, D. Pignol, and S. Mériaux. *In Vivo* characterization of MV1-magnetosomes as biogenic contrast agents dedicated to high field MRI: a dose study. *Groupe Thématique de Recherche sur la Vectorisation (now Société Française de Nanomédecine)*, Oral, Orléans –France, 2013. (see p. 6)
- [26] M. Boucher, N. Ginet, F. Geffroy, S. Prévéral, G. Adryanczyk-Perrier, M. Péan, C.T. Lefèvre, D. Garcia, D. Pignol, and S. Mériaux. Genetically functionalized magnetosomes as MRI contrast agent for molecular imaging: *in vitro* proof of binding and *in vivo* proof of contrast. *Neuroscience Workshop of Saclay*, Oral, Saclay –France, 2014. (see p. 6)
- [27] N. Ginet, S. Mériaux, M. Boucher, B. Marty, Y. Lalatonne, S. Prévéral, L. Motte, C. T. Lefèvre, F. Geffroy, F. Lethimonnier, M. Péan, D. Garcia, G. Adryanczyk, and D. Pignol. Towards molecular imaging with high-field MRI and biogenic contrast agents. *MagnetoTactic Bacteria*, Oral, Rio de Janeiro –Brazil, 2014. (see p. 6)
- [28] M. Boucher, N. Ginet, F. Geffroy, S. Prévéral, G. Adryanczyk-Perrier, M. Péan, C. T. Lefèvre, D. Garcia, D. Pignol, and S. Mériaux. Fonctionnalisation par génie génétique de magnétosomes pour l’imagerie moléculaire par IRM de biomarqueurs tumoraux. *Société Française de Résonance Magnétique en Biologie et Médecine*, Oral, Grenoble –France, 2015. (see pp. 6, 7)
- [29] M. Boucher, N. Ginet, F. Geffroy, S. Prévéral, G. Adryanczyk-Perrier, M. Péan, C. T. Lefèvre, D. Garcia, D. Pignol, and S. Mériaux. Genetically functionalized magnetosomes as MRI contrast agent for molecular imaging: *in vitro* proof of binding and *in vivo* proof of contrast. *International Society of Magnetic Resonance in Medicine*, Oral, Toronto –Canada, 2015. (see p. 7)
- [30] S. Richard, M. Boucher, A. Herbet, Y. Lalatonne, S. Mériaux, D. Boquet, and L. Motte. Endothelin B receptors targeted by iron oxide nanoparticles functionalized with a specific antibody: toward immunoimaging of brain tumors. *Journal of Materials Chemistry B*, **3**: 2939–2942, 2015. DOI: [10.1039/C5TB00103J](https://doi.org/10.1039/C5TB00103J) (see p. 7)
- [31] S. Richard, M. Boucher, A. Saric, A. Herbet, Y. Lalatonne, P. X. Petit, S. Mériaux, D. Boquet, and L. Motte. Optimization of pegylated iron oxide nanoplatfoms for Antibody coupling and bio-targeting. *Submitted to ACS Applied Materials & Interfaces*, 2016. (see p. 7)
- [32] S. Richard, A. Saric, M. Boucher, Françoise Geffroy, S. Mériaux, Y. Lalatonne, P. X. Petit, and L. Motte. Anti-oxidative theranostic iron oxide nanoparticles towards brain tumors imaging and ROS production. *Submitted to ACS Chemical Biology*, 2016. (see p. 7)
- [33] S. Richard, M. Boucher, A. Herbet, E. Guénin, Y. Lalatonne, S. Mériaux, J. P. Hugnot, D. Boquet, and L. Motte. Functionalization of nanoplatfom: toward a new contrast agent specific of brain tumors. *Nanotech*, Poster, Washington –USA, 2013. (see p. 7)
- [34] S. Richard, M. Boucher, A. Herbet, Y. Lalatonne, S. Mériaux, J. P. Hugnot, D. Boquet, and L. Motte. Nanoplatfom for immuno imaging of brain tumors by MRI. *Nano Bio Europe*, Poster, Toulouse –France, 2013. (see p. 7)

- [35] S. Richard, A. Herbet, M. Boucher, Y. Lalatonne, S. Mériaux, J. P. Hugnot, D. Boquet, and L. Motte. Superparamagnetic nanoparticles for immuno imaging of brain tumors by MRI. *European Materials Research Society Spring Meeting*, Poster, Lille –France, 2013. (see p. 7)
- [36] S. Richard, M. Boucher, A. Herbet, Y. Lalatonne, S. Mériaux, J. P. Hugnot, D. Boquet, and L. Motte. Superparamagnetic nanoparticles for MRI brain tumors molecular imaging. *Zing Bionanomaterials Conference*, Oral, Nerja –Spain, 2014. (see p. 7)
- [37] S. Richard, A. Herbet, M. Boucher, Y. Lalatonne, S. Mériaux, J. P. Hugnot, D. Boquet, and L. Motte. Development of nanoplateform for multimodal imaging of brain tumors. *European Materials Research Society Spring Meeting*, Oral, Lille –France, 2014. (see p. 7)
- [38] J. Bolley, M. Boucher, S. Mériaux, N. Pinna, L. Motte, and Y. Lalatonne. Iron oxide nanoparticles size effect on  $T_1$  and  $T_2$  MRI contrast. *European Materials Research Society Spring Meeting*, Oral, Lille –France, 2014. (see p. 7)
- [39] N. Chauffert, P. Weiss, M. Boucher, S. Mériaux, and P. Ciuciu. Variable density sampling based on physically plausible gradient waveform: application to 3D MRI angiography. *International Symposium on Biomedical Imaging*, Poster, New-York –USA, 2015. (see p. 7)
- [40] M. Boucher, N. Ginet, F. Geffroy, S. Prévéral, G. Adryanczyk-Perrier, M. Péan, C. T. Lefèvre, D. Garcia, D. Pignol, and S. Mériaux. Genetically functionalized RGD-magnetosomes as MRI contrast agent: *in vitro* proof of concept. *World Molecular Imaging Congress*, Poster, Seoul –Korea, 2014. (see p. 7)
- [41] S. Prévéral, G. Adryanczyk-Perrier, F. Geffroy, M. Péan, M. Boucher, C.T. Lefèvre, D. Garcia, S. Mériaux, D. Pignol, and N. Ginet. RGD-functionalized magnetosomes, a contrast agent with molecular affinity for diagnostic in Magnetic Resonance Imaging. *MagnetoTactic Bacteria*, Poster, Rio de Janeiro –Brazil, 2014. (see p. 7)
- [42] M. Boucher, F. Geffroy, E. Selingue, N. Ginet, S. Prévéral, L. Bellanger, G. Adryanczyk-Perrier, M. Péan, C.T. Lefèvre, D. Garcia, D. Pignol, and S. Mériaux. Genetically functionalized magnetosomes used as MRI probe for molecular imaging of U87 tumor. *European Nanomedicine Meeting and Société Française de Nanomédecine*, Poster, Grenoble –France, 2015. (see p. 7)
- [43] F. Geffroy, M. and. Boucher, N. Ginet, S. Prévéral, L. Bellanger, G. Adryanczyk-Perrier, M. Péan, C.T. Lefèvre, D. Garcia, D. Pignol, and S. Mériaux. *In vitro* characterization of AMB1 magnetosomes as biogenic functionalized contrast agents dedicated to molecular MRI. *World Molecular Imaging Congress*, Poster, Honolulu –USA, 2015. (see p. 7)
- [44] M. Boucher, F. Geffroy, E. Selingue, N. Ginet, S. Prévéral, L. Bellanger, G. Adryanczyk-Perrier, M. Péan, C.T. Lefèvre, D. Garcia, D. Pignol, and S. Mériaux. Genetically functionalized magnetosomes used as MRI contrast agent for *in vivo* molecular imaging of brain tumor in U87 mice. *MagnetoTactic Bacteria*, Oral, Marseille –France, 2016. (see p. 7)
- [45] M. Boucher, F. Geffroy, N. Ginet, S. Prévéral, L. Bellanger, Selingue, G. Adryanczyk-Perrier, M. Péan, C. T. Lefèvre, D. Garcia, D. Pignol, and S. Mériaux. Genetically tailored iron-oxide nanoparticles used as MRI probe for *in vivo* molecular imaging of brain tumor. *In preparation*, 2016. (see p. 7)

- 
- [46] M. Boucher, F. Geffroy, E. Selingue, N. Ginet, S. Prévéral, G. Adryancyk-Perrier, M. Péan, C.T. Lefèvre, D. Garcia, D. Pignol, and S. Mériaux. Multi-injection of RGD functionalized magnetosomes to improve *in vivo* iron uptake by U87 brain tumor. *World Molecular Imaging Congress*, Poster, New-York –USA, 2016. (see p. 8)
- [47] F. Geffroy, M. and. Boucher, N. Ginet, S. Prévéral, L. Bellanger, G. Adryancyk-Perrier, M. Péan, C.T. Lefèvre, D. Garcia, D. Pignol, and S. Mériaux. *In vitro* multimodal imaging characterization of RGD functionalized magnetosomes accumulation in U87 glioblastoma cells. *World Molecular Imaging Congress*, Poster, New-York –USA, 2016. (see p. 8)
- [48] F. Geffroy, M. and. Boucher, N. Ginet, S. Prévéral, L. Bellanger, G. Adryancyk-Perrier, M. Péan, C.T. Lefèvre, D. Garcia, D. Pignol, and S. Mériaux. *In vitro* multimodal imaging characterization of RGD functionalized magnetosomes accumulation in U87 glioblastoma cells. *MagnetoTactic Bacteria*, Poster, Marseille –France, 2016. (see p. 8)



# Iron-oxide nanoparticles for diagnostic and therapeutic applications

## Contents

---

<b>2.1</b>	<b>Why iron nanoparticles?</b> . . . . .	<b>16</b>
2.1.1	Physical origin of magnetism . . . . .	16
2.1.2	Magnetism of nanoparticles . . . . .	18
2.1.3	The interest of IONP in MRI . . . . .	20
2.1.4	Relaxation models for IONP . . . . .	22
<b>2.2</b>	<b>How to optimize IONPs contrasting properties?</b> . . . . .	<b>25</b>
2.2.1	Superparamagnetic iron core optimization . . . . .	26
2.2.2	Coating optimization . . . . .	29
<b>2.3</b>	<b>Interest of magnetosomes as MRI contrast agent</b> . . . . .	<b>31</b>
2.3.1	Magnetotactic bacteria and magnetosomes . . . . .	31
2.3.2	Magnetosomes physico-chemical properties . . . . .	34
<b>2.4</b>	<b>Other biomedical applications of IONP</b> . . . . .	<b>36</b>
2.4.1	IONP labeled cells . . . . .	37
2.4.2	Magnetic hyperthermia . . . . .	40
	<b>References</b> . . . . .	<b>42</b>

---

Molecular imaging is a multi-disciplinary field including medical imaging and contrast agent design. Notwithstanding medicine and biology are essential to define relevant biomarkers, this PhD work has been dedicated to improve contrast agent detection as introduced, and this second chapter focuses on the use of iron-oxide nanoparticle as contrast agent for MRI.

This chapter introduces iron-oxide nanoparticles in general, define their particular magnetic behaviors, and their properties as MRI contrast agent. Conventional chemically produced iron-oxide crystals are presented, followed by biogenic magnetosomes, and their MRI contrast efficiency is discussed. Finally, other biomedical applications of iron-oxide based nanoparticles, such as cell tracking and hyperthermia treatment, are highlighted.

## 2.1 Why iron nanoparticles?

Numerous nanoparticles have recently emerged from physics, chemistry and biology because of their unique properties that make them very interesting for biomedical applications. The limited size of nanoparticles versus bulk can dramatically modify the resulting physical features. Iron-oxide nanoparticles perfectly embody this phenomenon since magnetic properties are highly dependent on the size of the sample.

### 2.1.1 Physical origin of magnetism

Iron-oxides cover a broad range of materials composed of oxygen and iron atoms at various oxidation states. Iron(II) oxide ( $FeO$ ) is used as a flammable component, while iron(III) oxide ( $Fe_2O_3$ ) can be used as pigment. Finally, mixture of iron(II) and iron(III) ( $Fe_3O_4$  or  $FeO - Fe_2O_3$ ) is known as magnetite because it can naturally possess magnetic properties.

Let us assume that we have a lattice of ions which can be seen as discrete and independent sources of magnetic moment. No macroscopic magnetization is observed because of source independence. Adding an external magnetic field would induce an alignment of all magnetic sources leading to a macroscopic magnetization of the assembly. The resulting magnetization is either parallel or anti-parallel with the external magnetic field and the material is respectively

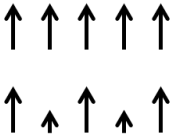
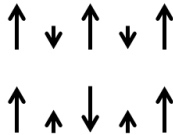
Spin lattice example			
Magnetic order	Ferromagnetic	Antiferromagnetic	Ferrimagnetic
Magnetization	Permanent	None	Permanent
Example	Fe	FeO	$Fe_3O_4$
Curie/Néel temperature	1043 K	198 K	858 K

Fig. 2.1 – Magnetic orders described with linear spin lattice, example of materials and their characteristic temperatures. Adapted from Ashcroft and Mermin<sup>1</sup>.

called **paramagnetic** or **diamagnetic**.

To understand how a material can have a macroscopic magnetization, even without any external magnetic field, it is needed to consider that interactions between the discrete sources of magnetization can occur in some cases, to eventually confer magnetic order to the assembly. Indeed, the exchange energy is decreased when all sources are parallel and point in the same direction. As displayed in Figure 2.1, magnetic sources can add up in a permanent magnetization or can compensate in a null magnetization. In the case where all sources have a component parallel to the resulting magnetic field, the order is called **ferromagnetic**, else it is called **ferrimagnetic**. Finally, if the magnetic order does not lead to a permanent magnetization because the sources compensate each other, the order is called **antiferromagnetic**.

Besides, above a characteristic temperature depending on the material, all magnetic orders disappear because of thermal motion, and the material becomes paramagnetic. This temperature is called the **Curie temperature** ( $T_C$ ) for ferromagnetic and ferrimagnetic materials or the **Néel temperature** ( $T_N$ ) for antiferromagnetic ones<sup>1</sup>.

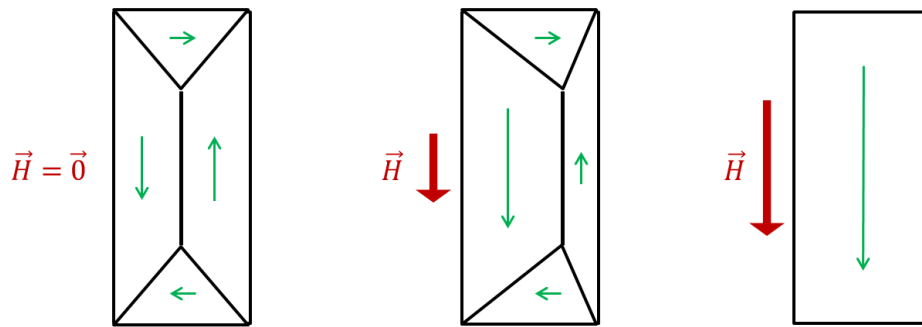


Fig. 2.2 – Theoretical example of magnetic domains that reduce magnetostatic energy at a null magnetization and the evolution of domain walls when an external magnetic field is applied. Domain magnetizations are drawn in green and external magnetic field in red.

A state where all magnetic sources are aligned (as the first ferromagnetic lattice in Figure 2.1) requires a high magnetostatic energy, whereas a system divided in macroscopic magnetic domains with different magnetizations (as the scheme of multidomain sample in Figure 2.2) presents a significantly lower one. Magnetic domains reduce magnetostatic energy but cost exchange energy to create walls. These walls correspond to the boundaries between two domains of different magnetizations where a smooth twist of magnetic moment occurs on few lattice parameters. The size of magnetic domains results from balance between saving magnetostatic energy without spending too much exchange energy. As a consequence, the resulting magnetization of a multidomain material is smaller than if it was monodomain, but it is possible to increase it until its **saturation magnetization** ( $M_S$ ) by applying an external magnetic field, that would induce alignment of some domain magnetizations given the field intensity (see Figure 2.2). Another important parameter is the presence of defects in the material that can hinder from moving or creating domain walls<sup>2</sup>. Crystallographic perfection is then important to easily

<sup>1</sup>N. W. Ashcroft et al. *Physique des Solides*. EDP Sciences 2002.

<sup>2</sup>Ö. Özdemir et al., *Journal of Geophysical Research: Solid Earth*, **102**: 20211–20224, 1997.

reach saturation magnetization under external magnetic field application. In addition, all magnetization directions are not equivalent in the crystal: thus the magnetocrystalline anisotropy energy is lower when sample magnetization is aligned with the crystal magnetization easy axis. This implies that magnetic domains orientation will also try to align with this easy axis. In particular, in a polycrystal, each monocrystalline grain will be divided in magnetic domains which magnetizations are mainly parallel or antiparallel to this easy axis, which may induce a null net magnetization.

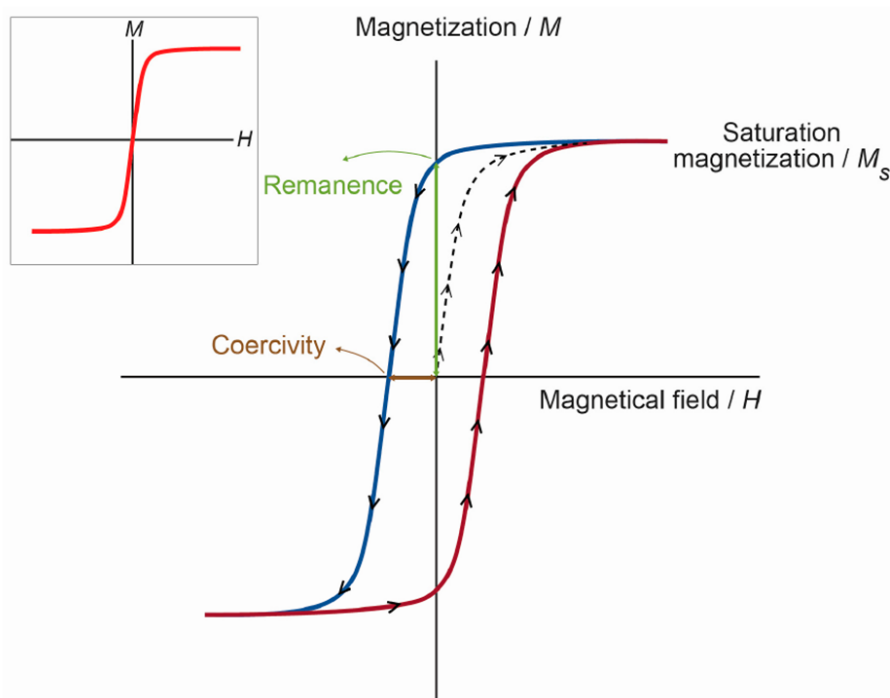


Fig. 2.3 – Magnetization loop of a ferromagnetic material, the inset represents the magnetization loop of a superparamagnetic material.  $H$  is the applied magnetic field and  $M$  the measured magnetization, from Estelrich *et al*<sup>3</sup>.

Magnetic hysteresis loop reflects that defects play a key role in magnetism. A magnetization cycle experiment consists in measuring the magnetization of a non-magnetized material (dashed line) during the application of an increasing or decreasing external magnetic field. In a multidomain material, one can increase the magnetic field intensity, giving sufficient energy to reach a state where a maximum of magnetic sources is aligned (saturation magnetization). This requires the displacement of domain walls across some defects. Then, if decreasing the applied magnetic field to zero, magnetization will not decrease as much because these defects block domain walls from moving back to their initial position. Thus, when the applied magnetic field is null, there is still a magnetization which is called the **remanence**. To demagnetize the material, it is necessary to apply a magnetic field in the other direction called **coercivity**. An illustration<sup>3</sup> of a hysteresis loop for a ferromagnetic material is given in Figure 2.3.

### 2.1.2 Magnetism of nanoparticles

These brief and non exhaustive considerations about solid state physics of magnetic materials lead us finally to exhibit the specificity that iron-oxide nanoparticles are gifted with. We just

<sup>3</sup>J. Estelrich et al., International Journal of Molecular Sciences, **16**: 8070–8101, 2015.

explained that magnetic domains occur to minimize material internal energy, but what become these domains in a nano-sized material? In particular when the domains size reaches particles size itself?

If we start from an infinite material segregated in multiple magnetic domains and we mentally reduce its size, we can get to a point where energy gain coming from the creation of two domains become smaller than the cost to create the wall between them. Thus, below this size called **critical diameter** ( $D_{CR}$ ), particles are characterized as **single domain** (or monodomain) and possess a net magnetization with or without external magnetic field application. If we continue to reduce the particle size, we reach another characteristic diameter called **superparamagnetic diameter** ( $D_{SPM}$ ), below which the thermal energy is higher than the energy barrier between two magnetization states (up and down). Sample magnetization can then flip-flop between both states and particles present no magnetization but can be magnetized under external magnetic field application. In such particle, called **superparamagnetic**, the sample magnetization follows the applied magnetic field, resulting in a S-shape curve for magnetization-demagnetization experiment, as illustrated by the inset Figure 2.3.

Perfection of nanoparticle crystal lattice (lack of defect in the crystalline lattice) is very important to ensure that saturation magnetization can be easily reached under magnetic field application. Polycrystalline nanoparticles or aggregate of monocrystalline nanoparticles will consequently have a smaller saturation magnetization than a monocrystal of comparable size. For specific applications requiring high magnetization, monocrystal with as less defects as possible will be preferred. However, applications where magnetized nanoparticles are needed without applying any external magnetic field, like in magnetic storage for example, defects can be important to increase nanoparticles remanence.

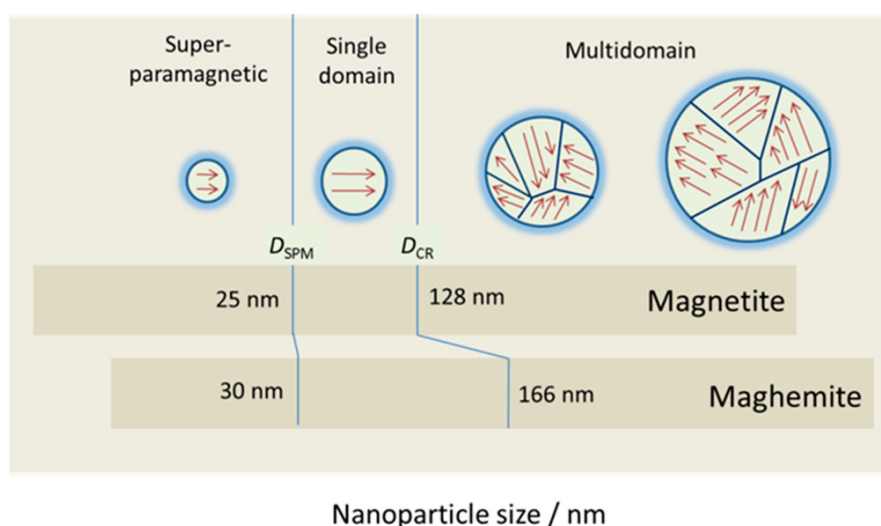


Fig. 2.4 – Magnetic regimes of magnetite and maghemite as a function of particle size (superparamagnetic, single domain, multidomain), from Estelrich *et al*<sup>3</sup>.

We just discussed how nanoparticles exhibit different magnetic properties compared to bulk because of volumic considerations, but surfacic effects have also a part to play. Indeed, magnetic sources at the surface present a certain disorder, because of symmetry breaking, that prevents the good alignment with their neighbors compared with material core. As a consequence, nanometric particles for which the surface-to-volume ratio increases will present a lower

magnetization than expected<sup>4</sup>. The saturation magnetization of nanoparticles is lower or, in the best case, equal to the bulk saturation magnetization ( $M_S^{Bulk}(Fe_3O_4) = 92 \text{ emu} \cdot g^{-1}$ ).

Now we can draw an overview of the magnetic behavior of both magnetite and maghemite nanoparticles. Magnetite is a ferrimagnetic material with a Curie temperature of  $T_C = 858 \text{ K}$ , that exhibits a permanent magnetic moment at room temperature. Until the micrometer scale, magnetite presents multidomain structure. Between 25 and 128  $nm$ , magnetite nanoparticles become single domain and still possess a magnetization. Below 25  $nm$ , magnetite nanoparticles are superparamagnetic without intrinsic magnetization. Maghemite nanoparticles have a similar behavior with different characteristic diameters (Maghemite,  $\gamma - Fe_2O_3$ , is obtained by oxidation of magnetite). The figure 2.4 schematically presents the presence or absence of magnetic domains given the particle size, and resumes characteristic diameter values for magnetite and maghemite<sup>3</sup>.

The acronym **IONP**, Iron Oxide NanoParticle, will now be used for both magnetite and maghemite nanoparticles, and type of materials will be indicated when needed.

### 2.1.3 The interest of IONP in MRI

We have settled that the magnetic properties of IONP are strongly dependent on their size, and that crystallinity needs to be considered. Let us now study a standard IONP and try to understand their potential interest for MRI applications, prior to highlight how to imagine the best iron-oxide based MRI Contrast Agent (CA).

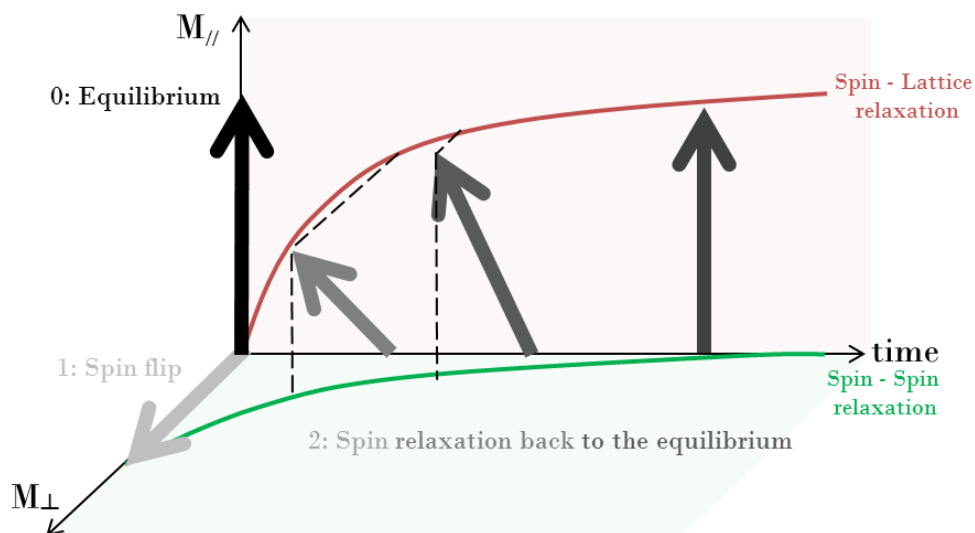


Fig. 2.5 – Scheme of nuclear spin magnetization relaxation after a  $90^\circ$  flip. The longitudinal component of magnetization grows back under the Spin-Lattice or  $T_1$  relaxation. The transverse component of magnetization decays under the Spin-Spin or  $T_2$  relaxation.

<sup>4</sup>B. Issa et al., International Journal of Molecular Sciences, **14**: 21266–21305, 2013.

The MR signal comes from the nuclear spin of water protons present in different biological tissues, and depends on three parameters, which vary with the tissue characteristics:

- $M_0$ , the proton density in the considered tissue.
- $T_1$ , the **longitudinal relaxation time**, which is characteristic of the **Spin-Lattice** relaxation. It is the mechanism by which the magnetization component parallel to the static magnetic field grows back to equilibrium through energy transfer to the surrounding spins in the lattice.
- $T_2$ , the **transverse relaxation time**, which is characteristic of the **Spin-Spin** relaxation. It is the mechanism by which all spins are not exposed to the same local magnetic field because of interactions with their neighbors, and then will not have the same precession frequency, resulting in a dephasing that increases the decay of the transverse component of the magnetization. Furthermore, an additional dephasing can also occur because of external sources of magnetic field inhomogeneities. The **resulting transverse relaxation time**  $T_2^*$ , shorter than  $T_2$ , gathers both the internal and external causes of Spin-Spin relaxation.

If we consider a classic MRI experiment like a Spin Echo sequence, the signal behaves as described by the equation 2.1, which is illustrated in Figure 2.5.

$$S^{MRI} \propto M_0 \cdot \left(1 - \exp\left(\frac{-T_R}{T_1}\right)\right) \cdot \exp\left(\frac{-T_E}{T_2}\right) \quad (2.1)$$

The times  $T_R$  (repetition time) and  $T_E$  (echo time), are experimental parameters that have to be adjusted considering the contrast enhancement that one seeks in the MR image.

MRI contrast agent will affect both  $T_1$  and  $T_2$ , generally with a greater effect on one of the two characteristic times. This rises up two types of MRI contrast agent called  $T_1$  or  $T_2$  agent considering their main effect. Usually,  $T_1$  agents will shorten  $T_1$  more than  $T_2$  and thus lead to an increase of MR signal in  $T_1$ -weighted image, whereas  $T_2$  ones will do the opposite and lead to a decrease of MR signal in  $T_2$ -weighted image. Indeed, all MRI contrast agents lead to local fluctuations of magnetic field because of their electronic spins which can interact with nuclear spins of protons. This interaction enhances energetic transitions between the different states of spins in the lattice (reduced  $T_1$ ) and the dephasing between spins (reduced  $T_2$ ). The relative impact between  $T_1$  and  $T_2$  depends on many parameters, for example: the distance between proton nuclear spin and contrast agent electronic spin, the intensity of the electronic magnetic moment of the contrast agent, the interaction time, the local concentration in contrast agent and the intensity of the static magnetic field  $B_0$ , among others (SBM theory<sup>5-7</sup>).

Those contrasting effects on either  $T_1$  or  $T_2$  are quantified using the respective longitudinal  $r_1$  and transverse  $r_2$  relaxivities, according to the following equation that links relaxation times decrease with CA concentration<sup>8</sup>. This relation is valid on a certain range of concentration that depends on the contrast agent. At high concentration, a saturation can be observed after the linear regime.

$$\frac{1}{T_i} = \frac{1}{T_i^0} + r_i \cdot [CA] \quad i = 1, 2 \quad (2.2)$$

<sup>5</sup>I. Solomon., Physical Review, **99**: 559–565, 1955.

<sup>6</sup>N. Bloembergen., The Journal of Chemical Physics, **27**: 572–573, 1957.

<sup>7</sup>N. Bloembergen et al., Journal of Chemical Physics, **34**: 842–850, 1961.

<sup>8</sup>T. J. Swift et al., The Journal of Chemical Physics, **37**: 307, 1962.

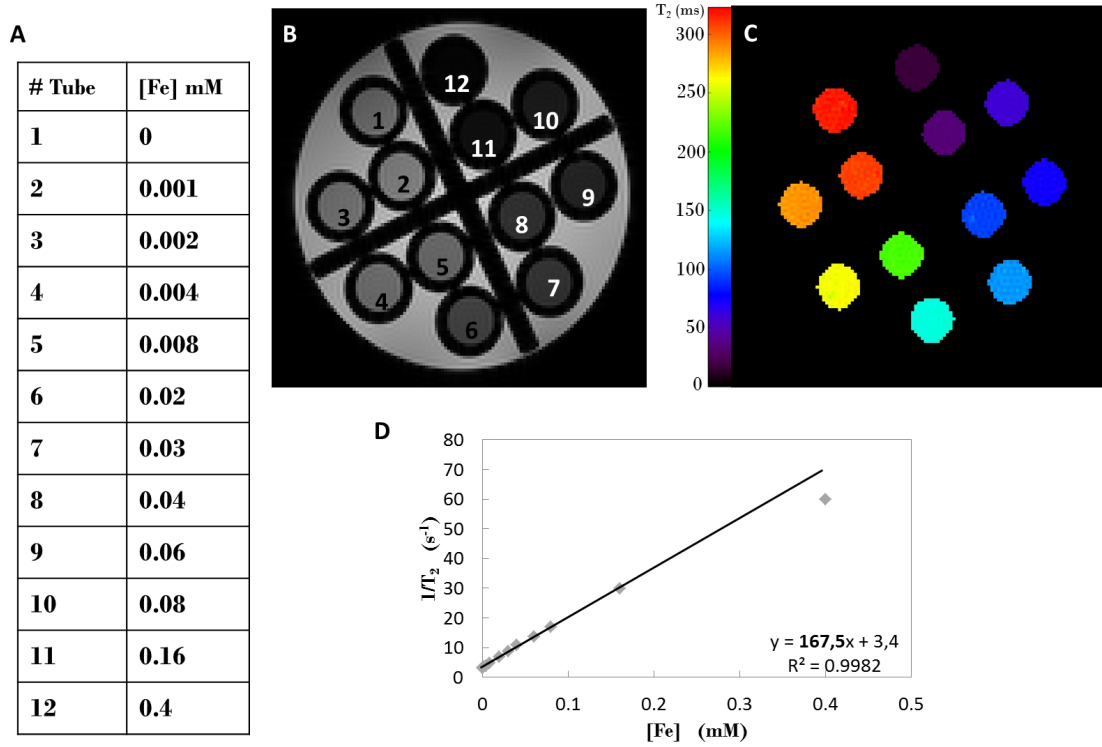


Fig. 2.6 – Phantom made with tubes containing concentrations of Endorem<sup>®</sup> (Guerbet) in agarose. A/ Table of iron concentration in each tube. B/  $T_2$ -weighted MRI image at 7 T that exhibits contrast enhancement induced by Endorem<sup>®</sup>. C/ Reconstructed  $T_2$  map that shows the  $T_2$  value obtained for each Endorem<sup>®</sup> concentration. D/ Linear fit to estimate the transverse relaxivity:  $r_2 = 167.5 \text{ mM}^{-1} \text{ s}^{-1}$ .

IONP possesses a high magnetic moment that can interact with the nuclear spin of surrounding protons by dipole-dipole interactions. Furthermore, this magnetic moment creates an important static magnetic field distortion that has a greater effect on  $T_2$  decrease than  $T_1$  one, and also induces a very strong  $T_2^*$  shortening. As a consequence, IONP will mainly be used for their properties to reduce MRI signal, either using  $T_2$  or  $T_2^*$  imaging strategies.

Figure 2.6 illustrates the difference of contrast observed on  $T_2$  images, induced by different concentrations of an IONP. According to Equation 2.2, the transverse relaxivity is measured as the slope of the linear fit of the relaxation rate  $R_2 = \frac{1}{T_2}$  versus iron concentration ( $T_i^0$  being the relaxation time of water proton without contrast agent). The detailed protocol of this experiment is described in Appendix A.1. In this example, one can notice that the higher concentration stands out of the linear regime, and then needs to be removed to estimate a relevant relaxivity value.

### 2.1.4 Relaxation models for IONP

Finding theories to describe and predict contrasting properties of IONP remains a very challenging task. Lately, Vuong *et al.*<sup>9</sup> have proposed a universal scaling law that gathers the different

<sup>9</sup>Q. L. Vuong et al., Advanced Healthcare Materials, 1: 502–512, 2012.

relaxation regimes that were introduced previously,<sup>10,11</sup> enabling to theoretically predict the transverse relaxivity from the physical features of nanoparticle.

To describe those regimes, we need to define:

- $\Delta\omega = \frac{\gamma\mu_0 M_{S,v}}{3}$ , the angular frequency shift experienced by a proton at the equator of the particle.  $\gamma$  is the gyromagnetic factor of the proton,  $\mu_0$  is the magnetic permeability of vacuum and  $M_{S,v}$  the volumic saturation magnetization of the particle. Notice that:  $M_{S,v} \neq M_S$ ,  $M_{S,v}$  is the volumic saturation magnetization, often measured in  $Oe$  or  $A \cdot m^{-1}$  in SI, while  $M_S$  is the mass saturation magnetization, often measured in  $emu \cdot g^{-1}$  or  $A \cdot m^2 \cdot kg^{-1}$  in SI.
- $\tau_D = \frac{d^2}{4D}$ , the translational diffusion time of the proton in the magnetic field inhomogeneities created by IONP.  $d$  is the IONP diameter and  $D$  is the translational diffusion coefficient of water.

**Motional Averaging Regime, (MAR)** Water molecules can diffuse across all the possible magnetic fields around IONP. This regime is then valid if  $\Delta\omega\tau_D < 1$ . In such conditions, the theoretical transverse relaxivity is equal to:

$$r_2 = \frac{R_2}{[Fe]} = \frac{4\gamma^2\mu_0^2\nu_{mat}M_{S,v}^2d^2}{405D} \quad (2.3)$$

where  $\nu_{mat}$  is the molar volume of the material, which is equal to the ratio of the molar mass on the number of magnetic ions times the mass density. For example, in the case of magnetite with  $M_{Fe_3O_4} = 232 \text{ g} \cdot \text{mol}^{-1}$  and  $\rho_{Fe_3O_4} = 5200 \text{ kg} \cdot \text{m}^{-3} = 5.2 \times 10^6 \text{ g} \cdot \text{m}^{-3}$ :

$$\begin{aligned} \nu_{Fe_3O_4} &= \frac{M_{Fe_3O_4}}{3\rho_{Fe_3O_4}} \\ &= 1,48 \times 10^{-5} \text{ m}^3 \cdot \text{mol}^{-1} \end{aligned}$$

In the MAR, transverse relaxivity strongly depends on volumic saturation magnetization and on size of IONP.

**Static Dephasing Regime, (SDR)** Protons of water molecules have access only to a reduced space compared to the MAR and then, their diffusion can be ignored. This regime is therefore valid for  $1 < \Delta\omega\tau_D < 20$ . In such conditions, the equation only applies to  $r_2^*$  but gives an upper bound for  $r_2$ . The theoretical apparent transverse relaxivity in this regime is equal to:

$$r_2^* = \frac{R_2^*}{[Fe]} = \frac{2\pi\gamma\mu_0\nu_{mat}M_{S,v}}{9\sqrt{3}} \sim r_2 \quad (2.4)$$

Then in the SDR, transverse relaxivity does not depend on IONP radius but only on its volumic saturation magnetization.

<sup>10</sup>R. A. Brooks et al., *Magnetic Resonance in Medicine*, **45**: 1014–1020, 2001.

<sup>11</sup>P. Gillis et al., *Magnetic Resonance in Medicine*, **47**: 257–263, 2002.

**Partial Refocusing Model, (PRM)** It is similar to SDR but in this regime, echo time of MRI sequence will have an effect on relaxation rates measurements. This regime is valid when  $\Delta\omega\tau_D > 20$ . No theoretical universal formula to estimate the transverse relaxivity is given since it is needed to take echo time into account<sup>11</sup>. The only indication available is that transverse relaxivity rate will decrease as  $1/\tau_D$ , which means it will decrease when the particle radius increases.

**Conclusion** These models are defined given  $\Delta\omega\tau_D$  range, but frontiers at 1 or 20 do not establish a clear transition of behavior. This is the reason why for  $\Delta\omega\tau_D$  values between 1 and 5, none of these models gives a relevant estimation for  $r_2$ . It is the same around 20, where the SDR formula is not totally valid anymore. In conclusion, theoretical  $r_2$  formulas are useful to estimate real relaxivities but need to be discussed given model validity and experimental conditions. The interesting work of Vuong *et al*<sup>9</sup> gives also rise to a theoretical maximum value of transverse relaxivity around  $750 \text{ mM}^{-1}\text{s}^{-1}$ . Authors claim this maximum value is achievable when  $\Delta\omega\tau_D \sim 10$ , which corresponds to single ferromagnetic cores with a diameter of  $55 \text{ nm}$  that fully falls in the SDR. One needs to keep in mind that these models stand for relatively high magnetic field intensity since they assume that IONPs are fully magnetized (magnetization reaches saturation magnetization). Finally, as pointed out by the authors, this maximal value of  $r_2$  will be achieved only with  $55 \text{ nm}$  diameter IONP as mono-disperse as possible<sup>9</sup>. Smaller particles might shift into MAR leading to lower mean relaxivity, while bigger particles might shift into PRM which also lead in lowering mean relaxivity.

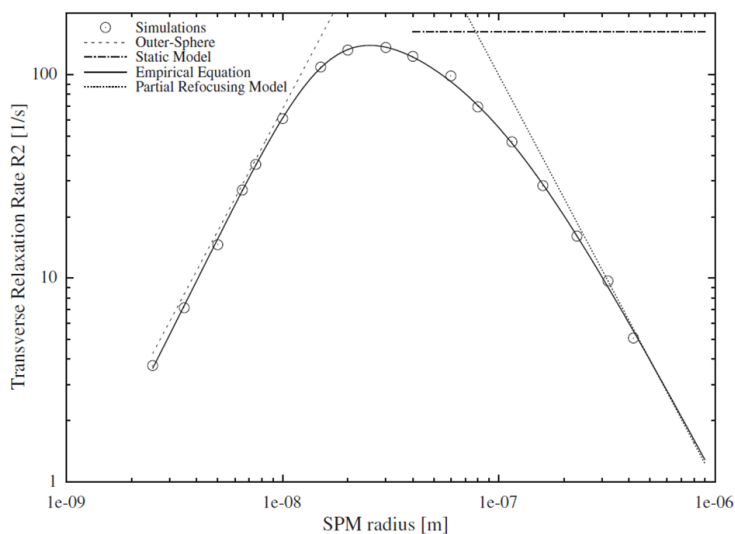


Fig. 2.7 – Simulations of theoretical  $R_2$  for a superparamagnetic IONP versus its radius. Display of the different models: outer sphere theory (equivalent to MAR), static model (equivalent to SDR) and PRM. From Vuong *et al*<sup>12</sup>.

The three regimes are well illustrated by Vuong *et al*<sup>12</sup> results displayed in Figure 2.7. Authors ran numerical simulations and displayed the different theoretical models that show the trend of the transverse relaxation rate  $R_2$  given the size of IONP. It is worth noting that in this study<sup>12</sup>, they found a maximum  $R_2$  for  $20 \text{ nm}$  nanoparticles, but it is slightly different than searching for a maximum transverse relaxivity<sup>9</sup>, where iron content is also considered.

<sup>12</sup>Q. L. Vuong et al., Journal of Magnetic Resonance, **212**: 139–148, 2011.

In conclusion, discrimination between regimes relies on saturation magnetization and particle radius. In all regimes, transverse relaxivity depends on saturation magnetization and on chemical composition of magnetic material ( $\nu_{mat}$ ). Then,  $r_2$  depends on particle radius only in MAR and PRM, whereas it is no longer the case in SDR. High magnetic properties are always required and diameter can be adjusted to optimize relaxivity case by case: diameter is chosen to lie in the wanted relaxation regime, and is afterward adjusted to refine relaxivity (if MAR or PRM). For magnetite nanoparticles with high saturation magnetization ( $M_S = 90 \text{ emu} \cdot \text{g}^{-1}$ ) and knowing the volumic mass of magnetite ( $\rho_{Fe_3O_4} = 5200 \text{ kg} \cdot \text{m}^{-3}$ ), we found that the limit between MAR and SDR is around  $15 \text{ nm}$ . This indicative value has to be reconsidered for each case by correcting with the measured value of saturation magnetization.

## 2.2 How to optimize IONPs contrasting properties?

IONPs present efficient MRI contrasting properties because they possess a high magnetic moment. As a consequence, the higher is the saturation magnetization of the particle and the better contrasting properties are expected to be, if only magnetism is taken into account. Many strategies can help increasing saturation magnetization toward bulk magnetization, like increasing the size of the crystal or doping part of iron ions with others cations.

Nevertheless magnetic properties of IONP are only one component of the contrasting properties. Indeed, IONPs used as contrast agent for *in vivo* applications must be coated with a biocompatible coating. This coating will stand in between water molecules and iron-oxide core, which can hinder interactions, thus degrade contrasting properties. This coating, which can differ in composition (PEG, Dextran, ...) or in thickness, is a key parameter to be optimized to benefit from all magnetic properties of iron core.

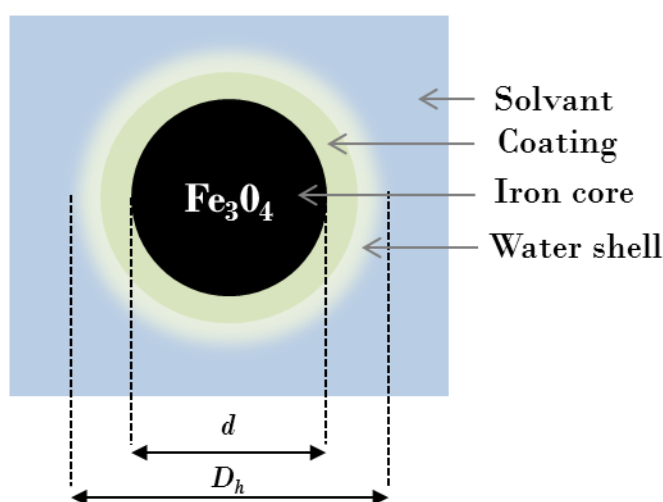


Fig. 2.8 – Difference between iron oxide core diameter ( $d$ ) and hydrodynamic diameter ( $D_h$ ) of the nanoparticle.

One has to keep in mind the difference between the iron-oxide core diameter,  $d$ , usually measured on transmission electron microscopy (TEM) images, and the **hydrodynamic diameter**,  $D_h$ . This diameter takes into account iron-oxide core, coating, and the surrounding water

molecules shell. This water shell, which often comes from coating charges, is essential for the colloidal stability of the suspension. The hydrodynamic diameter that can be measured by dynamic light scattering (DLS) is an important parameter to characterize coatings.

### 2.2.1 Superparamagnetic iron core optimization

Superparamagnetic IONPs (SPIONs) coated with biocompatible polymers are the most used IONPs as contrast agent for MRI-based diagnostic and molecular applications<sup>13,14</sup>. Here are the main advantages in favor of SPION<sup>4</sup>:

- Good colloidal stability without applying external magnetic field, because SPIONs are both lightweight and non magnetic in such condition. This leads to very few particles aggregation. Even under application of external magnetic field, their aggregation is limited because the dipolar interaction between particles decreases in  $r^6$ ,  $r$  being the diameter of the iron core. Finally, SPIONs reach high magnetization under external magnetic field application.
- Higher surface-to-volume ratio is in favor of a more efficient functionalization at the surface: less steric effects are observed, while maintaining an important surface to be functionalized.
- Blood half life is increased compared to bigger NP, in addition to the possibility to cross more easily some natural barriers (for example: crossing the blood brain barrier after transient opening by ultrasound is limited to smaller particles<sup>19</sup>).

These different advantages explain why many strategies for developing new contrast agents have tried to increase relaxivity of IONP while staying in the superparamagnetic range.

**Doping core with cation** It is possible to tune magnetic properties of IONP by doping magnetite with other ions that replace  $Fe^{2+}$  like  $Mn^{2+}$ ,  $Co^{2+}$  or  $Ni^{2+}$ . This method has been investigated by Lee et al<sup>16</sup> with nanoparticles called M-MEIO (Magnetism-engineered iron oxide nanoparticles with the ion M). Such particles present interesting features summarized in Figure 2.9 1: depending on the chosen ion M, the magnetization differs which leads to differences in transverse relaxivity. Compared to pure magnetite (MEIO), authors managed to increase the relaxivity by 1.5 by doping magnetite with manganese, but have also shown that doping with cobalt or nickel might be less interesting.

**Increasing core size** Another way to maximize the saturation magnetization, and thus to increase transverse relaxivity, is to increase core size of nanoparticles as shown by Jun *et al*<sup>15,17</sup> (Figure 2.9 2). Bigger NP have higher saturation magnetization which confers to them better contrasting properties, as seen in  $T_2$ -weighted image (Figure 2.9 2b). The authors concluded that transverse relaxivity gradually increases with the size of NP iron-oxide core while staying in the superparamagnetic domain.

<sup>13</sup>C. Corot et al., *Advanced Drug Delivery Reviews*, **58**: 1471–1504, 2006.

<sup>14</sup>M. Mahmoudi et al., *Nanoscale*, **3**: 3007–3026, 2011.

<sup>4</sup>B. Issa et al., *International Journal of Molecular Sciences*, **14**: 21266–21305, 2013.

<sup>19</sup>B. Marty et al., *Journal of Cerebral Blood Flow & Metabolism*, **32**: 1948–1958, 2012.

<sup>16</sup>J.-H. Lee et al., *Nature Medicine*, **13**: 95–99, 2007.

<sup>15</sup>Y.-W. Jun et al., *Accounts of Chemical Research*, **41**: 179–189, 2008.

<sup>17</sup>Y.-W. Jun et al., *Journal of the American Chemical Society*, **127**: 5732–5733, 2005.

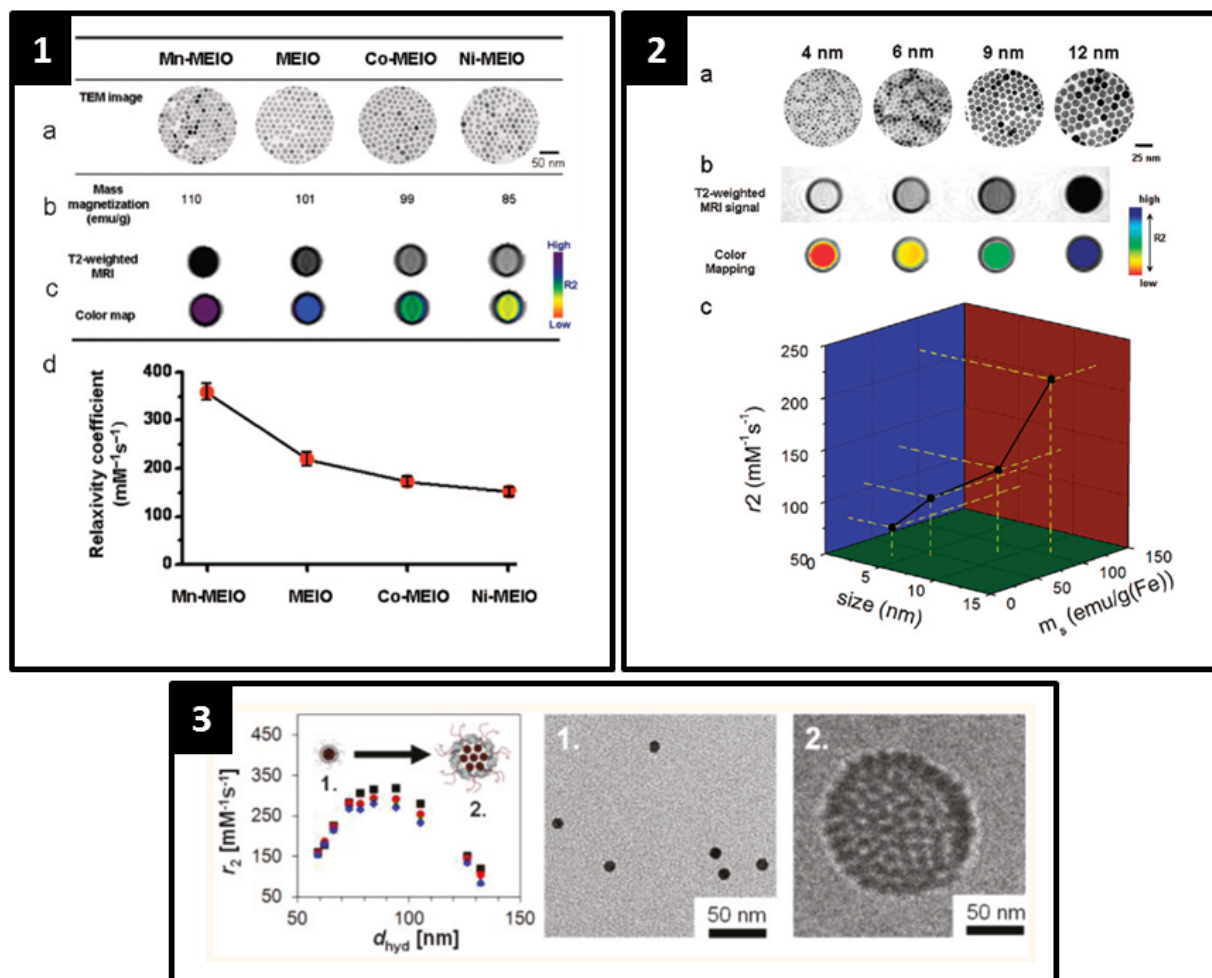


Fig. 2.9 – Improvement of transverse relaxivity through iron-oxide core optimization. **1/** Influence of doping ion on saturation magnetization and on transverse relaxivity from Jun *et al* and Lee *et al*<sup>15,16</sup>. (1a) TEM images of different MEIO nanoparticles, scale bar = 50 nm. (1b) Mass magnetization values of  $MFe_2O_4$ , M being the doping cation. (1c)  $T_2$ -weighted MR images and  $R_2 = \frac{1}{T_2}$  map at 1.5 T. (1d) Plot of transverse relaxivity versus doping ion. **2/** Influence of particle size on saturation magnetization and on transverse relaxivity from Jun *et al*<sup>15,17</sup>. (2a) TEM images of nanoparticles, scale bar = 25 nm. (2b)  $T_2$ -weighted MR images and  $R_2 = \frac{1}{T_2}$  map at 1.5 T. (2c) Plot of transverse relaxivity versus particles size and saturation magnetization. **3/** Influence of 11.8 nm iron cores clustering on transverse relaxivity from Pösel *et al*<sup>18</sup>. Plot of transverse relaxivity at 1.41 T versus hydrodynamic size of the assembly (left). TEM images of isolated nanoparticles (3.1) and raspberry-like nanocluster (3.2).

**Clustering cores in bigger assembly** Clustering small iron-oxide cores (around 10 nm) into assembly around 100 nm is a promising strategy to increase transverse relaxivity. Simulation predicts that transverse relaxivity increases with the number of cores in the assembly until a maximum is reached, beyond which relaxivity starts to fall down<sup>12</sup>. The simulation has been validated by experimental acquisitions performed by Pösel *et al*<sup>18</sup>. Figure 2.9 3 summarizes

<sup>12</sup>Q. L. Vuong *et al.*, Journal of Magnetic Resonance, **212**: 139–148, 2011.

<sup>18</sup>E. Pösel *et al.*, ACS Nano, **6**: 1619–1624, 2012.

their findings showing the bell-shaped curve, as predicted by simulation, when studying transverse relaxivity versus hydrodynamic diameters of nanoclusters for one given iron-oxide core size. TEM image (2.9 3c) reveals the nanocluster architecture (raspberry-like).

**Beyond superparamagnetic IONP?** We have reviewed the classic features of superparamagnetic IONP and have concluded on the necessity of improving iron-oxide core magnetic properties to produce efficient CA. One case has not been considered so far: IONP in the ferrimagnetic and single domain regime. Such particles present the great advantage of a high saturation magnetization, as well as a diameter in the SDR of relaxation, which is supposed to be the most sensitive. Ferrimagnetic single domain iron-oxide cores promise to reach the highest transverse relaxivity<sup>9,20</sup>.

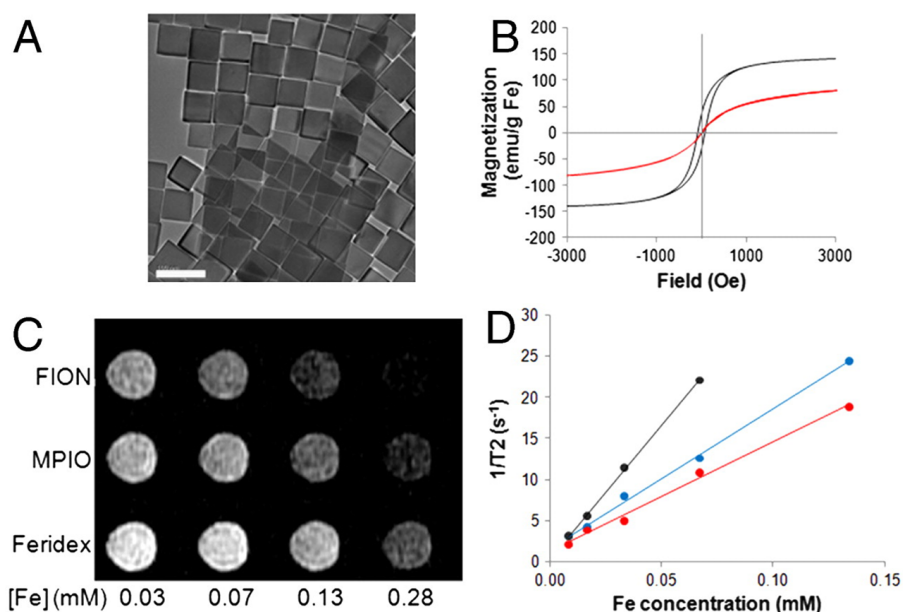


Fig. 2.10 – Comparison between single domain ferrimagnetic nanoparticles (FION) and superparamagnetic ones (Feridex) and micrometer aggregates of SPION (MPIO). A/ is a TEM image of FION, average size equal to  $57.8 \pm 9.9 \text{ nm}$ , scale bar equal to  $100 \text{ nm}$ . B/ Magnetization curve of FION in black and Feridex in red showing ferrimagnetism of FION and superparamagnetism of Feridex, and also confirming the higher magnetization of FION compared with Feridex ( $M_S^{FION} = 132.1 \text{ emu/gFe}$  and  $M_S^{Feridex} = 64.4 \text{ emu/gFe}$ ). C/  $T_2$ -weighted MR image at  $9.4 \text{ T}$  of FION, MPIO and Feridex. D/ Fit of transverse relaxivity of FION ( $r_2 = 324 \text{ mM}^{-1}\text{s}^{-1}$ , black), MPIO ( $r_2 = 169 \text{ mM}^{-1}\text{s}^{-1}$ , blue), and Feridex ( $r_2 = 133 \text{ mM}^{-1}\text{s}^{-1}$ , red). From Lee *et al*<sup>20</sup>.

Lee *et al*<sup>20</sup> managed to chemically produce magnetosome-like IONPs that are ferrimagnetic and single domain. Figure 2.10 presents an example of these large ferrimagnetic IONPs ( $d \sim 58 \text{ nm}$ ), that have a higher saturation magnetization than superparamagnetic ones, and also exhibit a higher transverse relaxivity. These promising magnetic properties yet raise some questions. Being in the ferrimagnetic domain leads to poor colloidal stability, with or without applied magnetic field. Plus their big size might also lead to faster wash-out from the blood stream, as well as disturbing access to target zone when functionalized. Nonetheless, Lee *et*

<sup>9</sup>Q. L. Vuong *et al.*, *Advanced Healthcare Materials*, **1**: 502–512, 2012.

<sup>20</sup>N. Lee *et al.*, *Proceedings of the National Academy of Sciences*, **108**: 2662–2667, 2011.

*al*<sup>20</sup> demonstrated the great interest of their ferrimagnetic particles in the case of single cells imaging. This new trend of IONPs might not find their purpose in replacing superparamagnetic ones (as blood pool agent for example), but might open the way to new applications, like single cell tracking with MRI to assist cell therapies.

## 2.2.2 Coating optimization

Polymers/molecules	Advantages
Polyethylene glycol (PEG)	Non-covalent immobilization of PEG on the surface improves biocompatibility, blood circulation time and internalization efficiency of the nanoparticles
Dextran	Enhances the blood circulation time, stabilizes the colloidal solution
Fatty acids	Colloidal stability, terminal functional carboxyl groups
Polyacrylic acid	Increases the stability and biocompatibility of the particles and also helps in bioadhesion
Polypeptides	Good for cell biology, e.g. targeting to cell
Chitosan	A natural cationic linear polymer that is widely used as non-viral gene delivery system, biocompatible, hydrophilic, used in agriculture, food, medicine, biotechnology, textiles, polymers, and water treatment

Tab. 2.1 – Different coating types for IONP, adapted from Gupta *et al*<sup>21</sup>.

**What is the best coating material?** Coating is essential to ensure sufficient colloidal stability of IONP suspension as well as good biocompatibility. Furthermore, coating needs to be designed considering the purpose of IONP. For example, dextran and PEG will lengthen blood half life and thus are of great interest for designing blood pool agents used in *in vivo* experiments, whereas polypeptides might be more interesting for targeting cells with IONP. Examples of widely used coatings reviewed by Gupta *et al*<sup>21</sup> are presented in Table 2.1. Numerous coatings have been tested and reported in literature but often, the size and the synthesis method of iron-oxide cores also differ. It is then not possible to compare  $r_2$  values versus coating types. Such a study will be tackled in Section 3.2 for two different coatings (PEG and Caffeic Acid) while keeping the same iron-oxide core.

**Finding the best coating thickness** Coating confers good colloidal stability and can enhance contrasting properties. But too thick coating might diminish interactions between water molecules and iron-oxide cores, leading to lower contrasting properties. This has been demonstrated with the widely used PEG coating by LaConte *et al*<sup>22</sup> whose study showed that transverse relaxivity decreases for PEG chains of molecular weight exceeding 750 (Figure 2.11).

<sup>21</sup>A. K. Gupta *et al.*, *Biomaterials*, **26**: 3995–4021, 2005.

<sup>22</sup>L. E.W. LaConte *et al.*, *Journal of Magnetic Resonance Imaging*, **26**: 1634–1641, 2007.

However, it is though important to keep in mind that this evaluation of contrasting properties versus coating thickness has been done by evaluating transverse relaxivity *in vitro*. For *in vivo* applications, as blood pool imaging for example, colloidal stability, and consequently, blood half life can be more important than the relaxivity value. In this case, having a lower relaxivity but a more efficient and a longer circulation of IONPs into blood stream might be more interesting. This question will be discussed in the study of IONP as blood pool agent carried out in Section 3.3.

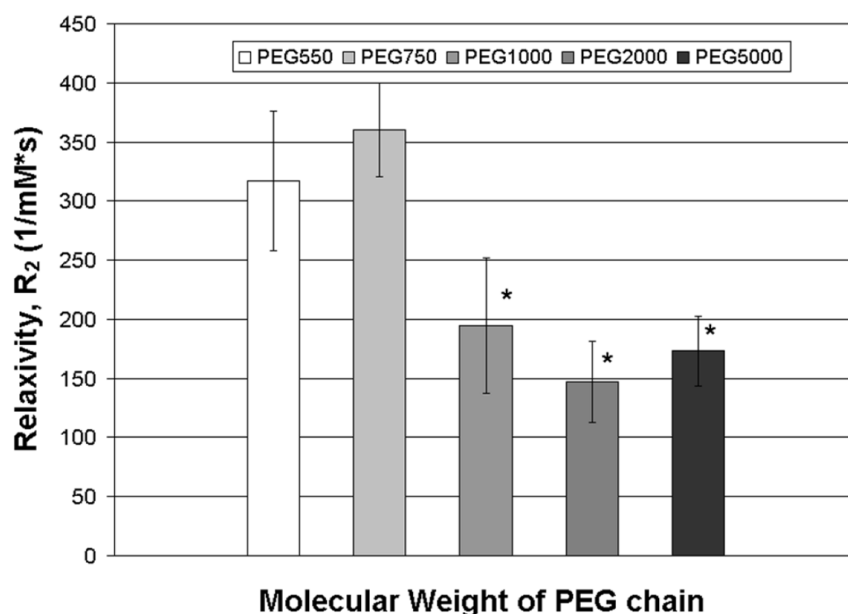


Fig. 2.11 – Influence of PEG chain size on transverse relaxivity at 0.47 T. Corresponding hydrodynamic diameters for PEG550, PEG750, PEG1000, PEG2000 and PEG5000 are respectively  $12.5 \pm 1.3$  nm,  $10.35 \pm 2.6$  nm,  $12.0 \pm 0.8$  nm,  $16.4 \pm 3.1$  nm and  $21.6 \pm 3.6$  nm. From Leslie LaConte *et al*<sup>22</sup>.

### Other parameters to consider for the use of IONPs in molecular imaging application *in vivo*

Optimized iron-oxide core is a promising tool for designing efficient contrast agent for MRI. Magnetic properties are the sources of MR contrast enhancement and then, optimizing them is crucial. Nonetheless, in pharmacology, it is well known that the galenic formulation can be even more important than the substance activity, which is also true for contrast agent design. In particular, it means ensuring biocompatibility and sufficient colloidal stability and above all, adapting coating content and features to the target to be imaged.

One further step in coating optimization is actually to design **MRI molecular imaging probe**, by a functionalization that makes IONP affine for one specific target. Functionalization is not supposed to affect (improve or degrade) contrasting properties, but is expected to change biodistribution to better reveal targeted area. Specific IONP functionalization for tumor targeting will be tackled with more details in Chapter 4.

## 2.3 Interest of magnetosomes as MRI contrast agent

This PhD thesis focuses on the study of a new class of IONPs for MRI, which is naturally produced by specific bacteria. This section introduces these bacteria and their specificities, and also highlights why this approach is interesting for MRI molecular imaging probe design.

### 2.3.1 Magnetotactic bacteria and magnetosomes

**The role of magnetosomes for MTB: Magnetotaxis** Magnetosomes are iron-oxide nanocrystals inside a lipid bilayer, biomineralized by some bacteria called **magnetotactic bacteria**, MTB. These bacteria can be found in almost all natural aquatic environments (fresh or sea water) and are supposed to produce magnetosomes to facilitate their navigation in water by magnetotaxis<sup>23</sup>: magnetosomes assembled in chain inside the bacteria, as in Figure 2.12 1A, act as a compass<sup>24,25</sup> that helps bacteria to swim along earth magnetic field direction, which appears to guide them in a suitable environment. Figure 2.12 1C shows magnetic induction map revealing that magnetic field lines are parallel to magnetosomes chains, confirming their magnetic dipole behavior. Briefly, MTB movements are restrained along magnetic field lines in two directions only, parallel or anti-parallel. It is hypothesized that MTB use aerotaxis (preferred displacement given gradient in oxygen concentration) in addition to magnetotaxis to easily reach their optimal oxygenated region. Figure 2.12 2 illustrates why MTB behave the opposite way whether they live in the Northern or Southern hemisphere. In the Northern hemisphere, MTB are swimming parallel to magnetic field lines to reach low oxygenated zone (OATZ: Oxic-Anoxic Transition Zone), while in the Southern hemisphere, they swim anti-parallel to magnetic field lines to reach the same environment. Magnetotaxis reduces a 3D search into one single dimension problem<sup>26</sup>.

**Diversity of magnetosomes core** The biomineralization of magnetosomes is performed under tight control of biological processes, which explain both the high reproducibility of crystals as well as their chain arrangement inside the bacteria<sup>27–29</sup>. Figure 2.14 1 shows TEM images of a whole MTB with its magnetosomes chain inside (A), and a higher magnification on magnetosomes (B) where the reproducibility of crystals and the presence of a membrane around iron-oxide core can be appreciated.

The whole biomineralization process of iron-oxide crystals has not been unraveled yet. Though, the size, the shape and the chemical content of crystal are known to be genetically determined and very stable within strain. The diversity of MTB strains, and as a result in magnetosome types<sup>30</sup>, can be observed in Figure 2.13. Besides, some MTB can also biomineralize greigite (iron sulfide:  $Fe_3S_4$ )<sup>31</sup>, but this will not be detailed here. Magnetosomes iron-oxide core can be cubo-octahedral, elongated or bullet-shaped. Furthermore, the number of magnetosomes per bacterium and their arrangement in one or multiple chains also vary between strains. Despite this diversity, the normal crystal size is always in the single magnetic domain range

<sup>23</sup>R. Blakemore., *Science*, **190**: 377–379, 1975.

<sup>24</sup>R. E. Dunin-Borkowski., *Science*, **282**: 1868–1870, 1998.

<sup>25</sup>M. Bennet et al., *Faraday Discuss.*, **181**: 71–83, 2015.

<sup>26</sup>D. A. Bazylinski et al., *Nature Reviews Microbiology*, **2**: 217–230, 2004.

<sup>27</sup>D. Faivre et al., *Chemical Reviews*, **108**: 4875–4898, 2008.

<sup>28</sup>E. Cornejo et al., *Current opinion in cell biology*, **26**: 132–138, 2014.

<sup>29</sup>C. T. Lefèvre et al., *Environmental Microbiology*, **15**: 2712–2735, 2013.

<sup>30</sup>D. Schüler., *FEMS Microbiology Reviews*, **32**: 654–672, 2008.

<sup>31</sup>C. T. Lefèvre et al., *Science*, **334**: 1720–1723, 2011.

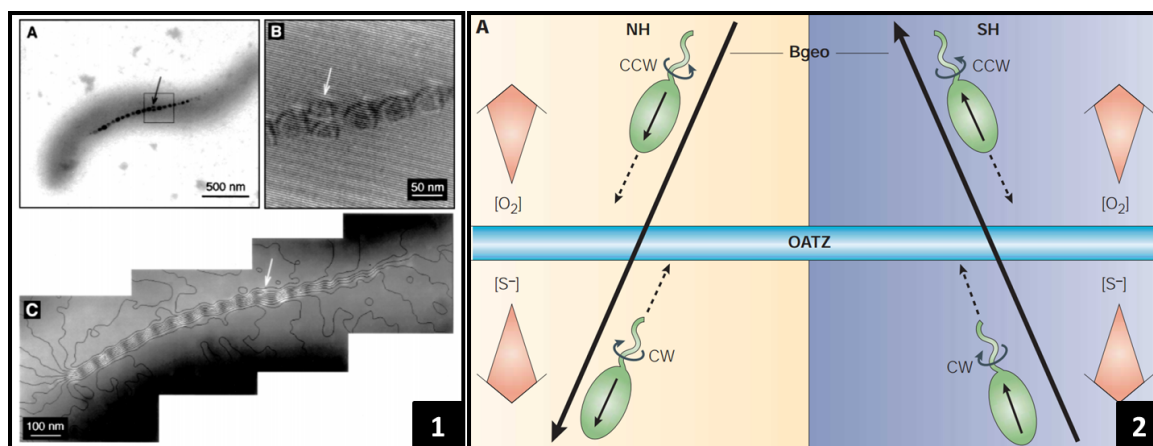


Fig. 2.12 – **1/** Magnetosomes magnetic microstructure from Dunin-Borkowski *et al*<sup>24</sup>. (1A) TEM image of whole MTB (MS-1) revealing magnetosomes chain. (1B) Off-axis electron hologram from the region marked in (1A). (1C) Magnetic induction map from off-axis electron holography. **2/** Magneto-aerotaxis principle, from Bazylnski and Frankel<sup>26</sup>. Magneto-aerotaxis is the process by which MTB find efficiently their optimal environment at the microaerobic oxic-anoxic transition zone (OATZ), in sediment with horizontal stratification in oxygen and sulphide. Earth magnetic field lines ( $B_{geo}$ ) restrain MTB movements onto one single axis, letting bacterial cells in the oxic/anoxic area to swim with their flagella counterclockwise (CCW) / clockwise (CW) whatever the hemisphere. In the Northern hemisphere (NH), MTB will move toward north, whereas it is the opposite in the Southern hemisphere (SH).

whatever the strain. This happens to be the optimal magnetic behavior that maximizes magnetotaxis efficiency. Indeed, superparamagnetic magnetosomes would have very low magnetic properties under earth magnetic field application, and multi-domain magnetosomes would require more iron for a reduced efficacy. Magnetosomes are then produced to be magnetically optimal<sup>27</sup>, which can also explain elongated or bullet-shaped magnetosomes formation. These anisotropic crystals present a limited size but a greater magnetization on the long axis, compared to cubo-octahedral ones with the same volume. Magnetosomes size is genetically defined but it is possible to modify it by changing culture media content or by creating mutant. For example, a low iron concentration medium will make MTB producing smaller magnetosomes<sup>32</sup> and genetic engineering can also give control on crystal size<sup>33</sup>. It is also possible to change magnetosomes iron-oxide core content by doping them with other atoms, for example with cobalt<sup>34</sup>.

In summary, inorganic cores of magnetosomes are then very promising iron nanoparticles for designing MRI contrast agent, which present interesting tunable properties such as their size, shape and chemical composition.

**Assets of magnetosome membrane** MTB biomineralize iron ions directly inside vesicles (the magnetosomes) which membrane looks alike internal cytoplasmic bacterial membrane. This membrane isolates inorganic iron core from surrounding medium, as shown in high magnification TEM image (Figure 2.14 1B). In addition to phospholipids, magnetosomes membrane harbors a set of proteins that are specific to magnetosomes and are not found in any other subcellular

<sup>32</sup>M. R. Benoit et al., *Clinical Cancer Research*, **15**: 5170–5177, 2009.

<sup>33</sup>D. Schuler et al., *World Intellectual Property Organization*, WO2009047301A1, 2009.

<sup>34</sup>S. Staniland et al., *Nature Nanotechnology*, **3**: 158–162, 2008.

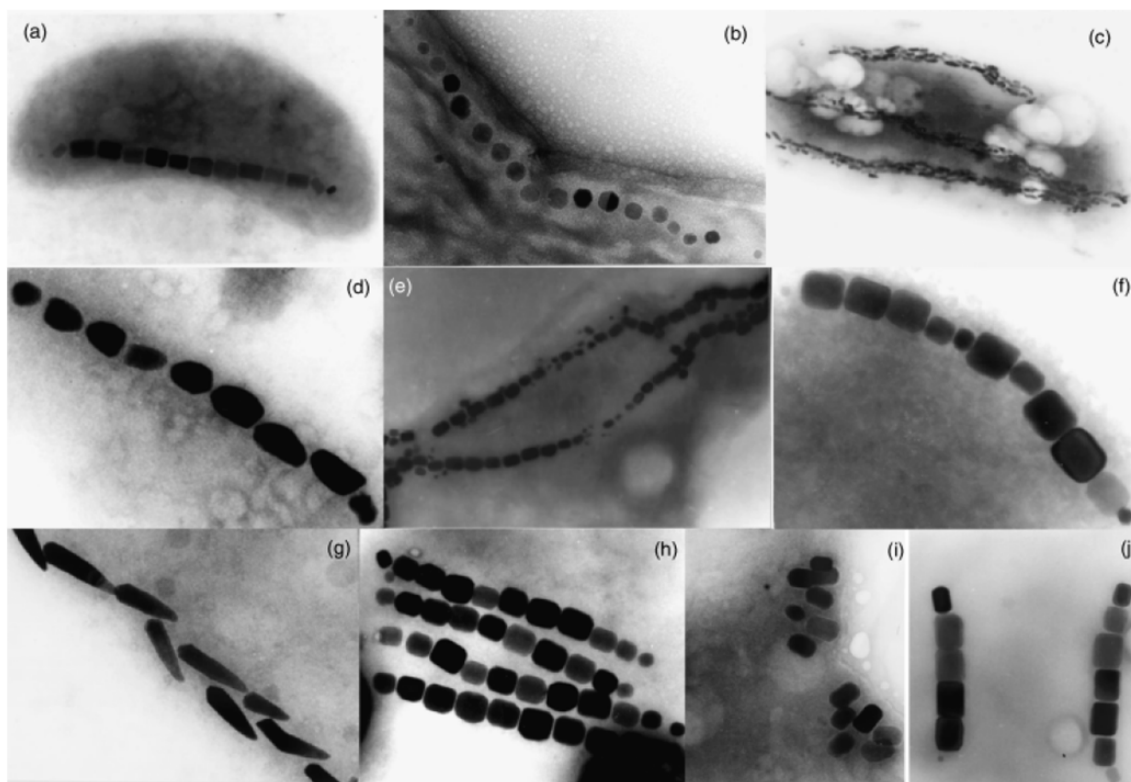


Fig. 2.13 – TEM images of magnetosomes inside MTB showing the diversity of shapes for different MTB strains. Magnetosomes can be cubo-octahedral (b), elongated (a,e,f,h,i,j) or bullet-shaped (c,d,g), and can form one or multiple chains inside bacteria, from Schüler<sup>30</sup>.

compartments<sup>37</sup>. Working on these specific proteins provides knowledge about magnetosomes formation and is of tremendous interest for membrane engineering. It is possible on principle to modify magnetosome membrane by genetically fusing a protein of interest (fluorophore, enzyme, fusion tag, biotinylation) with a magnetosome membrane protein, or also to conjugate membrane phospholipid with DNA linker for functionalization<sup>36</sup> (Figure 2.14 2). A genetically modification of magnetosome membrane has been previously performed by our collaborators from LBC laboratory: they successfully functionalized magnetosome membrane for pesticides bioremediation in contaminated effluents<sup>35</sup>. The same methods have been used in MEFISTO project to produce functionalized magnetosomes for molecular imaging: dedicated protocols and results in such an achievement will be presented in details in Chapter 4.

**Magnetosomes production** MTB can be easily cultured in bioreactors following dedicated protocols<sup>35,38,39</sup>. After culture, bacteria are harvested by centrifugation, and then disrupted using French press (cells are pressurized with a piston) or one shot apparatus (cells are pressurized by being accelerated through small holes), leading to a pellet containing both magnetosomes and cell debris. Purification of magnetosomes is made by passing the pellet through a magnetic column by flow gravity, which contains iron filings, and which is placed in the gap of a magnet.

<sup>37</sup>K. Grünberg et al., *Applied and Environmental Microbiology*, **70**: 1040–1050, 2004.

<sup>36</sup>C. Lang et al., *Journal of Physics: Condensed Matter*, **18**: S2815–S2828, 2006.

<sup>35</sup>N. Ginet et al., *PLoS ONE*, **6**: e21442, 2011.

<sup>38</sup>T. Orlando et al., *Contrast Media & Molecular Imaging*, **11**: 139–145, 2016.

<sup>39</sup>D. A. Bazylinski et al., *Nature*, **334**: 518–519, 1988.

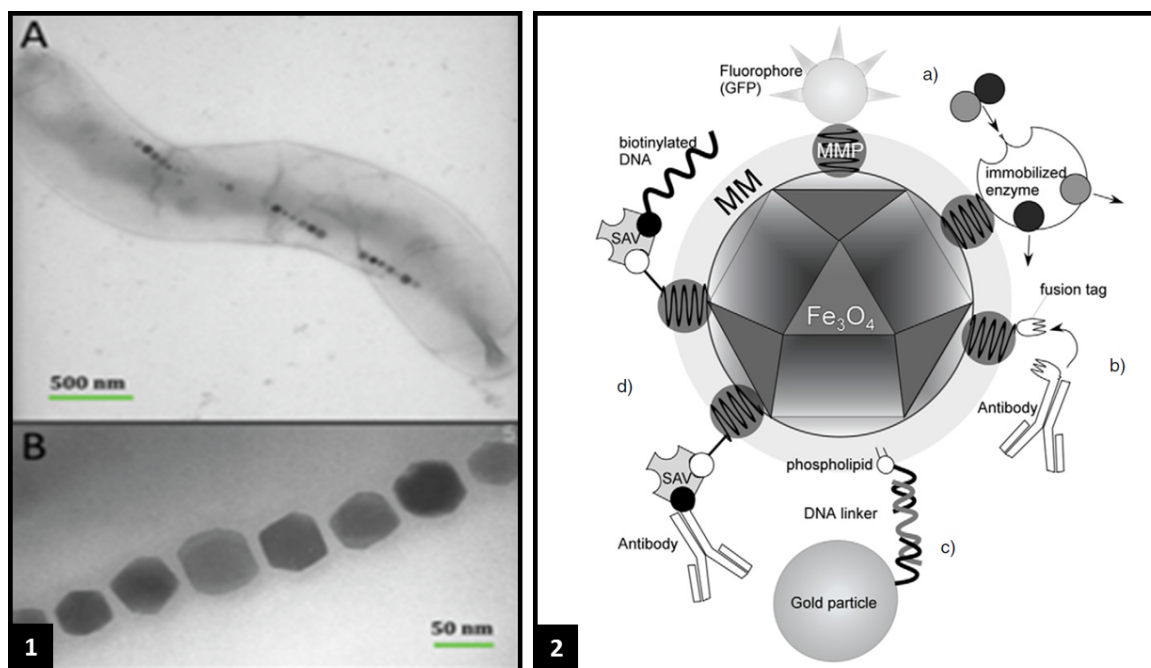


Fig. 2.14 – Importance of magnetosome membrane for functionalization. **1/** TEM image of whole MTB (1A) and zoom on magnetosomes chain inside bacteria where membrane can be seen (1B), from Ginet *et al*<sup>35</sup>. **2/** Scheme of potential magnetosome membrane modifications through genetic fusion with Magnetosome Membrane Protein (MMP) (a, b, d) or through phospholipid conjugation (c). Adapted from Lang and Schüler<sup>36</sup>.

Magnetosomes are thus retained and washed prior to be released by removing the magnetic field and by passing buffer through the column.

### 2.3.2 Magnetosomes physico-chemical properties

We just reminded that magnetosomes are naturally produced to have excellent magnetic properties insuring magnetotaxis. It is now interesting to investigate their physico-chemical properties from an imaging point of view.

**Magnetic properties of magnetosomes** Magnetization loop gives a good idea of magnetic properties of nanoparticle. Li *et al*<sup>40</sup> have studied magnetic properties of isolated magnetosomes compared with whole bacteria for the strain AMB-1, known to produce cubo-octahedral magnetosomes. These magnetization loops (Figure 2.15) firstly show the ferrimagnetic behavior of both whole MTB and isolated magnetosomes. Then, whole bacteria present greater coercivity than isolated magnetosomes due to magnetic interactions in magnetosomes chain, as expected. Finally, this also confirms ferrimagnetic behavior of isolated magnetosomes, in agreement with crystal size.

**Relaxivities of magnetosomes** Idea of using magnetosomes for MR-based medical imaging has raised quite a long time ago, but very few studies have been carried out. We report in Table 2.2 the transverse relaxivities that have been measured in different studies so far. Two different strains have been studied: MSR-1 and AMB-1. It is quite complex to compare these

<sup>40</sup>J. H. Li *et al.*, Chinese Science Bulletin, **55**: 38–44, 2010.

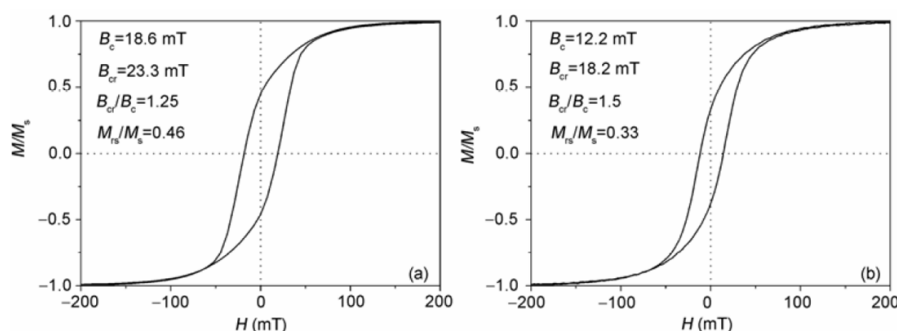


Fig. 2.15 – Magnetic properties of whole bacteria versus extracted magnetosomes. Normalized hysteresis loop of whole AMB-1 MTB (a) and of isolated AMB-1 magnetosomes (b), from Li *et al*<sup>40</sup>.

values since magnetic field intensity, extraction method, gelling agent and concentration range differ between studies. Nevertheless, it seems noticeable that transverse relaxivity values of extracted magnetosomes lie in the highest range compared to conventional chemically synthesized IONPs<sup>38,41,42</sup>. Indeed, Ferumoxide (also known as Endorem<sup>®</sup> by Guerbet) can be taken as a reference IONP chemically formulated for clinical use: its transverse relaxivity was measured equal to  $120 \text{ mM}^{-1}\text{s}^{-1}$  at  $1.5 \text{ T}$ <sup>13</sup>.

Concerning AMB-1, one study measured transverse relaxivity from whole magnetotactic bacteria with magnetosomes inside, but grown in either low or normal (high) iron condition<sup>32</sup>. Relaxivity of whole bacteria is completely different from extracted magnetosomes or chemical IONPs. Whole MTB cannot be seen as IONP aggregate, as those already presented in Section 2.2, because magnetosomes inside bacteria are ordered in a very anisotropic magnetic structure, which confers them compass-like magnetic properties. Finally, magnetosomes being inside bacteria have mainly access to water molecules inside the bacteria and less to free water. Both anisotropic order and restrained water pool make relaxivity measurements complicated to interpret and to compare. Benoit *et al*<sup>32</sup> demonstrated that magnetotactic bacteria grown in low iron condition produce smaller magnetosomes than in normal iron condition ( $25 \text{ nm}$  versus  $50 \text{ nm}$ ), and have a greater transverse relaxivity. This counter-intuitive result can be explained by the fact that linear assembly of small magnetosomes can present smaller or even comparable magnetization than normal magnetosomes assembly, but for a much smaller amount of iron. A comparison can be drawn with the bell-shape curve of transverse relaxivity versus hydrodynamic diameter obtained for IONP assemblies by Pösel *et al*<sup>18</sup> (see Figure 2.9), that illustrates the equilibrium between iron content versus surface availability for water. Finally, Benoit *et al*<sup>32</sup> have intravenously injected MTB raised in low iron condition to tumor bearing mice, and detected a positive contrast enhancement on  $T_1$ -weighted images confirming MTB accumulation in tumors. Interestingly, the authors benefited from the  $T_1$  contrast agent property of MTB, raising from the high  $r_1 = 9.3 \text{ mM}^{-1}\text{s}^{-1}$  at  $1.5 \text{ T}$  (for comparison, Gadolinium-based Dotarem<sup>®</sup> longitudinal relaxivity is equal to  $2.9 \text{ mM}^{-1}\text{s}^{-1}$ <sup>43</sup>), and also because at this relatively low magnetic field intensity, spins dephasing effects due to iron are less predominant.

<sup>41</sup>A. Hartung *et al.*, *Journal of Magnetism and Magnetic Materials*, **311**: 454–459, 2007.

<sup>42</sup>L. L. Hu *et al.*, *IEEE Transactions on Applied Superconductivity*, **20**: 822–825, 2010.

<sup>13</sup>C. Corot *et al.*, *Advanced Drug Delivery Reviews*, **58**: 1471–1504, 2006.

<sup>18</sup>E. Pösel *et al.*, *ACS Nano*, **6**: 1619–1624, 2012.

<sup>43</sup>M. Rohrer *et al.*, *Investigative Radiology*, **40**: 715–724, 2005.

As a conclusion, several studies revealed that magnetosomes have interesting magnetic properties leading to high transverse relaxivity values.

Magnetosomes sample	Magnetic field	Vehicle	Transverse relaxivity	Authors
<i>Magnetospirillum gryphiswaldense</i> extracted magnetosomes	1.5 T	2% agarose	526 $mM^{-1}s^{-1}$	2007, Hartung <i>et al</i> <sup>41</sup>
Whole AMB-1 bacteria grown in low iron condition	3 T	3% gelatin	337 $mM^{-1}s^{-1}$	2009, Benoit <i>et al</i> <sup>32</sup>
Whole AMB-1 bacteria grown in normal iron condition	3 T	3% gelatin	48 $mM^{-1}s^{-1}$	2009, Benoit <i>et al</i> <sup>32</sup>
AMB-1 extracted magnetosomes	3 T	unknown % of agarose	1175 $mM^{-1}s^{-1}$	2010, Hu <i>et al</i> <sup>42</sup>
MSR-1 extracted magnetosomes	4.7 T	0.25% agarose	204 $mM^{-1}s^{-1}$	2015, Orlando <i>et al</i> <sup>38</sup>

Tab. 2.2 – Measurements of transverse relaxivity of magnetosomes performed by different studies.

**Magnetosome membrane properties** As we already discussed in Section 2.2, coating of IONP plays a key role in MRI contrasting properties. Magnetosomes naturally harbor bilipid coating which must be physico-chemically characterized to study its influence on relaxation properties. Hydrodynamic diameter or surface charge have not been extensively studied so far, but there is no doubt that magnetosome membrane provides magnetosomes suspension with colloidal stability. Indeed, it is very easy to remove the membrane from iron-oxide core using tensioactive detergents like SDS (Sodium Dodecyl Sulfate). TEM images of SDS-treated and non treated magnetosomes clearly exhibit that magnetosomes suspensions collapse without membrane<sup>36,44</sup> (Figure 2.16 1 and 2). Besides, characterization of membrane proteins content revealed a great diversity of proteins specific to magnetosome membrane<sup>37</sup> (Figure 2.16 3). It is interesting to notice that MamC, the most abundant one, has been used for genetic modification of magnetosomes membrane by our collaborators from LBC<sup>35</sup>. Finally, the physico-chemical characterization of the different magnetosomes tested during this PhD work, especially in terms of hydrodynamic diameter and membrane proteins content, will be presented in Section 3.2.

## 2.4 Other biomedical applications of IONP

We have reviewed several examples of IONPs used as MRI contrast agent, but contrasting properties are not their only asset. Their magnetism, which is at the origin of MRI contrast enhancement, can also benefit other types of biomedical applications.

<sup>44</sup>E. Alphan ery *et al.*, ACS Nano, 5: 6279–6296, 2011.

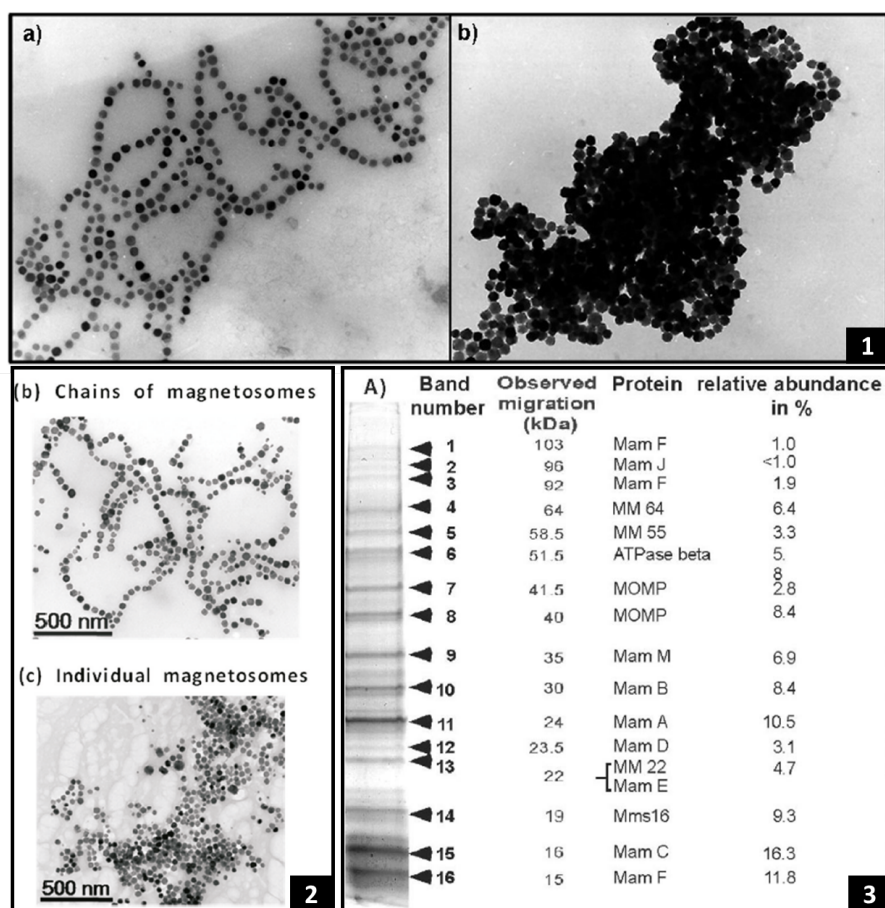


Fig. 2.16 – 1/ TEM images of extracted magnetosomes with (1a and 2b) and without (1b and 2c) their membrane, adapted from Lang and Schüler<sup>36</sup> and Alphanféry *et al*<sup>44</sup>. 2/ Magnetosome membrane protein content adapted from Grünberg *et al*<sup>37</sup>.

## 2.4.1 IONP labeled cells

Different types of cells can be labeled with IONP following dedicated protocol<sup>48</sup>, which will not be detailed here. We will rather focus on several applications: cells labeled with IONP become magnetic, which allows for example *in vivo* MRI cell tracking, or tissue engineering by applying mechanical stress.

**Cell tracking** Cell-based therapies are very promising for treating different diseases like diabetes or nerve injury, but also for bone regeneration that can be tackled using stem cell therapies, and for cancer cure using immune cell therapies<sup>46,49</sup>. Magnetically labeled cells enable for example long-term cells tracking after transplant as shown in Figure 2.17 1. Guzman *et al*<sup>45</sup> demonstrated that labeling human neural stem cells with dedicated SPIO nanoparticles allows post transplantation follow-up during at least 18 weeks, but also evidences *in vivo* cell migration pathways. Magnetic labeling of immune cells can also open the way to cancer treatment monitoring (Figure 2.17 2). Smirnov *et al*<sup>46</sup> intravenously injected magnetically labeled immune cells to tumor bearing mice, and followed cells migration with MRI acquisitions per-

<sup>48</sup>J. Kolosnjaj-Tabi *et al.*, *Journal of Nanobiotechnology*, **11**: S7, 2013.

<sup>46</sup>P. Smirnov *et al.*, *Magnetic Resonance in Medicine*, **56**: 498–508, 2006.

<sup>49</sup>A. Trounson *et al.*, *Cell Stem Cell*, **17**: 11–22, 2015.

<sup>45</sup>R. Guzman *et al.*, *Proceedings of the National Academy of Sciences*, **104**: 10211–10216, 2007.

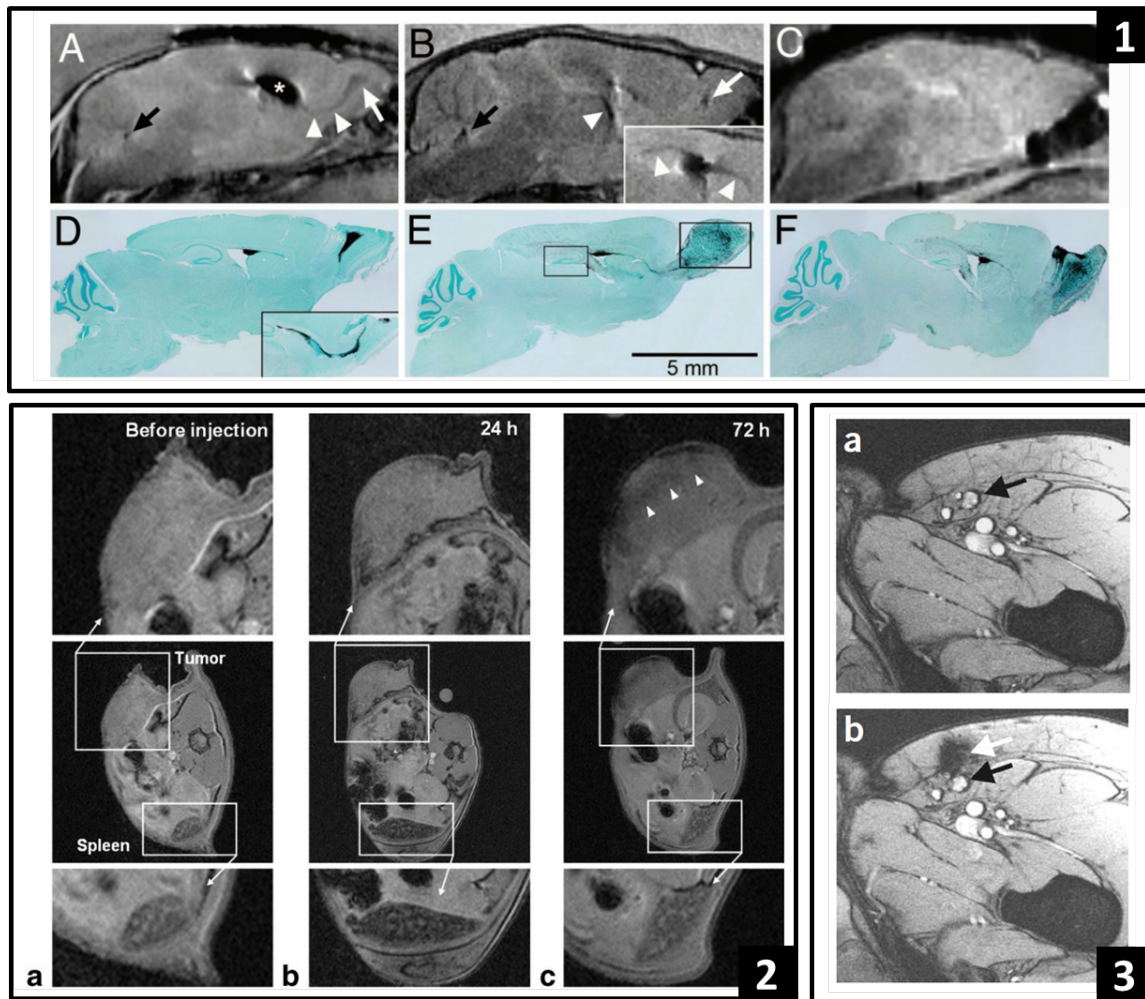


Fig. 2.17 – Example of *in vivo* magnetic cell tracking. **1/** SPIO-labeled human neural stem cells long-term migration after intraventricular injection. (A, B) MR images acquired respectively 3 and 18 weeks post transplantation, and (D,E) the corresponding histological slices stained with a human-specific cytoplasmic marker (revealed in black). (C) MR image of control animal acquired 18 weeks after transplantation of unlabeled human neural stem cells, and (F) the corresponding histological section. Adapted from Guzman *et al*<sup>45</sup>. **2/** *In vivo* MRI cell tracking in mice bearing subcutaneous tumor: MR images acquired before (a), 24 h (b) and 72 h (c) after intravenous injection of labeled OT-1 cells. Adapted from Smirnov *et al*<sup>46</sup>. **3/** MRI follow-up after delivery of SPIO-labeled lymphocytes. (a) MR image acquired before cell therapy; the target (inguinal lymph node) is indicated with a black arrow. (b) MR image acquired post injection reveals that labeled cells were not delivered in the target area (black arrow) but in the subcutaneous fat (white arrow). Adapted from de Vries *et al*<sup>47</sup>.

formed at different time points: they demonstrated that injected immune cells were firstly homed by the spleen prior to be recruited by the tumor. Furthermore, magnetic cells labeling can also be interesting to monitor exact implantation location right after transplant. de Vries *et al*<sup>47</sup> highlighted a failure to implant immune cells in a specific lymph node, thanks to the MRI tracking of magnetically labeled immune cells (Figure 2.17 3). Finally, one other application of

<sup>47</sup>I. de Vries *et al.*, *Nature Biotechnology*, **23**: 1407–1413, 2005.

magnetic labeling for cell therapy is the ability to use an external magnet to direct cells toward the organ of interest. For example, Chaudeurge *et al*<sup>50</sup> successfully demonstrated that homing of intraventricular injected magnetic stem cells in a model of myocardial infarction could be enhanced by applying an external magnetic field near the heart.

**Tissue engineering** Magnetic properties of IONP labeled cells can also give rise to new culture methods, and thus to innovative properties of macroscopic bio-engineered tissue. One interesting example is to use magnetism to constrain cells staying close one to each other. This mechanical stress can be used to condensate cells, and then induce chondrogenesis of stem cells (cartilage formation) that would not happen without mechanical stress. Cartilage tissues have been bio-engineered following this principle by Fayol *et al*<sup>51</sup> (Figure 2.18 1). On the contrary, this mechanical stress can be used to guide cells colonization of a specific scaffold. Tubular cell epithelium can be obtained using this principle by seeding cells in the lumen of a porous scaffold, prior to place it in radial magnetic field to force cells growing at lumen surface<sup>52</sup> (Figure 2.18 2).

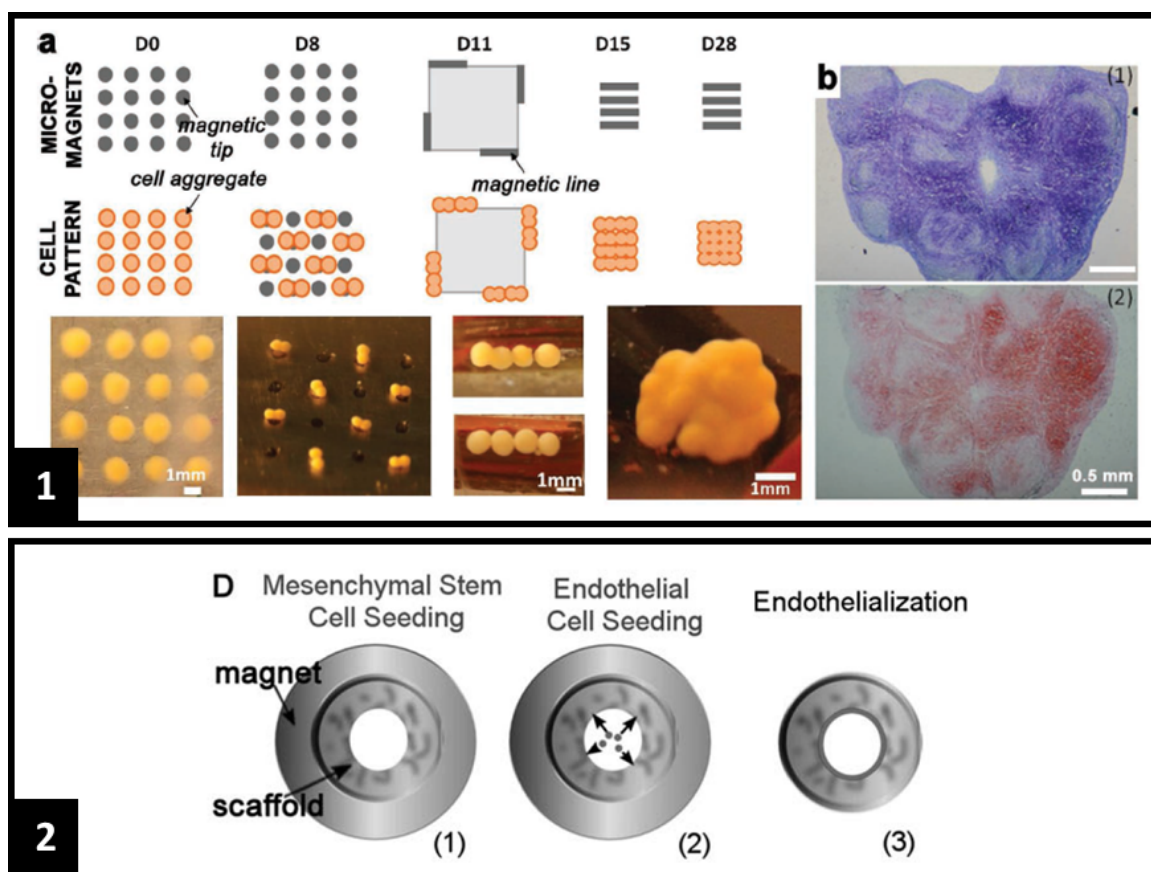


Fig. 2.18 – Example of tissue engineering with magnetic cells. 1/ Chondrogenesis with magnetically labeled stem cells enables to produce magnetic sheets of cartilage, from Fayol *et al*<sup>51</sup>. 2/ Endothelialization of a scaffold containing mesenchymal stem cells and magnetic endothelial cells, from Fayol *et al*<sup>52</sup>.

<sup>50</sup>A. Chaudeurge *et al.*, *Cell Transplantation*, **21**: 679–691, 2012.

<sup>51</sup>D. Fayol *et al.*, *Advanced Materials*, **25**: 2611–2616, 2013.

<sup>52</sup>D. Fayol *et al.*, *Cell Transplantation*, **22**: 2105–2118, 2013.

## 2.4.2 Magnetic hyperthermia

**Hyperthermia for cancer therapy** Hyperthermia or thermotherapy consist in the heating of pathological tissue between 40 to 44°C, which causes cell damages in low  $O_2$  and low pH conditions<sup>53</sup>, thus being promising to treat tumor while preserving healthy cells. These high temperatures are supposed to be cytotoxic, to generate alterations of tumor micro-environment that makes it more sensitive to other treatments (radiotherapy, chemotherapy), and also to induce apoptosis<sup>54</sup>. These effects are still studied since no consensus is found so far on their underlying mechanisms. However it seems established that hyperthermia used in combination with radio- or chemo-therapy enhances the efficiency of these standard treatments.

**Magnetic hyperthermia** Magnetic hyperthermia offers the possibility to locally deliver thermal energy, by applying a radio-frequency magnetic field to magnetic nanoparticles injected into targeted site. One great advantage is that injecting IONPs directly into the tumor insures to induce heat only in the pathological tissue and not in the healthy ones.

Optimization of magnetic hyperthermia requires to firstly investigate the physical part of the method, especially the interactions between magnetic nanoparticles and alternative magnetic field that generate heat. Indeed, transfers of thermal energy come from loss processes of different types: hysteresis, relaxation and friction<sup>55</sup>. Hysteresis losses originate from the fact that magnetization and de-magnetization cycles are not reversible as shown in Figure 2.3 (see Section 2.1), and therefore produce energy loss proportional to hysteresis area. Regarding these hysteresis losses, single domain nanoparticles are expected to be more efficient than multidomain ones, or than superparamagnetic ones<sup>55</sup>. Relaxation losses occur through both Néel (rotation of the magnetization) and Brown (rotation of the whole particle) relaxations. These relaxation losses are maximum when the size dispersion of nanoparticle is as narrow as possible, and when the frequency of alternative magnetic field is adjusted to the particle size. Finally, viscous losses arise through friction between the nanoparticle and its surrounding environment. To summarize, what is important to keep in mind here is that both frequency and amplitude of applied alternative magnetic field need to be carefully adjusted to the chosen magnetic nanoparticles, in order to maximize the hyperthermia effect.

Preclinic studies on mice showed strong anti-tumoral effects using a thermotherapy based on the use of iron-oxide nanoparticles<sup>56,57</sup>. A series of other *in vivo* studies carried out both on animals and humans shows the potential of the hyperthermia technology for cancer treatment<sup>56,58–61</sup>. In order to develop this new technology of cancer thermotherapy, a few companies have been set-up, mostly based on patents using synthetic SPIONs like Sirtex in Australia, Magforce in Germany and Aspen Medisys Inc. in the US. In Germany, brain thermotherapy has reached a phase II study, started in January 2005, which demonstrates that hyperthermia using magnetic nanoparticles in conjunction with a reduced radiation dose is safe and effective, and leads to

<sup>53</sup>J. van der Zee., *Annals of Oncology*, **13**: 1173–1184, 2002.

<sup>54</sup>B. Hildebrandt et al., *Critical Reviews in Oncology/Hematology*, **43**: 33–56, 2002.

<sup>55</sup>R. Hergt et al., *Journal of Physics: Condensed Matter*, **18**: S2919–S2934, 2006.

<sup>56</sup>S. J. DeNardo et al., *Journal of Nuclear Medicine*, **48**: 437–444, 2007.

<sup>57</sup>A. Ito et al., *Journal of Bioscience and Bioengineering*, **96**: 364–369, 2003.

<sup>58</sup>S. Hamaguchi et al., *Cancer Science*, **94**: 834–839, 2003.

<sup>59</sup>M. Johannsen et al., *International Journal of Hyperthermia: The Official Journal of European Society for Hyperthermic Oncology, North American Hyperthermia Group*, **21**: 637–647, 2005.

<sup>60</sup>N. Kawai et al., *The Prostate*, **68**: 784–792, 2008.

<sup>61</sup>T. Kikumori et al., *Breast Cancer Research and Treatment*, **113**: 435–441, 2009.

longer overall survival after the first tumor recurrence, compared to conventional therapies in the treatment of recurrent glioblastoma<sup>62</sup>.

In the context of the MEFISTO project, it is noteworthy that magnetic hyperthermia seems optimum with mono domain IONPs that present high remanent magnetization, as magnetosomes do. Recently, preclinical studies have demonstrated the efficiency of magnetic hyperthermia to treat glioblastoma, with an injection of magnetosomes directly inside the tumor. Alphandéry *et al*<sup>44</sup>, partners of the MEFISTO consortium, already showed that magnetosomes extracted from AMB-1 magnetotactic bacteria are more efficient for magnetic hyperthermia than chemically synthesized nanoparticles. Figure 2.19 presents an example of tumor total regression thanks to magnetic hyperthermia with magnetosomes.

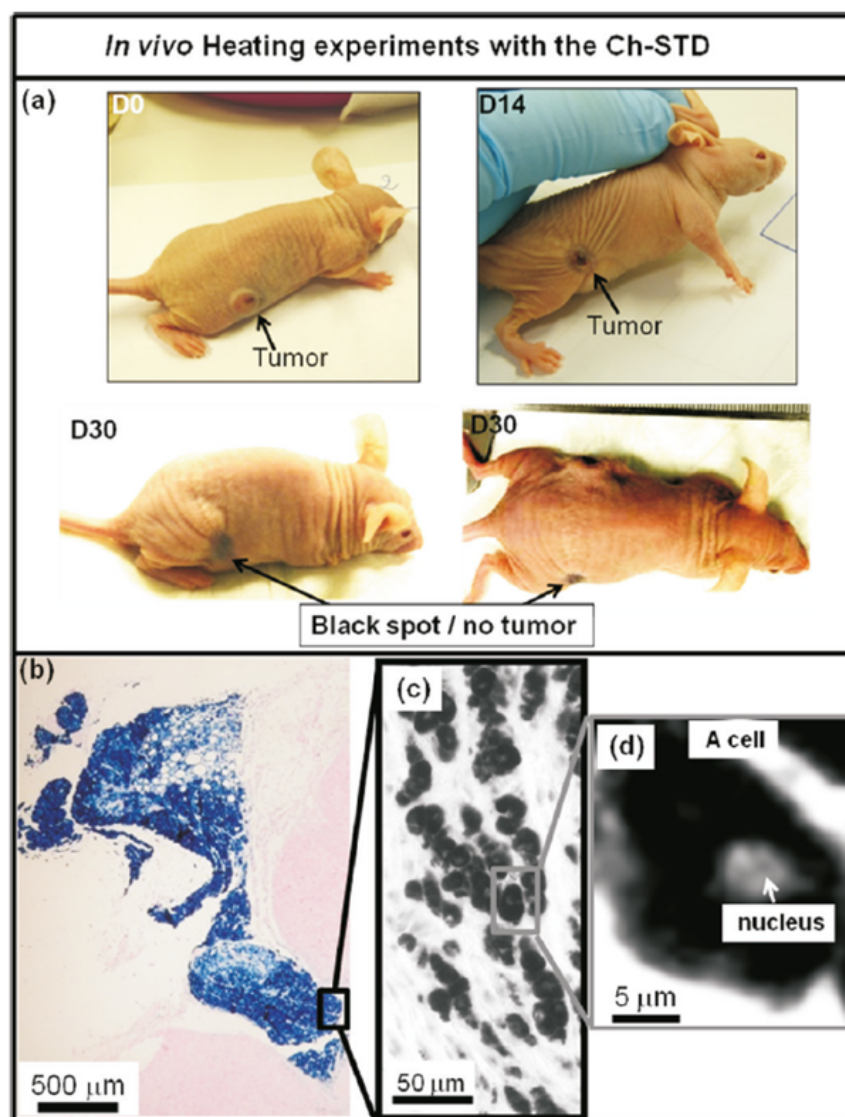


Fig. 2.19 – Example of hyperthermia therapy with intratumoral injection of extracted magnetosomes on a subcutaneous tumor from Alphandéry *et al*<sup>44</sup>.

<sup>62</sup>K. Maier-Hauff *et al.*, *Journal of Neuro-Oncology*, **103**: 317–324, 2011.

<sup>44</sup>E. Alphandéry *et al.*, *ACS Nano*, **5**: 6279–6296, 2011.

## References

- [1] N. W. Ashcroft and N. D. Mermin. *Physique des Solides*. EDP Sciences 2002. (see pp. 16, 17)
- [2] Ö. Özdemir and D. J. Dunlop. Effect of crystal defects and internal stress on the domain structure and magnetic properties of magnetite. *Journal of Geophysical Research: Solid Earth*, **102**: 20211–20224, 1997. DOI: [10.1029/97JB01779](https://doi.org/10.1029/97JB01779) (see p. 17)
- [3] J. Estelrich, E. Escribano, J. Queralt, and M. Busquets. Iron Oxide Nanoparticles for Magnetically-Guided and Magnetically-Responsive Drug Delivery. *International Journal of Molecular Sciences*, **16**: 8070–8101, 2015. DOI: [10.3390/ijms16048070](https://doi.org/10.3390/ijms16048070) (see pp. 18–20)
- [4] B. Issa, I. Obaidat, B. Albiss, and Y. Haik. Magnetic Nanoparticles: Surface Effects and Properties Related to Biomedicine Applications. *International Journal of Molecular Sciences*, **14**: 21266–21305, 2013. DOI: [10.3390/ijms141121266](https://doi.org/10.3390/ijms141121266) (see pp. 20, 26)
- [5] I. Solomon. Relaxation Processes in a System of Two Spins. *Physical Review*, **99**: 559–565, 1955. DOI: [10.1103/PhysRev.99.559](https://doi.org/10.1103/PhysRev.99.559) (see p. 21)
- [6] N. Bloembergen. Proton Relaxation Times in Paramagnetic Solutions. *The Journal of Chemical Physics*, **27**: 572–573, 1957. DOI: [10.1063/1.1743771](https://doi.org/10.1063/1.1743771) (see p. 21)
- [7] N. Bloembergen and L. O. Morgan. Proton Relaxation Times in Paramagnetic Solutions. Effects of Electron Spin Relaxation. *Journal of Chemical Physics*, **34**: 842–850, 1961. DOI: [10.1063/1.1731684](https://doi.org/10.1063/1.1731684) (see p. 21)
- [8] T. J. Swift and R. E. Connick. NMR-Relaxation Mechanisms of O17 in Aqueous Solutions of Paramagnetic Cations and the Lifetime of Water Molecules in the First Coordination Sphere. *The Journal of Chemical Physics*, **37**: 307, 1962. DOI: [10.1063/1.1701321](https://doi.org/10.1063/1.1701321) (see p. 21)
- [9] Q. L. Vuong, J.-F. Berret, J. Fresnais, Y. Gossuin, and O. Sandre. A Universal Scaling Law to Predict the Efficiency of Magnetic Nanoparticles as MRI T2-Contrast Agents. *Advanced Healthcare Materials*, **1**: 502–512, 2012. (see pp. 22, 24, 28)
- [10] R. A. Brooks, F. Moiny, and P. Gillis. On T2-shortening by weakly magnetized particles: The chemical exchange model. *Magnetic Resonance in Medicine*, **45**: 1014–1020, 2001. DOI: [10.1002/mrm.1135](https://doi.org/10.1002/mrm.1135) (see p. 23)
- [11] P. Gillis, F. Moiny, and R. A. Brooks. On T2-shortening by strongly magnetized spheres: A partial refocusing model. *Magnetic Resonance in Medicine*, **47**: 257–263, 2002. DOI: [10.1002/mrm.10059](https://doi.org/10.1002/mrm.10059) (see pp. 23, 24)
- [12] Q. L. Vuong, P. Gillis, and Y. Gossuin. Monte Carlo simulation and theory of proton NMR transverse relaxation induced by aggregation of magnetic particles used as MRI contrast agents. *Journal of Magnetic Resonance*, **212**: 139–148, 2011. DOI: [10.1016/j.jmr.2011.06.024](https://doi.org/10.1016/j.jmr.2011.06.024) (see pp. 24, 27)
- [13] C. Corot, P. Robert, J. Idee, and M. Port. Recent advances in iron oxide nanocrystal technology for medical imaging. *Advanced Drug Delivery Reviews*, **58**: 1471–1504, 2006. DOI: [10.1016/j.addr.2006.09.013](https://doi.org/10.1016/j.addr.2006.09.013) (see pp. 26, 35)
- [14] M. Mahmoudi, V. Serpooshan, and S. Laurent. Engineered nanoparticles for biomolecular imaging. *Nanoscale*, **3**: 3007–3026, 2011. DOI: [10.1039/c1nr10326a](https://doi.org/10.1039/c1nr10326a) (see p. 26)

- [15] Y.-W. Jun, J.-W. Seo, and J. Cheon. Nanoscaling Laws of Magnetic Nanoparticles and Their Applicabilities in Biomedical Sciences. *Accounts of Chemical Research*, **41**: 179–189, 2008. DOI: [10.1021/ar700121f](https://doi.org/10.1021/ar700121f) (see pp. 26, 27)
- [16] J.-H. Lee, Y.-M. Huh, Y.-W. Jun, J.-W. Seo, J.-T. Jang, H.-T. Song, S. Kim, E.-J. Cho, H.-G. Yoon, J.-S. Suh, and J. Cheon. Artificially engineered magnetic nanoparticles for ultra-sensitive molecular imaging. *Nature Medicine*, **13**: 95–99, 2007. DOI: [10.1038/nm1467](https://doi.org/10.1038/nm1467) (see pp. 26, 27)
- [17] Y.-W. Jun, Y.-M. Huh, J.-S. Choi, J.-H. Lee, H.-T. Song, S. Kim, S. Kim, S. Yoon, K.-Kim, and J.-S. Shin. Nanoscale size effect of magnetic nanocrystals and their utilization for cancer diagnosis via magnetic resonance imaging. *Journal of the American Chemical Society*, **127**: 5732–5733, 2005. (see pp. 26, 27)
- [18] E. Pösel, H. Kloust, U. Tromsdorf, M. Janschel, C.h Hahn, C. Maßlo, and H. Weller. Relaxivity Optimization of a PEGylated Iron-Oxide-Based Negative Magnetic Resonance Contrast Agent for  $T_2$ -Weighted Spin–Echo Imaging. *ACS Nano*, **6**: 1619–1624, 2012. DOI: [10.1021/nn204591r](https://doi.org/10.1021/nn204591r) (see pp. 27, 35)
- [19] B. Marty, B. Larrat, M. Van Landeghem, C. Robic, P. Robert, M. Port, D. Le Bihan, M. Pernot, M. Tanter, F. Lethimonnier, and S. Mériaux. Dynamic study of blood–brain barrier closure after its disruption using ultrasound: a quantitative analysis. *Journal of Cerebral Blood Flow & Metabolism*, **32**: 1948–1958, 2012. DOI: [10.1038/jcbfm.2012.100](https://doi.org/10.1038/jcbfm.2012.100) (see p. 26)
- [20] N. Lee, H. Kim, S. H. Choi, M. Park, D. Kim, H.-C. Kim, Y. Choi, S. Lin, B. H. Kim, and H. S. Jung. Magnetosome-like ferrimagnetic iron oxide nanocubes for highly sensitive MRI of single cells and transplanted pancreatic islets. *Proceedings of the National Academy of Sciences*, **108**: 2662–2667, 2011. (see pp. 28, 29)
- [21] A. K. Gupta and M. Gupta. Synthesis and surface engineering of iron oxide nanoparticles for biomedical applications. *Biomaterials*, **26**: 3995–4021, 2005. DOI: [10.1016/j.biomaterials.2004.10.012](https://doi.org/10.1016/j.biomaterials.2004.10.012) (see p. 29)
- [22] L. E.W. LaConte, N. Nitin, O. Zurkiya, D. Caruntu, C. J. O’Connor, X. Hu, and G. Bao. Coating thickness of magnetic iron oxide nanoparticles affects  $R_2$  relaxivity. *Journal of Magnetic Resonance Imaging*, **26**: 1634–1641, 2007. DOI: [10.1002/jmri.21194](https://doi.org/10.1002/jmri.21194) (see pp. 29, 30)
- [23] R. Blakemore. Magnetotactic bacteria. *Science*, **190**: 377–379, 1975. (see p. 31)
- [24] R. E. Dunin-Borkowski. Magnetic Microstructure of Magnetotactic Bacteria by Electron Holography. *Science*, **282**: 1868–1870, 1998. DOI: [10.1126/science.282.5395.1868](https://doi.org/10.1126/science.282.5395.1868) (see pp. 31, 32)
- [25] M. Bennet, L. Bertinetti, R. K. Neely, A. Schertel, A. Körnig, C. Flors, F. D. Müller, D. Schüler, S. Klumpp, and D. Faivre. Biologically controlled synthesis and assembly of magnetite nanoparticles. *Faraday Discuss.*, **181**: 71–83, 2015. DOI: [10.1039/C4FD00240G](https://doi.org/10.1039/C4FD00240G) (see p. 31)
- [26] D. A. Bazylinski and R. B. Frankel. Magnetosome formation in prokaryotes. *Nature Reviews Microbiology*, **2**: 217–230, 2004. DOI: [10.1038/nrmicro842](https://doi.org/10.1038/nrmicro842) (see pp. 31, 32)
- [27] D. Faivre and D. Schüler. Magnetotactic Bacteria and Magnetosomes. *Chemical Reviews*, **108**: 4875–4898, 2008. DOI: [10.1021/cr078258w](https://doi.org/10.1021/cr078258w) (see pp. 31, 32)

- [28] E. Cornejo, N. Abreu, and A. Komeili. Compartmentalization and Organelle Formation in Bacteria. *Current opinion in cell biology*, **26**: 132–138, 2014. DOI: [10.1016/j.ceb.2013.12.007](https://doi.org/10.1016/j.ceb.2013.12.007) (see p. 31)
- [29] C. T. Lefèvre, D. Trubitsyn, F. Abreu, S. Kolinko, C. Jogler, L. G. P. DE Almeida, A. T. R. DE Vasconcelos, M. Kube, R. Reinhardt, U. Lins, D. Pignol, D. Schüler, D. A. Bazylinski, and N. Ginet. Comparative genomic analysis of magnetotactic bacteria from the Deltaproteobacteria provides new insights into magnetite and greigite magnetosome genes required for magnetotaxis. *Environmental Microbiology*, **15**: 2712–2735, 2013. DOI: [10.1111/1462-2920.12128](https://doi.org/10.1111/1462-2920.12128) (see p. 31)
- [30] D. Schüler. Genetics and cell biology of magnetosome formation in magnetotactic bacteria. *FEMS Microbiology Reviews*, **32**: 654–672, 2008. DOI: [10.1111/j.1574-6976.2008.00116.x](https://doi.org/10.1111/j.1574-6976.2008.00116.x) (see pp. 31, 33)
- [31] C. T. Lefèvre, N. Menguy, F. Abreu, U. Lins, M. Pósfai, T. Prozorov, D. Pignol, R. B. Frankel, and D. A. Bazylinski. A Cultured Greigite-Producing Magnetotactic Bacterium in a Novel Group of Sulfate-Reducing Bacteria. *Science*, **334**: 1720–1723, 2011. DOI: [10.1126/science.1212596](https://doi.org/10.1126/science.1212596) (see p. 31)
- [32] M. R. Benoit, D. Mayer, Y. Barak, I. Y. Chen, W. Hu, Z. Cheng, S. X. Wang, D. M. Spielman, S. S. Gambhir, and A. Matin. Visualizing Implanted Tumors in Mice with Magnetic Resonance Imaging Using Magnetotactic Bacteria. *Clinical Cancer Research*, **15**: 5170–5177, 2009. DOI: [10.1158/1078-0432.CCR-08-3206](https://doi.org/10.1158/1078-0432.CCR-08-3206) (see pp. 32, 35, 36)
- [33] D. Schuler and A. Scheffel. Method for the recombinant production of magnetic nanoparticles. *World Intellectual Property Organization*, WO2009047301A1, 2009. (see p. 32)
- [34] S. Staniland, W. Williams, N. Telling, G. Van Der Laan, A. Harrison, and B. Ward. Controlled cobalt doping of magnetosomes *in vivo*. *Nature Nanotechnology*, **3**: 158–162, 2008. DOI: [10.1038/nnano.2008.35](https://doi.org/10.1038/nnano.2008.35) (see p. 32)
- [35] N. Ginet, R. Pardoux, G. Adryanczyk, D. Garcia, C. Brutesco, and D. Pignol. Single-Step Production of a Recyclable Nanobiocatalyst for Organophosphate Pesticides Biodegradation Using Functionalized Bacterial Magnetosomes. *PLoS ONE*, **6**: e21442, 2011. DOI: [10.1371/journal.pone.0021442](https://doi.org/10.1371/journal.pone.0021442) (see pp. 33, 34, 36)
- [36] C. Lang and D. Schüler. Biogenic nanoparticles: production, characterization, and application of bacterial magnetosomes. *Journal of Physics: Condensed Matter*, **18**: S2815–S2828, 2006. DOI: [10.1088/0953-8984/18/38/S19](https://doi.org/10.1088/0953-8984/18/38/S19) (see pp. 33, 34, 36, 37)
- [37] K. Grünberg, E.-C. Muller, A. Otto, R. Reszka, D. Linder, M. Kube, R. Reinhardt, and D. Schuler. Biochemical and Proteomic Analysis of the Magnetosome Membrane in *Magnetospirillum gryphiswaldense*. *Applied and Environmental Microbiology*, **70**: 1040–1050, 2004. DOI: [10.1128/AEM.70.2.1040-1050.2004](https://doi.org/10.1128/AEM.70.2.1040-1050.2004) (see pp. 33, 36, 37)
- [38] T. Orlando, S. Mannucci, E. Fantechi, G. Conti, S. Tambalo, A. Busato, C. Innocenti, L. Ghin, R. Bassi, P. Arosio, F. Orsini, C. Sangregorio, M. Corti, M. F. Casula, P. Marzola, A. Lascialfari, and A. Sbarbati. Characterization of magnetic nanoparticles from *Magnetospirillum Gryphiswaldense* as potential theranostics tools. *Contrast Media & Molecular Imaging*, **11**: 139–145, 2016. DOI: [10.1002/cmml.1673](https://doi.org/10.1002/cmml.1673) (see pp. 33, 35, 36)
- [39] D. A. Bazylinski, R. B. Frankel, and H. W. Jannasch. Anaerobic magnetite production by a marine, magnetotactic bacterium. *Nature*, **334**: 518–519, 1988. (see p. 33)

- [40] J. H. Li, Y. X. Pan, Q. S. Liu, H. F. Qin, C. L. Deng, R. C. Che, and X. A. Yang. A comparative study of magnetic properties between whole cells and isolated magnetosomes of *Magnetospirillum magneticum* AMB-1. *Chinese Science Bulletin*, **55**: 38–44, 2010. DOI: [10.1007/s11434-009-0333-x](https://doi.org/10.1007/s11434-009-0333-x) (see pp. 34, 35)
- [41] A. Hartung, M. R. Lisy, K.-H. Herrmann, I. Hilger, D. Schüler, C. Lang, M. E. Bellemann, W. A. Kaiser, and J. R. Reichenbach. Labeling of macrophages using bacterial magnetosomes and their characterization by magnetic resonance imaging. *Journal of Magnetism and Magnetic Materials*, **311**: 454–459, 2007. DOI: [10.1016/j.jmmm.2006.10.1153](https://doi.org/10.1016/j.jmmm.2006.10.1153) (see pp. 35, 36)
- [42] L. L. Hu, F. Zhang, Z. Wang, X. F. You, L. Nie, H. X. Wang, T. Song, and W. H. Yang. Comparison of the <sup>1</sup>H NMR Relaxation Enhancement Produced by Bacterial Magnetosomes and Synthetic Iron Oxide Nanoparticles for Potential Use as MR Molecular Probes. *IEEE Transactions on Applied Superconductivity*, **20**: 822–825, 2010. DOI: [10.1109/TASC.2010.2041218](https://doi.org/10.1109/TASC.2010.2041218) (see pp. 35, 36)
- [43] M. Rohrer, H. Bauer, J. Mintorovitch, M. Requardt, and H.-J. Weinmann. Comparison of Magnetic Properties of MRI Contrast Media Solutions at Different Magnetic Field Strengths. *Investigative Radiology*, **40**: 715–724, 2005. (see p. 35)
- [44] E. Alphanbéry, S. Faure, O. Seksek, F. Guyot, and I. Chebbi. Chains of Magnetosomes Extracted from AMB-1 Magnetotactic Bacteria for Application in Alternative Magnetic Field Cancer Therapy. *ACS Nano*, **5**: 6279–6296, 2011. DOI: [10.1021/nn201290k](https://doi.org/10.1021/nn201290k) (see pp. 36, 37, 41)
- [45] R. Guzman, N. Uchida, T. M. Bliss, D. He, K. K. Christopherson, D. Stellwagen, A. Capela, J. Greve, R. C. Malenka, and M. E. Moseley. Long-term monitoring of transplanted human neural stem cells in developmental and pathological contexts with MRI. *Proceedings of the National Academy of Sciences*, **104**: 10211–10216, 2007. (see pp. 37, 38)
- [46] P. Smirnov, E. Lavergne, F. Gazeau, M. Lewin, A. Boissonnas, B.-T. Doan, B. Gillet, C. Combadiere, B. Combadiere, and O. Clément. *In vivo* cellular imaging of lymphocyte trafficking by MRI: A tumor model approach to cell-based anticancer therapy. *Magnetic Resonance in Medicine*, **56**: 498–508, 2006. (see pp. 37, 38)
- [47] I. DE Vries, M. Jolanda, W. J. Lesterhuis, J. O. Barentsz, P. Verdijk, J. H. VAN Krieken, O. C. Boerman, W. J. G. Oyen, J. J. Bonenkamp, J. B. Boezeman, G. J. Adema, J.W. M. Bulte, T. W. J. Scheenen, C. J. A. Punt, A. Heerschap, and C. G. Figdor. Magnetic resonance tracking of dendritic cells in melanoma patients for monitoring of cellular therapy. *Nature Biotechnology*, **23**: 1407–1413, 2005. DOI: [10.1038/nbt1154](https://doi.org/10.1038/nbt1154) (see p. 38)
- [48] J. Kolosnjaj-Tabi, C. Wilhelm, O. Clément, and F. Gazeau. Cell labeling with magnetic nanoparticles: opportunity for magnetic cell imaging and cell manipulation. *Journal of Nanobiotechnology*, **11**: S7, 2013. (see p. 37)
- [49] A. Trounson and C. McDonald. Stem Cell Therapies in Clinical Trials: Progress and Challenges. *Cell Stem Cell*, **17**: 11–22, 2015. DOI: [10.1016/j.stem.2015.06.007](https://doi.org/10.1016/j.stem.2015.06.007) (see p. 37)

- [50] A. Chaudeurge, C. Wilhelm, A. Chen-Tournoux, P. Farahmand, V. Bellamy, G. Autret, C. Ménager, A. Hagège, J. Larghéro, F. Gazeau, O. Clément, and P. Menasché. Can Magnetic Targeting of Magnetically Labeled Circulating Cells Optimize Intramyocardial Cell Retention? *Cell Transplantation*, **21**: 679–691, 2012. DOI: [10.3727/096368911X612440](https://doi.org/10.3727/096368911X612440) (see p. 39)
- [51] D. Fayol, G. Frasca, C. Le Visage, F. Gazeau, N. Luciani, and C. Wilhelm. Use of Magnetic Forces to Promote Stem Cell Aggregation During Differentiation, and Cartilage Tissue Modeling. *Advanced Materials*, **25**: 2611–2616, 2013. DOI: [10.1002/adma.201300342](https://doi.org/10.1002/adma.201300342) (see p. 39)
- [52] D. Fayol, C. Le Visage, J. Ino, F. Gazeau, D. Letourneur, and C. Wilhelm. Design of Biomimetic Vascular Grafts With Magnetic Endothelial Patterning. *Cell Transplantation*, **22**: 2105–2118, 2013. DOI: [10.3727/096368912X661300](https://doi.org/10.3727/096368912X661300) (see p. 39)
- [53] J. VAN DER Zee. Heating the patient: a promising approach? *Annals of Oncology*, **13**: 1173–1184, 2002. DOI: [10.1093/annonc/mdf280](https://doi.org/10.1093/annonc/mdf280) (see p. 40)
- [54] B. Hildebrandt, P. Wust, O. Ahlers, A. Dieing, G. Sreenivasa, T. Kerner, R. Felix, and H. Riess. The cellular and molecular basis of hyperthermia. *Critical Reviews in Oncology/Hematology*, **43**: 33–56, 2002. DOI: [10.1016/S1040-8428\(01\)00179-2](https://doi.org/10.1016/S1040-8428(01)00179-2) (see p. 40)
- [55] R. Hergt, S. Dutz, R. Müller, and M. Zeisberger. Magnetic particle hyperthermia: nanoparticle magnetism and materials development for cancer therapy. *Journal of Physics: Condensed Matter*, **18**: S2919–S2934, 2006. DOI: [10.1088/0953-8984/18/38/S26](https://doi.org/10.1088/0953-8984/18/38/S26) (see p. 40)
- [56] S. J. DeNardo, G. L. DeNardo, A. Natarajan, L. A. Miers, A. R. Foreman, C. Gruettner, G. N. Adamson, and R. Ivkov. Thermal Dosimetry Predictive of Efficacy of <sup>111</sup>In-ChL6 Nanoparticle AMF-Induced Thermoablative Therapy for Human Breast Cancer in Mice. *Journal of Nuclear Medicine*, **48**: 437–444, 2007. (see p. 40)
- [57] A. Ito, K. Tanaka, H. Honda, S. Abe, H. Yamaguchi, and T. Kobayashi. Complete regression of mouse mammary carcinoma with a size greater than 15 mm by frequent repeated hyperthermia using magnetite nanoparticles. *Journal of Bioscience and Bioengineering*, **96**: 364–369, 2003. DOI: [10.1016/S1389-1723\(03\)90138-1](https://doi.org/10.1016/S1389-1723(03)90138-1) (see p. 40)
- [58] S. Hamaguchi, I. Tohnai, A. Ito, K. Mitsudo, T. Shigetomi, M. Ito, H. Honda, T. Kobayashi, and M. Ueda. Selective hyperthermia using magnetoliposomes to target cervical lymph node metastasis in a rabbit tongue tumor model. *Cancer Science*, **94**: 834–839, 2003. DOI: [10.1111/j.1349-7006.2003.tb01527.x](https://doi.org/10.1111/j.1349-7006.2003.tb01527.x) (see p. 40)
- [59] M. Johannsen, U. Gneveckow, L. Eckelt, A. Feussner, N. Waldöfner, R. Scholz, S. Deger, P. Wust, S. A. Loening, and A. Jordan. Clinical hyperthermia of prostate cancer using magnetic nanoparticles: presentation of a new interstitial technique. *International Journal of Hyperthermia: The Official Journal of European Society for Hyperthermic Oncology, North American Hyperthermia Group*, **21**: 637–647, 2005. (see p. 40)
- [60] N. Kawai, M. Futakuchi, T. Yoshida, A. Ito, S. Sato, T. Naiki, H. Honda, T. Shirai, and K. Kohri. Effect of heat therapy using magnetic nanoparticles conjugated with cationic liposomes on prostate tumor in bone. *The Prostate*, **68**: 784–792, 2008. DOI: [10.1002/pros.20740](https://doi.org/10.1002/pros.20740) (see p. 40)
- [61] T. Kikumori, T. Kobayashi, M. Sawaki, and T. Imai. Anti-cancer effect of hyperthermia on breast cancer by magnetite nanoparticle-loaded anti-HER2 immunoliposomes. *Breast Cancer Research and Treatment*, **113**: 435–441, 2009. DOI: [10.1007/s10549-008-9948-x](https://doi.org/10.1007/s10549-008-9948-x) (see p. 40)

- [62] K. Maier-Hauff, F. Ulrich, D. Nestler, H. Niehoff, P. Wust, B. Thiesen, H. Orawa, V. Budach, and A. Jordan. Efficacy and safety of intratumoral thermotherapy using magnetic iron-oxide nanoparticles combined with external beam radiotherapy on patients with recurrent glioblastoma multiforme. *Journal of Neuro-Oncology*, **103**: 317–324, 2011. DOI: [10.1007/s11060-010-0389-0](https://doi.org/10.1007/s11060-010-0389-0) (see p. 41)



# Magnetosomes and other chemical IONPs used as MRI blood pool contrast agents

## Contents

---

<b>3.1 Physico-chemical properties of magnetosomes</b> . . . . .	<b>50</b>
3.1.1 Iron core characterization . . . . .	50
3.1.2 Membrane characterization . . . . .	52
3.1.3 Benefits and drawbacks of magnetosomes . . . . .	54
<b>3.2 MRI contrasting properties of magnetosomes and chemical IONPs</b> . . . . .	<b>55</b>
3.2.1 Chemical IONPs transverse relaxivities . . . . .	56
3.2.2 Size effect in chemical IONPs transverse relaxivities . . . . .	58
3.2.3 Magnetosomes transverse relaxivities . . . . .	60
<b>3.3 Brain angiography of healthy mouse with contrast-enhanced MRI</b> . . . . .	<b>63</b>
3.3.1 <i>In vivo</i> contrasting properties of chemical IONPs . . . . .	64
3.3.2 <i>In vivo</i> contrasting properties of magnetosomes . . . . .	66
<b>3.4 Brain tumor contrast-enhanced MRI in a mouse model of glioblastoma</b> . . . . .	<b>68</b>
3.4.1 Tumor growth follow-up in diameter and volume . . . . .	68
3.4.2 Tumor vessels follow-up . . . . .	69
3.4.3 Tumor iron uptake measurements . . . . .	72
<b>3.5 Summary and perspectives</b> . . . . .	<b>75</b>
<b>References</b> . . . . .	<b>77</b>

---

This chapter presents the use of magnetosomes and other chemically synthesized IONPs for contrast-enhanced MRI. The first study to achieve during this PhD work was to characterize their magnetic properties with standard tools, in order to be able to compare their contrasting effects afterward. Physico-chemical characterization of magnetosomes iron-oxide core and membrane has been therefore performed to exhibit their potential as contrast agent. Transverse relaxivity is the easiest measure to evaluate *in vitro* contrasting properties of the different tested contrast agents: several types of chemical IONPs and two types of magnetosomes. These contrasting properties were then challenged *in vivo* by performing mouse brain vessels imaging after systemic injection at the tail vein, leading to question the characterization of IONPs contrasting properties only by their transverse relaxivity. Finally, contrast-enhanced MRI on tumor bearing mice has been investigated through two approaches: the first study consisted in characterizing vessels evolution throughout tumor growth and the second one focused on the dynamics of contrast enhancement induced by IONPs injection in tumor versus contralateral zone.

## 3.1 Physico-chemical properties of magnetosomes

Magnetosomes present similar features compared to chemically produced IONPs: an iron-oxide core surrounded by a biocompatible material. It was then interesting to characterize magnetosomes using state-of-the-art of physico-chemical techniques. This work<sup>1</sup> was carried out in collaboration with Yoann Lalatonne and Sophie Richard from CSPBAT team (Chimie, Structures, Propriétés de Biomatériaux et d'Agents Thérapeutiques) at Paris 13 University, under the supervision of Pr. Laurence Motte.

### 3.1.1 Iron core characterization

The biomineralization process of iron-oxide core is genetically controlled by bacteria, meaning both shape and size are determined for a given strain. This is a great advantage since it leads to a diversity of shapes and to narrow distributions of crystal size, as described in 2.3.1. Another advantage is to provide excellent magnetic properties to magnetosomes, and therefore high transverse relaxivities.

**Size and shape analysis** Size of iron-oxide cores of two magnetosomes (AMB1 and MV1) from strains *AMB-1* and *MV-1*, has been measured by our collaborators from LBC on TEM images. A drop of a diluted magnetosomes suspension was placed on copper grids covered by a formvar-carbon film. Magnetosomes were let to sediment for one minute and excess of liquid was gently removed with filter paper. TEM images were acquired with a Tecnai G2 BioTWIN microscope (FEI, USA). Length and width of iron-oxide crystals were measured and the shape factor (width/length) was computed. Dispersions of length and shape factor are presented in Figure 3.1 and mean values are summed up in Table 3.1. For MV1 magnetosomes, the mean length is around 54 nm with a shape factor of 0.69. For AMB1, the mean length is around 48 nm with a shape factor of 0.86. These results corroborate that both MV1 and AMB1 magnetosomes are in the single magnetic domain range with a characteristic size around 50 nm. The shape factors estimated for the two strains<sup>2</sup> are also in good agreement with the expected iron crystal

<sup>1</sup>S. Mériaux et al., *Advanced Healthcare Materials*, **4**: 1076–1083, 2015.

<sup>2</sup>D. A. Bazylinski et al., *Advances in Applied Microbiology*, **62**: 21–62, 2007.

geometries: MV1 magnetosomes are elongated-prismatic nanoparticles (shape factor closer to 0.5), whereas AMB1 are cubo-octahedral (shape factor closer to 1). Furthermore, it is interesting to notice that standard deviation on size does not exceed 24% for AMB1 and 13% for MV1 which is very interesting given the experimental conditions. In comparison, chemical production of highly monodisperse iron-oxide crystals can be quite challenging: several studies already reported the development of IONPs with diameters around 10 nm<sup>3,4</sup>, or from 20 up to 160 nm<sup>5</sup>, but the synthesis protocols required most of the time a series of multiple manufacturing steps and the use of toxic solvents.

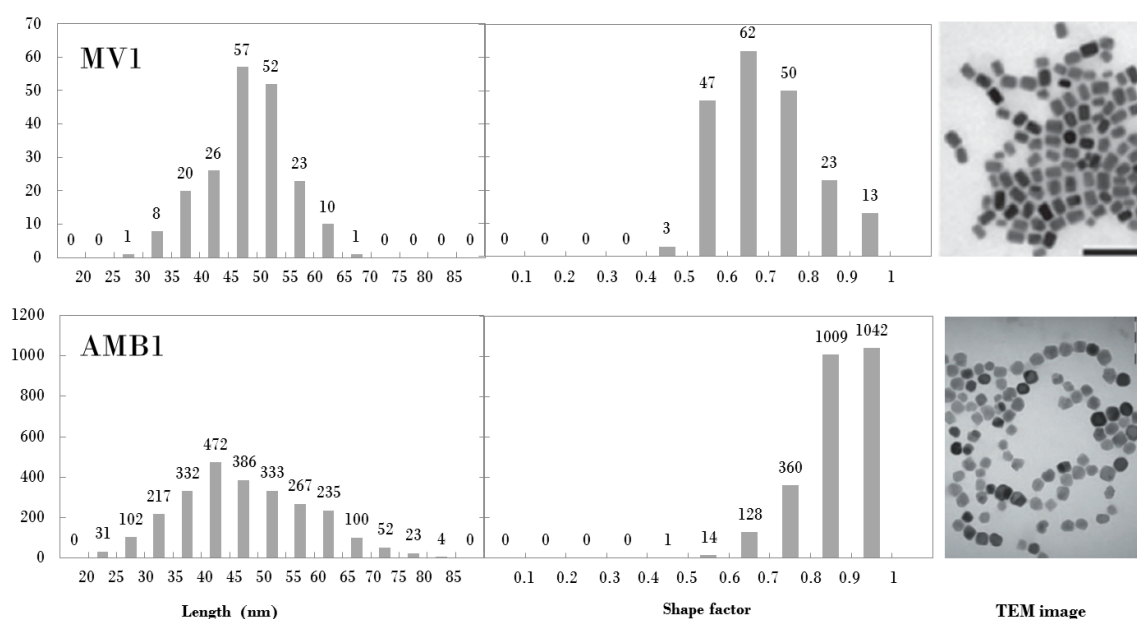


Fig. 3.1 – Magnetosome size analysis to measure diameter and shape factor dispersion. Scale bar 200 nm.

Strain	Length (nm)	Shape factor
MV1	$53.6 \pm 7.2$	$0.69 \pm 0.12$
AMB1	$47.6 \pm 11.4$	$0.86 \pm 0.08$

Tab. 3.1 – Magnetosomes mean length and mean shape factor.

**Magnetic properties** Magnetization loop for MV1 magnetosomes suspension has been acquired with a vibrating sample magnetometer<sup>6</sup> (Versalab VSM, Quantum Design), able to measure magnetization cycle when applying a magnetic field from  $-2400$  to  $2400$  kA  $\cdot$  m<sup>-1</sup> at a

<sup>3</sup>T. Hyeon et al., Journal of the American Chemical Society, **123**: 12798–12801, 2001.

<sup>4</sup>W. W. Yu et al., Chemical Communications (Cambridge, England), 2306–2307, 2004.

<sup>5</sup>D. Kim et al., Journal of the American Chemical Society, **131**: 454–455, 2009.

<sup>6</sup>Simon Foner., Review of scientific instruments, **30**: 548–557, 1959.

step rate of  $8 \text{ kA} \cdot \text{s}^{-1}$  for two times at  $310 \text{ K}$ . Furthermore, identification of electronic diffraction pattern for MV1 magnetosomes suspension measured with TEM provided information on the material nature.

The magnetization loop and the electronic diffraction pattern are presented in Figure 3.2. The presence of coercivity, *i.e.* of a hysteresis, in the magnetization loop evidences that MV1 magnetosomes exhibit ferrimagnetic behavior at room temperature, which is consistent with the measured mean size. As expected, this experiment also confirms that MV1 magnetosomes have a very high saturation magnetization  $M_S^{MV1} = 83 \text{ Am}^2\text{kg}^{-1}$ , close to that of bulk magnetite ( $M_S^{Fe_3O_4} = 92 \text{ Am}^2\text{kg}^{-1}$ ), which is a good indicator of a high crystallinity<sup>7</sup>. Finally, the high crystallinity of MV-1 magnetosomes is also highlighted by the electronic diffraction pattern, which reveals characteristic diffraction rays of magnetite.

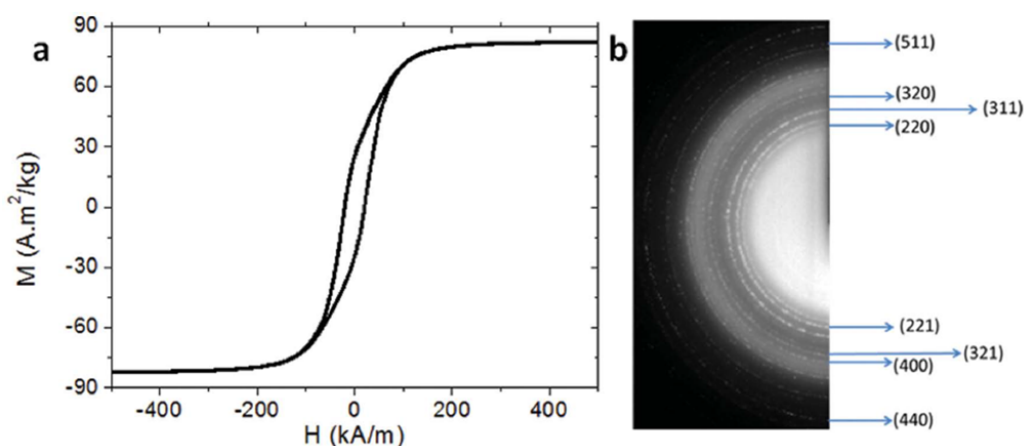


Fig. 3.2 – Magnetic properties of MV1 magnetosomes. a/ Hysteresis magnetization loop, and b/ electronic diffraction pattern and indexed magnetite structure from JCPDS N°00–019–0629.

### 3.1.2 Membrane characterization

**Membrane integrity** Magnetosomes are harvested from magnetotactic bacteria already coated with their bilipid membrane following the protocol described in Figure 3.3. It is interesting to see that extracted magnetosomes seems to form "chains" because of their magnetism but it is very different from the ones observed in the MTB where each magnetosomes are linked to an actin filament<sup>8</sup>. The chains observed with extracted magnetosomes can be broken under agitation for example, and are not expected to exist in diluted samples. Note that when the membrane is removed, aggregated magnetosomes can be observed and it is more difficult to see chains<sup>9</sup>. In comparison, magnetic chains are rarely observed in TEM with chemically synthesized IONP because they often lay in the superparamagnetic range.

The magnetosome membrane has already been bio-chemically studied, revealing the presence of proteins specific to magnetosome membrane, and not to bacterial one<sup>10</sup>. MV1 magnetosome membrane, after being harvested and suspended in physiological vehicle, has been characterized

<sup>7</sup>S. Chikazumi et al. *Physics of Magnetism*. Wiley, New York 1964.

<sup>8</sup>M. Bennet et al., *Faraday Discuss.*, **181**: 71–83, 2015.

<sup>9</sup>C. Lang et al., *Journal of Physics: Condensed Matter*, **18**: S2815–S2828, 2006.

<sup>10</sup>K. Grünberg et al., *Applied and Environmental Microbiology*, **70**: 1040–1050, 2004.

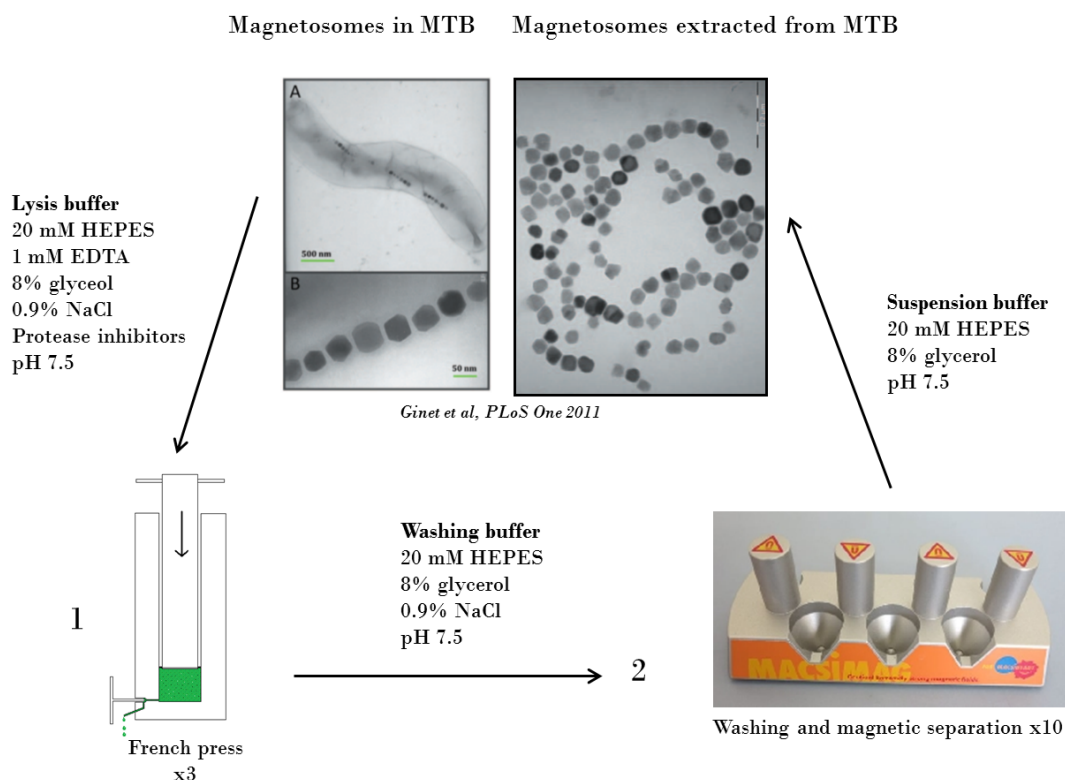


Fig. 3.3 – Magnetosomes extraction protocol from magnetotactic bacteria.

with denaturing polyacrylamide gel electrophoresis (SDS-PAGE) and infra-red spectroscopy. A comparison between magnetosomes suspensions treated or not with SDS, a detergent able to remove phospholipids, has been performed to see whether the membrane is altered by extraction and preparation procedures. Indeed, SDS-PAGE results presented in Figure 3.4 a show that proteins from magnetosome membrane are found in the supernatant when removing the membrane with SDS treatment, and in the pellet when no SDS treatment was applied. This confirms that magnetosomes extracted from MTB and prepared for *in vivo* imaging still present an intact membrane. Then the proteins content of magnetosome membrane was evidenced with FTIR (Fourier Transform Infra Red) spectroscopy. The acquired spectrum (Figure 3.4 b) reveals typical absorption bands of bacterial phospholipids:  $CH_2$ ,  $CH_3$ , amide and  $P-O$  bands for non treated magnetosomes suspension, and a characteristic absorption band of magnetite  $Fe-O$  for both treated and non treated suspensions. These FTIR spectroscopy measurements corroborate the membrane integrity when no SDS treatment is made, thus confirming that extraction and preparation procedures do not alter magnetosome membrane.

**Water dispersibility** Water dispersibility can be estimated with two measurements performed with DLS technique (Dynamic Light Scattering). The measure of Zeta potential estimates the degree of electrostatic repulsions between nanoparticles, and the stronger they are, the better the stability of nanoparticles in a water dispersion will be. In the case of MV1 magnetosomes, the negative Zeta potential measured around  $-40$  mV (Figure 3.4 c) is consistent with the presence of phospholipids in magnetosome membrane, and predicts a good stability of magnetosomes in aqueous suspension. On the other hand, the measure of hydrodynamic diameter gives an idea of the hydration shell around nanoparticles. This diameter is estimated around  $100$  nm (Figure 3.4 d), confirming that magnetosomes in suspension are in a low aggregation

state with water molecules shell around.

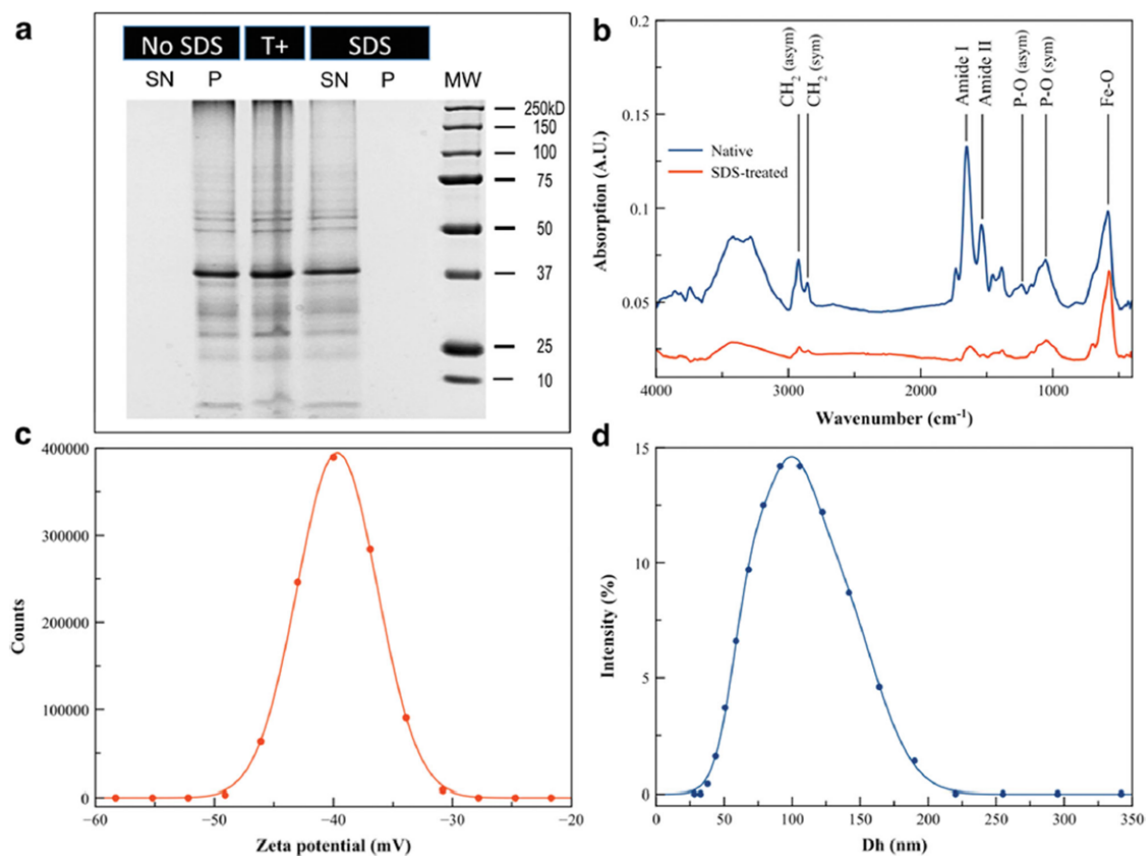


Fig. 3.4 – Physico-chemical characterization of MV1 magnetosomes membrane. (a) Proteins profile of magnetosomes membrane. Supernatant (SN) presents proteins only after SDS treatment and pellet (P) presents proteins only when no SDS was used. The T+ lane shows unprocessed magnetosomes. (b) FTIR spectrum revealing characteristic absorption bands of Amide I and II (proteins),  $Fe - O$  (magnetite),  $P - O$  and  $CH_2$  (phospholipids). (c) Zeta potential of magnetosomes suspension. (d) Hydrodynamic diameter distribution showing a broad peak, that can be fitted by the sum of three Gaussians centered at  $66.6 \text{ nm}$  (19.4%),  $92.8 \text{ nm}$  (40.4%) and  $128.7 \text{ nm}$  (40.1%). From Mériaux *et al*<sup>1</sup>.

### 3.1.3 Benefits and drawbacks of magnetosomes

Together with information from literature, this study of both iron-oxide core and membrane of magnetosomes corroborates that bacterial magnetosomes, prepared as described in Subsection 2.3.1, are fully suitable for molecular imaging applications, and can even compete with chemical IONPs. Here is a summary of the main benefits and drawbacks of magnetosomes as MRI contrast agent.

Benefits:

- Magnetosomes are easy to produce (growing the bacteria, harvesting magnetosomes from bacteria and suspending them in physiological vehicle) with a good reproducibility compared to chemical methods for manufacturing monodisperse IONP<sup>3,4</sup>. Furthermore, mag-

netotactic bacteria make possible to produce iron-oxide nanocubes simpler than with chemical methods (iron nanocubes<sup>11</sup>, core-shell iron-iron oxide nanocubes<sup>12</sup> or iron-oxide nanocubes<sup>5</sup>).

- Magnetosomes iron-oxide cores are awarded with very good magnetic properties.
- Magnetosomes are already coated with a biocompatible material.
- With suitable genetic modifications, the magnetosome membrane can be functionalized with any peptide or protein ligands.<sup>13</sup>

Drawbacks:

- It is difficult to obtain magnetosomes with a different size/shape than their genetically determined one.
- The complex proteins content of magnetosome membrane may induce a potential immunogenicity, and therefore lead to immune reaction *in vivo*.
- Changing magnetosomes shape by selecting another MTB strain may require to adapt bacteria culture conditions, and corresponding membrane engineering in case of functionalization.

## 3.2 MRI contrasting properties of magnetosomes and chemical IONPs

Transverse relaxivity embodies the ability of one contrast agent to decrease  $T_2$  relaxation rates of surrounding water protons. In this section, the transverse relaxivity measurements of IONPs with different coatings and different iron-oxide core sizes, as well as for MV1 and AMB1 magnetosomes, are presented. These measurements raise discussions on coating and iron-oxide core size/shape influence on contrasting properties.

All transverse relaxivity measurements have been performed following the protocol presented in Appendix A.1.

Longitudinal relaxivity  $r_1$  of IONP could have also been measured following the same type of protocol but with a  $T_1$  mapping imaging. However, such a measure is very difficult to achieve with a good precision since the longitudinal relaxivity of IONP is known to decrease at high magnetic field. Indeed, between 7 and 17.2 T, the transverse relaxivities are expected to be close to one but are not often measured. The maximum magnetic field investigated in most NMRD curves is around 100 MHz ( $\sim 2.5$  T) and  $r_1$  values have been found equal to 5 for Endorem<sup>®</sup> and to 1 for MSR-1 magnetosomes<sup>14</sup>. Measuring simultaneously the  $r_2$  between 200 and 500  $mM^{-1}s^{-1}$  and the  $r_1$  close to 1  $mM^{-1}s^{-1}$  is thus not feasible using the same phantom, as shown by the Figure 3.5. One solution could be to create new dedicated phantom for  $r_1$  measurement, but it would require to prepare very concentrated nanoparticles suspensions in agar. This is difficult firstly because of the nanoparticles magnetism that induces fast

<sup>11</sup>J. Park et al., Nature Materials, **3**: 891–895, 2004.

<sup>12</sup>A. Shavel et al., Advanced Functional Materials, **17**: 3870–3876, 2007.

<sup>13</sup>N. Ginet et al., PLoS ONE, **6**: e21442, 2011.

<sup>14</sup>T. Orlando et al., Contrast Media & Molecular Imaging, **11**: 139–145, 2016.

collapse at such concentration, and secondly because the susceptibility effect induced by this very intense magnetism might disturb the acquisition of a satisfying  $T_1$  map. Furthermore, it is not considered, for all these reasons, to use IONP at high magnetic field MRI in  $T_1$  weighted of mapping imaging. As a consequence, only transverse relaxivities  $r_2$  have been measured for the IONP studied in this thesis.

Transverse relaxivities  $r_2$  will be used to characterize contrast properties of IONP and to compared them to each other and with literature but not to perform quantification. Using the transverse relaxivity to quantify iron content of IONP in physiological condition (*e.g.* IONP circulating in the blood vessels, IONP internalized in cells, IONP attached to cells, ...) is indeed quite unprecise considering MRI contrast is highly dependent of the water pool accessible to the nanoparticle, which will always be very different that the very homogeneous one in agar phantom. Moreover, this effect is even more important with  $T_2^*$  weighted or mapping imaging. Despite the fact most *in vivo* experiment will be performed with such imaging ( $T_2^*$  weighted or mapping) to investigate change in contrast, no  $r_2^*$  have been investigated.

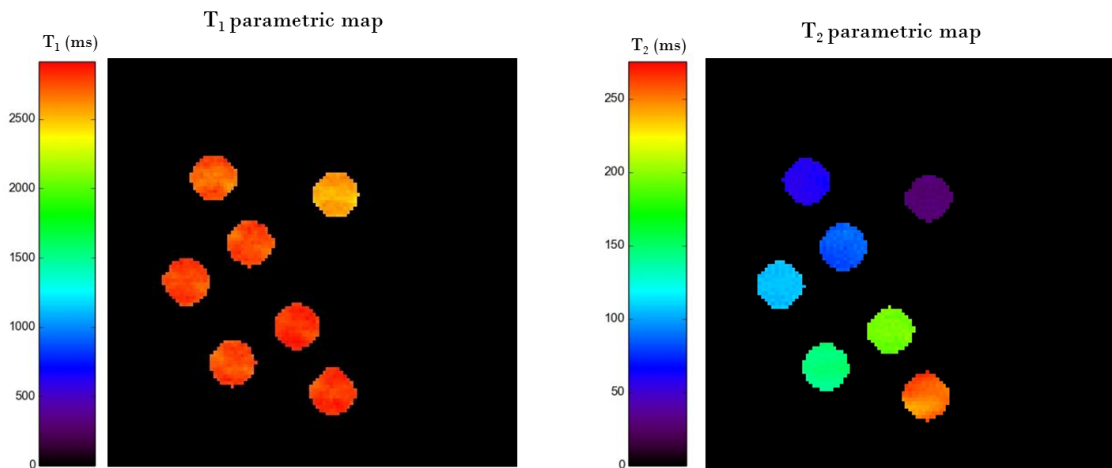


Fig. 3.5 –  $T_1$  and  $T_2$  mapping using the same phantom of AMB1 magnetosomes at 11.7 T. A contrast is observed in the  $T_2$  map whereas none can be detected on the  $T_1$  one.

### 3.2.1 Chemical IONPs transverse relaxivities

The transverse relaxivity of four different types of chemical IONPs was investigated. Firstly, P904<sup>15</sup> and Endorem<sup>®16</sup>, two IONPs suspensions from Guerbet company, have been studied, followed by NPAC and NPPO-PEG<sub>85</sub> produced by CSPBAT laboratory, in order to afterward relate their measured transverse relaxivities with their *in vivo* contrasting properties.

Furthermore, NPAC and NPPO-PEG<sub>85</sub> are made of the same maghemite core of 9 nm, and produced in aqueous micelles<sup>17</sup> but with different coatings: caffeic acid or PEG chains.

- Caffeic acid (3,4-dihydroxy-cinnamic acid) is a phenolic acid present in medicinal plants, vegetables, bee propolis and beverages, that presents anti-oxidative, anti-inflammatory

<sup>15</sup>A. Boni et al., Contrast Media & Molecular Imaging, **9**: 229–236, 2014.

<sup>16</sup>D. J. Grootendorst et al., Contrast Media & Molecular Imaging, **8**: 83–91, 2013.

<sup>17</sup>Y. Lalatonne et al., Nature Materials, **3**: 121–125, 2004.

IONP	Origin	Coating	$d$ nm	$D_H$ nm	$r_2$ at 7 T $mM^{-1}s^{-1}$
P904	Guerbet	Glucose derivative	9 <sup>15</sup>	21 <sup>15</sup>	90
Endorem <sup>®</sup> (multi-core)	Guerbet	Dextran	5 <sup>16</sup>	150 <sup>16</sup>	150
NPAC	CSPBAT	Caffeic Acid	9	17	280
NPPO-PEG <sub>85</sub>	CSPBAT	PEG	9	21	127
NPPO-PEG <sub>85</sub> -Ab	CSPBAT	PEG	9	23	224
NPPO-PEG <sub>85</sub> -2Ab	CSPBAT	PEG	9	26	235

Tab. 3.2 – Transverse relaxivity measurements of different chemical IONPs.

and anti-tumor properties<sup>18–20</sup>. This compound has on one side, a catecholic function that can form a complex with iron ion<sup>21</sup>, while on the other side, the carboxylic acid function can be used for chemical functionalization<sup>22–24</sup>. Caffeic acid thus presents interesting bio-chemical properties for designing multifunctional nanoplateforms.

- PEG chains are known for being highly biocompatible. These chains enhance colloidal stability in biological environment (stealth) by modifying surface charges and increasing steric effects at the nanoparticle surface<sup>25</sup>. The chosen PEG chains have on one side a phosphonate group that enables their adsorption onto nanoparticle surface, and on the other side, either a carboxylic function for functionalization or a simple  $CH_3$ . Moreover, the molecular mobility of these chains adsorbed onto nanoparticle surface can reduce osponization and thus, diminish macrophages uptake leading to longer blood circulation times<sup>26</sup>. An optimum coating, resulting in a blend of two PEG chains with different lengths, has been developed to insure excellent stability and stealthiness, while allowing efficient functionalization and cell internalization:  $PEG-2100-CH_3$  (at 15%) chains were used for stability and  $PEG-1200-COOH$  (at 85%) chains used for functionalization. Besides, this optimum (NPPO-PEG<sub>85</sub>) has been functionalized with either one or two antibodies of interest (NPPO-PEG<sub>85</sub>-Ab or NPPO-PEG<sub>85</sub>-2Ab)<sup>24,27</sup>.

**Results** Measured transverse relaxivities are listed in Table 3.2. P904 and Endorem<sup>®</sup> are very different, both in terms of iron-oxide core (respectively, single core versus multi-core and

<sup>18</sup>G. Ozturk et al., European Review for Medical and Pharmacological Sciences, **16**: 2064–2068, 2012.

<sup>19</sup>Y. Sato et al., International Journal of Pharmaceutics, **403**: 136–138, 2011.

<sup>20</sup>A. A. P. Almeida et al., Journal of Agricultural and Food Chemistry, **54**: 8738–8743, 2006.

<sup>21</sup>H. Gulley-Stahl et al., Environmental Science & Technology, **44**: 4116–4121, 2010.

<sup>22</sup>S. Richard et al., Journal of Materials Chemistry B, **3**: 2939–2942, 2015.

<sup>23</sup>S. Richard et al., Submitted to ACS Chemical Biology, , 2016.

<sup>24</sup>S. Richard., PhD Thesis, Paris 13 University, , 2015.

<sup>25</sup>J. V. Jokerst et al., Nanomedicine (London, England), **6**: 715–728, 2011.

<sup>26</sup>F. M. Veronese et al., Drug Discovery Today, **10**: 1451–1458, 2005.

<sup>27</sup>S. Richard et al., Submitted to ACS Applied Materials & Interfaces, , 2016.

maghemite versus  $(Fe_2O_3)_m(FeO)_n$ ) and coating (glucose derivative versus dextran). Thus, no direct comparison can be made, but it is possible to explain this difference in transverse relaxivity from the size difference that leads Endorem<sup>®</sup> to have an increased rotational correlation time, and so a longer interaction between the electronic spins of the contrast agent and the nuclear spins of proton. For *in vivo* experiments, one must keep in mind that Endorem<sup>®</sup> has a transverse relaxivity 1.7 times higher than P904.

As already mentioned, NPAC and NPPO-PEG<sub>85</sub> are made of the same iron-oxide core but with different coatings, though, NPAC presents a  $r_2$  value 2.2 times higher than the one of NPPO-PEG<sub>85</sub>. This can be explained considering NPAC coating being slightly thinner than the one of NPPO-PEG<sub>85</sub>, probably allowing water molecules to approach closer to iron-oxide core, where the intensity of local magnetic field is higher.

Transverse relaxivity values are also increasing with the number of antibodies grafted at NPPO-PEG<sub>85</sub> surface, as well as the hydrodynamic diameters. This seems to disagree with the previous observation between NPAC and NPPO-PEG<sub>85</sub>, so the significance of hydrodynamic diameter may be precised. Indeed, between the different NPPO-PEG<sub>85</sub> nanoparticles, the coating is the same but the increase in hydrodynamic diameter comes from the volume occupied by grafted antibodies. These one or two antibodies at nanoparticle surface do not surround the whole nanoparticle as coating does, which justifies why the apparent increase in hydrodynamic diameter must not be interpreted as an increase in coating thickness. Finally, antibodies have a significant size compared to nanoparticle scale: they can break nanoparticle symmetry and also modify nanoparticle movements. In particular, it could be possible that antibodies at nanoparticle surface act like arms that restrain nanoparticle rotation, and therefore lead to an increase in transverse relaxivity<sup>28</sup>.

In conclusion, Endorem<sup>®</sup> presents a higher transverse relaxivity value at 7 T than P904, and so does NPAC compared with NPPO-PEG<sub>85</sub>. This result only insures that Endorem<sup>®</sup> and NPAC exhibit higher contrasting properties when nanoparticles are static and trapped in agarose network, so their relevance for *in vivo* MRI contrast enhancement still needs to be characterized.

### 3.2.2 Size effect in chemical IONPs transverse relaxivities

The great majority of IONPs used as MRI contrast agent is in the superparamagnetic domain as presented in Section 2.2. It is possible to change nanoparticle size while staying in this regime, leading to transverse relaxivity values increasing with IONPs radius<sup>29</sup>.

IONPs with different iron-oxide core sizes from 2.5 to 11 nm, and coated with the same PEG chains ( $PEG - 2100 - CH_3$ ), were synthesized by the CSPBAT laboratory using a sol-gel process under microwaves<sup>24,30</sup>.

**Results** Table 3.3 presents different measurements performed on these IONPs: the iron-oxide core diameter  $d$  measured with TEM, the hydrodynamic diameter  $D_H$ , the saturation magnetization  $M_S$ , and the transverse relaxivity  $r_2$  measured at 7 T. The general trend is that hydro-

<sup>28</sup>M. Botta et al., European Journal of Inorganic Chemistry, **2012**: 1945–1960, 2012.

<sup>29</sup>Y.-W. Jun et al., Journal of the American Chemical Society, **127**: 5732–5733, 2005.

<sup>30</sup>R. J. P. Corriu et al., Angewandte Chemie International Edition in English, **35**: 1420–1436, 1996.

$d$	$D_H$	$M_S$	$r_2$ at 7 T
$nm$	$nm$	$emu.g^{-1}$	$mM^{-1}s^{-1}$
2.5	5.8	3	24
3.5	16.5	23	188
4	11	29	60
7	17	42	258
9	21.5	51	633
11	22	60	245

Tab. 3.3 – Transverse relaxivity values of chemical IONPs with different iron-oxide core diameters but coated with the same PEG chains.

dynamic diameter and saturation magnetization grow with iron-oxide core diameter, whereas transverse relaxivity increases with iron-oxide core diameter until 9 nm and decreases for 11 nm nanoparticles. Interestingly, the relaxivity increases with the hydrodynamic diameter, as predicted by the SBM theory that explains that lengthening the rotation correlation time leads to increased transverse relaxivity.

A closer look to the saturation magnetization as a function of iron-oxide core diameter (Figure 3.6, left) reveals that saturation magnetization grows faster with core size until 4 nm, and then a slower increasing rate is observed. Similar behavior of saturation magnetization growing fast until reaching a plateau has already been observed<sup>31</sup>. This phenomenon is attributed to the spin canting that appears at nanoparticle surface because of symmetry breaking, which reduces the volume of material that contributes to nanoparticle magnetic properties. Such disordered spin layer thickness mainly depends on material type and thus, it is not expected to significantly vary with nanoparticle size<sup>32</sup>, meaning that the non-magnetic volume in small tested IONPs (2.5 nm to 4 nm) represents a greater fraction of entire nanoparticle volume than for bigger ones (4 nm to 11 nm), which could explain the shape of the curve of  $M_S$  versus  $d$ .

In Chapter 2, theoretical relationships between physical features of nanoparticles and their transverse relaxivity  $r_2$  were presented. Superparamagnetic nanoparticles are generally expected to be in the Motional Averaging Regime (see Section 2.1.4), which is consistent with the  $\Delta\omega\tau_D$  values that are found below 1 ( $10^{-3} < \Delta\omega\tau_D < 10^{-1}$ ) when computed with the measured core diameter and saturation magnetization. The equation 2.3 estimates  $r_2$  values from physical features of this superparamagnetic IONPs in MAR range, and in particular, one can see that:

$$\begin{aligned}
 r_2 &\propto \nu_{mat} M_{S,v}^2 d^2 \\
 &\propto \nu_{mat} \left( \frac{M_S}{\rho_{mat}} \right)^2 d^2
 \end{aligned}$$

<sup>31</sup>E. D. Smolensky et al., Journal of materials chemistry. B, **1**: 2818–2828, 2013.

<sup>32</sup>B. H. Kim et al., Journal of the American Chemical Society, **133**: 12624–12631, 2011.

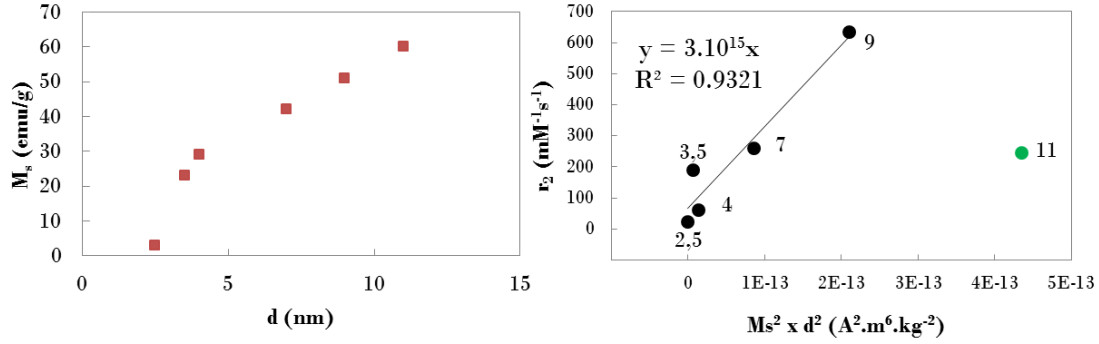


Fig. 3.6 – IONP size effect on saturation magnetization and transverse relaxivity. The left plot shows the evolution of saturation magnetization versus iron-oxide core diameter. The right plot shows the evolution of transverse relaxivity versus the product of squared saturation magnetization with squared iron-oxide core diameter, and the corresponding linear fit for all nanoparticles except the one of 11 nm.

This relationship  $r_2 = f(M_S^2 \times d^2)$  has been plotted to check if the theoretical model was verified with our experimental data (Figure 3.6, right). Except for the 11 nm nanoparticles, the other tested ones seem to follow a linear trend as expected. Furthermore, the slope order of magnitude is found close to  $10^{15}$ , whereas the theoretical one is around  $10^{14}$  (computed using equation 2.3). This results illustrates that the theoretical models are useful to predict or to interpret scaling laws of IONPs toward contrasting properties. Though, no reason has been found to explain why the 11 nm nanoparticles do not fit the theoretical model, since their  $\Delta\omega\tau_D$  value is well in the MAR range.

### 3.2.3 Magnetosomes transverse relaxivities

The transverse relaxivity of magnetosomes from two different strains of magnetotactic bacteria has been measured at three different magnetic field intensities. The two strains are AMB1, that produces cubo-octahedral magnetosomes, and MV1, that produces elongated ones. Their respective mean size and shape factor have been also estimated, as well as MV1 saturation magnetization, and results were previously shown in the subsection 3.1.1 of this chapter.

Strain	Shape	$l$ nm	$r_2$ at 7 T $mM^{-1}s^{-1}$	$r_2$ at 11.7 T $mM^{-1}s^{-1}$	$r_2$ at 17.2 T $mM^{-1}s^{-1}$
MV1	Elongated	53.6	784	-	728
AMB1	cubo- octahedral	47.6	545	565	490

Tab. 3.4 – Transverse relaxivity values of different magnetosomes measured at three magnetic field intensities.

**Results** As presented in Table 3.4, the transverse relaxivities of MV1 magnetosomes are always higher than the ones of AMB1, whatever the magnetic field intensity. In addition, changing the magnetic field intensity does not seem to have a clear effect on magnetosomes transverse

relaxivities. For AMB1,  $r_2$  value can be considered nearly constant between 7 T and 11.7 T, and then slightly decreases at 17.2 T. For MV1,  $r_2$  value measured at 17.2 T is also a little bit lower than the one at 7 T. Indeed, it is already known that at high magnetic field intensity, the transverse relaxivity of IONPs reaches a plateau as demonstrated by other experiments<sup>31,33</sup>. However, the magnetosomes magnetic properties at 17.2 T are quite difficult to discuss considering the lack of data available at such high magnetic field intensity.

This experiment gives the opportunity to analyze the influence of nanoparticle shape on the transverse relaxivity. The ideal situation would have been to compare different shapes with a constant volume, which is not the case considering mean sizes reported in Subsection 3.1.1. AMB1 magnetosomes seem to have a volume approximately 25% smaller than the one of MV1. Besides, it would have been interesting to have equivalent spherical nanoparticles, in order to compare with the great majority of other chemical IONPs. Nevertheless, this important difference of transverse relaxivity in favor of elongated magnetosomes, can be explained by the fact that the nanoparticle shape is known to have a significant influence on magnetic properties<sup>31,34</sup>, due to differences of surface-to-volume ratio, aspect ratio and crystallinity for example. Both AMB1 and MV1 magnetosomes can be theoretically compared to spherical nanoparticles, and then highlight why they present high transverse relaxivities, and why higher values are observed for MV1 than for AMB1.

- **Cube versus sphere** Several studies already reported that iron-oxide nanocubes present higher saturation magnetization and higher  $T_2$ -shortening property compared to spherical nanoparticles<sup>34–36</sup>.

Firstly, cubic magnetic nanoparticles exhibit shape anisotropy energy in addition to the magnetocrystalline one, because of the demagnetization effect that leads the easy axis to follow a preferred direction<sup>37</sup>. Though, this anisotropy energy seems to impact the coercivity but not the saturation magnetization and thus, it might not be the origin of the higher transverse relaxivity of nanocubes. On the other hand, this enhanced coercivity may be of great interest for magnetic hyperthermia.

A second interesting feature is that cubes have a higher surface-to-volume ratio than spheres for a constant volume (Figure 3.7). This allows a larger surface to be explored by water molecules, which may partly explain the higher transverse relaxivity.

Finally, one other possible cause may be the better crystallization of cubic nanoparticles compared with spherical ones<sup>36,38</sup>. The shape appears as a signature of how the particles were crystallized, since faceted nanoparticles were *a priori* grown more slowly than spherical ones. Faceted, and so cubic nanoparticles, are more likely to result from epitaxial growth, and then to exhibit a better crystallinity. The better magnetic properties of cubes versus spheres may not only originate from their shape, but also from their intrinsic crystallographic properties.

In conclusion, it remains difficult to comment on AMB1 magnetosomes transverse relaxivity, since we do not have access to iron-oxide nanospheres with similar features, and even

<sup>33</sup>C. Corot et al., *Advanced Drug Delivery Reviews*, **58**: 1471–1504, 2006.

<sup>34</sup>N. Lee et al., *Proceedings of the National Academy of Sciences*, **108**: 2662–2667, 2011.

<sup>35</sup>C. Martinez-Boubeta et al., *Scientific Reports*, **3**: 1652, 2013.

<sup>36</sup>G. Zhen et al., *The Journal of Physical Chemistry C*, **115**: 327–334, 2011.

<sup>37</sup>R. S. M. Rikken et al., *Soft Matter*, **10**: 1295–1308, 2014.

<sup>38</sup>B. Luigjes et al., *The Journal of Physical Chemistry C*, **115**: 14598–14605, 2011.

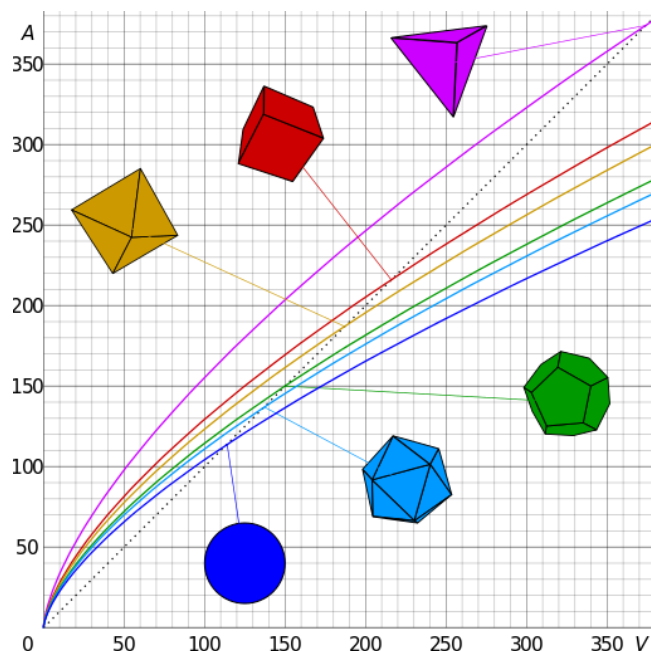


Fig. 3.7 – Graphs of surface area  $A$  versus volume  $V$  for different shapes (from Cmglee contributor, Wikimedia Commons). Whatever their volume, spheres have smaller surface-to-volume ratio than cubes.

if we do, the synthesis process may also not be comparable. Their extremely good contrasting properties would not originate from their cubo-octahedral shape itself, but rather from the biological control of the mineralization, which provides an excellent crystallinity to magnetosomes iron-oxide core, and thus a higher saturation magnetization.

- **Elongated prism versus sphere** Elongated nanoparticles like nanorods have also drawn attention because of their particular magnetic properties and enhanced relaxation properties<sup>39,40</sup>. Nanorods present an increased shape anisotropy that leads to an increased coercivity. As previously mentioned, this has no influence on relaxation properties, but it is of great interest for magnetic hyperthermia. Besides, when nanorods exhibit a high aspect ratio, their saturation magnetization is smaller than the one of comparable spheres, and yet nanorods have higher transverse relaxivity<sup>41</sup>. This counter-intuitive result comes from the fact that theories describing  $r_2$  as a function of  $M_S$  and  $d$  (see 2.1.4), rely on the hypothesis of a spherical IONP. As explained by Mohapatra *et al*<sup>41</sup> (Figure 3.8), the local magnetic field inhomogeneities created by a nanorod compared to a nanosphere occupy a larger volume around the nanoparticle, which can explain the experimental measurement of higher transverse relaxivity. Besides, this result has been also observed for other shapes of iron-oxide nanoparticle. Indeed, researchers have successfully produced octapod iron-oxide nanoparticles, and have demonstrated that they present increased contrasting properties because the surrounding magnetic field spreads on a larger area compared to nanosphere<sup>42</sup>.

In conclusion, MV1 magnetosomes exhibit a higher  $r_2$  compared with AMB1. Both magnetosomes contain iron-oxide nanocrystals awarded with good crystallinity, because

<sup>39</sup>S. Nath et al., *Chemistry of Materials*, **21**: 1761–1767, 2009.

<sup>40</sup>H. Kloust et al., *Chemistry of Materials*, **27**: 4914–4917, 2015.

<sup>41</sup>Je. Mohapatra et al., *Nanoscale*, **7**: 9174–9184, 2015.

<sup>42</sup>Z. Zhao et al., *Nature Communications*, **4**: 2266, 2013.

of their mineralization under biological control. The difference in measured  $r_2$  values seems to come from the difference in shape, since elongated geometry is supposed to favor larger magnetic field inhomogeneities.

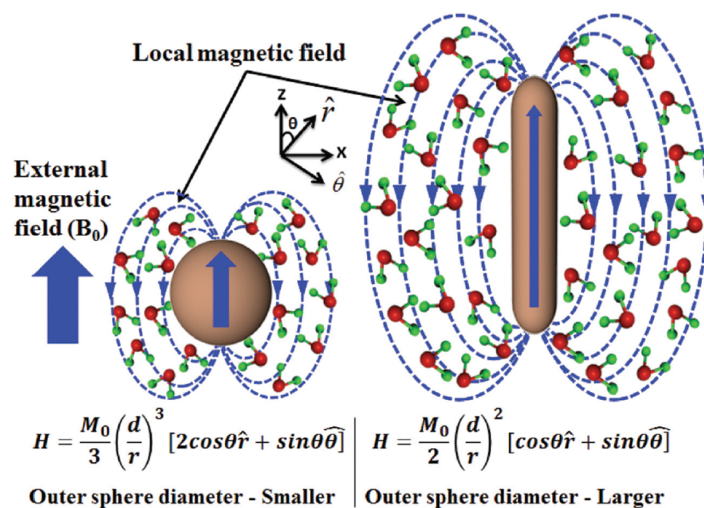


Fig. 3.8 – Schematic representation of the local magnetic field around nanosphere (left) versus nanorod (right).  $H$  is the induced local magnetic field around nanoparticle,  $d$  the effective diameter,  $r$  the distance between the nuclear spin of water molecule and the nanoparticle, and  $\theta$  the inclination angle between the nuclear spin and the nanoparticle (from Mohapatra *et al*<sup>41</sup>).

### 3.3 Brain angiography of healthy mouse with contrast-enhanced MRI

All the different chemical IONPs and magnetosomes, for which we performed an *in vitro* characterization of their contrasting properties, were designed for *in vivo* MRI applications. Because IONPs are particularly known to be efficient blood pool contrast agents, we decided to perform brain vasculature MRI acquisitions, after a systemic injection to mice, as a key test to evaluate their *in vivo* contrasting properties. Note that all *in vivo* experiments of this PhD were conducted in agreement with recommendations (see details in Appendix B.1).

**Protocol** Contrast agents ability to reveal mouse brain vasculature was assessed using  $T_2^*$ -weighted sequences, that are very sensitive to iron-induced susceptibility effect (or  $T_2^*$  effect). FLASH sequence (Fast Low Angle SHot) has been chosen for revealing the  $T_2^*$  negative contrast at high acquisition speed: the sequence was run before and after contrast agent injection (sequence parameters are given in Appendix B.2). The intravenous injection consisted in removing the cradle from the MRI scanner tunnel to inject, at the mouse tail vein, a dose of  $200 \mu\text{mol}_{Fe}/\text{kg}_{BW}$  (between 100 and 200  $\mu\text{L}$ ) with a 29 G syringe, before inserting the cradle back in the tunnel for post injection scans. Blood vessels are expected to be revealed as hypo-intense voxels in  $T_2^*$ -weighted images, since IONPs circulating in the blood stream after intravenous injection have no possibility to cross the blood-brain barrier due to their size<sup>43</sup>.

<sup>43</sup>B. Marty *et al.*, Journal of Cerebral Blood Flow & Metabolism, **32**: 1948–1958, 2012.

Therefore, a dedicated filtering method that extracts vessels from contrast difference in FLASH images, based on the work of Frangi<sup>44,45</sup>, has been used to allow a clear visualization of brain vessels (3D angiograms), before and after IONPs injection. One needs to keep in mind that some large brain vessels may be visualized on  $T_2^*$ -weighted images before any contrast agent injection, due to the circulating endogenous iron (haemoglobin protein complexes binding iron ions in red blood cells). Furthermore, a specific score  $s$  was computed to embody the improvement in vessels detection in percent related to IONPs injection. Data processing protocols are detailed in Appendix C.1.

*In vivo* MRI experiments have been run on several scanners with different magnetic field intensities: 7 T, 11.7 T and 17.2 T. Since the iron-induced susceptibility effect is higher at higher field intensity, the 7 T scanner was used for standard tests whereas the 17.2 T scanner was kept for more advanced experiments. The 11.7 T scanner installed at NeuroSpin thanks to FLI investment (France Life Imaging), is equipped with a radiofrequency cryogenic coil dedicated to mouse brain that reduces electronic noise, and thus enables faster acquisitions while reaching excellent signal-to-noise ratio.

### 3.3.1 *In vivo* contrasting properties of chemical IONPs

The same chemical IONPs, which transverse relaxivity was investigated *in vitro* (see Section 3.2), have been intravenously injected to mice, in order to study their *in vivo* contrasting properties.

P904 and Endorem<sup>®</sup> from Guerbet company have been tested on nude mice at 11.7 T. Note that these mice received a sham injection in the right brain hemisphere, since they were control animals for U87 tumor model study (surgery protocol detailed in Appendix B.3): this intracerebral injection is expected to have no significant impact on the *in vivo* evaluation of contrast agent properties, since each animal is its own control (pre injection versus post injection).

NPAC and NPPO-PEG<sub>85</sub> from CSPBAT laboratory have been tested on healthy Swiss mice at 7 T.

**Results** FLASH images, computed 3D angiograms and their corresponding score  $s$  are presented in Figure 3.9 for Endorem<sup>®</sup>, P904, NPAC and NPPO-PEG<sub>85</sub>.

The comparison of FLASH images before and after injection enables to estimate, on one brain slice, the number of hypo-intense voxels that appear because of IONPs injection. The 3D angiogram allows a global visualization of this effect. Finally, the computation of score  $s$  is used as an index to compare contrast agents together. However, comparing IONPs imaged at different magnetic field intensities may not be relevant, considering that the iron-induced susceptibility effect is not comparable, as well as the spatial resolution of FLASH images (voxels in images acquired at 11.7 T are 20 times smaller than the ones in images acquired at 7 T). Indeed the MRI signal resulting from the same amount of IONPs in a voxel of  $75 \times 75 \times 75 \mu\text{m}^3$

<sup>44</sup>A. F. Frangi et al., MICCAI (Medical Image Computing and Computer-Assisted Intervention), **1496**: 130–137, 1998.

<sup>45</sup>R. Manniesing et al., Medical Image Analysis, **10**: 815–825, 2006.

(11.7  $T$ ) will be lower than the one in a voxel of  $160 \times 160 \times 320 \mu m^3$  (7  $T$ ), because of a dilution effect called the partial volume effect. This difference of spatial resolution will modify the detection sensitivity of IONPs, and will therefore impact the vessels detection algorithm. Thus P904 and Endorem<sup>®</sup> will be compared together on one hand, and NPAC and NPPO-PEG<sub>85</sub> on the other hand. These comparisons will enable to investigate the consistency of *in vitro* measured transverse relaxivity versus *in vivo* contrasting properties, but also the impact of coating for IONPs synthesized by CSPBAT.

FLASH images acquired post injection of Endorem<sup>®</sup> and P904 reveal a significative increase of hypo-intense voxels number, confirming that both IONPs are very efficient blood pool agents. The post injection angiograms enable to confirm this observation, by highlighting numerous small vessels compared with the pre injection ones. Finally, the scores  $s$  show a very important increase in the number of voxels detected as vessels, this number being multiplied by more than 200% for both IONPs. Even if Endorem<sup>®</sup> has a transverse relaxivity around 1.7 times higher than the one of P904, both IONPs seem to exhibit similar vessels enhancement properties. This first study demonstrates that higher transverse relaxivity will not always induce higher *in vivo* contrasting properties. Difference in IONPs clearance cannot be invoked considering the short scan duration (5 *min*) of the FLASH sequence used at 11.7  $T$ . One possible explanation could be that P904, which hydrodynamic diameter is nearly 7 times smaller than the one of Endorem<sup>®</sup>, may be more stealth, which compensates for its lower transverse relaxivity. Indeed, IONPs can be altered by floating in the blood, for example because of interactions between the coating and blood proteins, or because of their internalization by immune cells, which modifies their transverse relaxivity *in vivo*.

FLASH images acquired post injection of NPAC and NPPO-PEG<sub>85</sub> reveal two different behaviors: NPAC injection does not seem to enhance MRI contrast in mouse brain, whereas NPPO-PEG<sub>85</sub> one does. Computed angiograms corroborate this insight: after injection, NPPO-PEG<sub>85</sub> leads to a better visualization of mouse brain vasculature, while injection of NPAC only reveals few more vessels. Finally, the scores  $s$  show a great increase in hypo-intense vessels detection for NPPO-PEG<sub>85</sub> and a low increase for NPAC. The *in vivo* contrasting properties are therefore in complete opposition with the measured *in vitro* relaxivity measurements, that have awarded NPAC with a 2.2 times higher relaxivity value than NPPO-PEG<sub>85</sub>. This result has to be interpreted regarding the nature of coating since it is the only difference between the two IONPs. Indeed, even if NPPO-PEG<sub>85</sub> nanoparticles have a 1.2 times bigger hydrodynamic diameter, their PEG coating is known to have excellent biocompatibility properties, and to increase blood circulation time compared with caffeic acid. Furthermore, blood clearance is a parameter which needs to be considered here, because the FLASH sequence duration at 7  $T$  is around 40 *min*, which may be long enough to see a difference in IONPs circulation time: in literature, reported blood half lives of some IONPs developed for clinical use go from 2 to 10 hours, depending of iron-oxide core size and coating<sup>33</sup>. The high transverse relaxivity value of NPAC does not imply efficient *in vivo* MRI contrast enhancement, probably because of biocompatibility issues, while NPPO-PEG<sub>85</sub> with lower transverse relaxivity shows excellent *in vivo* contrasting properties.

In conclusion, this comparison of *in vivo* contrasting properties versus *in vitro* measured relaxivities assesses that the complexity of IONPs biodistribution needs to be taken into account for evaluating contrast agent efficiency. In particular, coating nature is of tremendous

---

<sup>33</sup>C. Corot et al., *Advanced Drug Delivery Reviews*, **58**: 1471–1504, 2006.

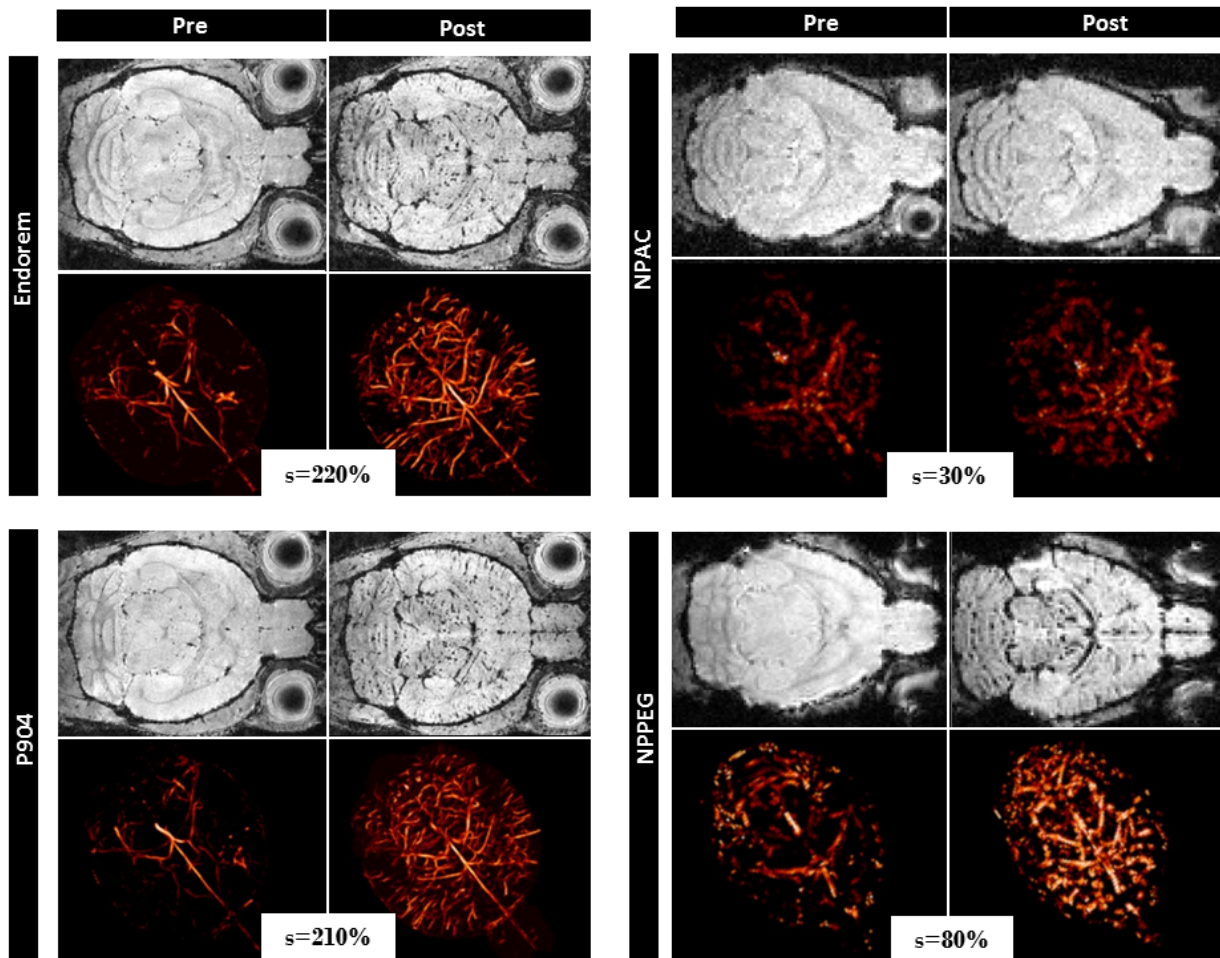


Fig. 3.9 – Comparison of *in vivo* contrasting properties of chemical IONPs: Endorem<sup>®</sup> (top left), P904 (down left), NPAC (top right) and NPPO-PEG<sub>85</sub> (down right); first and third columns correspond to pre injection acquisitions, while second and fourth ones correspond to post injection. FLASH images are in grayscale (top and third rows) and the renderings of 3D angiogram are displayed with red colored gradient (second and fourth rows).

importance to fully benefit from the contrasting power of the iron-oxide core. Nevertheless, this angiogram based evaluation of contrasting properties can also be criticized since it only focuses on the ability of nanoparticles to reveal brain vasculature, which may not be relevant for other MRI applications. Indeed, in molecular imaging, functionalized IONPs are expected to target a specific biomarker, meaning that the evaluation of their contrasting properties would focus on their ability to specifically reveal the targeted zone.

### 3.3.2 *In vivo* contrasting properties of magnetosomes

AMB1 and MV1 magnetosomes have been injected intravenously to mice in order to characterize their *in vivo* contrasting properties. MV1 magnetosomes have been tested on healthy Swiss mice at 17.2 T, while AMB1 ones have been tested on healthy nude mice at 11.7 T.

**Results** Results are presented in Figure 3.10. One needs to be careful when comparing AMB1 and MV1 *in vivo* contrasting properties because experiments have not been run at the same magnetic field intensities. Indeed,  $T_2^*$ -weighted images reveal magnetic field inhomogeneities induced by IONPs, these inhomogeneities being more important at higher field. However, the partial volume effect is expected to be limited, considering that the voxels in images acquired at 17.2 T are only 3.5 times bigger than the ones in images acquired at 11.7 T, which may allow us to carefully compare experiments. For AMB1, FLASH images acquired 25 *min* post injection during 5 *min* were chosen to compare with MV1, where FLASH images were acquired during 30 *min* post injection. This shall enable to be less influenced by differences in blood clearance, which is unknown so far for both magnetosomes.

MV1 injection leads to an important number of hypo-intense voxels detected on FLASH image, which is also illustrated by the 3D angiogram unveiling numerous small vessels. AMB1 injection only reveals few hypo-intense voxels on FLASH image, and thus few small vessels appear on 3D angiogram. The scores  $s$  computed from 3D angiogram confirm these observations. The spatial resolution tends to favor AMB1 (acquisition at 11.7 T,  $75 \times 75 \times 75 \mu\text{m}^3$  voxels), while the susceptibility effect tends to favor MV1 (acquired at 17.2 T,  $90 \times 90 \times 180 \mu\text{m}$  voxels), but overall, it still seems that MV1 exhibits higher *in vivo* contrasting properties compared to AMB1. Hypothesizing that this comparison is valid, this result is in agreement with the transverse relaxivity measurements, MV1 having the highest  $r_2$  (see Table 3.4). Finally, measuring magnetosomes *in vivo* contrasting properties, in relation with their transverse relaxivity, supports the idea that if coating, iron-oxide core synthesis method, and nanoparticle volume are comparable (which is the case for magnetosomes), biocompatibility and blood clearance are also comparable, which leads the *in vivo* behavior to mirror iron-oxide core contrasting properties.

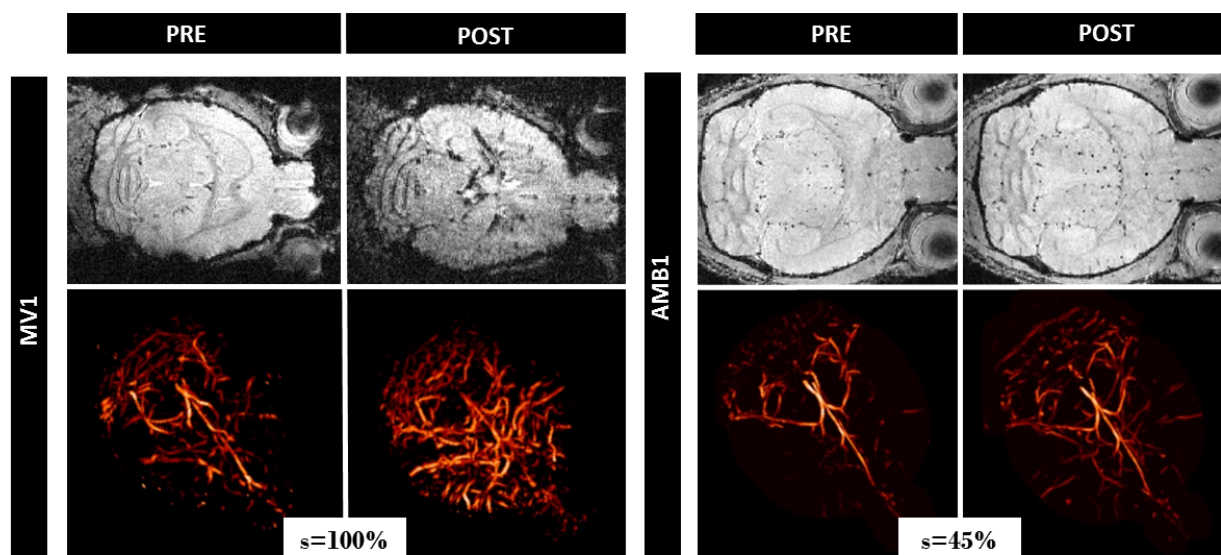


Fig. 3.10 – Comparison of *in vivo* contrasting properties of magnetosomes: MV1 (left) and AMB1 (right); first and third columns correspond to pre injection acquisitions, while second and fourth ones correspond to post injection. FLASH image are in grayscale (top and third rows) and the renderings of 3D angiogram are displayed with red colored gradient (second and fourth rows).

### 3.4 Brain tumor contrast-enhanced MRI in a mouse model of glioblastoma

In the previous sections, IONPs have been characterized *in vitro*, and their contrasting properties to reveal *in vivo* mouse brain vasculature have also been assessed. In this section, IONPs are used to study neoangiogenic vessels growth and iron uptake in brain tumors, more specifically in a U87 mouse model of human glioblastoma.

Firstly, shape and growth of brain tumors of our U87 mouse model have been characterized. In a second step, our algorithm designed to reveal brain vessels from  $T_2^*$ -weighted images was used to investigate changes in vasculature due to tumor growth, at different times after tumor implantation. Finally, the enhanced permeability and retention effect (EPR) of the tumor has been assessed with different IONPs.

#### 3.4.1 Tumor growth follow-up in diameter and volume

U87 human glioblastoma cells were cultured to be later implanted in nude mouse brain, following a protocol described in Appendix B.3. It was interesting to characterize tumor shape and growth with time, in order to allow the inclusion of animals with comparable brain tumors.

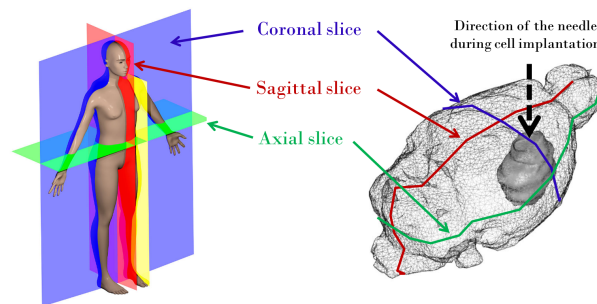


Fig. 3.11 – Anatomical slices from human to mouse. The left scheme displays the different anatomical slices defined for human (from Wikipedia), and the right scheme displays a reconstructed mouse brain mesh with a segmented tumor, and the corresponding slice orientations. Tumor cells are implanted with a needle inserted perpendicularly to axial slice.

**Protocol** 24 nude mice were scanned with a RARE sequence at 11.7 T (details in Appendix B.2) from 8 to 27 days post tumor cells implantation, 8 being the minimum time ensuring a complete wound healing after surgery, and 27 days being the maximum duration of tumor growth without exceeding a 6 mm diameter (as measured on brain axial slice, see Figure 3.11), which is one of the severity limits defined in the ethical permit of this study. While regularly following tumor growth after cells implantation, it seems that this growth was not isotropic but rather cylindrical or ellipsoidal. To investigate this hypothesis, tumor volume has been manually segmented on RARE anatomical image, and the highest radius has been measured among all axial slice.

**Results** The tumor volumes as a function of days after cells implantation are plotted in Figure 3.12 A. This plot clearly reveals a slow and reproducible growth until 15 days, after which

individual differences lead to high variability in measured tumor volumes. From 15 to 27 days, it is then very difficult to predict with good precision the tumor size: this implies a precise and regular imaging follow-up of tumor growth before including animals in studies requiring similar tumors.

The tumor volume, together with the maximum axial radius, have been used to investigate tumor shape. Equivalent spherical, ellipsoidal and cylindrical volumes have been computed with the maximum axial radius. For cylinder and ellipsoid, the characteristic distance in third dimension (direction of cell implantation) has been set to  $2.75\text{ mm}$ , which is the typical height of tumors observed on RARE images (around 5.5 slices of extension). Note that this characteristic distance is also consistent with the fact that tumor cells are injected  $3.5\text{ mm}$  deep to the bregma, which lets a free column of around  $3\text{ mm}$  height for the cells to grow. Results of tumor size and shape analysis are plotted in Figure 3.12 B. It appears that the best Pearson correlation coefficients of the linear fit are obtained for the quadratic dependence of tumor volume with maximum axial radius (cylinder or ellipsoid) versus cubic dependence (sphere), thus eliminating the description of tumor shape as a sphere and confirming the observations of non isotropic tumor growth. Then, the slope of the linear fit reveals that the cylinder shape overestimates the actual tumor volume, letting the most probable geometry to be the ellipsoid. This experiment validates that, in most case, tumor will grow as an ellipsoid, oriented in the direction of the hole drilled by the injection needle. Finally, this also demonstrates that in general, tumor maximum axial diameter or radius, which is easy to measure, is relevant to estimate tumor volume. In the following experiments, tumor maximum axial radius will be used as tumor size criteria to include animals in molecular imaging studies.

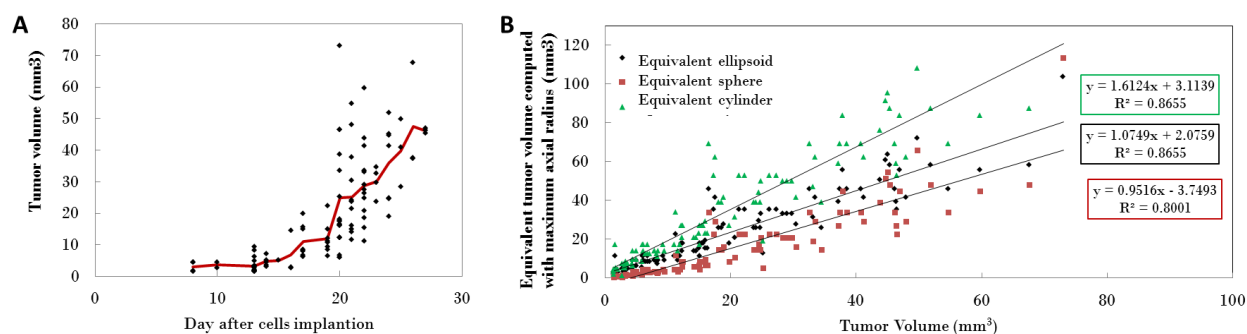


Fig. 3.12 – U87 tumor growth, size and shape analysis. The left plot shows the segmented tumor volume as a function of the days after cells implantation. The right plot shows, as a function of measured tumor volumes, the results of tumor volume modelization with a sphere, a cylinder or an ellipsoid, the equivalent volumes being computed from the maximum axial radius.

### 3.4.2 Tumor vessels follow-up

Our angiography method, based on detection of hypo-intense voxels in  $T_2^*$ -weighted images acquired post injection of IONPs, has been used on tumor bearing mice at different times after cells implantation.

**Protocol** P904 was chosen for its excellent *in vivo* contrasting properties as blood pool agent. The experiment described in Section 3.3 was simply repeated from 6 to 17 days post tumor cells implantation, letting at least 3 days between two P904 injections. P904 blood half-life has been found equal to 2.7 h for an injected dose of  $350 \mu\text{mol}_{[Fe]}/\text{kg}_{BW}$ <sup>46</sup>, which ensures a complete blood clearance before the next injection 3 days later. 5 tumor bearing mice and 2 sham surgery ones were planned for this experiment (see Appendix B.3 for more details on tumor implantation). Unfortunately, this multi-injections protocol turned out to be very difficult to perform without optimized injection system (implanted catheter for example): the vein of some mice did not properly heal during the 3 days after one injection, and thus making the following injection very complicated to realize while insuring a precise dose. At the end, only 2 tumor bearing and 1 sham animals went through all injections and were analyzed.

**Data Processing** After the experiment, FLASH images were reconstructed and the corresponding 3D angiograms were computed. An additional step of skeletonization was applied to the 3D angiogram to detect the center of each vessel. This enables to quantify the number of branches, their length and the corresponding Euclidean distance. The detailed protocol to obtain such measurements from 3D angiograms is presented in Appendix C.2. Following the work of Kim *et al*<sup>47</sup>, micro-vessels density, tortuosity and length per unit volume have been computed as follows:

$$\text{Micro - vessels density} = \frac{\text{Number of branches}}{\text{ROI volume}}$$

$$\text{Tortuosity} = \frac{\text{Vessels length}}{\text{Vessels Euclidean length}}$$

$$\text{Length per unit volume} = \frac{\text{Total sum of vessels length}}{\text{ROI volume}}$$

**Results** Evolution of skeletonized 3D angiogram on a tumor bearing mouse is illustrated in Figure 3.13 A. For this mouse, the first obvious observation is that the skeleton at D9 reveals less vessels than others: this might be explained by a small difference in injected dose of P904, that leads to difference in vessels detection. The great challenge of this experiment was clearly to repeat identical injections in order to reliably compare 3D angiograms. On Figure 3.13 A, the tumor zone is indicated in light red and the contralateral one in light gray: similar vessels distribution is found in contralateral zone throughout the time (except at D9), while slight differences can be observed in the tumor zone. Finally, these angiograms seem to reveal only large vessels, which suggests that the spatial resolution in FLASH images is not sufficient enough to detect smaller vessels. In literature, tumor vasculature is mainly assessed by acquiring images at micrometer scale: for example, high spatial resolution MRI of *post-mortem* brain samples, previously perfused with a silicone rubber compound, reveals much smaller and complex vascular structures<sup>47,48</sup>. For this study, we chosen to focus on *in vivo* experiments, in order to follow the tumor vessels evolution on the same animal. Moreover, the acquisition time was reduced to avoid contrast enhancement loss due to contrast agent clearance from blood. To optimize

<sup>46</sup>M. Sigovan et al., *Radiology*, **252**: 401–409, 2009.

<sup>47</sup>E. Kim et al., *Journal of Cerebral Blood Flow & Metabolism*, **31**: 1623–1636, 2011.

<sup>48</sup>A. P. Pathak et al., *PLoS ONE*, **6**: e22643, 2011.

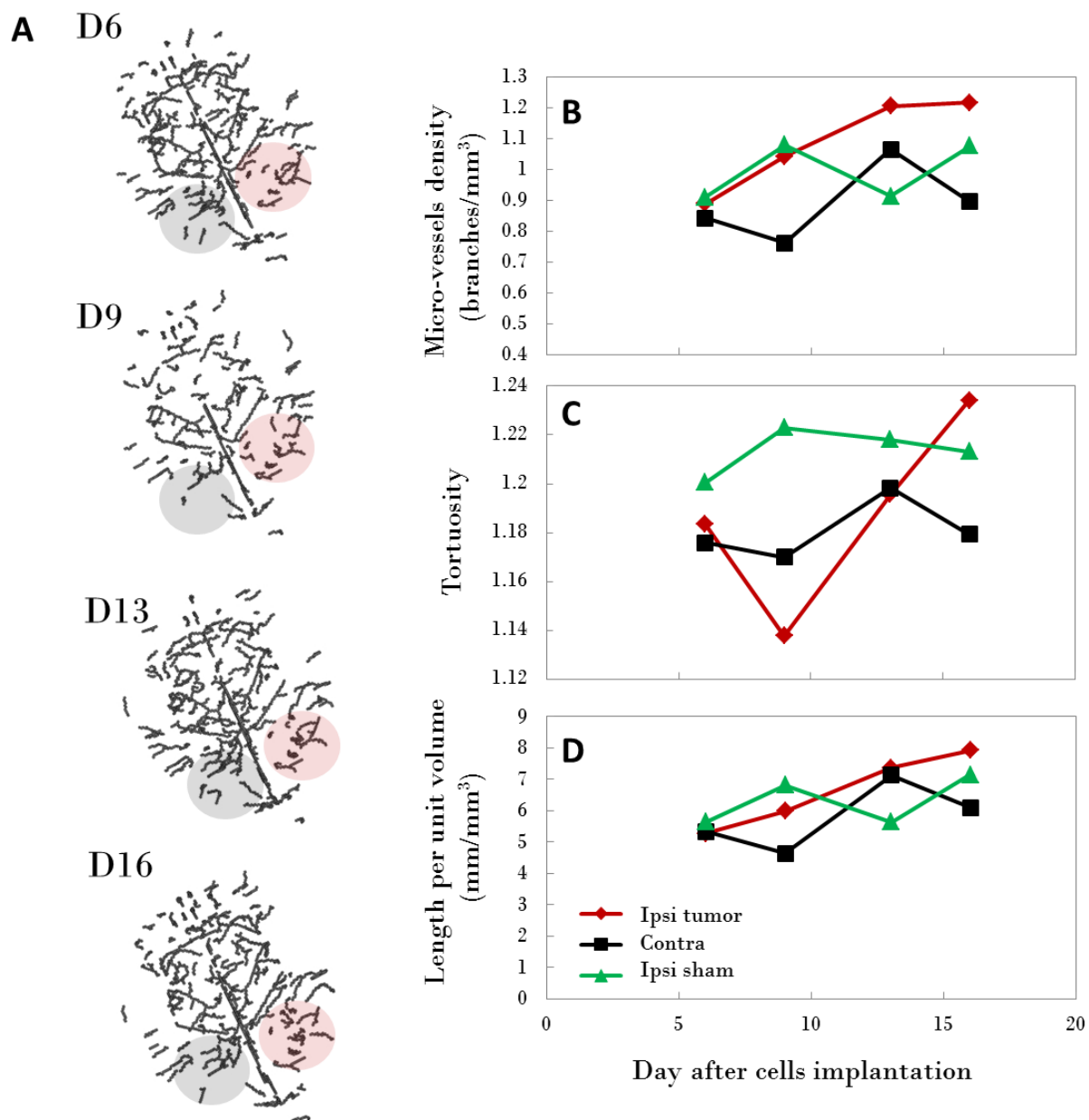


Fig. 3.13 – U87 tumor vessels analysis with *in vivo* contrast-enhanced MRI. A/ Skeletonized 3D angiogram after P904 injection obtained at different times after tumor cells implantation. Tumor area is indicated in light red and contralateral one in light gray. B,C,D/ Morphometric indexes computed from the analysis of the skeletonized 3D angiograms: micro-vessels density (A), tortuosity (B) and length per unit volume (C).

tumor vessels detection, this study would require the enhancement of the spatial resolution in  $T_2^*$ -weighted images, while keeping the acquisition time compatible with contrast agent blood half-life.

Analysis of skeletons was expected to be quite difficult, given the lack of sufficient spatial resolution coupled with the low number of animals in the study. The results of morphometric indices computation are presented in Figure 3.13 B,C,D: for each index, no significant diffe-

rence between the three regions of interest (tumor zone for U87 mice in red, ipsilateral tumor zone for sham mice in green, and contralateral zone for all mice in black) is observed at the different times after cells implantation (except at D9 probably due to a lower dose of injected P904). Only an overall trend can be noticed: the three morphometric indices seem to increase with time in the tumor zone, reaching after 15 days the highest values compared to the two other regions of interest. This observation is consistent with previous studies<sup>49,50</sup>, reporting that elevated micro-vessels density, tortuosity and length per unit volume are hallmarks of brain tumor angiogenesis which occurs during tumor growth. Though, it is important to keep in mind that the main change detected in tumor zone throughout time, with our method, is the appearance of new vessels. Micro-vessels density may be the index that gives the less biased result and it seems to grow for tumor zone while it stays quite steady in contralateral and in sham ipsilateral zone. Tortuosity and length per unit volume give an interesting overall trend for the tumor but proper comparison between tumor, sham ipsilateral and contralateral zones is not possible because of measure variability.

In conclusion, this unfruitful study shows the challenges to be faced when studying tumor vessels evolution with *in vivo* contrast-enhanced MRI. Firstly, it is necessary to significantly increase the spatial resolution in acquired  $T_2^*$ -weighted images, but also the number of tumor bearing and sham mice, in order to better characterize tumor vasculature during growth, and try to meet some results of *post-mortem* microscopy MRI. Secondly, it is possible that tumors contain vessels intermittently or poorly perfused by the injected contrast agent, because of abnormal blood hemodynamics or elevated interstitial pressure: these vessels are therefore very difficult to detect. Finally, it has been already shown that abnormal tumor vessel morphology can profoundly affect susceptibility-induced MRI contrast<sup>51</sup>: specific computational models, incorporating the actual tumor vascular structure, are required to elucidate this complex relationship<sup>52</sup>.

### 3.4.3 Tumor iron uptake measurements

Tumor vessels are very different from healthy ones, in terms of morphometry but also functionality. These abnormalities are usually gathered under the concept of Enhanced Permeability and Retention effect (EPR): tumors present an hyper-vasculature with an increased tortuosity induced by a non functional architecture, and coupled with a defective lymphatic drainage<sup>53</sup>. One consequence of this EPR effect is that IONPs of suitable hydrodynamic size can passively accumulate in the tumor interstitial space, due to the enhanced permeability of blood-brain barrier in neoangiogenic vessels.

**Protocol** NPAC, NPPO-PEG<sub>85</sub> and AMB1 magnetosomes have been injected to U87 tumor bearing mice. A new protocol has been designed to follow the contrast enhancement dynamically after injection, with a high imaging rate. A FLASH sequence lasting 5 minutes (see details in Appendix B.2) has been parametrized on the 11.7 T scanner to acquire baseline (pre injection) and dynamic follow-up images (post injection). Between 1 and 5 FLASH images

<sup>49</sup>P. Vajkoczy et al., *Journal of Neuro-Oncology*, **50**: 99–108, 2000.

<sup>50</sup>R. K. Jain et al., *Nature Reviews Neuroscience*, **8**: 610–622, 2007.

<sup>51</sup>A. P. Pathak et al., *Journal of Magnetic Resonance Imaging*, **18**: 397–403, 2003.

<sup>52</sup>A. P. Pathak et al., *NeuroImage*, **40**: 1130–1143, 2008.

<sup>53</sup>Y. Matsumura et al., *Cancer Research*, **46**: 6387–6392, 1986.

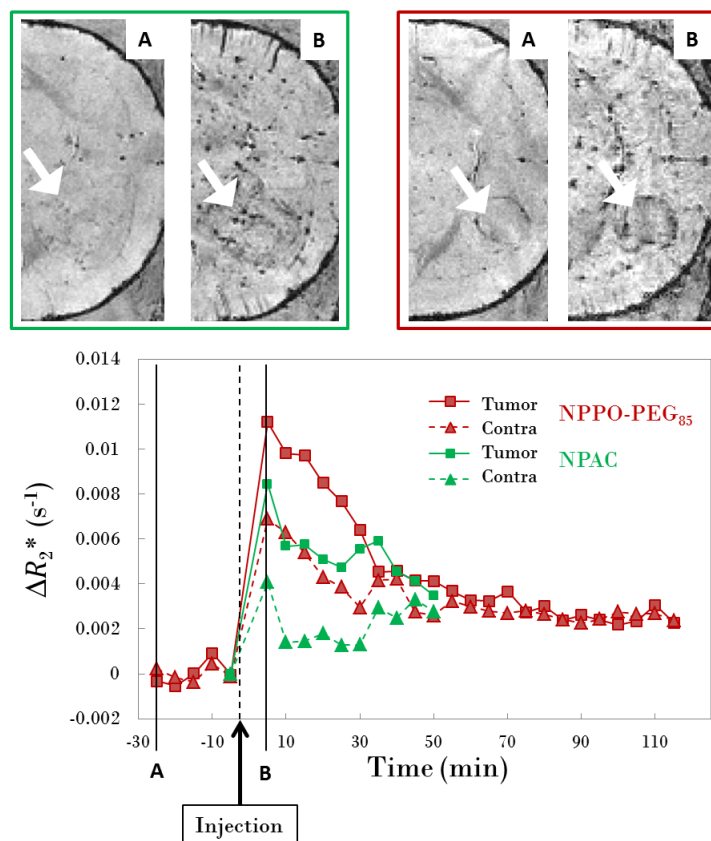


Fig. 3.14 – Iron uptake measurements in tumor bearing mice after injection of NPAC or NPPO-PEG<sub>85</sub>. First row shows FLASH images acquired at two different times (A before injection and B after injection), which are indicated in the graph below, showing  $\Delta R_2^*(t)$  dynamic evolution in two regions of interest (tumor and contralateral zones) for both tested IONPs. Tumor area is pointed out with a white arrow. FLASH images with the green outline are for NPAC injected mouse, while the red outline is for NPPO-PEG<sub>85</sub>. Injection time is indicated with a dashed line on  $\Delta R_2^*(t)$  evolution graph.

were acquired pre injection, and between 10 and 20 FLASH images post injection. In the meantime, the cradle was removed from the tunnel, contrast agent injected at the tail vein ( $200 \mu\text{mol}_{[\text{Fe}]} / \text{kg}_{\text{BW}}$ ), while keeping the animal positioned, before inserting the cradle back in the scanner. Four mice were included in this study, injected with NPAC ( $n=1$ ), NPPO-PEG<sub>85</sub> ( $n=1$ ) or AMB1 magnetosomes ( $n=2$ ).

**Data processing** The priority was given to high imaging rate, to the detriment of quantitative measurements. Indeed, FLASH images are not  $T_2^*$  parametric images, but only  $T_2^*$ -weighted ones. Nevertheless, the imaging protocol was designed to ensure that the shim parameters, set at the beginning of pre injection scans, were kept identical for post injection scans, meaning that  $T_2^*$ -weighted FLASH images were comparable within one experiment. Besides, baseline images acquired for each animal were used to normalize MRI signal, and therefore compare animals together. Finally,  $\Delta R_2^*(t)$  parameter was computed as follows into two manually segmented

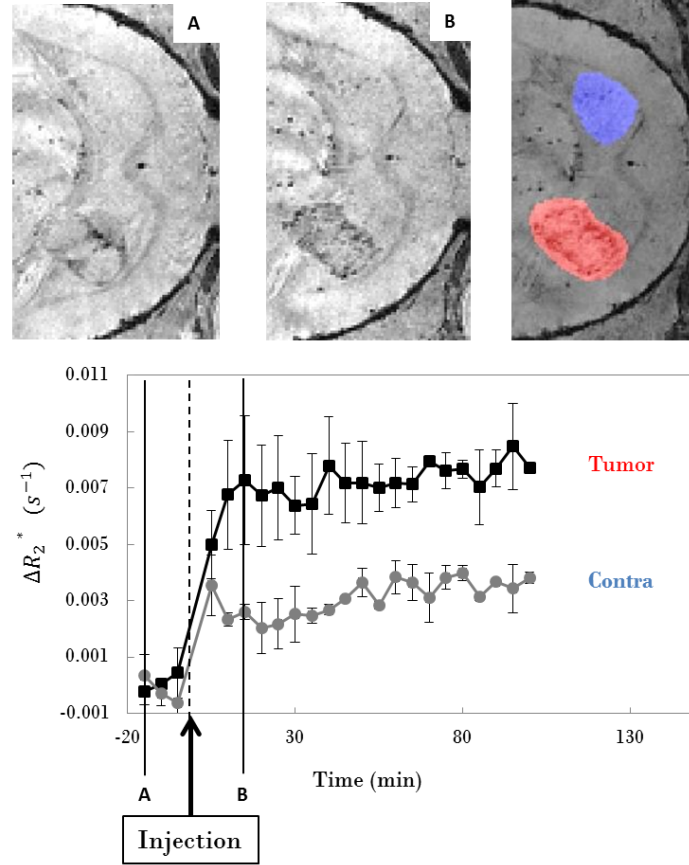


Fig. 3.15 – Iron uptake measurements in tumor bearing mice after injection of AMB1 magnetosomes. First row shows FLASH images acquired at two different times (A before injection and B after injection), which are indicated in the graph below, showing  $\Delta R_2^*(t)$  dynamic evolution in two regions of interest (tumor and contralateral zones). Tumor (red) and contralateral zones (blue) are pointed out on the third image. Injection time is indicated with a dashed line on  $\Delta R_2^*(t)$  evolution graph.

regions of interest, the tumor zone and the contralateral zone:

$$\Delta R_2^*(t) = \frac{1}{T_E} \cdot \log\left(\frac{\text{mean}(S(t_{PRE}))}{S(t)}\right) \quad (3.1)$$

This  $\Delta R_2^*(t)$  parameter is a measure of MRI contrast enhancement (signal drop) induced by IONPs injection<sup>54</sup>, thus it can be used as a semi-quantitative measure of iron uptake.

**Results** MRI results obtained with NPAC and NPPO-PEG<sub>85</sub> injections are presented in Figure 3.14. FLASH images show clear contrast enhancement effect of IONPs injection in both contralateral and tumor zones, where numerous hypo-intense voxels appear. This result is confirmed by the  $\Delta R_2^*$  mean values computed in each zone, which are clearly increased post injection. For both injected IONPs, tumor shows a greater iron uptake when compared to contralateral healthy region, probably due to the EPR effect. The comparison between tested IONPs reveals that NPPO-PEG<sub>85</sub> induces higher contrast enhancement than NPAC in both regions of interest, as already observed in previous experiment (see Figure 3.9). However, both

<sup>54</sup>G. Gambarota et al., British Journal of Cancer, **98**: 1784–1789, 2008.

IONPs seem to have similar blood half-lives (estimated around 30 *min*), which is surprising since one could expect that PEG chains lengthen blood circulation time. Finally, all these observations need to be balanced by the fact that only one animal has been tested per condition. Further experiments are then required to confirm these results.

MRI results obtained with AMB1 magnetosomes injection are presented in Figure 3.15. FLASH images acquired after magnetosomes injection reveal an important loss of signal in the tumor zone, and only few hypo-intense voxels in contralateral one.  $\Delta R_2^*$  dynamic evolution estimated in both zones confirms this observation. Injection of magnetosomes leads to a significative increase of  $\Delta R_2^*$  in both zones, but still a greater one in the tumor compared to contralateral healthy region, probably due to the EPR effect. Interestingly, this difference in iron uptake between tumor and contralateral zones seems to maintain during the first 100 *min* post injection.

Finally, chemical IONPs and magnetosomes exhibit different behaviors: magnetosomes seem to have a much longer blood half-life compared with the tested chemical IONPs, which leads to higher iron uptake in the tumor due to the EPR effect.

### 3.5 Summary and perspectives

- Magnetosomes show very interesting physico-chemical properties. Their iron-oxide cores exhibit high saturation magnetization which can induce high MRI contrasting properties. Furthermore, magnetosomes extraction and preparation in injectable suspension preserve the membrane integrity.
- Transverse relaxivity is one of the most used parameters to characterize and compare IONPs contrasting properties. This parameter has been measured for chemical IONPs produced by Guerbet company, and the obtained values demonstrated that Endorem<sup>®</sup> presents a higher transverse relaxivity than P904. In a second step, this parameter has also been measured for chemical IONPs with the same iron-oxide core but with different coatings, and with the add of a functionalization, all these IONPs being synthesized by the CSPBAT laboratory. The thicker coating obtained with PEG chains compared to caffeic acid seems to induce a lower transverse relaxivity at 7 *T* for the PEGylated nanoparticles. Adding functionalization, like antibodies, to PEG coated nanoparticles enhances their transverse relaxivity, which was explained by antibodies restraining IONPs rotation. Finally, magnetosomes with two different shapes were investigated. AMB1 magnetosomes (cubo-octahedral shape) present a higher transverse relaxivity at 7 *T* compared to conventional chemical IONPs, which seems to be due to the good crystallinity of magnetosomes iron core. MV1 magnetosomes (elongated shape) present very high transverse relaxivities at different magnetic field intensities, even higher than the ones of AMB1, which can be explained by the fact that elongated nanoparticles produce magnetic field inhomogeneities on a larger volume than equivalent spherical ones.
- *In vivo* contrasting properties of all previously tested IONPs were investigated. The results reveal that both Guerbet nanoparticles have similar *in vivo* contrasting properties, even if Endorem<sup>®</sup> has higher transverse relaxivity, probably because P904 exhibits higher circulation time in mouse brain vasculature. For PEG and caffeic acid coated nanoparticles, their *in vivo* contrasting properties were opposite considering what was expected

from their transverse relaxivity values, because PEG chains enhance nanoparticles biocompatibility. Finally, magnetosomes *in vivo* contrasting properties were assessed, and the results demonstrate that, when iron-oxide core synthesis and coating are similar, a good agreement is found with transverse relaxivity values.

- U87 mouse model of glioblastoma has been characterized in terms of tumor growth and shape. An attempt to measure tumor vasculature changes throughout tumor growth has been carried out, but mostly because of the lack of sufficient spatial resolution in the acquired images, no significant result was found. The used technique was not sensitive enough to reveal changes in small vessels, that make the difference between tumor and contralateral zones. Finally, the EPR effect has been evidenced for this tumor model, by injecting different chemical IONPs and magnetosomes. These experiments enable to demonstrate that AMB1 magnetosomes exhibit quite long blood half-life (longer than 100 *min*).

## References

- [1] S. Mériaux, M. Boucher, B. Marty, Y. Lalatonne, S. Prévéral, L. Motte, C. T. Lefèvre, F. Geffroy, F. Lethimonnier, M. Péan, D. Garcia, G. Adryanczyk-Perrier, D. Pignol, and N. Ginet. Magnetosomes, Biogenic Magnetic Nanomaterials for Brain Molecular Imaging with 17.2 T MRI Scanner. *Advanced Healthcare Materials*, **4**: 1076–1083, 2015. DOI: [10.1002/adhm.201400756](https://doi.org/10.1002/adhm.201400756) (see pp. 50, 54)
- [2] D. A. Bazylinski and S. Schübbe. Controlled Biomineralization by and Applications of Magnetotactic Bacteria. *Advances in Applied Microbiology*, **62**: 21–62, 2007. (see p. 50)
- [3] T. Hyeon, S. S. Lee, J. Park, Y. Chung, and H. B. Na. Synthesis of Highly Crystalline and Monodisperse Maghemite Nanocrystallites without a Size-Selection Process. *Journal of the American Chemical Society*, **123**: 12798–12801, 2001. DOI: [10.1021/ja016812s](https://doi.org/10.1021/ja016812s) (see pp. 51, 54)
- [4] W. W. Yu, J. C. Falkner, C. T. Yavuz, and V. L. Colvin. Synthesis of monodisperse iron oxide nanocrystals by thermal decomposition of iron carboxylate salts. *Chemical Communications (Cambridge, England)*, 2306–2307, 2004. DOI: [10.1039/b409601k](https://doi.org/10.1039/b409601k) (see pp. 51, 54)
- [5] D. Kim, N. Lee, M. Park, Byung H. Kim, K. An, and T. Hyeon. Synthesis of Uniform Ferrimagnetic Magnetite Nanocubes. *Journal of the American Chemical Society*, **131**: 454–455, 2009. DOI: [10.1021/ja8086906](https://doi.org/10.1021/ja8086906) (see pp. 51, 55)
- [6] Simon Foner. Versatile and sensitive vibrating sample magnetometer. *Review of scientific instruments*, **30**: 548–557, 1959. DOI: [10.1063/1.1716679](https://doi.org/10.1063/1.1716679) (see p. 51)
- [7] S. Chikazumi and S. H. Charap. *Physics of Magnetism*. Wiley, New York 1964. (see p. 52)
- [8] M. Bennet, L. Bertinetti, R. K. Neely, A. Schertel, A. Körnig, C. Flors, F. D. Müller, D. Schüler, S. Klumpp, and D. Faivre. Biologically controlled synthesis and assembly of magnetite nanoparticles. *Faraday Discuss.*, **181**: 71–83, 2015. DOI: [10.1039/C4FD00240G](https://doi.org/10.1039/C4FD00240G) (see p. 52)
- [9] C. Lang and D. Schüler. Biogenic nanoparticles: production, characterization, and application of bacterial magnetosomes. *Journal of Physics: Condensed Matter*, **18**: S2815–S2828, 2006. DOI: [10.1088/0953-8984/18/38/S19](https://doi.org/10.1088/0953-8984/18/38/S19) (see p. 52)
- [10] K. Grünberg, E.-C. Muller, A. Otto, R. Reszka, D. Linder, M. Kube, R. Reinhardt, and D. Schuler. Biochemical and Proteomic Analysis of the Magnetosome Membrane in *Magnetospirillum gryphiswaldense*. *Applied and Environmental Microbiology*, **70**: 1040–1050, 2004. DOI: [10.1128/AEM.70.2.1040-1050.2004](https://doi.org/10.1128/AEM.70.2.1040-1050.2004) (see p. 52)
- [11] J. Park, K. An, Y. Hwang, J.-G. Park, H.-J. Noh, J.-Y. Kim, J.-H. Park, N.-M. Hwang, and T. Hyeon. Ultra-large-scale syntheses of monodisperse nanocrystals. *Nature Materials*, **3**: 891–895, 2004. DOI: [10.1038/nmat1251](https://doi.org/10.1038/nmat1251) (see p. 55)
- [12] A. Shavel, B. Rodríguez-González, M. Spasova, M. Farle, and L. M. Liz-Marzán. Synthesis and Characterization of Iron/Iron Oxide Core/Shell Nanocubes. *Advanced Functional Materials*, **17**: 3870–3876, 2007. DOI: [10.1002/adfm.200700494](https://doi.org/10.1002/adfm.200700494) (see p. 55)
- [13] N. Ginet, R. Pardoux, G. Adryanczyk, D. Garcia, C. Brutesco, and D. Pignol. Single-Step Production of a Recyclable Nanobiocatalyst for Organophosphate Pesticides Biodegradation Using Functionalized Bacterial Magnetosomes. *PLoS ONE*, **6**: e21442, 2011. DOI: [10.1371/journal.pone.0021442](https://doi.org/10.1371/journal.pone.0021442) (see p. 55)

- [14] T. Orlando, S. Mannucci, E. Fantechi, G. Conti, S. Tambalo, A. Busato, C. Innocenti, L. Ghin, R. Bassi, P. Arosio, F. Orsini, C. Sangregorio, M. Corti, M. F. Casula, P. Marzola, A. Lascialfari, and A. Sbarbati. Characterization of magnetic nanoparticles from *Magnetospirillum Gryphiswaldense* as potential theranostics tools. *Contrast Media & Molecular Imaging*, **11**: 139–145, 2016. DOI: [10.1002/cmami.1673](https://doi.org/10.1002/cmami.1673) (see p. 55)
- [15] A. Boni, D. Ceratti, A. Antonelli, C. Sfara, M. Magnani, E. Manuali, S. Salamida, A. Gozzi, and A. Bifone. USPIO-loaded red blood cells as a biomimetic MR contrast agent: a relaxometric study. *Contrast Media & Molecular Imaging*, **9**: 229–236, 2014. DOI: [10.1002/cmami.1562](https://doi.org/10.1002/cmami.1562) (see pp. 56, 57)
- [16] D. J. Grootendorst, J. Jose, R. M. Fratila, M. Visscher, A. H. Velders, B. Ten Haken, T. G. Van Leeuwen, W. Steenberg, S. Manohar, and T. J. M. Ruers. Evaluation of superparamagnetic iron oxide nanoparticles (Endorem®) as a photoacoustic contrast agent for intra-operative nodal staging. *Contrast Media & Molecular Imaging*, **8**: 83–91, 2013. DOI: [10.1002/cmami.1498](https://doi.org/10.1002/cmami.1498) (see pp. 56, 57)
- [17] Y. Lalatonne, J. Richardi, and M. P. Pileni. Van der Waals versus dipolar forces controlling mesoscopic organizations of magnetic nanocrystals. *Nature Materials*, **3**: 121–125, 2004. DOI: [10.1038/nmat1054](https://doi.org/10.1038/nmat1054) (see p. 56)
- [18] G. Ozturk, Z. Ginis, S. Akyol, G. Erden, A. Gurel, and O. Akyol. The anticancer mechanism of caffeic acid phenethyl ester (CAPE): review of melanomas, lung and prostate cancers. *European Review for Medical and Pharmacological Sciences*, **16**: 2064–2068, 2012. (see p. 57)
- [19] Y. Sato, S. Itagaki, T. Kurokawa, J. Ogura, M. Kobayashi, T. Hirano, M. Sugawara, and K. Iseki. *In vitro* and *in vivo* antioxidant properties of chlorogenic acid and caffeic acid. *International Journal of Pharmaceutics*, **403**: 136–138, 2011. DOI: [10.1016/j.ijpharm.2010.09.035](https://doi.org/10.1016/j.ijpharm.2010.09.035) (see p. 57)
- [20] A. A. P. Almeida, A. Farah, D. A. M. Silva, E. A. Nunan, and M. B. A. Gloria. Antibacterial activity of coffee extracts and selected coffee chemical compounds against enterobacteria. *Journal of Agricultural and Food Chemistry*, **54**: 8738–8743, 2006. DOI: [10.1021/jf0617317](https://doi.org/10.1021/jf0617317) (see p. 57)
- [21] H. Gulley-Stahl, P. A. Hogan, W. L. Schmidt, S. J. Wall, A. Buhrlage, and H. A. Bullen. Surface Complexation of Catechol to Metal Oxides: An ATR-FTIR, Adsorption, and Dissolution Study. *Environmental Science & Technology*, **44**: 4116–4121, 2010. DOI: [10.1021/es902040u](https://doi.org/10.1021/es902040u) (see p. 57)
- [22] S. Richard, M. Boucher, A. Herbet, Y. Lalatonne, S. Mériaux, D. Boquet, and L. Motte. Endothelin B receptors targeted by iron oxide nanoparticles functionalized with a specific antibody: toward immunoimaging of brain tumors. *Journal of Materials Chemistry B*, **3**: 2939–2942, 2015. DOI: [10.1039/C5TB00103J](https://doi.org/10.1039/C5TB00103J) (see p. 57)
- [23] S. Richard, A. Saric, M. Boucher, Françoise Geffroy, S. Mériaux, Y. Lalatonne, P. X. Petit, and L. Motte. Anti-oxidative theranostic iron oxide nanoparticles towards brain tumors imaging and ROS production. *Submitted to ACS Chemical Biology*, 2016. (see p. 57)
- [24] S. Richard. Elaboration de nanoplateformes bimodales pour l'imagerie moléculaire des cancers. *PhD Thesis, Paris 13 University*, 2015. (see pp. 57, 58)

- [25] J. V. Jokerst, T. Lobovkina, R. N. Zare, and S. S. Gambhir. Nanoparticle PEGylation for imaging and therapy. *Nanomedicine (London, England)*, **6**: 715–728, 2011. DOI: [10.2217/nnm.11.19](https://doi.org/10.2217/nnm.11.19) (see p. 57)
- [26] F. M. Veronese and G. Pasut. PEGylation, successful approach to drug delivery. *Drug Discovery Today*, **10**: 1451–1458, 2005. DOI: [10.1016/S1359-6446\(05\)03575-0](https://doi.org/10.1016/S1359-6446(05)03575-0) (see p. 57)
- [27] S. Richard, M. Boucher, A. Saric, A. Herbet, Y. Lalatonne, P. X. Petit, S. Mériaux, D. Boquet, and L. Motte. Optimization of pegylated iron oxide nanoplatfoms for Antibody coupling and bio-targeting. *Submitted to ACS Applied Materials & Interfaces*, 2016. (see p. 57)
- [28] M. Botta and L. Tei. Relaxivity Enhancement in Macromolecular and Nanosized GdIII-Based MRI Contrast Agents. *European Journal of Inorganic Chemistry*, **2012**: 1945–1960, 2012. DOI: [10.1002/ejic.201101305](https://doi.org/10.1002/ejic.201101305) (see p. 58)
- [29] Y.-W. Jun, Y.-M. Huh, J.-S. Choi, J.-H. Lee, H.-T. Song, S. Kim, S. Kim, S. Yoon, K.-. Kim, and J.-S. Shin. Nanoscale size effect of magnetic nanocrystals and their utilization for cancer diagnosis via magnetic resonance imaging. *Journal of the American Chemical Society*, **127**: 5732–5733, 2005. (see p. 58)
- [30] R. J. P. Corriu and . Leclercq. Recent Developments of Molecular Chemistry for Sol–Gel Processes. *Angewandte Chemie International Edition in English*, **35**: 1420–1436, 1996. DOI: [10.1002/anie.199614201](https://doi.org/10.1002/anie.199614201) (see p. 58)
- [31] E. D. Smolensky, H.-Y. E. Park, Y. Zhou, G. A. Rolla, M. Marjańska, M. Botta, and V. C. Pierre. Scaling Laws at the Nano Size: The Effect of Particle Size and Shape on the Magnetism and Relaxivity of Iron Oxide Nanoparticle Contrast Agents. *Journal of materials chemistry. B*, **1**: 2818–2828, 2013. DOI: [10.1039/C3TB00369H](https://doi.org/10.1039/C3TB00369H) (see pp. 59, 61)
- [32] B. H. Kim, N. Lee, H. Kim, K. An, Y. I. Park, Y. Choi, K. Shin, Y. Lee, S. G. Kwon, H. B. Na, J.-G. Park, T.-Y. Ahn, Y.-W. Kim, W. K. Moon, S. H. Choi, and T. Hyeon. Large-Scale Synthesis of Uniform and Extremely Small-Sized Iron Oxide Nanoparticles for High-Resolution  $T_1$  Magnetic Resonance Imaging Contrast Agents. *Journal of the American Chemical Society*, **133**: 12624–12631, 2011. DOI: [10.1021/ja203340u](https://doi.org/10.1021/ja203340u) (see p. 59)
- [33] C. Corot, P. Robert, J. Idee, and M. Port. Recent advances in iron oxide nanocrystal technology for medical imaging. *Advanced Drug Delivery Reviews*, **58**: 1471–1504, 2006. DOI: [10.1016/j.addr.2006.09.013](https://doi.org/10.1016/j.addr.2006.09.013) (see pp. 61, 65)
- [34] N. Lee, H. Kim, S. H. Choi, M. Park, D. Kim, H.-C. Kim, Y. Choi, S. Lin, B. H. Kim, and H. S. Jung. Magnetosome-like ferrimagnetic iron oxide nanocubes for highly sensitive MRI of single cells and transplanted pancreatic islets. *Proceedings of the National Academy of Sciences*, **108**: 2662–2667, 2011. (see p. 61)
- [35] C. Martinez-Boubeta, K. Simeonidis, A. Makridis, M. Angelakeris, O. Iglesias, P. Guardia, A. Cabot, L. Yedra, F. Estradé S.AND PEIRÓ, Z. Saghi, P. A. Midgley, I. Conde-Leborán, D. Serantes, and D. Baldomir. Learning from Nature to Improve the Heat Generation of Iron-Oxide Nanoparticles for Magnetic Hyperthermia Applications. *Scientific Reports*, **3**: 1652, 2013. DOI: [10.1038/srep01652](https://doi.org/10.1038/srep01652) (see p. 61)

- [36] G. Zhen, B. W. Muir, B. A. Moffat, P. Harbour, K. S. Murray, B. Moubaraki, K. Suzuki, I. Madsen, N. Agron-Olshina, L. Waddington, P. Mulvaney, and P. G. Hartley. Comparative Study of the Magnetic Behavior of Spherical and Cubic Superparamagnetic Iron Oxide Nanoparticles. *The Journal of Physical Chemistry C*, **115**: 327–334, 2011. DOI: [10.1021/jp104953z](https://doi.org/10.1021/jp104953z) (see p. 61)
- [37] R. S. M. Rikken, R. J. M. Nolte, J. C. Maan, J. C. M. VAN Hest, D. A. Wilson, and P. C. M. Christianen. Manipulation of micro- and nanostructure motion with magnetic fields. *Soft Matter*, **10**: 1295–1308, 2014. DOI: [10.1039/C3SM52294F](https://doi.org/10.1039/C3SM52294F) (see p. 61)
- [38] B. Luigjes, S. M. C. Woudenberg, R. DE Groot, J. D. Meeldijk, H. M. Torres Galvis, K. P. DE Jong, A. P. Philipse, and B. H. Ern . Diverging Geometric and Magnetic Size Distributions of Iron Oxide Nanocrystals. *The Journal of Physical Chemistry C*, **115**: 14598–14605, 2011. DOI: [10.1021/jp203373f](https://doi.org/10.1021/jp203373f) (see p. 61)
- [39] S. Nath, C. Kaittanis, V. Ramachandran, N. Dalal, and J. M. Perez. Synthesis, magnetic characterization and sensing applications of novel dextran-coated iron oxide nanorods. *Chemistry of Materials*, **21**: 1761–1767, 2009. DOI: [10.1021/cm8031863](https://doi.org/10.1021/cm8031863) (see p. 62)
- [40] H. Kloust, R. Zierold, J.-P. Merkl, C. Schmidtke, A. Feld, E. P selt, A. Kornowski, K. Nielsch, and H. Weller. Synthesis of Iron Oxide Nanorods Using a Template Mediated Approach. *Chemistry of Materials*, **27**: 4914–4917, 2015. DOI: [10.1021/acs.chemmater.5b00513](https://doi.org/10.1021/acs.chemmater.5b00513) (see p. 62)
- [41] Je. Mohapatra, A. Mitra, H. Tyagi, D. Bahadur, and M. Aslam. Iron oxide nanorods as high-performance magnetic resonance imaging contrast agents. *Nanoscale*, **7**: 9174–9184, 2015. DOI: [10.1039/C5NR00055F](https://doi.org/10.1039/C5NR00055F) (see pp. 62, 63)
- [42] Z. Zhao, Z. Zhou, J. Bao, Z. Wang, J. Hu, X. Chi, K. Ni, R. Wang, X. Chen, Z. Chen, and J. Gao. Octapod iron oxide nanoparticles as high-performance  $T_2$  contrast agents for magnetic resonance imaging. *Nature Communications*, **4**: 2266, 2013. DOI: [10.1038/ncomms3266](https://doi.org/10.1038/ncomms3266) (see p. 62)
- [43] B. Marty, B. Larrat, M. Van Landeghem, C. Robic, P. Robert, M. Port, D. Le Bihan, M. Pernot, M. Tanter, F. Lethimonnier, and S. M riaux. Dynamic study of blood–brain barrier closure after its disruption using ultrasound: a quantitative analysis. *Journal of Cerebral Blood Flow & Metabolism*, **32**: 1948–1958, 2012. DOI: [10.1038/jcbfm.2012.100](https://doi.org/10.1038/jcbfm.2012.100) (see p. 63)
- [44] A. F. Frangi, W. J. Niessen, K. L. Vincken, and M. A. Viergever. Multiscale vessel enhancement filtering. *MICCAI (Medical Image Computing and Computer-Assisted Intervention)*, **1496**: 130–137, 1998. DOI: [10.1007/BFb0056195](https://doi.org/10.1007/BFb0056195) (see p. 64)
- [45] R. Manniesing, M. Viergever, and W. Niessen. Vessel enhancing diffusion: A scale space representation of vessel structures. *Medical Image Analysis*, **10**: 815–825, 2006. DOI: [10.1016/j.media.2006.06.003](https://doi.org/10.1016/j.media.2006.06.003) (see p. 64)
- [46] M. Sigovan, L. Boussel, A. Sulaiman, D. Sappey-Marini r, H. Alsaïd, C. Desbleds-Mansard, D. Ibarrola, D. Gamond s, C. Corot, E. Lancelot, J.-S. Raynaud, V. Vives, C. Lacl d re, X. Violas, P. C. Douek, and E. Canet-Soulas. Rapid-Clearance Iron Nanoparticles for Inflammation Imaging of Atherosclerotic Plaque: Initial Experience in Animal Model. *Radiology*, **252**: 401–409, 2009. DOI: [10.1148/radiol.2522081484](https://doi.org/10.1148/radiol.2522081484) (see p. 70)
- [47] E. Kim, J. Zhang, K. Hong, N. E. Benoit, and A. P. Pathak. Vascular phenotyping of brain tumors using magnetic resonance microscopy (muMRI). *Journal of Cerebral Blood Flow & Metabolism*, **31**: 1623–1636, 2011. DOI: [10.1038/jcbfm.2011.17](https://doi.org/10.1038/jcbfm.2011.17) (see p. 70)

- [48] A. P. Pathak, E. Kim, J. Zhang, and M. V. Jones. Three-Dimensional Imaging of the Mouse Neurovasculature with Magnetic Resonance Microscopy. *PLoS ONE*, **6**: e22643, 2011. DOI: [10.1371/journal.pone.0022643](https://doi.org/10.1371/journal.pone.0022643) (see p. 70)
- [49] P. Vajkoczy and M. D. Menger. Vascular microenvironment in gliomas. *Journal of Neuro-Oncology*, **50**: 99–108, 2000. (see p. 72)
- [50] R. K. Jain, E. Di Tomaso, D. G. Duda, J. S. Loeffler, A. G. Sorensen, and T. T. Batchelor. Angiogenesis in brain tumours. *Nature Reviews Neuroscience*, **8**: 610–622, 2007. DOI: [10.1038/nrn2175](https://doi.org/10.1038/nrn2175) (see p. 72)
- [51] A. P. Pathak, S. D. Rand, and K. M. Schmainda. The effect of brain tumor angiogenesis on the in vivo relationship between the gradient-echo relaxation rate change ( $\Delta R_2^*$ ) and contrast agent (MION) dose. *Journal of Magnetic Resonance Imaging*, **18**: 397–403, 2003. DOI: [10.1002/jmri.10371](https://doi.org/10.1002/jmri.10371) (see p. 72)
- [52] A. P. Pathak, B. D. Ward, and K. M. Schmainda. A Novel Technique for Modeling Susceptibility-Based Contrast Mechanisms for Arbitrary Microvascular Geometries: The Finite Perturber Method. *NeuroImage*, **40**: 1130–1143, 2008. DOI: [10.1016/j.neuroimage.2008.01.022](https://doi.org/10.1016/j.neuroimage.2008.01.022) (see p. 72)
- [53] Y. Matsumura and H. Maeda. A New Concept for Macromolecular Therapeutics in Cancer Chemotherapy: Mechanism of Tumoritropic Accumulation of Proteins and the Antitumor Agent Smancs. *Cancer Research*, **46**: 6387–6392, 1986. (see p. 72)
- [54] G. Gambarota, W. Leenders, C. Maass, P. Wesseling, B. VAN DER Kogel, O. VAN Tellingen, and A. Heerschap. Characterisation of tumour vasculature in mouse brain by USPIO contrast-enhanced MRI. *British Journal of Cancer*, **98**: 1784–1789, 2008. DOI: [10.1038/sj.bjc.6604389](https://doi.org/10.1038/sj.bjc.6604389) (see p. 74)



# Magnetosomes for molecular imaging of a mouse glioblastoma model

## Contents

---

<b>4.1 Genetic functionalization of AMB1 magnetosomes</b>	<b>84</b>
4.1.1 Genetic modification of AMB1 strain	85
4.1.2 Assessment of successful genetic modification	85
<b>4.2 <i>In vitro</i> characterization of functionalized magnetosomes</b>	<b>86</b>
4.2.1 MR contrasting properties of functionalized magnetosomes	86
4.2.2 Affinity study on U87 cells culture	88
4.2.3 Study of RGD functionalized magnetosomes internalization into U87 cells	89
4.2.4 Affinity study on spheroid culture of U87 cells	91
<b>4.3 <i>In vivo</i> molecular imaging of a mouse glioblastoma model with RGD functionalized magnetosomes</b>	<b>94</b>
4.3.1 Dynamic continuous follow-up: assessment of magnetosomes circulation in tumor vessels	95
4.3.2 24 h follow-up: <i>in vivo</i> assessment of RGD magnetosomes affinity for U87 tumor	96
4.3.3 Cross-validation of MRI results with <i>post mortem</i> histology	99
4.3.4 <i>Post-mortem</i> MRI acquisitions: toward histology-like MRI?	100
<b>4.4 In which cells can magnetosomes be found after intravenous injection?</b>	<b>103</b>
4.4.1 Interaction between liver macrophages and magnetosomes	104
4.4.2 Interaction between microglia and magnetosomes	104
<b>4.5 Summary and perspectives</b>	<b>107</b>
<b>References</b>	<b>108</b>

---

The main goal of MEFISTO project was to demonstrate the feasibility of producing functionalized magnetosomes for MR-based molecular imaging, and to realize a first *in vivo* proof-of-concept of their efficiency. This proof-of-concept is presented in this chapter, starting from the successful production of functionalized magnetosomes, followed by the *in vitro* study of such nanoparticles properties, to finally highlight *in vivo* their targeting properties.

## 4.1 Genetic functionalization of AMB1 magnetosomes

Functionalization of magnetosomes using genetic engineering has been achieved thanks to previous studies performed by LBC laboratory<sup>1</sup>, as introduced in Section 2.3. AMB1 strain has been chosen since it is not possible up to now to genetically modify MV1. Such functionalization consists in building a chimeric bacteria, from a wild type one, using a translational fusion between the gene coding for an abundant protein specific to the magnetosome membrane, like MamC<sup>2</sup>, and a gene encoding the targeting ligand. Here, RGD peptide (Arginine-Glycine-Aspartic Acid) has been chosen for the simplicity of its sequence, combined with its good affinity properties for tumor cells through  $\alpha_v\beta_3$  integrins targeting<sup>3,4</sup>. The decoration is thus naturally sorted to the membrane leading to RGD functionalized magnetosomes. The Venus fluorescent protein was also incorporated to verify efficiency of functionalization, and also to study *in vitro* functionalized magnetosomes interaction with U87 cells. Figure 4.1 illustrates the concept of targeting  $\alpha_v\beta_3$  integrins *in vivo* with genetically functionalized magnetosomes.

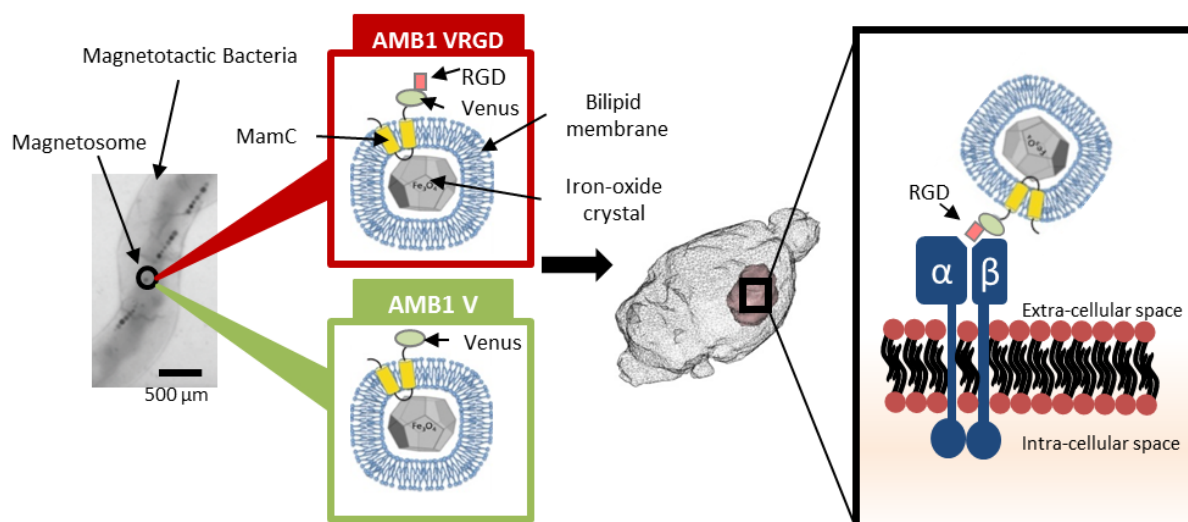


Fig. 4.1 – RGD functionalization of AMB1 magnetosomes. Two different genetic modifications have been performed to decorate magnetosome membrane with proteins of interest, one with Venus-RGD to create the functionalized probe, one with Venus only as control. RGD peptide has been chosen for its ability to bind to  $\alpha_v\beta_3$  integrins, over-expressed at membrane of tumor cells and neoangiogenic vessel endothelial cells.

<sup>1</sup>N. Ginet et al., PLoS ONE, **6**: e21442, 2011.

<sup>2</sup>K. Grünberg et al., Applied and Environmental Microbiology, **70**: 1040–1050, 2004.

<sup>3</sup>F. Danhier et al., Molecular Pharmaceutics, **9**: 2961–2973, 2012.

<sup>4</sup>F. Zhang et al., Biomaterials, **33**: 5414–5422, 2012.



comes from the dimerization of the protein which happens because of RGD peptide.

## 4.2 *In vitro* characterization of functionalized magnetosomes

RGD functionalized and control magnetosomes were expected to have physico-chemical properties very similar to those of wild type ones, since V or VRGD proteins are very small compared to the size of whole magnetosome. Transverse relaxivities have been measured *in vitro* to investigate magnetosomes contrasting properties. Furthermore, it was important to verify the functionality of RGD peptide inserted into the membrane through genetic engineering, by studying *in vitro* the specific affinity of functionalized magnetosomes for  $\alpha_v\beta_3$  integrins.

### 4.2.1 MR contrasting properties of functionalized magnetosomes

Contrasting properties of magnetosomes were evaluated following the protocol detailed in Appendix A.1. First measurements were performed without sonicating aliquots prior to prepare MRI phantoms, in order to avoid functionalization deterioration. Only a rapid homogenization of magnetosomes suspension was done by mechanical agitation with a pipette. The values of measured transverse relaxivities were found very fluctuating and lower than expected (see Figure 4.4). Considering the fact that Venus-RGD proteins at magnetosome membrane do not add significant steric effect, transverse relaxivities of functionalized magnetosomes should not differ from the one of wild type AMB1 magnetosomes.

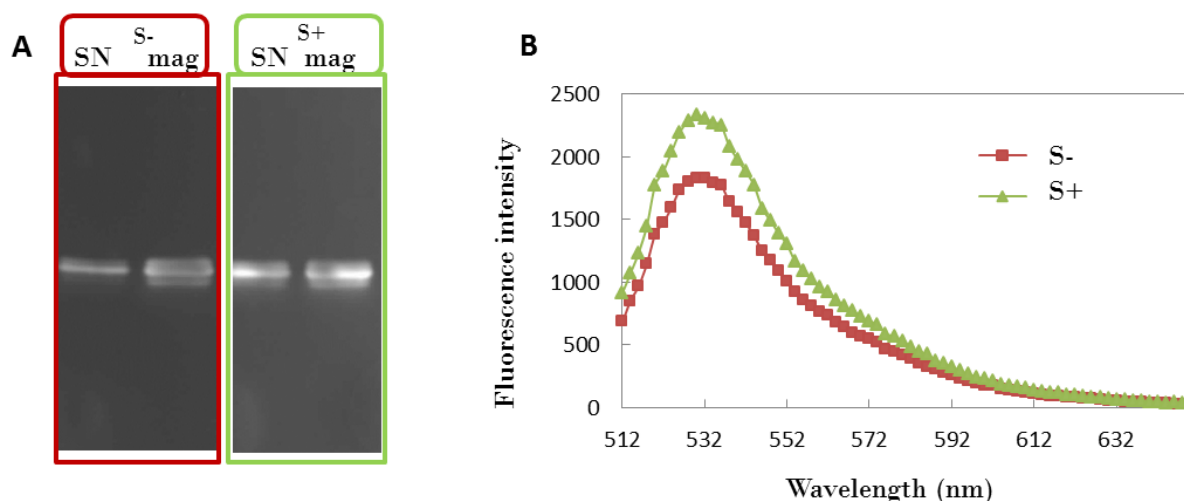


Fig. 4.3 – Impact of sonication on fluorescence release from functionalized magnetosomes. A/ Western Blot showing the presence of Venus protein in the supernatant (SN) or magnetosomes pellet (mag) whether the samples were beforehand sonicated (S+) or non-sonicated (S-). B/ Fluorescence spectrum of supernatant whether the samples were beforehand sonicated (S+) or non-sonicated (S-).

**Sonication effect on magnetosomes functionalization** The influence of sonication on magnetosome membrane functionalization has been studied to investigate whether a sonication step could be considered to ensure suspension homogenization, and if detrimental, to what extent.

AMB1 V magnetosomes sample was divided in two equal samples of the same volume and concentration, one being sonicated 10 *min* at 30°C and the other being kept 10 *min* at 30°C. Magnetosomes were separated from the supernatant with centrifugation followed by magnetic sorting. Supernatants and pellets were analyzed with Western Blot, and supernatants were also analyzed with a spectrofluorometer. Western Blot results presented in Figure 4.3 A exhibit that fluorescence is found in both supernatants and pellets whether sonicated or not. The fluorescence spectrum (see Figure 4.3 B) demonstrates that sonication does not lead to an important difference in fluorescence release compared to non-sonicated condition. This experiment validates the use of sonication to homogenize functionalized magnetosomes suspensions.

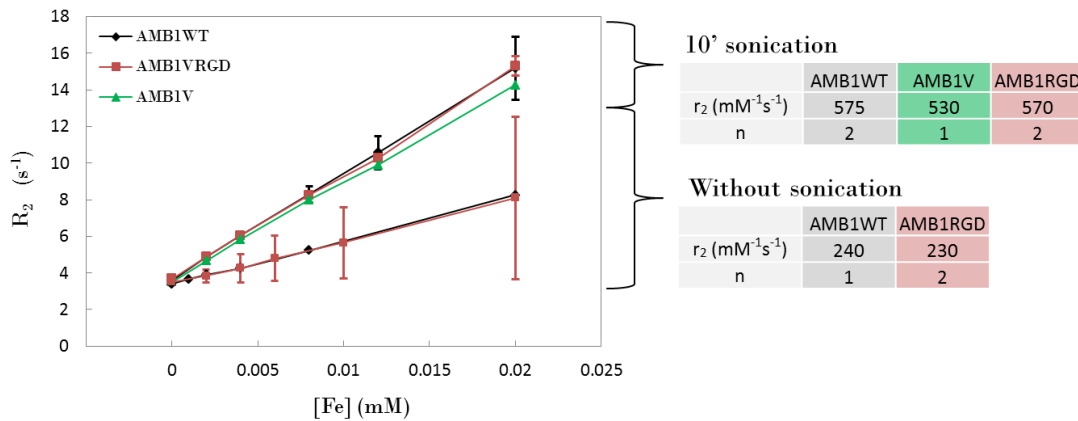


Fig. 4.4 – Transverse relaxivities of functionalized magnetosomes with or without sonication. The graph presents the mean  $R_2$  relaxation rates versus iron concentration, for several phantoms filled with AMB1 WT, AMB1 V and AMB1 VRGD magnetosomes. Experiment was repeated when possible on n different phantoms leading to the plotted error bars.

**Transverse relaxivities of functionalized magnetosomes with or without sonication** When no sonication step was done prior to sample highly concentrated magnetosomes suspensions (around  $3 g/L_{[Fe]} = 54 mM_{[Fe]}$ ), relaxivity measurements were absolutely not reliable (see Figure 4.4). Sedimentation occurs very fast when homogenizing the suspension with pipette flushes and therefore, magnetosomes content in the same sampled volume could considerably vary. Furthermore, it is impossible to measure a reliable transverse relaxivity value if the iron content of each tube in the phantom is not very precisely known. In addition, magnetosomes were probably in a highly aggregated state without sonication, which also explains why lower transverse relaxivity values were measured. This is in agreement with both simulations and experiments which have demonstrated that IONPs aggregates have different contrasting properties than isolated ones, and that above a certain size of aggregates, transverse relaxivity drops (see section 2.2).

Since sonication was not deteriorating magnetosomes functionalization (see Figure 4.3), phantoms were realized after sonicating magnetosomes suspensions. The transverse relaxivity of AMB1 V magnetosomes was found, after pooling duplicate measurements, equal to  $530 mM^{-1}s^{-1}$  and the one of AMB1 VRGD to  $570 mM^{-1}s^{-1}$  at 11.7 T (see Figure 4.4), which is in agreement with the previously measured values (see Table 3.4).

### 4.2.2 Affinity study on U87 cells culture

Binding properties of RGD functionalized magnetosomes were evaluated on cultured U87 cells. These human glioblastoma cells over-expressed  $\alpha_v\beta_3$  integrins when making sufficient contacts between them, which occurs around three days post seeding in our culture conditions. This observation is actually consistent with the active role played by these integrins in cell motility and neo-angiogenesis<sup>5,6</sup>. Affinity between RGD functionalized magnetosomes and their targets has been qualitatively validated after careful observation of fluorescence microscopy images, and also semi-quantitatively after post-processing of wide-field fluorescence images acquired in mosaic.

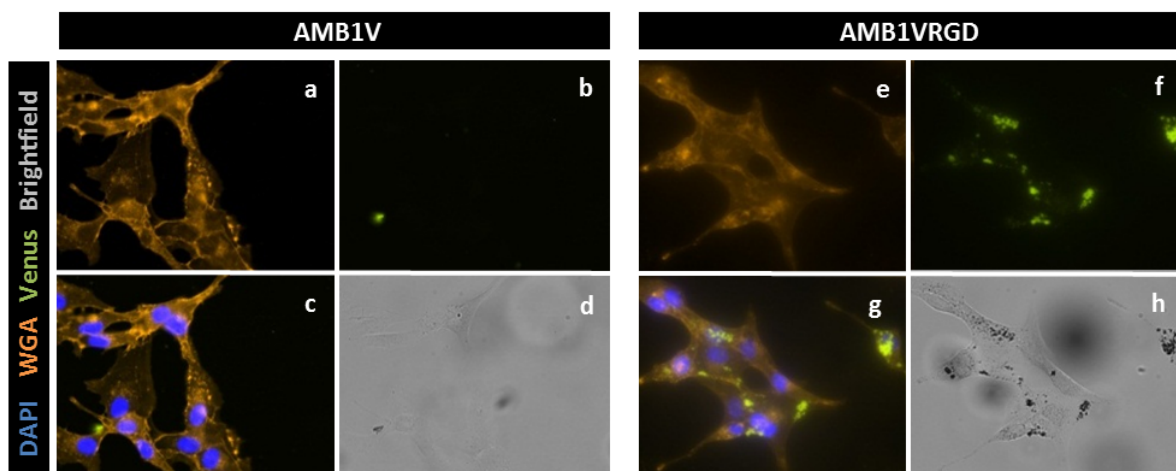


Fig. 4.5 – *In vitro* qualitative validation of RGD functionalized magnetosomes affinity for U87 cells. a,e/ Orange channel shows cell membrane (WGA staining). b,f/ Green channel shows Venus fluorescence. c,g/ Merged orange, blue (cell nuclei, DAPI staining) and green channels. d,h/ Brightfield images show magnetosomes iron-oxide core aggregates.

**Protocol** Qualitative analysis of the efficient binding between RGD functionalized magnetosomes and U87 cells has been performed *in vitro* using microscopy imaging of Venus fluorescence. U87 cells, 3 days after being seeded in glass bottom plates, were incubated at  $37^{\circ}\text{C}$  during 3 h 30, with either AMB1 V or AMB1 VRGD suspended in PBS at  $2\text{ mg}[Fe]/L$ . Plates were afterward washed twice with PBS, and prepared for microscopy. Representative field-of-views of images acquired for both AMB1 V and AMB1 VRGD treatments are reported in Figure 4.5. Cell membranes were stained using Wheat Germ Agglutinin (WGA) revealed in orange, in order to delineate cells from background and to evaluate if Venus spots were co-localized with U87 cells. Cell nuclei were revealed in blue with DAPI staining (4',6-diamidino-2-phenylindole). Finally, aggregates of magnetosome iron-oxide cores appeared as dark spots in brightfield images. Details of U87 cell culture are found in Appendix A.2 and on immunochemical staining in Appendix A.4.

<sup>5</sup>P. C. Brooks et al., *Science*, **264**: 569–571, 1994.

<sup>6</sup>P. T. Caswell et al., *Traffic*, **7**: 14–21, 2006.

**Results of qualitative analysis** The first interesting observation is the excellent correlation between Venus spots on fluorescence images and dark spots on brightfield images, which reveals that Venus fluorophore remained attached to the iron-oxide core, *i.e.* that magnetosomes were still unaltered in such experimental conditions. The second interesting observation is that higher number of Venus spots is observed with AMB1 VRGD treatment compared with AMB1 V one, highlighting effective interaction between RGD functionalized magnetosomes and U87 cells due to RGD peptide.

**Results of quantitative analysis** The previous qualitative results have been reinforced by acquiring wide-field images on microscope slides, using the mosaic acquisition mode. Given the large amount of cells (hundreds), such images are difficult to analyze with human eyes only, but quantitative data can be extracted with dedicated image processing. For this purpose, co-localization between channels has been analyzed with an algorithm detailed in Appendix C.3.

Results of such image processing are given in Figure 4.6, that displays the number of Venus+ pixels normalized per cell for AMB1 V and AMB1 VRGD treatments, distinguishing pixels that are also WGA+ or WGA-. [Venus+/WGA-] pixels can be interpreted as residues of magnetosomes on plates, that were not effectively removed during the washing steps ([Venus+/WGA-] pixels correspond to approximately 8 % of Venus+ pixels in each case). This quantitative analysis clearly confirms the qualitative observation, exhibiting a larger amount of Venus+ pixels per cell after AMB1 VRGD treatment compared with AMB1 V one. This important difference validates *in vitro* that AMB1 VRGD magnetosomes specifically bind to U87 cells due to RGD peptide.

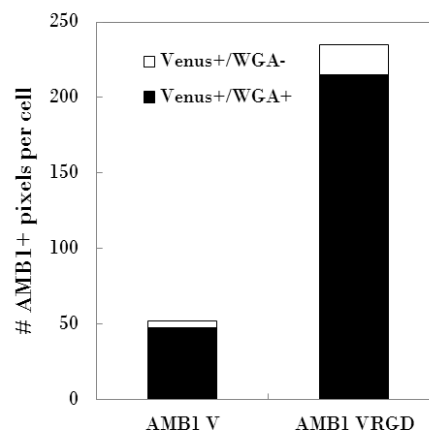


Fig. 4.6 – *In vitro* quantification of magnetosomes affinity for U87 cells. Bar plot shows the count of Venus+ pixels, differentiating those WGA+ from those WGA-.

### 4.2.3 Study of RGD functionalized magnetosomes internalization into U87 cells

**Protocol** Effective binding between AMB1 VRGD magnetosomes and U87 cells has been demonstrated in comparison with AMB1 V ones. Furthermore,  $\alpha_v\beta_3$  integrins are known to be

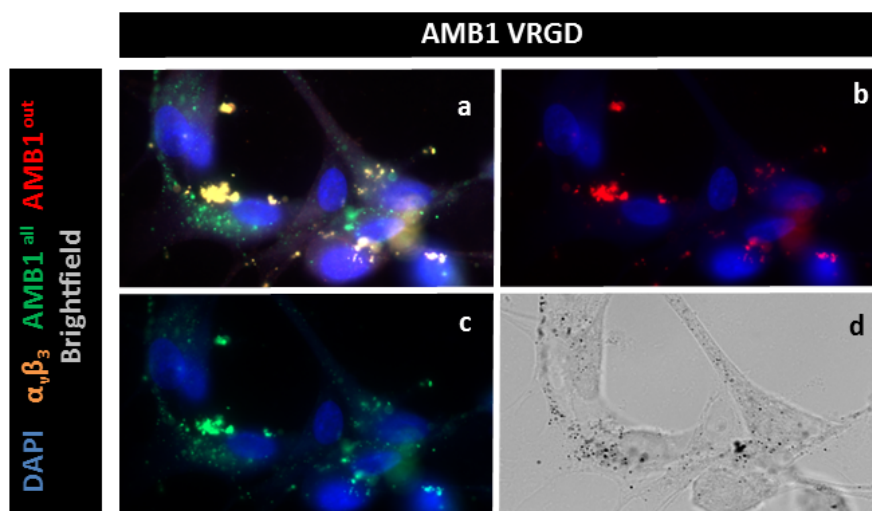


Fig. 4.7 – Qualitative validation of RGD magnetosomes internalization into U87 cells after binding. a/ Merge blue (cell nuclei), orange ( $\alpha_v\beta_3$  integrins), green (AMB1<sup>all</sup>) and red (AMB1<sup>out</sup>) channels. b/ Merge blue and red channels show cell nuclei and magnetosomes located outside cells. c/ Merge blue and green channels show cell nuclei and all magnetosomes. d/ Brightfield image revealing magnetosome iron-oxide cores.

recycled back and forth from cells membrane, which enables internalization of bonded ligand<sup>7,8</sup>. Internalization of AMB1 VRGD magnetosomes bonded to U87 cells has then been investigated, by modifying the previous *in vitro* protocol. AMB1 VRGD magnetosomes dose was reduced to  $250 \mu\text{g}_{[\text{Fe}]} / \text{L}$  in order to diminish magnetosomes aggregation and thus, the saturation of their Venus fluorescence. Incubation time has been considerably lengthened up to 24 h, to observe both binding and internalization. Finally, AMB1 VRGD magnetosomes bonded to the outer cell membrane were distinguished from those internalized inside cells. An anti-AMB1 antibody (see Appendix A.4) was used to specifically stain magnetosome membranes. AMB1 VRGD magnetosomes located outside have been revealed prior to permeabilization of U87 cell membranes with Triton<sup>®</sup> X-100, whereas the whole population of AMB1 VRGD magnetosomes were revealed post cell membranes permeabilization. For each condition, the anti-AMB1 antibody was coupled to a different fluorescent secondary antibody.

**Results** The two different secondary antibodies used for each step (red for magnetosomes located outside U87 cells and green for all magnetosomes) allow to precisely determine magnetosomes localization. Microscopy images presented in Figure 4.7 reveal the two populations of magnetosomes: AMB1<sup>out</sup>+ spots (red spots corresponding to magnetosomes outside U87 cells) are mainly localized at cell periphery and co-localized with  $\alpha_v\beta_3$  integrins, whereas [AMB1<sup>all</sup>+ / AMB1<sup>out</sup>-] spots (green but not red spots corresponding to magnetosomes inside U87 cells) are mainly localized within cell membranes. Moreover, it seems that AMB1<sup>out</sup>+ spots mostly look like bigger aggregates while [AMB1<sup>all</sup>+ / AMB1<sup>out</sup>-] spots appear better dispersed in cell cytoplasm. This fluorescence microscopy study confirms that AMB1 VRGD magnetosomes can be internalized by U87 cells after binding to  $\alpha_v\beta_3$  integrins.

<sup>7</sup>S. Hak et al., *Angiogenesis*, **17**: 93–107, 2014.

<sup>8</sup>D. Moncelet et al., *PLoS ONE*, **8**: e82777, 2013.

**Cross-validation with TEM imaging** Finally, to investigate with higher precision magnetosomes internalization, TEM images analysis was carried out on U87 cells incubated with AMB VRGD or AMB1 V, following a protocol detailed in Appendix A.6. The obtained TEM micrographs reveal the presence of magnetosomes inside U87 cells incubated with AMB1 VRGD, whereas none is found with AMB1 V treatment (Figure 4.8 a,b). In accordance with the previous fluorescence microscopy results, TEM micrographs at higher magnification confirm that most magnetosomes located inside U87 cell are engulfed in vesicles, confirming the internalization of magnetosomes in presence of RGD peptide (Figure 4.8 c,d).

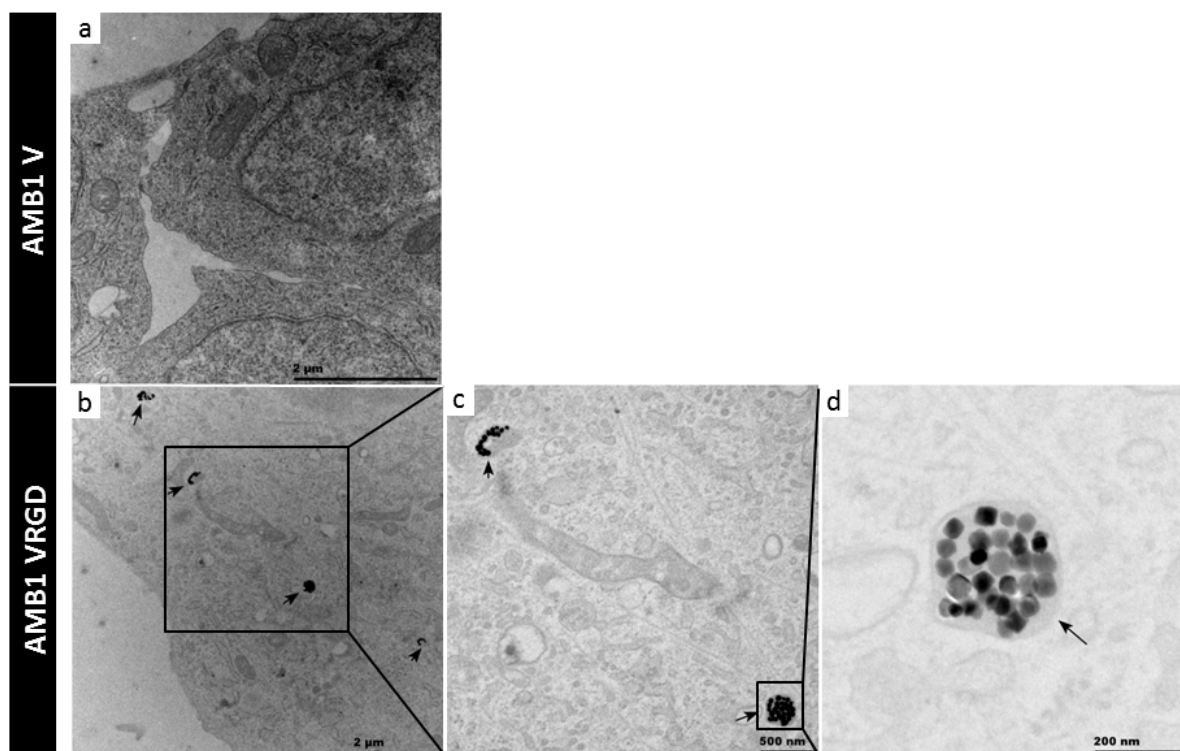


Fig. 4.8 – TEM micrographs of U87 cells incubated with magnetosomes. a/ Micrograph of U87 cells incubated with AMB1 V shows no magnetosomes internalization. b/ Micrograph of U87 cells incubated with AMB1 VRGD reveals internalized magnetosomes (indicated with arrows). c,d/ Higher magnification micrographs of U87 cells incubated with AMB1 VRGD show cell vesicles containing magnetosomes (arrows).

#### 4.2.4 Affinity study on spheroid culture of U87 cells

Spheroids of tumor cells raise great interest in research because of their 3D structures that better mimic tumors<sup>9</sup>. In particular, studies focusing on  $\alpha_v\beta_3$  integrins, known to be highly involved in cell motility and to depend on cells communication state, may benefit from such complex structures. U87 spheroids were firstly grown in inverted droplets and then transferred into an hydrogel-based extracellular matrix (Matrigel<sup>®</sup> from Corning company). Spheroids grown up in these conditions easily reached 2 – 5 mm in diameter. It is noteworthy that Matrigel<sup>®</sup> binds to cells through adhesive receptors different from  $\alpha_v\beta_3$  integrins. Matrigel<sup>®</sup> is mainly made of laminin, collagen IV, heparin sulfate proteoglycans, entactin/nidogen and a number of growth factors (see [Corning Documentation](#)), none of these compounds being expected to be

<sup>9</sup>M. Zanoni et al., Scientific Reports, **6**: 19103, 2016.

recognized by  $\alpha_v$  integrins<sup>3,10</sup>.

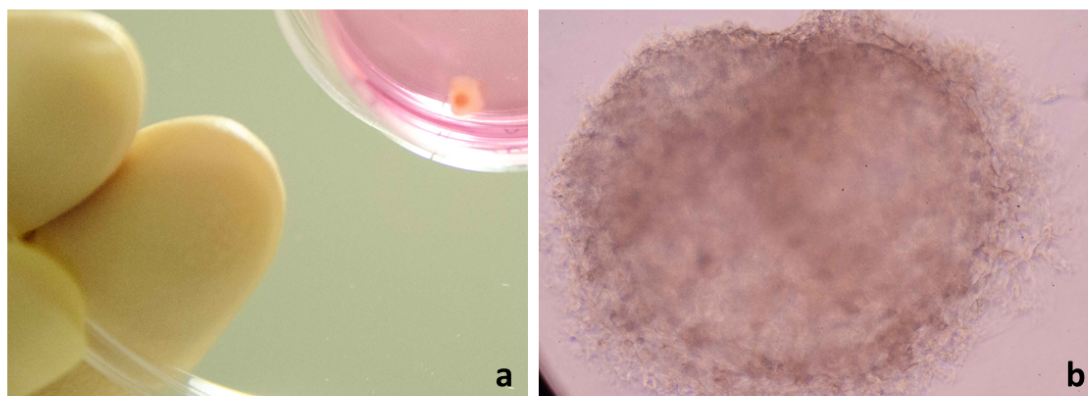


Fig. 4.9 – Pictures of U87 spheroids in Matrigel<sup>®</sup>. a/ Camera picture of a large U87 spheroid ( $\varnothing \sim 5 \text{ mm}$ ). b/ Microscope picture of a small U87 spheroid ( $\varnothing \sim 1 \text{ mm}$ ).

Microscope image of one U87 spheroid is presented in Figure 4.9. Its structure can be described as core-shell, the core being the U87 cells densely aggregated from the inverted droplet culture, surrounded by the shell made of a loose network of U87 cells in Matrigel<sup>®</sup>. It is possible to remove spheroids from surrounding Matrigel<sup>®</sup> (because Matrigel<sup>®</sup> remains softer than spheroids), and replace them in a fresher one to insure regular growth. Details on spheroids culture protocol are given in Appendix A.3.

**Different protocols for incubating magnetosomes with spheroids** The first issue to tackle, when using spheroids to study magnetosomes affinity for U87 cells, was the incubation process. Matrigel<sup>®</sup> is an hydrogel-based extracellular matrix in which nanoparticles cannot easily diffuse<sup>11</sup>. Two protocols were tested: the first one consisted in incubating magnetosomes directly with spheroids suspended in Matrigel<sup>®</sup> during 2 days, and the second one in removing spheroids from Matrigel<sup>®</sup> to soak them during 2 h in a liquid culture medium containing magnetosomes.

**Different protocols for rinsing spheroids** Rinse step was mandatory in conventional 2D cell culture to compare specific affinity for U87 cells of AMB1 VRGD magnetosomes and AMB1 V ones, otherwise plates surface would have been equally covered with nanoparticles in both cases. This simple but essential step became also problematic with spheroids, as the incubation protocol was. Once again, ensuring efficient diffusion of magnetosomes out of Matrigel<sup>®</sup> was difficult to achieve. Various rinse procedures were tested: change of Matrigel<sup>®</sup> repeated two times, change of Matrigel<sup>®</sup> after rinsing spheroids in liquid medium, using or not a magnet at the bottom of the plate to help magnetosomes movements.

**Results** Unfortunately, none of the tested incubation and rinse protocols has been satisfying, mainly because magnetosomes did not efficiently diffuse into Matrigel<sup>®</sup>: thus it was difficult to ensure that magnetosomes could reach the U87 cells, as well as to remove magnetosomes

<sup>3</sup>F. Danhier et al., *Molecular Pharmaceutics*, **9**: 2961–2973, 2012.

<sup>10</sup>P.C. Brooks., *European Journal of Cancer*, **32**: 2423–2429, 1996.

<sup>11</sup>S. Ramanujan et al., *Biophysical journal*, **83**: 1650–1660, 2002.

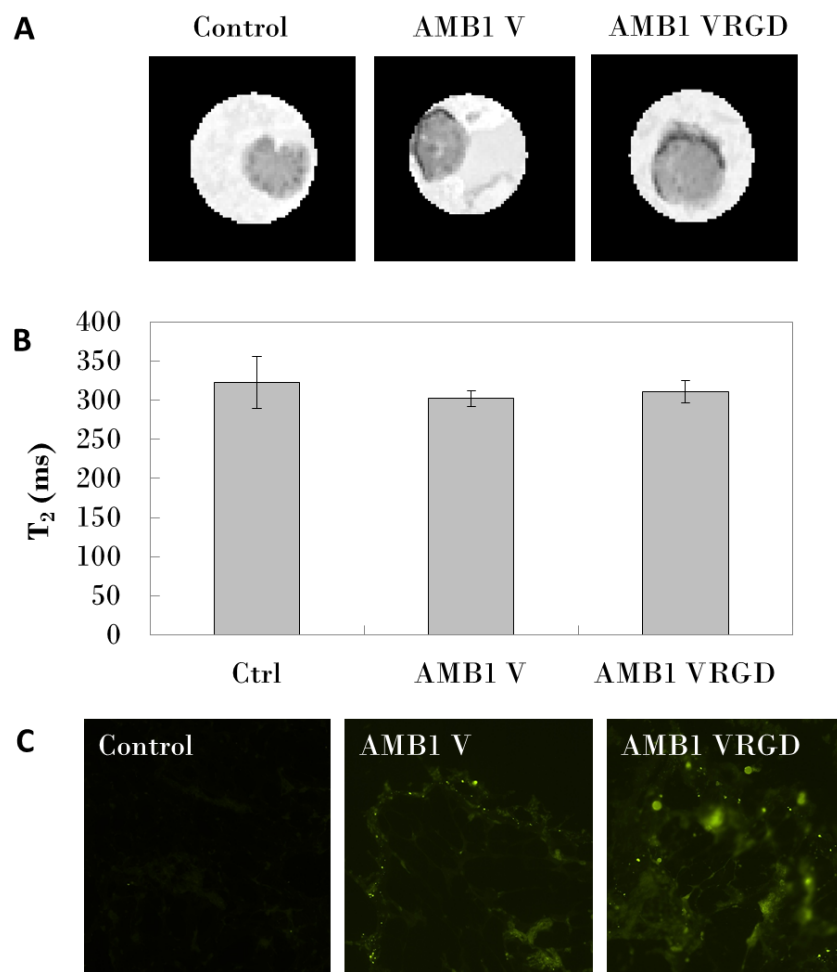


Fig. 4.10 – MRI acquisitions at 7 T on spheroid culture of U87 cells. A/  $T_2$  parametric maps of U87 spheroids incubated with no magnetosomes (Control), AMB1 V or AMB1 VRGD ones. B/ Mean  $T_2$  values in U87 spheroids for the different incubation conditions. C/ Fluorescence microscopy images of Venus fluorophore in U87 spheroids for the different incubation conditions.

residuals after incubation.

All the incubation/rinse conditions were tested by measuring  $T_2$  values of U87 spheroids, thanks to relaxivity measurements at 7 T. Observation of  $T_2$  parametric maps reveals that no significant difference can be found between incubation/rinse protocols, or between both AMB1 V and AMB1 VRGD magnetosomes treatments (see the example in Figure 4.10 A). This result is confirmed by the  $T_2$  values measured in U87 spheroids (see Figure 4.10 B), that are pooled for all tested conditions. Some spheroids were fixed and frozen post MRI acquisitions, to be afterward sliced for fluorescence microscopy. As shown on Figure 4.10 C, Venus fluorescence can be observed at spheroid periphery for both AMB1 V and AMB1 VRGD magnetosomes treatments, localized on U87 cells or in the Matrigel<sup>®</sup> around. Furthermore, MRI images highlight that U87 spheroids can be very different one to the other in terms of MRI contrast, revealing our production method is probably not reproducible enough. Finally, it is quite complicated to draw any conclusions from this study. The low diffusivity of magnetosomes in Matrigel<sup>®</sup> makes them inaccessible to many U87 cells and impossible to wash out after

incubation. And the high inhomogeneity within different spheroids revealed by MRI may also overtake differences from the potential differences between magnetosomes treatments.

**Perspective** Finally, a difference between AMB1 VRGD and AMB1 WT magnetosomes has been observed on one experiment, where U87 cells beforehand incubated with magnetosomes were used to seed spheroids. As shown on Figure 4.11, these spheroids exhibit lower  $T_2$  values (measured at 7 T) in the center, where U87 cells at the origin of the 3D structure (inverted droplets) are supposed to be, and higher  $T_2$  values where U87 cells are supposed to grow. This experiment indicates that it is possible to detect, with *in vitro* MRI acquisitions, U87 cells in 3D structure loaded with magnetosomes. To precisely study the affinity of RGD functionalized magnetosomes on spheroid culture of U87 cells, further developments of dedicated incubation/rinse/MRI protocols have to be investigated. Nevertheless, if this experiment could be reproducible and show statistical difference, its conclusion would be very similar to the one where incubated cells were dispersed in agar for MRI (see Subsection 5.1.2), but much more time consuming and expensive. However, use of 3D tumor spheroids could still be valuable if one manages to solve the issues of magnetosomes low diffusivity in culture medium. This hydrogel culture media can actually be replaced by solid scaffold or by fiber mesh structure to grow 3D spheroid, which could enable an easier and more efficient magnetosomes incubation and rinse<sup>12</sup>.

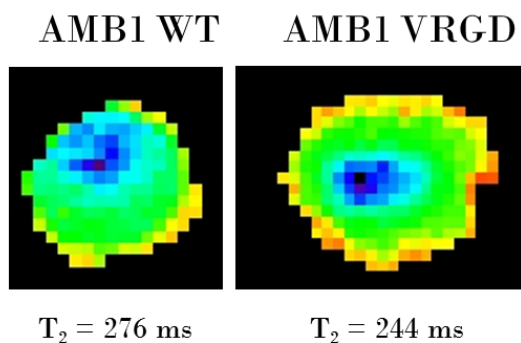


Fig. 4.11 –  $T_2$  parametric maps acquired at 7 T of U87 spheroids grown from cells beforehand incubated with AMB1 WT or AMB1 VRGD magnetosomes. Mean  $T_2$  values in each U87 spheroid are reported below each image.

### 4.3 *In vivo* molecular imaging of a mouse glioblastoma model with RGD functionalized magnetosomes

*In vivo* affinity of AMB1 VRGD magnetosomes for U87 brain tumor remains to demonstrate so far. In a first step, circulation of both magnetosomes (RGD and control) in mouse brain vasculature was questioned to insure a good overall biocompatibility and a blood circulation time sufficient for binding to occur. This dynamic blood circulation study has been performed by acquiring dynamic contrast-enhanced MR images of U87 mouse brains at high imaging rate, as long as possible after magnetosomes intravenous injection. The obtained results confirmed that both magnetosomes are similar blood pool agents, which makes AMB1 V a suitable control of AMB1 VRGD for molecular imaging studies. In a second step, similar injection protocol was

<sup>12</sup>M. P. Carvalho et al., Carbohydrate Polymers, **150**: 139–148, 2016.

carried out, but contrast-enhanced MR images of U87 mouse brains were acquired much longer post injection after clearance of the magnetosomes vascular part, to highlight magnetosome fraction trapped in the tumor.

### 4.3.1 Dynamic continuous follow-up: assessment of magnetosomes circulation in tumor vessels

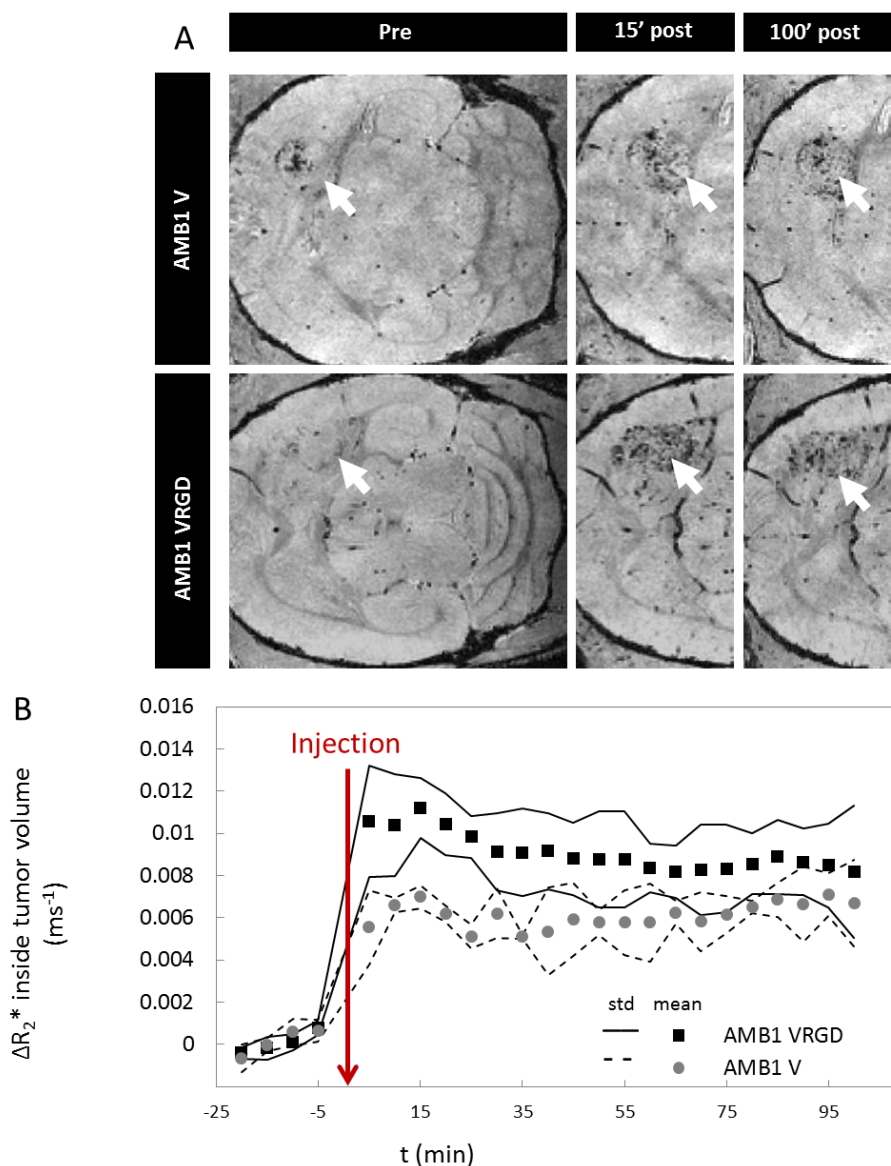


Fig. 4.12 – Short term follow-up of MRI contrast enhancement in mouse brain tumor after magnetosomes intravenous injection. A/ FLASH images of mouse brain acquired before, 15 *min* and 100 *min* post injection of AMB1 V or AMB1 VRGD, tumor being underlined by white arrows. B/ Contrast enhancement through time after magnetosomes injection for both AMB1 V ( $n = 2$ ) and AMB1 VRGD ( $n = 4$ ) groups.

**MRI protocol** The short term follow-up of MRI contrast enhancement induced in brain vasculature after magnetosomes injection has been carried out at 11.7 *T* on U87 mouse model of

glioblastoma, for both AMB1 VRGD and AMB1 V magnetosomes. One experiment consisted of a series of pre injection scans: one anatomical RARE image for tumor size measurement and four FLASH images as contrast baseline (scan parameters are detailed in Appendix B.2). The cradle was then removed from the MRI scanner tunnel, a dose of  $200 \mu\text{mol}/\text{kg}$  ( $[Fe] = 54 \text{ mM}$ ) of magnetosomes was injected at the mouse tail vein (injection volume around  $100 \mu\text{L}$ ) while keeping the animal positioned, before inserting the cradle back in the tunnel for post injection scans. Finally, a series of 20 FLASH images were acquired to follow brain contrast enhancement within the first 100 minutes post injection. A total of  $n = 2$  mice received AMB1 V magnetosomes and  $n = 4$  mice received AMB1 VRGD ones.

**Data processing** The same protocol as in Section 3.4.3 was used to semi-quantitatively measure iron uptake in brain tumor by computing  $\Delta R_2^*(t)$  parameter.

**Results** Figure 4.12 A shows representative FLASH images for both magnetosomes injections, which lead to an increase of the number of hypo-intense voxels inside brain tumor (underlined by white arrows), 15 *min* and 100 *min* post injection. This observation highlights that the two types of injected magnetosomes have access to brain tumor vessels (at least during 100 *min*), probably due to the EPR effect (as already shown in Figure 3.15). The tumor of the mouse injected with AMB1 VRGD looks at 15 *min* slightly darker than the one that received AMB1 V, but they look similar at 100 *min* post injection.

The dynamic evolution of  $\Delta R_2^*$  parameter is presented in Figure 4.12 B for both groups. A sharp increase of  $\Delta R_2^*$  confirms that both magnetosome injections lead to a high enhancement of tumor vasculature. Until 30 *min* post injection, AMB1 VRGD magnetosomes seem to induce a more significant contrast enhancement in brain tumor than AMB1 V, but this significant difference does not maintain in time: between 30 *min* and 100 *min* post injection, it was not possible to statistically differentiate both groups given their standard deviation.

This experiment evidences that, on average, both magnetosomes steadily circulate into tumor vessels for at least 100 *min*, which is expected to be long enough for interactions between RGD magnetosomes and their targets to happen, if any. The results also confirm that 100 *min* post injection is not long enough for blood clearance to happen, thus for seeing a significant effect of magnetosomes functionalization.

### 4.3.2 24 h follow-up: *in vivo* assessment of RGD magnetosomes affinity for U87 tumor

**MRI protocol** This long term follow-up of MRI contrast enhancement induced in brain vasculature after post magnetosomes injection has also been carried out at 11.7 T on U87 mouse model of glioblastoma, for both AMB1 VRGD and AMB1 V magnetosomes. Unlike for the short term study, tumor contrast enhancement needed to be followed until 24 h, to insure blood clearance, which implies to wake up the mouse between scans. The dynamic strategy of acquiring continuous FLASH images could not be used anymore to quantitatively assess MRI contrast changes, and thus a parametric imaging strategy was required to measure contrast enhancement at different time points post magnetosomes injection. This new protocol consisted in acquiring a series of MGE images to produce  $T_2^*$  parametric maps. One experiment began with the acquisition of a RARE image for tumor volume monitoring, a FLASH image for visualizing  $T_2^*$  contrast changes and MGE images to quantify these contrast changes on computed

$T_2^*$  parametric maps. Then, magnetosomes injection was performed using the protocol of the previous study, followed by the acquisitions of one series of MGE images and one FLASH image post injection. Mice were woken up after the acquisition of this last FLASH image. A new imaging session started 24 h post injection, consisting in the acquisition of one RARE image, one FLASH image and one series of MGE images. A total of  $n = 4$  mice received AMB1 V magnetosomes and  $n = 5$  mice received AMB1 VRGD ones.

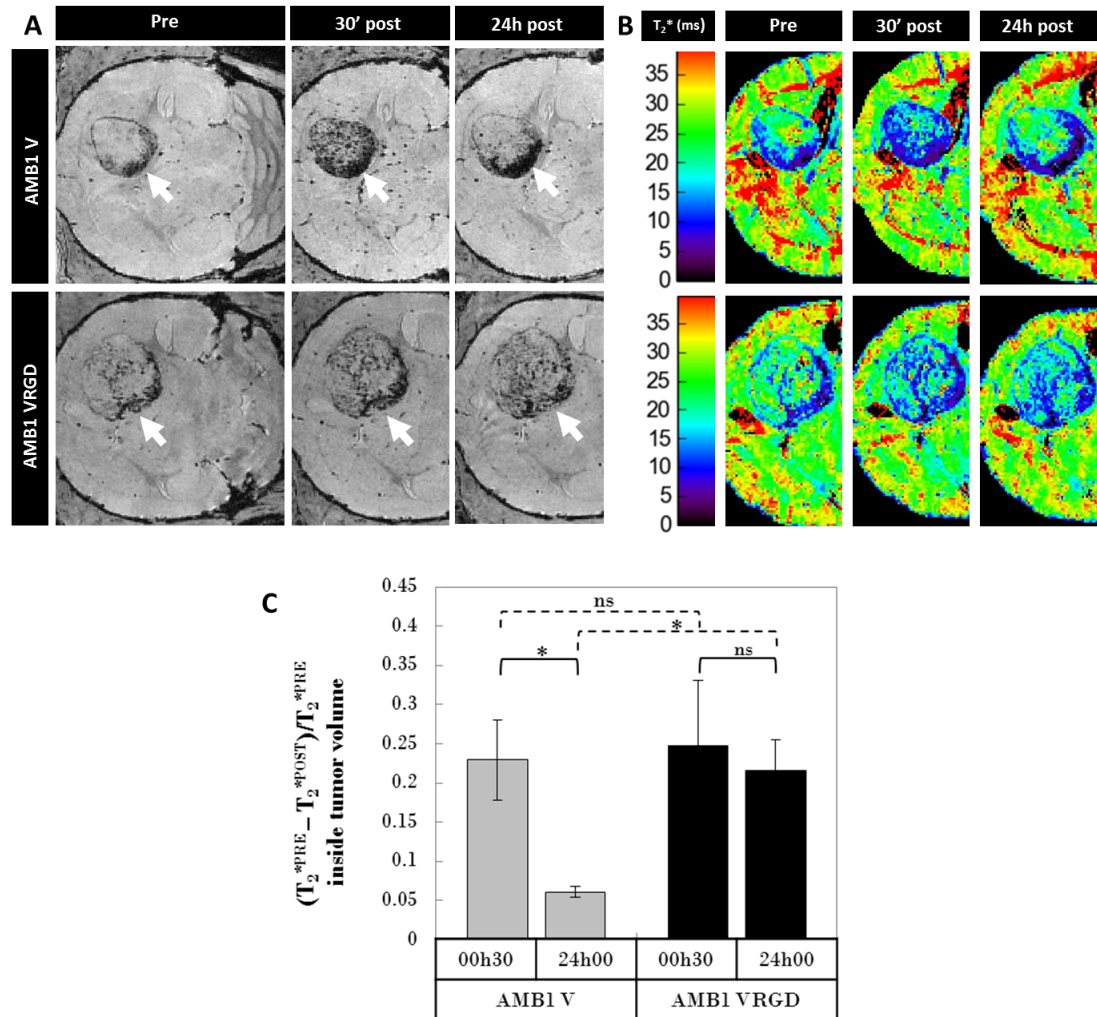


Fig. 4.13 – Long term follow-up of MRI contrast enhancement in mouse brain tumor after magnetosomes intravenous injection. A/ FLASH images of mouse brain acquired before, 30 min and 24 h post injection of AMB1 V or AMB1 VRGD, tumor being underlined by white arrows. B/ Corresponding  $T_2^*$  maps from MGE scans. C/ Normalized decrease of  $T_2^*$  values estimated inside tumor volume after magnetosomes injection for the two groups ( $n = 4$  for AMB1 V and  $n = 5$  for AMB1 VRGD). Statistical significance of differences, defined as p-value < 0.05 for non-parametric Wilcoxon signed-rank test, is mentioned with an asterix (\*).

**Data Processing** Each series of MGE images acquired for different echo times was reconstructed into a  $T_2^*$  parametric map, by fitting the MRI signal pixel-by-pixel with the following

equation :

$$S(t) = S_0 \cdot \exp\left(\frac{-t}{T_2^*}\right) \quad (4.1)$$

Tumor volumes were manually segmented on the first echo of MGE images to compute mean  $T_2^*$  values in each tumor. To quantitatively compare results obtained on different mice, it was necessary to define normalized  $T_2^*$  values. A normalized decrease of  $T_2^*$  was computed as follows:

$$\Delta^{norm}T_2^* = \frac{T_2^{*PRE} - T_2^{*POST}}{T_2^{*PRE}} \quad (4.2)$$

This normalized decrease of  $T_2^*$  is an indirect measure of iron load inside the tumor, but not directly proportional as it could have been with  $T_2$  values measurement. Nevertheless, this  $\Delta^{norm}T_2^*$  parameter is well appropriate to compare magnetosomes accumulation in mouse brain tumor between AMB1 VRGD and AMB1 V conditions.  $T_2$  mapping strategies were not chosen, firstly because the acquisition time is longer than for  $T_2^*$  ones, and secondly because the high cells density in tumor leads to a significant increase of  $T_2$ , which disturbs the measurement of  $T_2$  decrease induced by magnetosomes.

**Results** Figure 4.13 summarizes the results of this long term follow-up study. FLASH images (Figure 4.13 A) highlight that numerous hypo-intense voxels appear in the tumor (white arrows) immediately after injection of both magnetosome types, confirming the results of short term study presented in Figure 4.12. 24 h later, some hypo-intense voxels still remain while others have already disappeared: it seems that a greater number of hypo-intense voxels remains in AMB1 VRGD condition compared with AMB1 V.

Corresponding  $T_2^*$  parametric maps reconstructed from MGE images are displayed in Figure 4.13 B, corroborating observations made on FLASH images:  $T_2^*$  value is lower in the tumor 30 min post injection, and this decrease seems to maintain longer with AMB1 VRGD magnetosomes compared with AMB1 V ones.

Tumor segmentation enables to quantify these observations by pooling all acquired data per post injection time and per group (see Figure 4.13 C). A non-parametric Wilcoxon signed-rank test is run to evaluate the statistical significance of differences between groups and post injection times. Both types of injected magnetosomes lead to a similar tumor iron uptake (non-significant difference at 30 min between bar plots of AMB1 VRGD and AMB1 V), result in agreement with short term study, which has revealed that no difference could be observed at this time frame between both magnetosomes. Then, for AMB1 V group, there is a significant decrease of tumor iron uptake between 30 min and 24 h (significant difference for AMB1 V between bar plots at 30 min and 24 h), while the tumor iron uptake is found steady for AMB1 VRGD group (non-significant difference for AMB1 VRGD between bar plots at 30 min and 24 h). This result corroborates the observations made on FLASH images and  $T_2^*$  parametric maps: 24 h post injection, a significantly higher iron uptake is found inside tumor for AMB1 VRGD group compared with AMB1 V one.

Studying contrast enhancement in the tumor up to 24 h post magnetosomes injection enables to demonstrate that RGD peptide confers active tumor targeting properties to magnetosomes. This establishes *in vivo* that biogenic AMB1 VRGD magnetosomes exhibit efficient MRI contrasting and tumor cells targeting properties.

### 4.3.3 Cross-validation of MRI results with *post mortem* histology

The acquisition of *post mortem* histological data has been used to cross-validate MRI results, especially by imaging magnetosomes trapped inside the tumor with fluorescence microscopy. Details on sample preparation can be found in Appendix B.4.

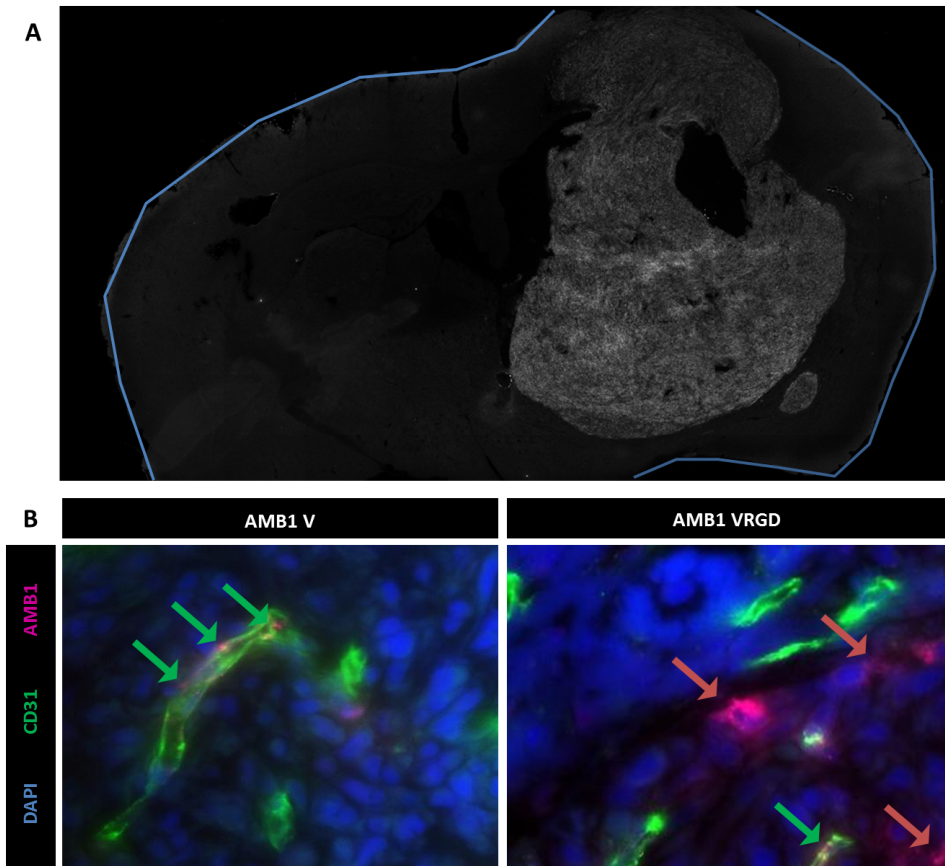


Fig. 4.14 – Stained histological slices of AMB1 V or AMB1 VRGD injected mouse brain. A/ Anti- $\alpha_v\beta_3$  antibody enables to clearly visualize tumor contour on x10 mosaic images. Brain contour is highlighted with a blue line to facilitate visualization of contralateral zone. B/ x63 magnification images of tumor area: red arrows point out AMB1 signal in cells located outside vessels, while green arrows point out AMB1 signal co-localized with vessels.

**Protocol** Detailed protocol of immunohistochemical stainings performed on mouse brain slices can be found in Appendix B.4. Magnetosomes were intravenously injected and  $\alpha_v\beta_3$  integrins, their target, can be found at the membrane of tumor cells as well as endothelial cells of neo-angiogenic vessels, hence tumor vessels have been stained with an anti-CD31 antibody. Cell nuclei have been stained with DAPI, and  $\alpha_v\beta_3$  integrins with a dedicated antibody to reveal tumor area. Finally, magnetosome membranes were stained with a specific anti-AMB1 antibody, produced by our collaborators from LI2D laboratory.

**Results** Observation of representative stained histological slices acquired on mice from each group confirms that  $\alpha_v\beta_3$  integrins are over-expressed on whole tumor area compared with con-

tralateral hemisphere (see Figure 4.14 A), where almost no AMB1 signal is found. Inside the tumor, the greater amount of AMB1 signal is located inside vessels for both groups. Though, it appears that in AMB1 VRGD treated mice, AMB1 signal can be found in different cells located outside vessels. These observations are highlighted in Figure 4.14 B: green arrows show typical AMB1 positive pixels co-localized with CD31 ones, while red arrows point out cells with positive AMB1 signal but no CD31 signal.

Finding more magnetosomes in the tumor area for AMB1 VRGD group corroborates MRI results. However it remains complicated to conclude on the nature of AMB1 signal found in cells located outside vessels for the AMB1 VRGD condition. Further staining of the different types of cells in the brain could be investigated, like immune cells, glial cells, neurons,... but the exploration of their colocalization with AMB1 staining are expected to be very difficult to analyze.

**Semi-quantitative analysis of histological images** Results of descriptive histology can be reinforced by applying semi-quantitative analysis based on channels co-localization, using an algorithm similar to the one applied on *in vitro* microscopy images in Subsection 4.2.2.

Mosaic images at x20 magnification were acquired in order to cover the whole tumor area, on a slice approximately at the center of the tumor. The same immunohistochemical stainings were used, revealed with the following channels:  $\alpha_\nu\beta_3$  integrins in orange, vessels in green, AMB1 magnetosome membranes in red and cell nuclei in blue. Tumor area was manually segmented on orange channel. Finally, co-localization between green and red channels was processed as detailed in Appendix C.3.

Representative stained histological slices of AMB1 VRGD or AMB1 V treated mouse brain are presented in Figure 4.15 A. The anti- $\alpha_\nu\beta_3$  staining enables easy and reproducible segmentation of tumor area. Then co-localization between red and green clusters can be computed only in tumor area. Results of this image processing on  $n = 3$  mice for AMB1 VRGD and  $n = 2$  mice for AMB1 V (one representative brain slice per mouse) are presented in Figure 4.15 B. Percentage of pixels in tumor area which are positive to anti-AMB1 and anti-CD31 stainings ([AMB1+/CD31+]) is plotted to measure the amount of magnetosomes detected inside vessels for each group. This plot clearly exhibits that AMB1 VRGD injection induces higher magnetosomes retention in mouse brain tumor, since there is more than 6 times more [AMB1+/CD31+] pixels in this case compared with AMB1 V injection. However, as already mentioned, the fraction of [AMB1+/CD31-] remains quite difficult to interpret so far.

#### 4.3.4 *Post-mortem* MRI acquisitions: toward histology-like MRI?

Both histological and MRI data have confirmed that RGD magnetosomes present a specific affinity for U87 tumor *in vivo*. The interest of coupling these two methods is to cross-validate, by two different physical measures, that a significantly higher iron uptake is observed in the tumor 24 h after the injection of RGD magnetosomes compared with control. But a major difference to keep in mind is that MR images were acquired *in vivo* while histological data were acquired *post mortem* after intracardiac perfusion of mouse. This means that histology was performed after removing the blood from vasculature, thus eliminating non bonded magnetosomes if any. Therefore, it was very interesting to image such perfused mouse brain with MRI, taking advantage of the possibility to lengthen the scan duration, and thus significantly

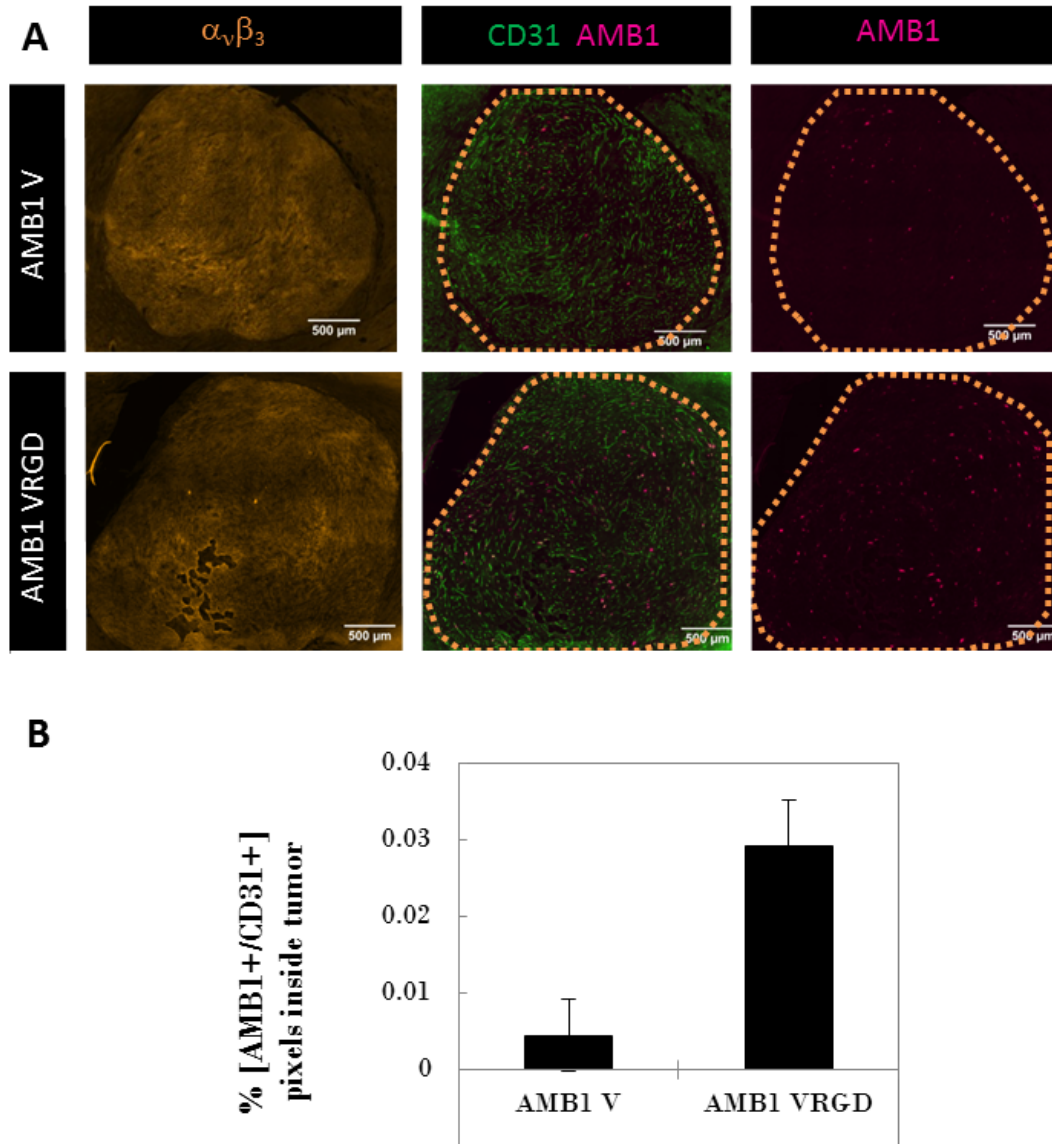


Fig. 4.15 – Quantification of AMB1+ pixels in stained histological slices. A/ Histological slices of mouse brains injected with AMB1 V and AMB1 VRGD magnetosomes. Anti- $\alpha_v\beta_3$  staining is in orange, anti-CD31 staining reveals vessels in green and anti-AMB1 staining shows magnetosome membranes in red. B/ Percentage of AMB1 positive pixels located inside tumor area and inside vessels ( $[AMB1+]/[CD31+]$ ).

enhance the spatial resolution of acquired images.

*Post mortem* MRI acquisition has been run only on one mouse injected with AMB1 VRGD magnetosomes as a test, because the acquisition of histological data was carried out in priority. Spatial resolution of MGE images skips from  $100\ \mu m$  isotropic *in vivo* (17 min acquisition time) to  $50\ \mu m$  isotropic *post mortem* (14 h 30 acquisition time), which corresponds to a voxel volume divided by 8, implying the multiplication by 50 of the acquisition time to maintain sufficient signal-to-noise ratio. The MGE sequence used for *post mortem* acquisition is detailed in Appendix B.2. Figure 4.16 shows MGE images acquired 24 h post AMB1 VRGD injection both right before (*in vivo*) and right after mouse euthanasia (*post mortem*).

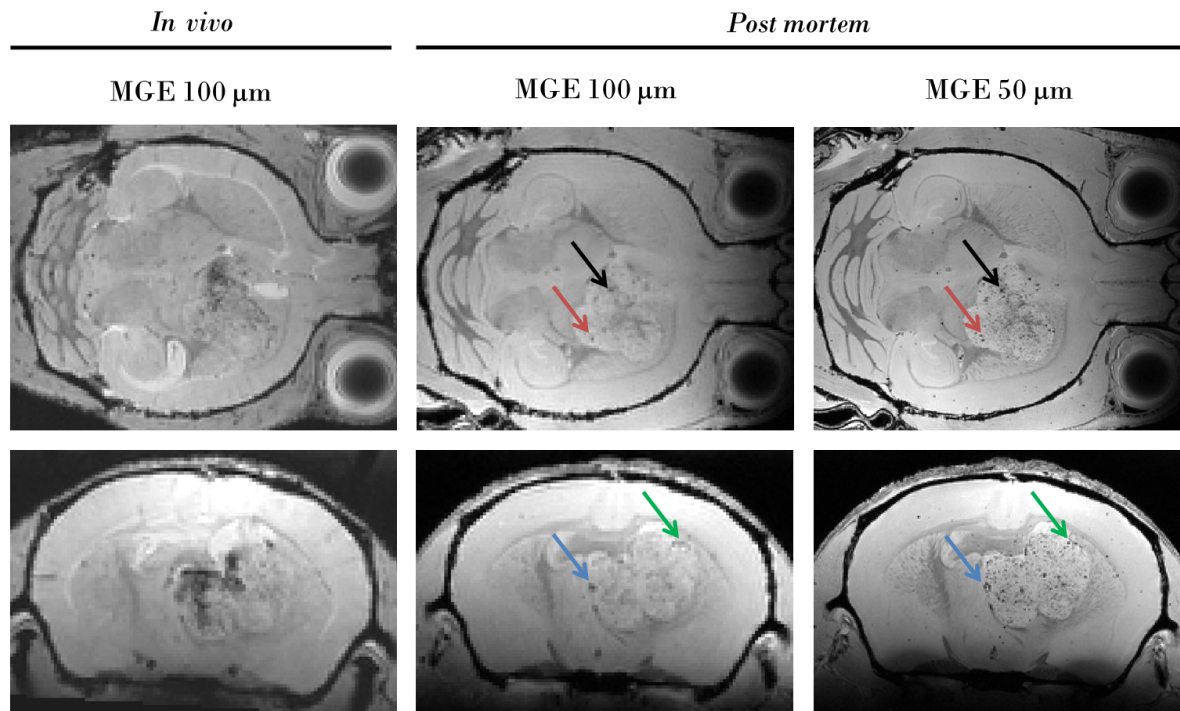


Fig. 4.16 – *Post mortem* MRI images acquired 24 *h* after AMB1 VRGD magnetosomes intravenous injection. Comparison between the MGE 100  $\mu\text{m}$  sequence (100  $\mu\text{m}$  isotropic spatial resolution, 17 *min* acquisition time) used for *in vivo* and *post mortem* MRI acquisitions, and the MGE 50  $\mu\text{m}$  sequence (50  $\mu\text{m}$  isotropic spatial resolution, 14 *h* 30 acquisition time) used only *post mortem* MRI acquisitions. Pairs of colored arrows point out how the partial volume effect affects the sensitivity of magnetosomes detection.

The comparison between the two MGE 100  $\mu\text{m}$  images reveals that an important part of signal drop in the tumor seems due to non bonded magnetosomes (even 24 *h* after injection) or to blood itself. Besides, MGE 100  $\mu\text{m}$  image acquired *post mortem* exhibits very few dark spots inside tumor, whereas numerous of them appear on MGE 50  $\mu\text{m}$  image. This clearly illustrates the partial volume effect responsible for the dilution of contrast enhancement when increasing the voxel size (see for example pairs of colored arrows on Figure 4.16). On MGE 50  $\mu\text{m}$  image, the voxel size is probably closer to the typical size of magnetosome aggregates, which are therefore better resolved.

Finally, it is also interesting to compare this high resolution *post mortem* MR image with the corresponding stained histological slices imaged by fluorescence microscopy. Figure 4.17 shows the histological slice (4.17 B C) corresponding to the MRI one (4.17 A), both *post mortem*. Numerous AMB1 positive spots are located in the tumor area, where numerous dark spots are also seen on MR image, both supposed to come from magnetosomes presence. This experiment demonstrates that *post mortem* MR images approach the same level of detail than histological images.

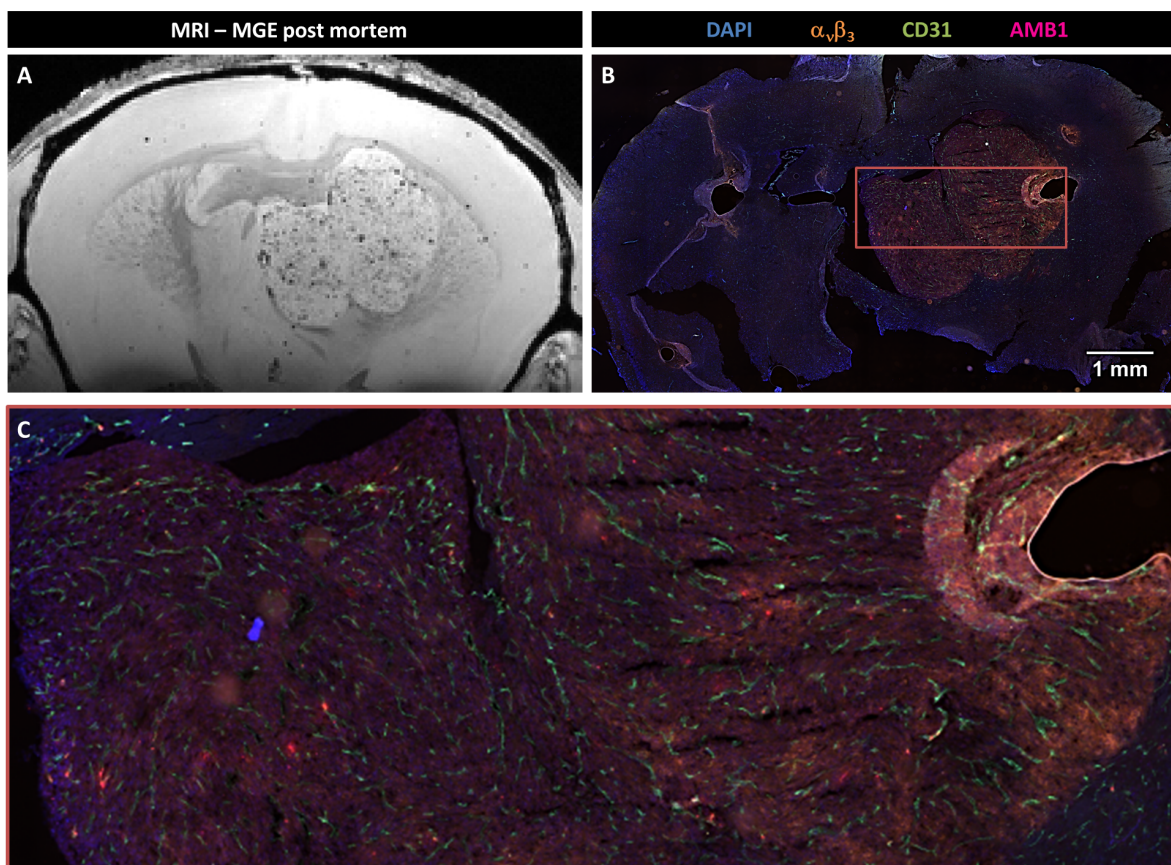


Fig. 4.17 – Comparison between high resolution *post mortem* MR image (A) and histological image (B and C).

#### 4.4 In which cells can magnetosomes be found after intravenous injection?

Fate of intravenously injected IONPs has been widely studied, and the results showed that they are usually taken up by macrophages, and can be found in the liver, the spleen and the bone marrow<sup>13–15</sup>. Besides, biocompatibility of magnetosomes was also studied on Sprague Dawley rats<sup>16</sup>, and the authors concluded that they present no specific toxicity and that a large amount of magnetosomes can also be detected in the liver after sublingual injection. During our *in vivo* studies, no evident sign of toxicity induced by magnetosomes injection was observed, and the color of mouse liver, systematically checked after brain extraction, was always darker for injected animals compared to non-injected ones.

During this PhD, histological slices of liver and brain were prepared from mice used for the molecular imaging study presented in Section 4.3. A specific immunohistochemical staining was used to label liver macrophages, and another one to label microglia, the brain resident macrophage cells.

<sup>13</sup>R. Weissleder et al., *American Journal of Roentgenology*, **152**: 167–173, 1989.

<sup>14</sup>C. Corot et al., *Advanced Drug Delivery Reviews*, **58**: 1471–1504, 2006.

<sup>15</sup>M. Longmire et al., *Nanomedicine (London, England)*, **3**: 703–717, 2008.

<sup>16</sup>J. Sun et al., *Nanotoxicology*, **4**: 271–283, 2010.

#### 4.4.1 Interaction between liver macrophages and magnetosomes

Major part of magnetosomes is expected to accumulate in the liver after intravenous injection<sup>16</sup>. Therefore, histological liver slices of animals injected with magnetosomes have been analyzed to verify if magnetosomes could be detected with dedicated immunohistochemical stainings.

**Protocol** The livers of one mouse injected with AMB1 V and one with AMB1 VRGD were cryo-preserved following the same protocol than for brain conservation (see Appendix B.4). 20  $\mu\text{m}$  thick slices of liver were prepared for immunohistochemical stainings. The anti-CD68 antibody (revealed in green) was used to highlight macrophages and especially Kupffer cells, which are specialized macrophages residing inside liver. Magnetosome membranes were also stained in red with our dedicated anti-AMB1 antibody and cell nuclei were revealed in blue with DAPI (see details in Appendix B.5).

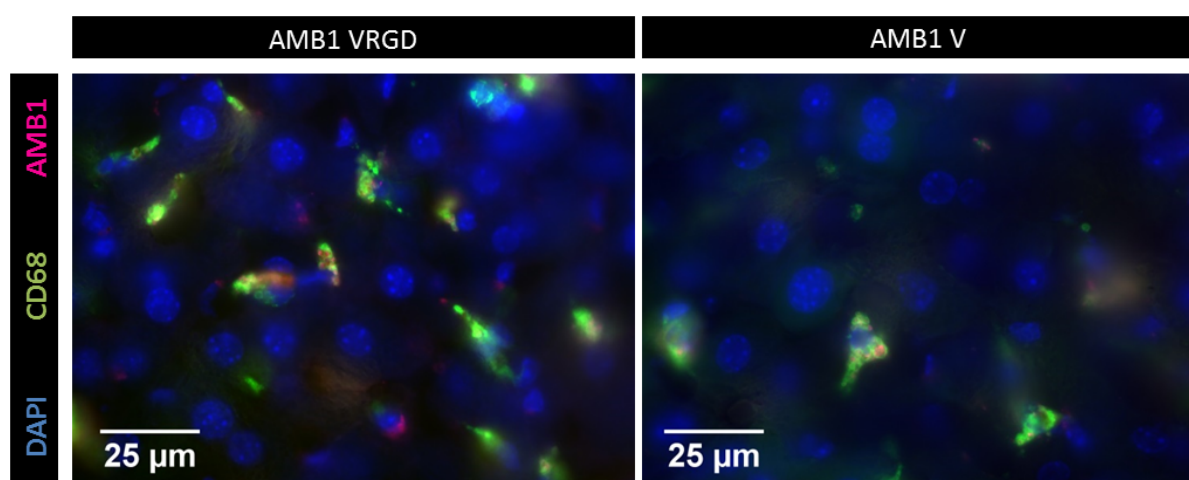


Fig. 4.18 – Stained histological slices of liver from mice injected with AMB1 VRGD (left) or AMB1 V (right). Liver macrophages are revealed in green (anti-CD68), AMB1 magnetosome membrane in red (anti-AMB1) and cell nuclei in blue (DAPI).

**Results** Figure 4.18 presents histological liver slices of two mice injected with AMB1 VRGD (left) or AMB1 V (right). Numerous CD68+ cells with small AMB1+ vesicles inside are detected in both cases. In summary, no evident difference occurs between the two types of injected magnetosomes, which both lead to an important magnetosomes accumulation in liver macrophages.

#### 4.4.2 Interaction between microglia and magnetosomes

Microglia are a type of glial cells, equivalent to macrophages but dedicated to insure brain immune defense. As an example, microglia activation after IONPs treatment has been demonstrated after intra-nasal exposure<sup>17</sup>. It was then interesting to investigate the interaction between microglia and magnetosomes after their intravenous injection to brain tumor bearing mice.

<sup>17</sup>Y. Wang et al., *Toxicology Letters*, **205**: 26–37, 2011.

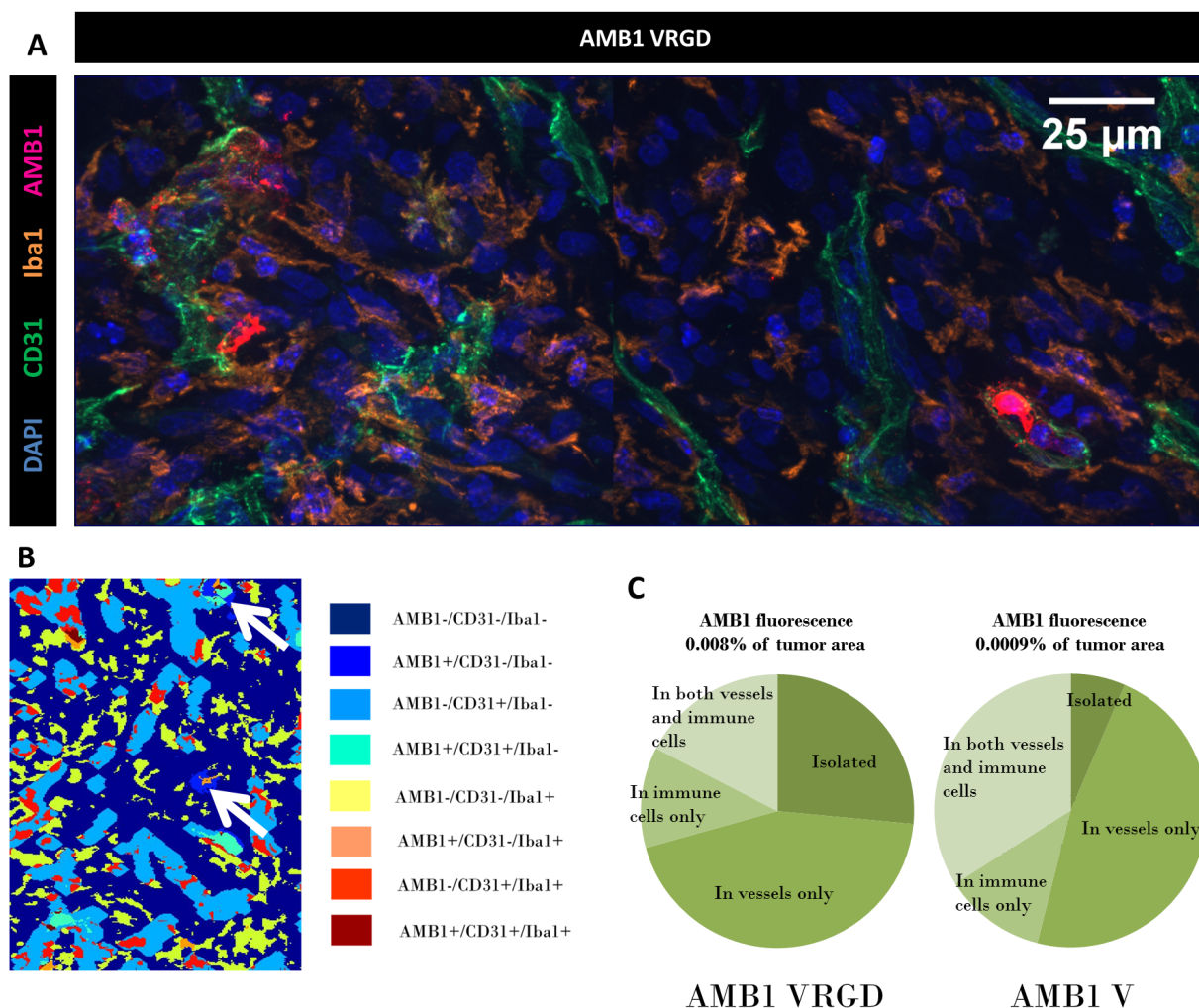


Fig. 4.19 – Interaction between magnetosomes and microglia. A/ Example of maximum intensity projection of fluorescence image acquired in ApoTome mode at x63 magnification, revealing cell nuclei in blue (DAPI), vessels in green (anti-CD31), microglia in orange (anti-Iba1) and magnetosome membranes in red (anti-AMB1). B/ Example of pixels classification given the co-localization of the three anti-AMB1, anti-CD31 and anti-Iba1 stainings. C/ Pie charts show the relative proportion of anti-AMB1 staining fluorescence given the different co-localizations with anti-CD31 or anti-Iba1 stainings. The percentage of AMB1 positive pixels in the tumor is mentioned in bold above the pie charts.

**Protocol** Detailed protocol of immunohistochemical stainings on brain slices can be found in Appendix B.5. Vessels were stained with an anti-CD31 antibody (revealed in green), microglia with an anti-Iba1 antibody (revealed in orange), magnetosome membranes with our dedicated anti-AMB1 antibody (revealed in red) and cell nuclei with DAPI (blue). One needs to keep in mind that the anti-Iba1 antibody can also stain other immune cells like T-lymphocytes and monocytes<sup>18</sup>.

One x63 magnification fluorescence image has been acquired in ApoTome mode, which

<sup>18</sup>K. Ohsawa et al., Journal of Neurochemistry, **88**: 844–856, 2004.

enables to create optical sections in depth, and then better resolve co-localization for several stainings.

**Data processing** Mosaic images at x20 magnification, covering the whole tumor area on a central slice of tumor, were acquired for  $n = 2$  mice per group (treated with either AMB1 V or AMB1 VRGD). Considering all the possible co-localizations of positive and negative stainings, each pixel was classified in one of the 8 possible groups presented in Figure 4.19 B. Only the four AMB1+ cases (described in Table 4.1) were investigated to specify the magnetosomes localization in brain tumor after intravenous injection. Numbers of pixels positive to anti-AMB1 staining were counted and normalized by tumor areas, and the proportion of AMB1+ pixels in the four classes of interest was computed (see Figure 4.19 C).

Classification	Interpretation
AMB1+/CD31+/Iba1+	Magnetosomes both in vessels and immune cells
AMB1+/CD31+/Iba1-	Magnetosomes in vessels only
AMB1+/CD31-/Iba1+	Magnetosomes in immune cells only
AMB1+/CD31-/Iba1-	Isolated magnetosomes

Tab. 4.1 – Co-localization classification for triple immunohistochemical staining: vessels, microglia and magnetosomes.

**Results** The anti-Iba1 staining reveals that microglia are well spread in whole tumor area whatever the type of injected magnetosomes. An example of x63 magnification fluorescence image for a mouse injected with AMB1 VRGD, displayed in Figure 4.19 A, shows that tumor vessels and immune cells form two interconnected networks. It was thus very difficult to interpret stainings co-localization based on AMB1+ clusters (as done in Subsection 4.3.3), so a simple pixel-to-pixel co-localization was performed. This classification step builds a composite image assigning each pixel to one class represented by a specific color, as presented in Figure 4.19 B. This image reveals several unlikely situations where one AMB1+ cluster can spread in different classes (see white arrows). So this classification procedure tends to overestimate the number of isolated AMB1+ clusters.

AMB1+ pixels are 8 times more numerous in AMB1 VRGD treated mice versus AMB1 V ones, which is in accordance with the results presented in Subsection 4.3.3. The proportion of AMB1+ pixels in the four classes of interest are presented in pie charts on Figure 4.19 C. The proportion of AMB1+ pixels in vessels only, and in immune cells only, are comparable between both AMB1 VRGD and AMB1 V treatments. On the other hand, AMB1 VRGD treatment induces more isolated magnetosomes in the tumor, and less magnetosomes in both vessels and immune cells than AMB1 V one. Hypothesizing that this quantification gives the good overall trend despite the bias, the latter result could be interpreted as AMB1 V magnetosomes embodied in immune cells being driven inside vessels to be cleared out the tumor, whereas AMB1 VRGD magnetosomes seem actively internalized by other cells, like tumor ones.

This experiment paves the way for further investigation of AMB1+ pixels localization, especially by designing more precise quantification methods that overcome the evident bias of

pixel-to-pixel co-localization technique.

## 4.5 Summary and perspectives

- Genetic functionalization of AMB1 strain was successfully achieved, and the produced AMB1 V and AMB1 VRGD magnetosomes present all the required properties: Venus fluorescence, expression of functional RGD peptide when appropriate, and efficient MRI contrasting properties.
- AMB1 VRGD magnetosomes exhibit a specific affinity for U87 tumor cells *in vitro*. The binding observed after 3 h 30 of incubation seems to induce internalization later on. This has been demonstrated *in cellulo* by both immunohistochemical stainings and TEM analysis.
- AMB1 VRGD magnetosomes also present a specific affinity for U87 tumor cells *in vivo* (cells implanted in mouse brain). This was demonstrated by measuring MRI contrast enhancement in the tumor 24 h after magnetosomes injection. This result was cross-validated by histology, which also demonstrated *post mortem* that higher number of magnetosomes was found in the brain tumor of mouse treated with AMB1 VRGD. Furthermore, most functionalized magnetosomes were localized in vessels, which is consistent with their target ( $\alpha_v\beta_3$  integrins) over-expressed in neovessels.
- Finally, the precise localization of magnetosomes was investigated, especially the interactions between magnetosomes and macrophages and microglia. Magnetosomes have been abundantly found in liver macrophages for both AMB1 V and AMB1 VRGD magnetosomes treatments. In brain tumor, magnetosomes have been similarly detected in microglia and vessels for both AMB1 V and AMB1 VRGD injected mice. Though, magnetosomes embodied in immune cells appeared to be more abundant inside vessels with AMB1 V treatment, while isolated magnetosomes were more numerous with AMB1 VRGD ones. This means that AMB1 V magnetosomes are more likely to be cleared out of the tumor by the immune system, while AMB1 VRGD ones are more likely to be taken up by tumor cells. However, the latter result was obtained with a biased quantification method which needs to be upgraded.

## References

- [1] N. Ginet, R. Pardoux, G. Adryanczyk, D. Garcia, C. Brutesco, and D. Pignol. Single-Step Production of a Recyclable Nanobiocatalyst for Organophosphate Pesticides Biodegradation Using Functionalized Bacterial Magnetosomes. *PLoS ONE*, **6**: e21442, 2011. DOI: [10.1371/journal.pone.0021442](https://doi.org/10.1371/journal.pone.0021442) (see pp. 84, 85)
- [2] K. Grünberg, E.-C. Muller, A. Otto, R. Reszka, D. Linder, M. Kube, R. Reinhardt, and D. Schuler. Biochemical and Proteomic Analysis of the Magnetosome Membrane in *Magnetospirillum gryphiswaldense*. *Applied and Environmental Microbiology*, **70**: 1040–1050, 2004. DOI: [10.1128/AEM.70.2.1040-1050.2004](https://doi.org/10.1128/AEM.70.2.1040-1050.2004) (see p. 84)
- [3] F. Danhier, A. Le Breton, and V. Pr at. RGD-Based Strategies To Target Alpha(v) Beta(3) Integrin in Cancer Therapy and Diagnosis. *Molecular Pharmaceutics*, **9**: 2961–2973, 2012. DOI: [10.1021/mp3002733](https://doi.org/10.1021/mp3002733) (see pp. 84, 92)
- [4] F. Zhang, X. Huang, L. Zhu, N. Guo, G. Niu, M. Swierczewska, S. Lee, H. Xu, A. Y. Wang, K. A. Mohamedali, M. G. Rosenblum, G. Lu, and X. Chen. Noninvasive monitoring of orthotopic glioblastoma therapy response using RGD-conjugated iron oxide nanoparticles. *Biomaterials*, **33**: 5414–5422, 2012. DOI: [10.1016/j.biomaterials.2012.04.032](https://doi.org/10.1016/j.biomaterials.2012.04.032) (see p. 84)
- [5] P. C. Brooks, R. A. Clark, and D. A. Cheres. Requirement of vascular integrin alpha v beta 3 for angiogenesis. *Science*, **264**: 569–571, 1994. DOI: [10.1126/science.7512751](https://doi.org/10.1126/science.7512751) (see p. 88)
- [6] P. T. Caswell and J. C. Norman. Integrin Trafficking and the Control of Cell Migration: Integrin Trafficking and Cell Migration. *Traffic*, **7**: 14–21, 2006. DOI: [10.1111/j.1600-0854.2005.00362.x](https://doi.org/10.1111/j.1600-0854.2005.00362.x) (see p. 88)
- [7] S. Hak, J. Cebulla, E. M. Huuse, C. de L. Davies, W. J. M. Mulder, H. B. W. Larsson, and O. Haraldseth. Periodicity in tumor vasculature targeting kinetics of ligand-functionalized nanoparticles studied by dynamic contrast enhanced magnetic resonance imaging and intravital microscopy. *Angiogenesis*, **17**: 93–107, 2014. DOI: [10.1007/s10456-013-9380-7](https://doi.org/10.1007/s10456-013-9380-7) (see p. 90)
- [8] D. Moncelet, V. Bouchaud, P. Mellet, E. Ribot, S. Miraux, J.-M. Franconi, and P. Voisin. Cellular Density Effect on RGD Ligand Internalization in Glioblastoma for MRI Application. *PLoS ONE*, **8**: e82777, 2013. DOI: [10.1371/journal.pone.0082777](https://doi.org/10.1371/journal.pone.0082777) (see p. 90)
- [9] M. Zanoni, F. Piccinini, C. Arienti, A. Zamagni, S. Santi, R. Polico, A. Bevilacqua, and A. Tesi. 3D tumor spheroid models for in vitro therapeutic screening: a systematic approach to enhance the biological relevance of data obtained. *Scientific Reports*, **6**: 19103, 2016. DOI: [10.1038/srep19103](https://doi.org/10.1038/srep19103) (see p. 91)
- [10] P.C. Brooks. Role of Integrins in Angiogenesis. *European Journal of Cancer*, **32**: 2423–2429, 1996. (see p. 92)
- [11] S. Ramanujan, A. Pluen, T. D. McKee, E. B. Brown, Y. Boucher, and R. K. Jain. Diffusion and convection in collagen gels: implications for transport in the tumor interstitium. *Biophysical journal*, **83**: 1650–1660, 2002. (see p. 92)
- [12] M. P. Carvalho, E. C. Costa, S. P. Miguel, and I. J. Correia. Tumor spheroid assembly on hyaluronic acid-based structures: A review. *Carbohydrate Polymers*, **150**: 139–148, 2016. DOI: [10.1016/j.carbpol.2016.05.005](https://doi.org/10.1016/j.carbpol.2016.05.005) (see p. 94)

- [13] R. Weissleder, D. Stark, B. Engelstad, B. Bacon, C. Compton, D. White, P. Jacobs, and J. Lewis. Superparamagnetic iron oxide: pharmacokinetics and toxicity. *American Journal of Roentgenology*, **152**: 167–173, 1989. DOI: [10.2214/ajr.152.1.167](https://doi.org/10.2214/ajr.152.1.167) (see p. 103)
- [14] C. Corot, P. Robert, J. Idee, and M. Port. Recent advances in iron oxide nanocrystal technology for medical imaging. *Advanced Drug Delivery Reviews*, **58**: 1471–1504, 2006. DOI: [10.1016/j.addr.2006.09.013](https://doi.org/10.1016/j.addr.2006.09.013) (see p. 103)
- [15] M. Longmire, P. L. Choyke, and H. Kobayashi. Clearance Properties of Nano-sized Particles and Molecules as Imaging Agents: Considerations and Caveats. *Nanomedicine (London, England)*, **3**: 703–717, 2008. DOI: [10.2217/17435889.3.5.703](https://doi.org/10.2217/17435889.3.5.703) (see p. 103)
- [16] J. Sun, T. Tang, J. Duan, P.-X. Xu, Z. Wang, Y. Zhang, L. Wu, and Y. Li. Biocompatibility of bacterial magnetosomes: Acute toxicity, immunotoxicity and cytotoxicity. *Nanotoxicology*, **4**: 271–283, 2010. DOI: [10.3109/17435391003690531](https://doi.org/10.3109/17435391003690531) (see pp. 103, 104)
- [17] Y. Wang, B. Wang, M.-T. Zhu, M. Li, H.-J. Wang, M. Wang, H. Ouyang, Z.-F. Chai, W.-Y. Feng, and Y.-L. Zhao. Microglial activation, recruitment and phagocytosis as linked phenomena in ferric oxide nanoparticle exposure. *Toxicology Letters*, **205**: 26–37, 2011. DOI: [10.1016/j.toxlet.2011.05.001](https://doi.org/10.1016/j.toxlet.2011.05.001) (see p. 104)
- [18] K. Ohsawa, Y. Imai, Y. Sasaki, and S. Kohsaka. Microglia/macrophage-specific protein Iba1 binds to fimbrin and enhances its actin-bundling activity. *Journal of Neurochemistry*, **88**: 844–856, 2004. DOI: [10.1046/j.1471-4159.2003.02213.x](https://doi.org/10.1046/j.1471-4159.2003.02213.x) (see p. 105)



# Multi-injections protocol to enhance iron uptake in U87 tumor

## Contents

---

<b>5.1</b>	<b><i>In vitro</i> enhancement of magnetosomes uptake by U87 tumor cells . . . . .</b>	<b>112</b>
5.1.1	<i>In vitro</i> kinetics of RGD magnetosomes uptake . . . . .	113
5.1.2	Dose effect on <i>in vitro</i> RGD magnetosomes uptake . . . . .	115
<b>5.2</b>	<b><i>In vivo</i> comparative study of tumor iron uptake for single versus multiple in-</b>	
	<b>jections of magnetosomes . . . . .</b>	<b>118</b>
5.2.1	Two injections of half dose . . . . .	118
5.2.2	Toward the injection of smaller doses? . . . . .	120
<b>5.3</b>	<b>Summary . . . . .</b>	<b>122</b>
	<b>References . . . . .</b>	<b>123</b>

---

The most common administration route of contrast agents used for MRI acquisitions is the intravenous injection, often a bolus and more rarely an infusion, the imaging session being performed between minutes and days post administration given the application<sup>1</sup>. This question of adapting the administration route and the imaging timing becomes even more important in molecular imaging, which aims at imaging a contrast agent in interaction with a biological target. Indeed, it is essential to select an administration route that enables the contrast agent reaching its target, and to acquire MR images when specific interactions have occurred and the non-bonded contrast agents have been cleared out. This issue has been partly tackled in the previous chapter, when comparing the two *in vivo* experiments that consecutively demonstrate that magnetosomes were efficiently circulating in brain tumor vessels (where their target, the  $\alpha_v\beta_3$  integrins, is located) at least during the first two hours post injection, and that 24 h post injection, their clearance from blood circulation was sufficient to exhibit a difference between the RGD functionalized magnetosomes and the control ones.

This chapter investigates a new path to increase magnetosomes load inside brain tumor, focusing on new administration technique for RGD magnetosomes only. Given the latter observation, the idea of performing multiple injections at different time points emerges. This could considerably lengthen the time during which RGD magnetosomes are circulating in the blood stream, and thus are likely to meet  $\alpha_v\beta_3$  integrins, hypothesizing that the clearance always occurs at the same time post injection. Furthermore, previous experiments already demonstrated that the dose of  $200 \mu\text{mol}_{[Fe]}/\text{kg}_{BW}$  was probably in excess since it led to a huge contrast enhancement in the tumor immediately post injection. Diminishing this dose for one barely detectable shortly after injection, but which increases the contrast in brain tumor with time because of RGD magnetosomes accumulation, could also be a very interesting approach, especially regarding toxicity issues in other organs than the brain.

Finally, an optimized delivery of RGD magnetosomes to brain tumor could be used to enhance the efficiency of magnetic hyperthermia treatment, and therefore confer theranostic properties to RGD magnetosomes. Indeed, it has been previously demonstrated that AMB1 magnetosomes present very interesting properties for magnetic hyperthermia, when injected directly into the subcutaneous tumor<sup>2</sup>.

In this chapter are firstly detailed the *in vitro* experiments demonstrating that RGD magnetosomes accumulate in U87 cells over days, justifying the idea of repeated injections *in vivo*. Finally, a comparative study between two injections of a half dose of RGD magnetosomes, versus one single injection of the whole dose, is performed *in vivo* on our U87 mouse model.

## 5.1 *In vitro* enhancement of magnetosomes uptake by U87 tumor cells

The hypothesis that multiple injections of smaller doses might enhance the magnetosomes uptake by cells over-expressing  $\alpha_v\beta_3$  integrins has been tested *in vitro* on U87 cells. Since no clearance occurs *in vitro*, the idea was to firstly investigate if tumor cells can internalize more and more RGD magnetosomes throughout time, and in a second step, if the accumulation of RGD magnetosomes inside U87 cells is increasing with the dose.

---

<sup>1</sup>C. Corot et al., *Advanced Drug Delivery Reviews*, **58**: 1471–1504, 2006.

<sup>2</sup>E. Alphandéry et al., *ACS Nano*, **5**: 6279–6296, 2011.

### 5.1.1 *In vitro* kinetics of RGD magnetosomes uptake

It was previously shown in Section 4.2 that U87 cells were able to specifically interact with RGD magnetosomes after 3 h 30 of incubation, which led to magnetosomes internalization at 24 h. The following questions still remain to be tackled: do internalized magnetosomes stay inside cell cytosol, or can they be thrown out of tumor cells long time after binding? and if magnetosomes stay inside cells, how long can tumor cells internalize RGD magnetosomes, considering that the incubation dose is surely in large excess?

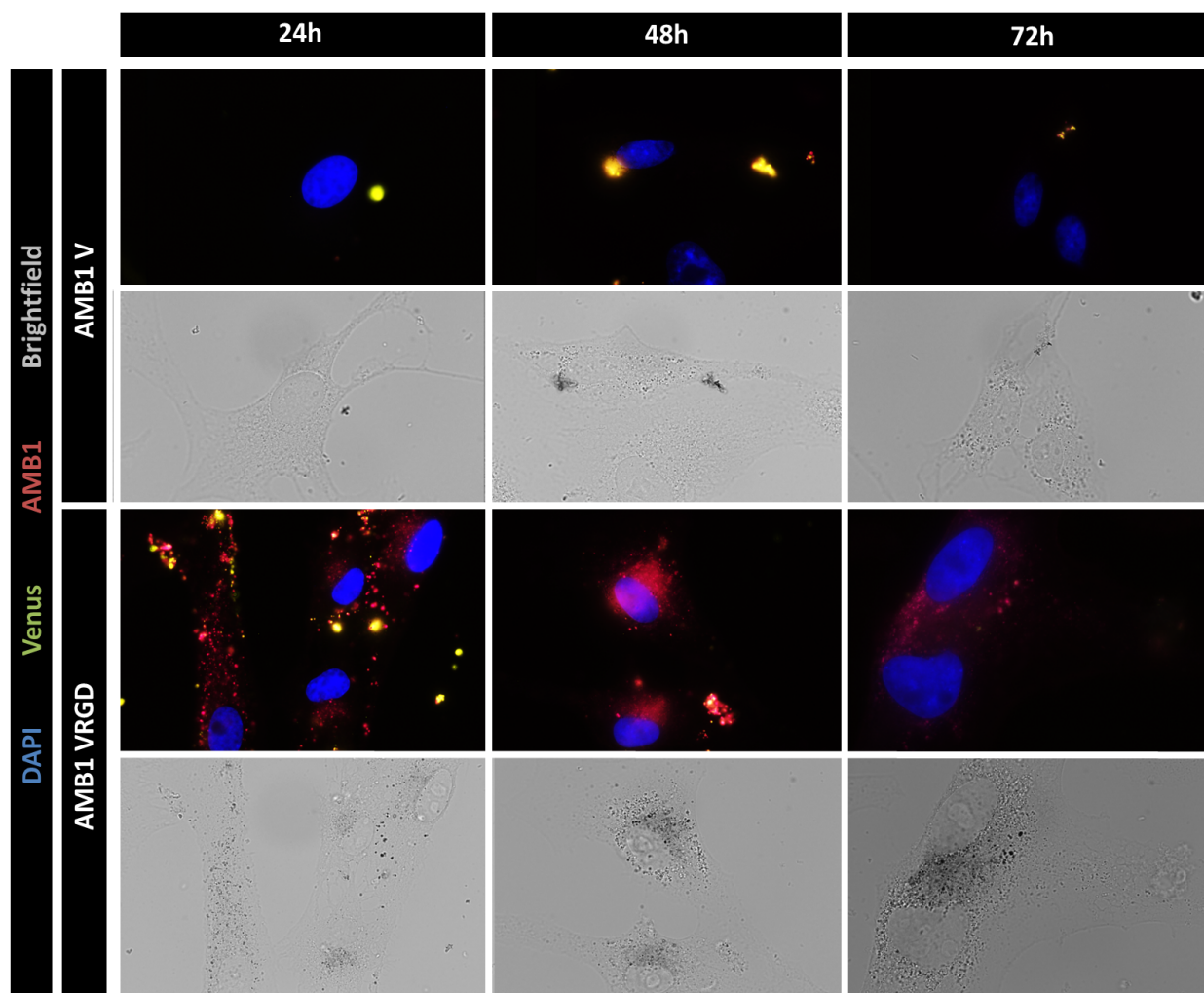


Fig. 5.1 – *In vitro* kinetics of RGD or control magnetosomes uptake by U87 cells followed by fluorescence microscopy. Cells nuclei are stained with DAPI revealed in blue, Venus fluorescence at magnetosomes membrane is seen in green, AMB1 magnetosome membranes are stained with an anti-AMB1 antibody revealed in red, and iron aggregates are seen as dark spots in brightfield images.

**Protocol** To investigate these questions, a specific protocol was designed, inspired from the one demonstrating magnetosomes internalization after 24 h of incubation (see Subsection 4.2.3).

U87 cells were incubated with AMB1 VRGD or AMB1 V magnetosomes at 250  $\mu\text{g}/\text{L}$  during 24 h, 48 h or 72 h on glass bottom plates. A first set of immunohistochemical stainings was

performed. No distinction between magnetosomes inside or outside cells was taken into account: the whole population of magnetosomes was stained post U87 cells membrane permeabilization with an anti-AMB1 antibody revealed in red. Venus fluorescence was detected in green and as usual, cell nuclei were stained with DAPI revealed in blue and magnetite core of magnetosomes was detected on brightfield images. A second set of stainings was performed on other glass plates, to specifically reveal the presence of iron ions (see details of Perl's blue staining in Appendix A.5).

**Results** Fluorescence microscopy images are presented in Figure 5.1. The first observation is that Venus fluorescence seems less intense with time in both AMB1 V and AMB1 VRGD treatments, whereas the anti-AMB1 antibody appears more efficient for detecting long term fate of magnetosomes (up to 48 h). This can actually come from a change in Venus protein conformation that reduces or alters its fluorescence because of the biological environment. Then, the results confirm that AMB1 V magnetosomes only lead to non specific interactions, with no spontaneous endocytosis even at long term. Finally, this study reveals that AMB1+ patterns observed on U87 cells incubated with AMB1 VRGD are very changing with time. The small focused AMB1+ spots seen at 24 h seem more numerous and blurred at 48 h, while at 72 h, AMB1+ fluorescence becomes really blurred and less intense. Moreover, the brightfield images corroborate AMB1+ fluorescence observations at 24 h and 48 h, but seem contradictory at 72 h. Indeed, at 72 h, blurred and low AMB1+ fluorescence is observed whereas numerous diffuse dark areas appear in brightfield. This difference raises the question of magnetosome membrane integrity at this time frame after internalization. Magnetosomes could be stripped of their membranes, which could explain the diminution of AMB1+ fluorescence (the anti-AMB1 antibody specifically stains magnetosome membranes) while the iron-oxide cores stay into the cells.

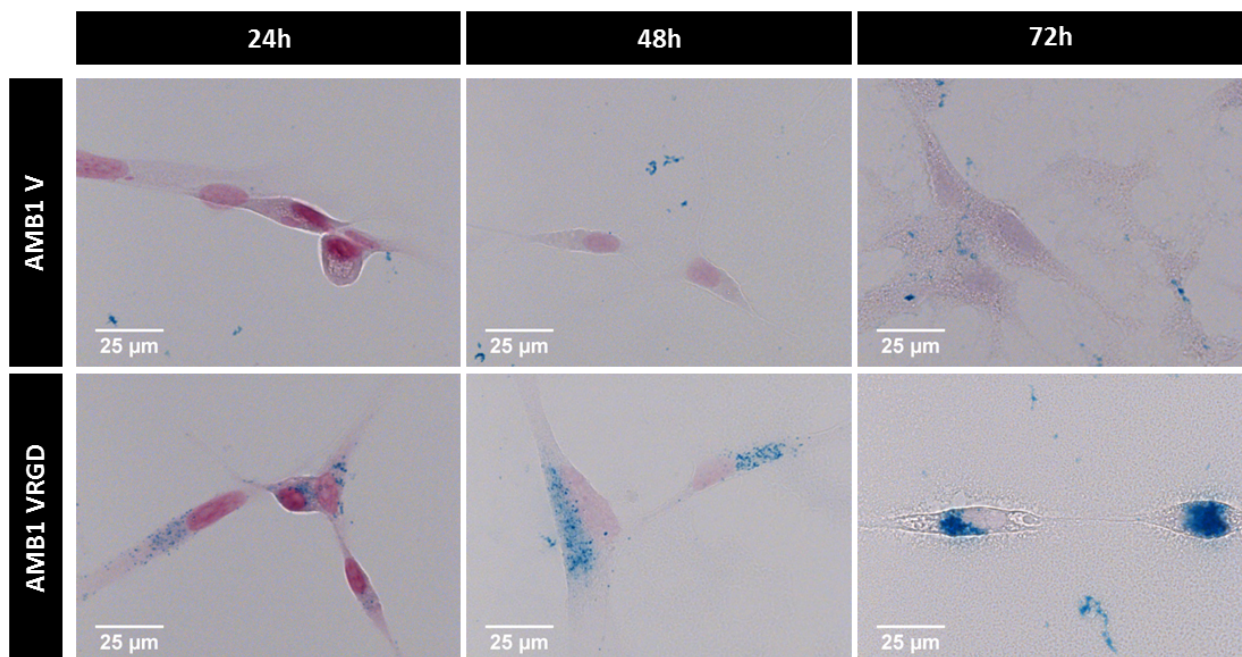


Fig. 5.2 – *In vitro* kinetics of magnetosomes uptake by U87 cells followed by Perl's blue staining. Cell nuclei are revealed in red and iron aggregates in blue.

Perl's blue staining, which reveals iron elements, was then very useful to further investigate the latter observations. Results of this staining obtained in the same experimental conditions are presented in Figure 5.2. U87 cells incubated with AMB1 V during 24 *h* and 48 *h* show no iron signal (blue spots), which is consistent with fluorescence observations. Likewise, cells incubated with AMB1 VRGD exhibit numerous blue spots at 24 *h*, and even more numerous ones at 48 *h*. However, after 72 *h* of incubation, few blue spots could be seen in cells treated with AMB1 V, revealing that some spontaneous endocytosis could indeed happen in the long run. Finally, cells incubated with AMB1 VRGD during 72 *h* show diffuse blue staining in cell cytoplasm, which is in agreement with brightfield observation in Figure 5.1. This iron staining reveals that 72 *h* of incubation allows RGD magnetosomes to bind to U87 cells prior to be internalized, and that this internalization is a dynamic process during which magnetosomes are processed by cells and may be altered. This experiment also demonstrates that Venus fluorescence emitted by magnetosome membrane is efficient on the hour scale, the anti-AMB1 antibody targeting AMB1 magnetosome membranes is efficient on the day scale, whereas only the iron staining seems relevant to later follow magnetosomes core fate inside cells *in vitro*.

In conclusion, this *in vitro* kinetics study of magnetosomes fate during long incubation with U87 cells is in agreement with previous results demonstrating that RGD magnetosomes are internalized after binding<sup>3</sup>, and also validates the hypothesis that a longer contact time between RGD magnetosomes and their target induces higher uptake by U87 cells.

### 5.1.2 Dose effect on *in vitro* RGD magnetosomes uptake

The previous study shows that RGD magnetosomes are internalized into U87 cells, at least until 72 *h*. 48 *h* has been chosen as the optimal time to investigate if a dose-dependent effect is observable *in vitro* with AMB1 VRGD, since at this moment, magnetosomes are presumably still intact inside cell cytosol (iron-oxide core plus membrane). Furthermore, it was interesting to wonder whether the dose of internalized magnetosomes was sufficient to confer magnetic properties to U87 cells and to be detectable by MRI.

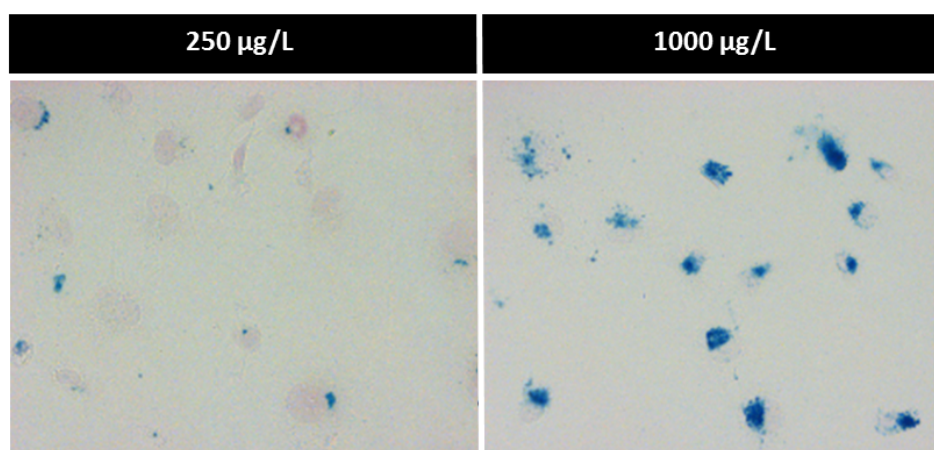


Fig. 5.3 – *In vitro* dose effect on RGD magnetosomes uptake by U87 cells revealed with Perl's blue staining. Two magnetosomes doses are tested (250  $\mu\text{g/L}$  and 1000  $\mu\text{g/L}$ ).

<sup>3</sup>S. Hak et al., *Angiogenesis*, **17**: 93–107, 2014.

**Protocol** U87 cells were incubated with AMB1 VRGD at 250  $\mu\text{g}/\text{L}$  or 1000  $\mu\text{g}/\text{L}$  during 48 h. The same experiment was performed in parallel in glass bottom plates for microscopy imaging and in culture flasks for MRI.

**Microscopy imaging** Perl’s blue staining was done to reveal iron atoms, following the protocol detailed in Appendix A.5.

**MRI quantification** Unlike the preparation for microscopy imaging, U87 cells were trypsinized from culture flasks and separated from supernatant by centrifugation. The number of U87 cells in each pellet was estimated with a Thoma cell counting chamber (Dominique Dutscher, France) and  $10 \cdot 10^6$  cells/mL suspensions were prepared. Magnetic properties of U87 cells suspension were assessed by approaching a magnet next to the Eppendorf tube during 5 min. Cells samples were prepared for MRI quantification, in order to compare incubation conditions. U87 cells, initially concentrated at  $10 \cdot 10^6$  cells/mL, were diluted 1:1 with a warm solution of 0.6% agar w/w. Tubes containing cells in agar were scanned with the same sequence used for relaxivity measurement at 11.7 T (details in Appendix A.1), in order to measure the  $T_2$  values for each incubation condition. Besides, control U87 cells, that underwent the same protocol without magnetosome, were prepared to measure the  $T_2^0$  value of cells in such incubation condition. Because free magnetosomes in agar matrix and magnetosomes internalized in U87 cells are expected to exhibit different transverse relaxivity values, it was then chosen not to compute equivalent iron concentration using  $r_2$  values of AMB1 magnetosomes estimated at 11.7 T, but to study MRI results in terms of signal decrease as follows:

$$\Delta R_2 = \frac{T_2^0 - T_2}{T_2^0 \times T_2} \quad (5.1)$$

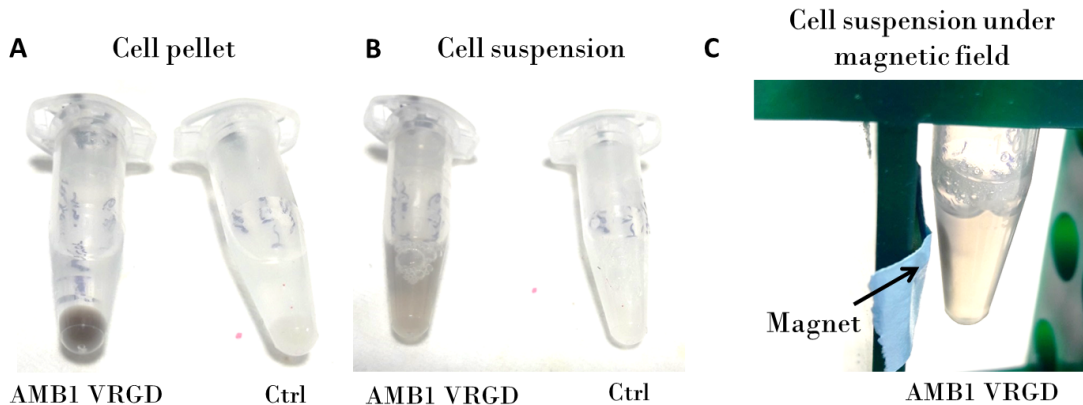


Fig. 5.4 – Visual inspection of different preparations of U87 cells incubated with AMB1 VRGD (1000  $\mu\text{g}/\text{L}$ ) versus control (no magnetosome). The colors of cell pellets (A), cell suspensions (B) and cell suspension under magnetic field (C) can be appreciated.

**Results** Figure 5.3 shows microscopy images acquired after Perl’s blue staining to reveal iron content in U87 cells, which were beforehand incubated with AMB1 VRGD magnetosomes. The images reveal that most cells are loaded with iron in both conditions, but the higher magnetosomes concentration seems to induce the higher cellular iron uptake.

Figure 5.4 presents different Eppendorf tubes containing cells in pellet or in suspension. Both cells pellet and suspension in AMB1 VRGD condition are darker than control ones, confirming that U87 cells have internalized magnetosomes (Figure 5.4 A and B). Indeed, since trypsinization is used to remove cells from flask surface, it may also remove magnetosomes just bounded at U87 cell surface, meaning that cells are harvested with their internalized iron content only. The magnetic properties of AMB1 VRGD treated cells suspension are clearly highlighted by the fact that a magnet is able to attract cells to its side of the Eppendorf tube (Figure 5.4 C).

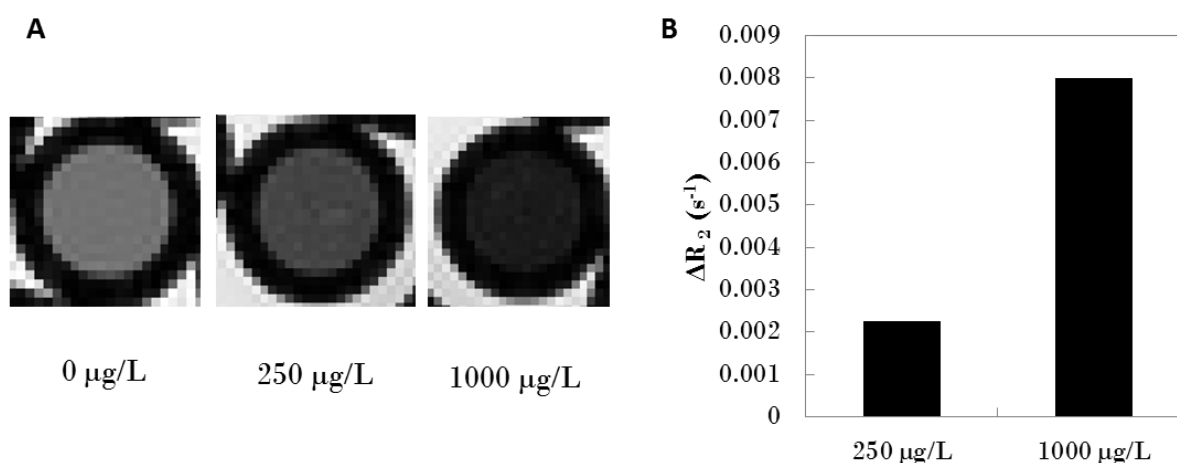


Fig. 5.5 – MRI signal drop observed for different preparations of U87 cells incubated with AMB1 VRGD. Two magnetosomes doses are tested (250  $\mu\text{g}/\text{L}$  and 1000  $\mu\text{g}/\text{L}$ ). A/  $T_2$ -weighted images of cells incubated with the two doses of magnetosomes or without magnetosome as control. B/ Loss of MRI signal for cells incubated with magnetosomes, normalized by the signal of control cells.

MRI analysis of cellular iron uptake is presented in Figure 5.5.  $T_2$ -weighted images clearly evidence a MRI signal drop induced by iron content of U87 cells incubated with magnetosomes compared to control cells (Figure 5.5 A). As expected from cells observation with microscopy imaging (Figure 5.3), the highest dose of magnetosomes induces the most important MRI signal loss. The analysis of relative MRI signal loss, presented in Figure 5.5 B, shows that the iron uptake generates a contrast enhancement 3.5 times higher when cells were incubated during 48 h with the 1000  $\mu\text{g}_{\text{Fe}}/\text{L}$  dose of magnetosomes, compared with a 4 times smaller dose (250  $\mu\text{g}_{\text{Fe}}/\text{L}$ ).

In conclusion, the iron uptake by U87 cells after AMB1 VRGD incubation is sufficient to confer magnetic properties to cells, as well as to detect them easily with MRI acquisitions at 11.7 T compared to non treated cells. Furthermore, a clear dose effect is evidenced when comparing U87 cells incubated with 250  $\mu\text{g}_{\text{Fe}}/\text{L}$  and 1000  $\mu\text{g}_{\text{Fe}}/\text{L}$  of magnetosomes.

## 5.2 *In vivo* comparative study of tumor iron uptake for single versus multiple injections of magnetosomes

The previous *in vitro* study shows that U87 cells are capable of incorporating large amount of magnetosomes if sufficient contact time and dose are ensured. *In vivo*, the contact time and the delivered dose are limited by the blood clearance that removes circulating magnetosomes from the blood stream. The idea to overcome this clearance was to perform multiple injections of RGD magnetosomes at smaller dose, hoping to lengthen the contact time. Therefore, a multi-injection protocol was set up to investigate if tumor uptake of AMB1 VRGD magnetosomes could be optimized by changing the administration method.

Two main experimental constraints, the maximum duration during which one animal can be kept under anesthesia and the minimum time between two anesthetics, have to be considered to design an achievable protocol. Besides, as already pointed out by the study on tumor vessels follow-up presented in Subsection 3.4.2, multiple intravenous injections are very challenging to achieve, considering the healing time of the vein. Keeping these constraints in mind, preliminary tests have been carried out, revealing that a protocol with 6 *h* between two anesthetics of about one hour seems to fit the requirements: the mouse wakes up rapidly after both anesthetics and behaves normally. Regarding the multiple injection itself, two injections on the same mouse imply to use its two caudal veins, which is easy to perform and does not require a complete healing of veins between injections. Furthermore, two injections followed by a MRI session at 6 *h* interval is feasible within a day, as well as performing an imaging session 24 *h* after the last injection.

The first subsection shows the results of tumor iron uptake obtained with two injections spaced by 6 *h*, compared with one single injection ( $n = 9$  mices per group). In a second subsection, the difficulties encountered when testing a triple injection protocol on one mouse are discussed.

### 5.2.1 Two injections of half dose

Two injections of half dose have been chosen as the simplest and lightest protocol to investigate the effect on tumor iron uptake of multiple injections of functionalized magnetosomes.

**Protocol** The protocol was directly derived from the one presented in Subsection 4.3.2: it was based on the acquisition of MGE images, to compute  $T_2^*$  parametric maps and thus measure the contrast enhancement in brain tumor at different time points after magnetosomes injection. One experiment started with the acquisition of a RARE image for tumor volume monitoring, a FLASH image for visualizing  $T_2^*$  contrast changes and MGE images to quantify the baseline contrast on computed  $T_2$  parametric map. Then, magnetosomes injection ( $200 \mu\text{mol}_{[Fe]}/\text{kg}_{BW}$  for the single injection as control and  $100 \mu\text{mol}_{[Fe]}/\text{kg}_{BW}$  for the first half dose injection) was performed, followed by the acquisition of one series of MGE images and one FLASH image post injection. Animal was woken up after the last image acquisition. For the double injection protocol, a similar imaging and injection session was repeated 6 *h* after the first half dose injection. Finally, a new imaging session was scheduled 24 *h* post injection of the whole dose ( $200 \mu\text{mol}_{[Fe]}/\text{kg}_{BW}$ ), consisting of the acquisition of one RARE image, one FLASH image and one series of MGE images. The timeline of these two protocols is plotted in Figure 5.6. A total of  $n = 9$  mice received a single injection, and  $n = 9$  mice a double injection of AMB1 VRGD.

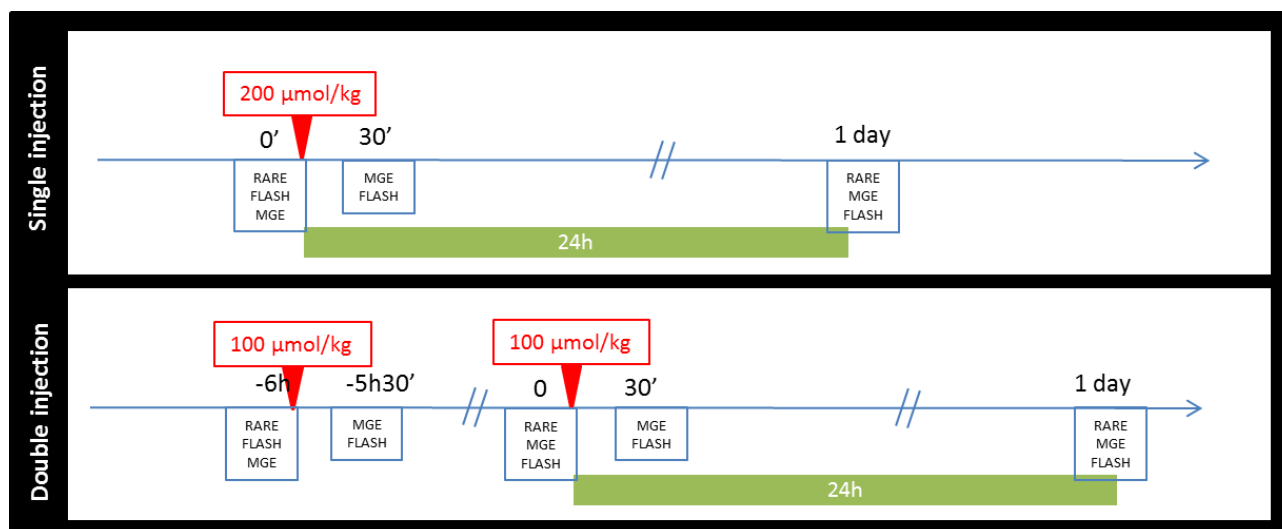


Fig. 5.6 – Timeline of the single and double injection protocols.

The mice were included in the study when their tumor size (defined by the maximum axial diameter) was estimated between 2 and 3 *mm*. This criteria was less strict than the one used for the *in vivo* affinity study presented in Section 4.3, but it allowed to free some scanning time dedicated to tumor monitoring for MRI sessions on injected mice, these experiments being very time consuming.

**Results** Examples of FLASH images acquired on two animals treated either with a single or a double injection of AMB1 VRGD are presented in Figure 5.7 A. These FLASH images show that the first injected half dose still leads to numerous hypo-intense voxels appearing in the mouse brain tumor, meaning that this dose is still high enough to induce a detectable contrast enhancement in the tumor. 30 *min* after the second half dose injection of magnetosomes, a very important number of hypo-intense voxels arises in the tumor, apparently more than after one single injection.

Quantitative measures of MRI signal loss in the tumor for the two injection methods are presented in Figure 5.7 B. The black curve shows the tumor contrast evolution for a single injection of  $200 \mu\text{mol}_{[Fe]}/\text{kg}_{BW}$ : this evolution is in agreement with the results from Section 4.3.2 demonstrating that a single injection of magnetosomes leads to a significant contrast enhancement in the tumor which seems to maintain until 24 *h*. Moreover, a faster clearance is observed in the tumor for this study compared to the previous one (see Figure 4.13), probably because mice with smaller tumors were included. Smaller tumors may express a lower level of  $\alpha_v\beta_3$  integrins (few neoangiogenic vessels), which may induce a weaker RGD magnetosomes uptake. The red curve shows the tumor contrast evolution for a double injection of  $100 \mu\text{mol}_{[Fe]}/\text{kg}_{BW}$ . The first injection of half dose produces around the half of tumor iron uptake obtained with the whole dose (red square at  $-5 \text{ h } 30$  versus black circle at  $0 \text{ h } 30$ ), but interestingly, the second half dose induces a higher uptake compared to whole dose (red square at  $0 \text{ h } 30$  versus black circle at  $0 \text{ h } 30$ ). At 24 *h*, both groups of mice have received the same dose of  $200 \mu\text{mol}_{[Fe]}/\text{kg}_{BW}$ , but the difference of tumor iron uptake observed 30 *min* post last injection seems to maintain.

The inclusion of mice with dispersed tumor sizes in this study might also explain the very large standard deviation found on iron uptake measurements. The conclusion of this study is then conditional to the fact that the mean certainly exhibits differences between the two

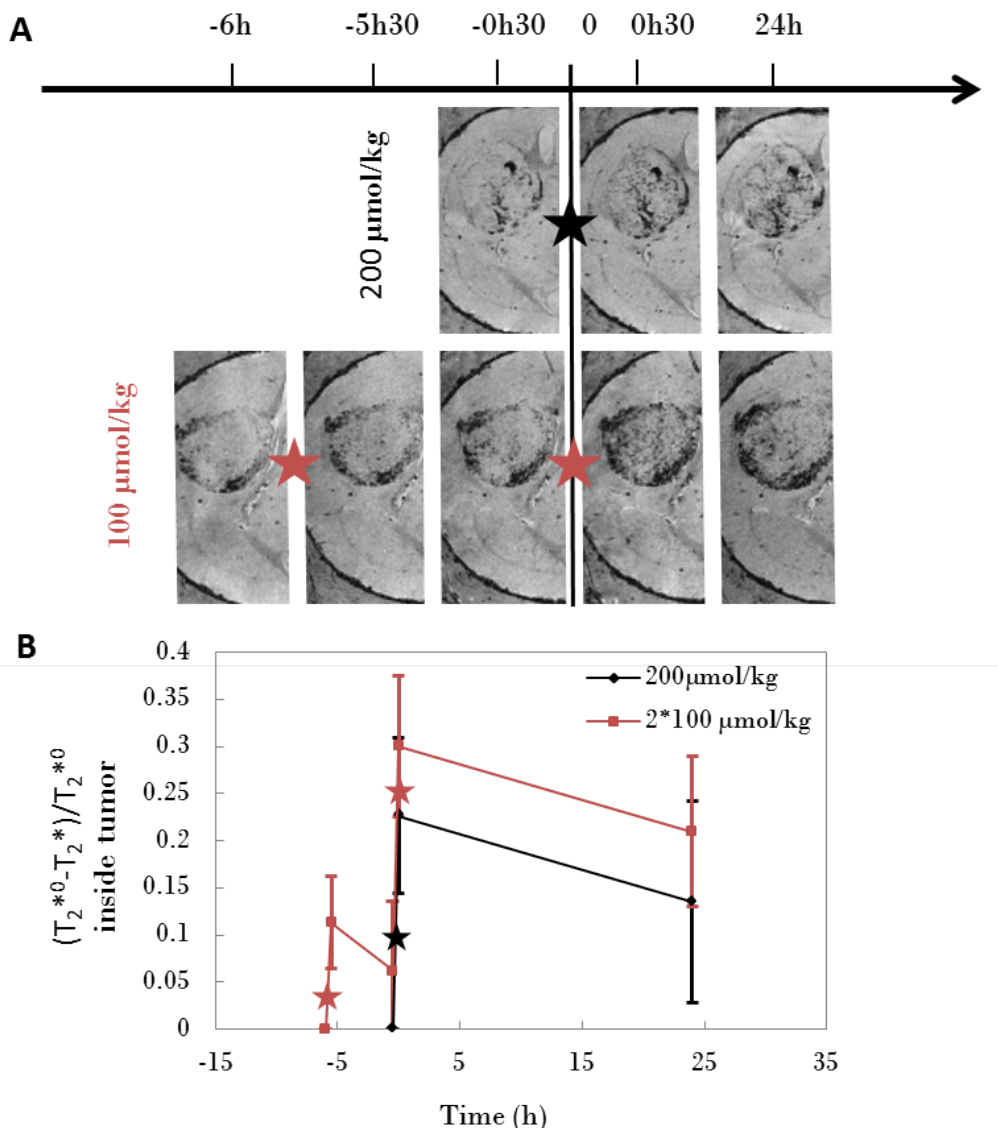


Fig. 5.7 – FLASH images (A) and estimation of tumor iron uptake (B) obtained after one single injection of  $200 \mu\text{mol}_{[Fe]}/\text{kg}_{BW}$  of RGD magnetosomes (black star) versus two injections of  $100 \mu\text{mol}_{[Fe]}/\text{kg}_{BW}$  (red stars).

injection protocols, but not significant because of interindividual variability. The results show a trend whereby multi-injections of functionalized magnetosomes lead to a cumulative iron uptake in tumor. This is in agreement with *in vitro* results that confirm the interest of maximizing the functionalized probe access to its target, in order to foster interactions and thus increase the magnetosomes accumulation in targeted zone.

### 5.2.2 Toward the injection of smaller doses?

The latter results pave the way for splitting the functionalized contrast agent administration in several injections. Therefore, a preliminary experiment has been run on one U87 mouse to test a triple injection of  $66 \mu\text{mol}_{[Fe]}/\text{kg}_{BW}$  dose of RGD magnetosomes. One difficulty arose from the impossibility to derive the protocol directly from the double injection one, since three injections spaced by 6 h would have led to 18 h of experiment, which does not fit in a single

day. It was then chosen to keep a delay of 6 h between the two first injections, and to skip to 18 h between the second and the third, as described by the timeline in Figure 5.8.

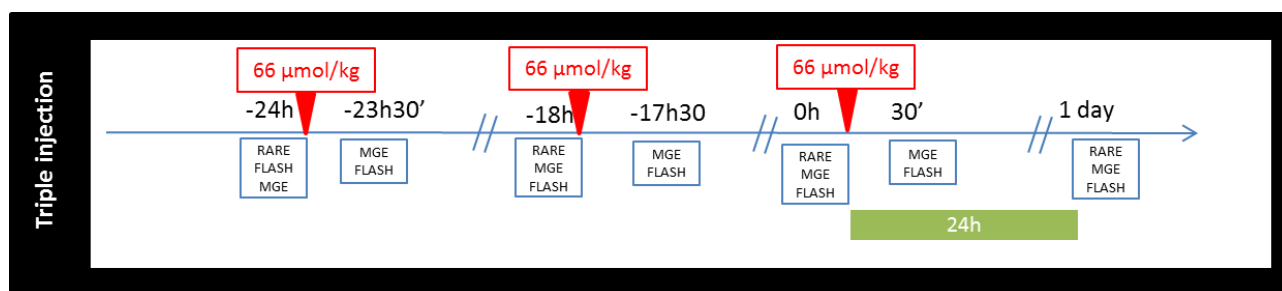


Fig. 5.8 – Timeline of the triple injection protocol.

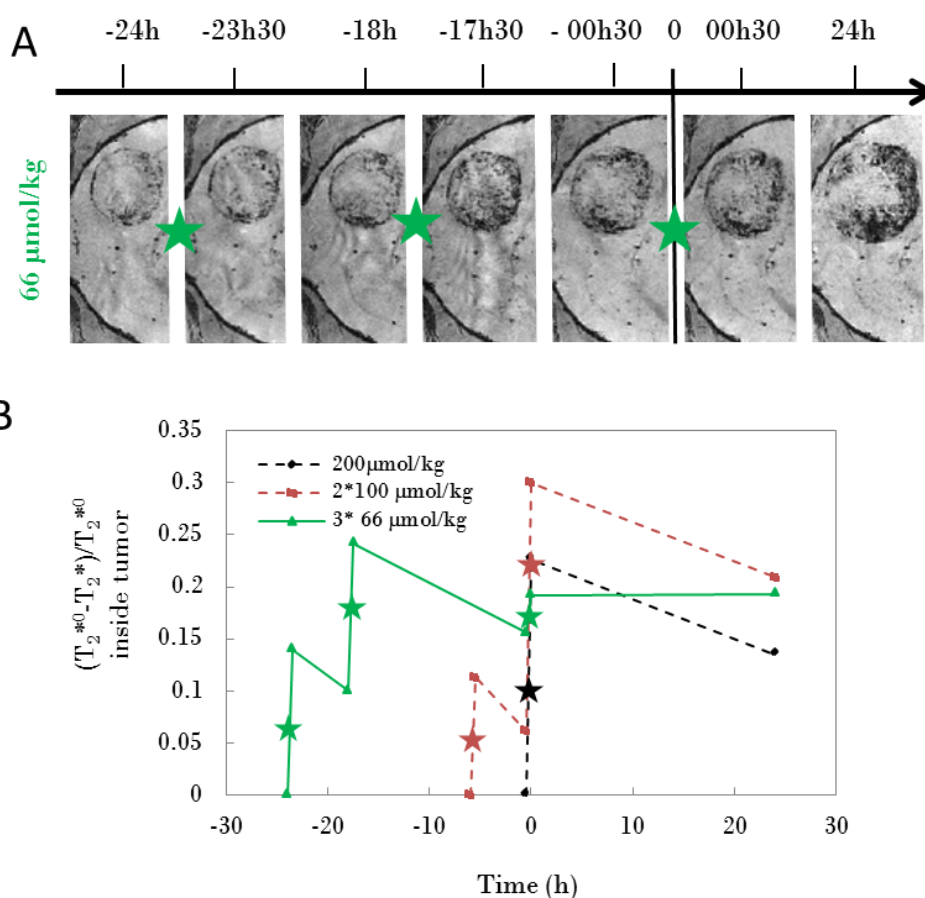


Fig. 5.9 – FLASH images (A) and estimation of tumor iron uptake (B) obtained after three injections of  $66 \mu\text{mol}_{[Fe]}/\text{kg}_{BW}$  of RGD magnetosomes (green stars). The contrast enhancements estimated in tumor after single and double injections are also plotted in dashed lines for comparison.

**Results** FLASH images acquired on the U87 mouse treated with three injections of AMB1 VRGD are presented in Figure 5.9 A. These FLASH images show that the first injection of a third of the whole dose already leads to an increase in the number of hypo-intense voxels appearing in the mouse brain tumor. The second injection increases this effect as already observed with the double injection protocol. The third injection also induces the emergence of

additional hypo-intense voxels in the tumor, but in smaller proportion than for the two previous ones. Finally, 24 *h* after the whole dose of  $200 \mu\text{mol}_{[\text{Fe}]} / \text{kg}_{\text{BW}}$  has been injected, a vast extend of tumor area still appears dark, especially the tumor periphery.

Despite having only one animal scanned for this study, the normalized decrease of  $T_2^*$  has been computed in the tumor zone, to compare its evolution with the previous multi-injections results. Results are presented in Figure 5.9 B. The first and second injections seem equivalent to the two injections performed for the double injection protocol. However, the third injection does not induce any additional contrast enhancement in the tumor. When looking at the FLASH images in Figure 5.9 A, it is obvious that the tumor has significantly grew throughout this experiment, which lasted two days between the first injection of contrast agent and the last imaging session. Indeed, the tumor volume growth, between the first and the last FLASH images, is estimated to 50% for this experiment while it is around 23% for the single and double injection protocols. The contact time between the RGD functionalized magnetosomes and the targeted  $\alpha_\nu\beta_3$  integrins is probably lengthened using this triple injection protocol, but the tumor growth may induce an increase of targets number: thus, the accumulation of magnetosomes is constantly diluted, leading to a constant contrast enhancement observed in the tumor.

Finally, the tested protocols were performed by dividing the same whole dose in several injections (total of  $200 \mu\text{mol}_{[\text{Fe}]} / \text{kg}_{\text{BW}}$ ), but another approach would have been to iterate injections of the same dose (for example  $200 \mu\text{mol}_{[\text{Fe}]} / \text{kg}_{\text{BW}}$ ). In such experiment, an increase of contrast enhancement in the tumor might have occurred with time, in contrast to our triple injection protocol. Nevertheless, this approach was not tested to avoid the issue of injecting significant iron-oxide dose and the associated risk to induce toxicity.

### 5.3 Summary

- *In vitro* studies on U87 cells demonstrated that these tumor cells were able to greatly incorporate RGD magnetosomes with time, and that for a given incubation time, the highest magnetosomes concentration led to the highest cellular uptake. These results confirm that promoting the interactions between U87 cells and RGD magnetosomes maximizes their internalization, such hypothesis still to be tested *in vivo*.
- Tumor iron uptake observed after two injections of  $100 \mu\text{mol}_{[\text{Fe}]} / \text{kg}_{\text{BW}}$  of RGD magnetosomes has been compared with the one after single injection of  $200 \mu\text{mol}_{[\text{Fe}]} / \text{kg}_{\text{BW}}$ . The results tend to favor double injections versus single ones, but a high variability prevented the observation of statistically significant differences. This variability might come from the inclusion of mice bearing tumors with quite different sizes (between 2 and 3 *mm* in maximum axial diameter). Thus, this study might benefit from increasing the number of mice with comparable tumor size to confirm the latter results.

## References

- [1] C. Corot, P. Robert, J. Idee, and M. Port. Recent advances in iron oxide nanocrystal technology for medical imaging. *Advanced Drug Delivery Reviews*, **58**: 1471–1504, 2006. DOI: [10.1016/j.addr.2006.09.013](https://doi.org/10.1016/j.addr.2006.09.013) (see p. 112)
- [2] E. Alphan ery, S. Faure, O. Seksek, F. Guyot, and I. Chebbi. Chains of Magnetosomes Extracted from AMB-1 Magnetotactic Bacteria for Application in Alternative Magnetic Field Cancer Therapy. *ACS Nano*, **5**: 6279–6296, 2011. DOI: [10.1021/nn201290k](https://doi.org/10.1021/nn201290k) (see p. 112)
- [3] S. Hak, J. Cebulla, E. M. Huuse, C. de L. Davies, W. J. M. Mulder, H. B. W. Larsson, and O. Haraldseth. Periodicity in tumor vasculature targeting kinetics of ligand-functionalized nanoparticles studied by dynamic contrast enhanced magnetic resonance imaging and intravital microscopy. *Angiogenesis*, **17**: 93–107, 2014. DOI: [10.1007/s10456-013-9380-7](https://doi.org/10.1007/s10456-013-9380-7) (see p. 115)



# Conclusion and perspectives

Nanoparticles present numerous features of interest for biomedical applications. In particular, iron-oxide nanoparticles are gifted with specific magnetic properties which can be useful for both diagnosis and therapy. Indeed, their magnetic properties lead to very high contrast enhancement in MRI, but also to the possibility to locally deliver thermal energy for tumor treatment. In the context of the MEFISTO project, a new kind of iron-oxide nanoparticles, entirely produced by magnetotactic bacteria, has been investigated throughout this PhD thesis. Magnetosomes, consisting of an iron-oxide core surrounded by a bilipid membrane, represent a fully integrated biogenic approach for producing MR molecular imaging probes.

## **Magnetosomes as MRI contrast agent**

It has been firstly demonstrated, by measuring *in vitro* relaxivities, that magnetosomes were awarded with very high MRI contrasting properties. This *in vitro* measurement allows to characterize the maximum potential of one contrast agent to induce MRI contrast enhancement. Nevertheless, relaxivity alone is not sufficient to predict with precision *in vivo* contrast enhancement efficiency.

The ability of magnetosomes to flow in the blood stream and thus to induce contrast enhancement between brain parenchyma and blood vessels, *i.e.* to act as blood pool agent, has been investigated to supplement the relaxivity measurements with an *in vivo* characterization of contrasting properties. This method presents the advantage to embody the contrast enhancement induced by magnetosomes circulating in the blood stream, thus taking into account the interaction between magnetosome membrane and the biological environment. Furthermore, the 3D angiogram of mouse brain built from such *in vivo* MRI acquisitions enables to clearly visualize how the contrast agent is perfusing the brain. These *in vitro* and *in vivo* characterizations of contrast agent are not exhaustive yet, and it is very important to study the contrast agent efficiency regarding its final diagnostic or/and therapeutic application.

## **Functionalized magnetosomes for brain tumor molecular imaging**

Wild type magnetotactic bacteria have been genetically modified to produce magnetosomes harboring a peptide of interest at their membrane, leading to a functionalized MRI contrast agent. A mouse model of U87 human glioblastoma has been chosen to obtain the first proof of concept of using these genetically functionalized magnetosomes for molecular imaging. The RGD peptide, fused with a Venus fluorophore, has been chosen to decorate magnetosomes membrane and induce specific affinity for  $\alpha_v\beta_3$  integrins over-expressed by tumor cells. These

RGD functionalized magnetosomes have been studied *in vitro* to assess their affinity for U87 tumor cell line. Furthermore, effective RGD magnetosomes internalization after binding has also been highlighted *in vitro*.

RGD magnetosomes have then been tested *in vivo*: their specific accumulation in mouse brain tumor, 24 h after intravenous administration, has been found statistically higher than the one obtained with control magnetosomes injection. This result has been obtained by cross-validating MRI acquisitions with histological data. Finally, this *in vivo* study demonstrates that producing a functionalized probe for molecular imaging applications with an integrated biogenic approach is feasible, thereby validating one main deliverable of MEFISTO project.

### Accumulation of functionalized magnetosomes in brain tumor

The administration route of RGD magnetosomes has been questioned to maximize their uptake by brain tumor. Splitting the dose in multiple smaller ones could lengthen the contact time between functionalized magnetosomes and their target, leading to higher magnetosomes accumulation in the tumor. A study comparing double injection of half dose with single injection seems to show that the double injection leads to a higher dose of iron delivered inside tumor. The latter result could be of great interest for coupling RGD functionalized magnetosomes with magnetic hyperthermia treatment of brain tumor in our U87 mouse model.

### Perspectives

Studies actually in progress might help to complement this PhD thesis. Firstly, a toxicity study planned in the MEFISTO project will soon be started to evaluate the acute toxicity of AMB1 VRGD magnetosomes on rodents. It is noteworthy that for all the *in vivo* experiments performed in this thesis, no noticeable abnormalities have been observed on mice up to 3 days after the administration of functionalized magnetosomes. Secondly, a scale up of magnetosomes production is actually ongoing to insure magnetosomes production up to clinical dose of contrast agent, which is up to now very challenging with the bio-reactors used in MEFISTO project (A. Fernández-Castané, University of Birmingham, UK)<sup>1</sup>.

Magnetosomes extracted from magnetotactic bacteria embody an innovative approach for MRI contrast agent design. This PhD work has thus paved the way for future studies combining functionalization with iron-oxide core engineering for molecular imaging applications. For example, the magnetosomes core, which size, shape and chemical composition can vary between magnetotactic bacteria strains, constitutes a very interesting element to investigate for enhancing contrast agent sensitivity, and working on more affine peptides to decorate magnetosomes membrane may improve contrast agent specificity. As an example, it could be possible to change the RGD for more complex structures, like transmembrane receptors or like nanobodies<sup>2</sup> for example. Furthermore, the precise evaluation of the number of RGD per magnetosomes is still in progress and the first estimation is around 50 RGD per magnetosomes (experiment carried out by the LBC, using an enzyme to cut VenusRGD protein from MamC and dosage of the fluorescence). It could be very important to study the optimum number of functionalization per magnetosomes, and also the optimum distance between the iron core and the targeting part.

---

<sup>1</sup>A. Fernandez-Castane et al., MagnetoTactic Bacteria, Oral, Marseille –France, 2016.

<sup>2</sup>A. Pollithy et al., Applied and Environmental Microbiology, **77**: 6165–6171, 2011.

A clinical trial is currently run by the society MagForce (Germany) which aim at demonstrating the performance of intra-tumor injection of IONP (chemically produced) followed magnetic hyperthermia to treat brain tumor<sup>3</sup>. Magnetosomes are expected to be excellent for this purpose<sup>4</sup> (because of their increased coercivity) and might improve this therapy efficacy<sup>5</sup>. Finally, recent study demonstrated that it was possible to achieve significant temperature enhancement in the tumor after intravenous injection by taking advantage of the EPR effect<sup>6</sup> (and by insuring a low temperature enhancement in muscle as control). This less invasive method is also underlined for leading to more homogeneous heating, the magnetic sources being better spread in the tumor area. Further experiments need thus to be carried out to investigate the feasibility of magnetic hyperthermia treatment of brain tumor after an intravenous injection of functionalized magnetosomes. Besides, investigating new administration techniques (like infusion for example) might also help increase the iron-oxide load in the tumor, thus enhancing magnetic hyperthermia efficiency.

RGD/ $\alpha_v\beta_3$  in U87 model has been chosen to perform the proof of concept of using functionalized magnetosomes for molecular imaging, but it will be necessary to extend this concept to more realistic models that enable to target new biomarkers. To do so, collaborations with research teams specialized in new biomarkers for oncology would be to develop.

Functionalized magnetosomes could also be modified to carry drug to the target site (drug linked to magnetosomes membrane or in inside the vesicle) which could be another theranostic approach than the one with hyperthermia. To go even further, it might also being very interesting to couple magnetic hyperthermia with anti-tumor drug, with the same nano-plateform.

Finally, this PhD work has gathered many experimental and technical developments, starting from MRI relaxivities measurement and *in vitro* probe testing on cell culture, to *in vivo* mouse brain angiography and molecular imaging acquisitions on human glioblastoma model combined with histology validation, which are valuable tools for future molecular imaging studies.

This work has also raise many questions, among the non-exhaustive ones listed here, which hopefully will be tackled in future works.

---

<sup>3</sup>Sabine Müller., *Nanomedicine: Nanotechnology, Biology, and Medicine*, **5**: 387–393, 2009.

<sup>4</sup>R. Hergt et al., *Journal of Magnetism and Magnetic Materials*, **293**: 80–86, 2005.

<sup>5</sup>R. Liu et al., *Progress in Natural Science: Materials International*, **22**: 31–39, 2012.

<sup>6</sup>H.S. Huang et al., *International Journal of Nanomedicine*, **8**: 2521–2532, 2013.

## References

- [1] A. Fernandez-Castane, H. Li, M. Franzreb, O. Thomas, and T. Overton. Bioprocessing magnetotactic bacteria and production of magnetosomes: challenges toward industrial applications. *MagnetoTactic Bacteria*, Oral, Marseille –France, 2016. (see p. 126)
- [2] A. Pollithy, T. Romer, C. Lang, F.D. Muller, J. Helma, H. Leonhardt, U. Rothbauer, and D. Schuler. Magnetosomes expression of functional camelid antibody fragments (nanobodies) in *Magnetospirillum gryphiswaldense*. *Applied and Environmental Microbiology*, **77**: 6165–6171, 2011. DOI: [10.1128/AEM.05282-11](https://doi.org/10.1128/AEM.05282-11) (see p. 126)
- [3] Sabine Müller. Magnetic fluid hyperthermia therapy for malignant brain tumors—an ethical discussion. *Nanomedicine: Nanotechnology, Biology, and Medicine*, **5**: 387–393, 2009. DOI: [10.1016/j.nano.2009.01.011](https://doi.org/10.1016/j.nano.2009.01.011) (see p. 127)
- [4] R. Hergt, R. Hiergeist, M. Zeisberger, D. Schüler, U. Heyen, I. Hilger, and W. A. Kaiser. Magnetic properties of bacterial magnetosomes as potential diagnostic and therapeutic tools. *Journal of Magnetism and Magnetic Materials*, **293**: 80–86, 2005. DOI: [10.1016/j.jmmm.2005.01.047](https://doi.org/10.1016/j.jmmm.2005.01.047) (see p. 127)
- [5] R. Liu, J. Liu, J. Tong, T. Tang, W. Kong, X. Wang, Y. Li, and J. Tang. Heating effect and biocompatibility of bacterial magnetosomes as potential materials used in magnetic fluid hyperthermia. *Progress in Natural Science: Materials International*, **22**: 31–39, 2012. DOI: [10.1016/j.pnsc.2011.12.006](https://doi.org/10.1016/j.pnsc.2011.12.006) (see p. 127)
- [6] H.S. Huang and J.F. Hainfeld. Intravenous magnetic nanoparticle cancer hyperthermia. *International Journal of Nanomedicine*, **8**: 2521–2532, 2013. DOI: [10.2147/IJN.S43770](https://doi.org/10.2147/IJN.S43770) (see p. 127)





# PhD student role in collaboration

This PhD work was highly multidisciplinary and has implied many collaborations: some of them were planned from the beginning in the framework of the MEFISTO project, like with the LBC laboratory, and the LI2D laboratory, and others were set up to bring new insights and expertise, as the one with the CSPBAT laboratory. At NeuroSpin, two members of the MIDAS team (Molecular Imaging and Delivery of Active Substances), Françoise Geffroy and Erwan Selingue, have also contributed to this work.

Here is a list that clearly exhibits the PhD student involvement in all these collaborations and in the performed experiments. The work of LBC laboratory was done under the supervision of Dr. David Pignol and Dr. Nicolas Ginet. The work of LI2D laboratory work was done under the supervision of Dr. Laurent Bellanger. The work of CSPBAT laboratory was done under the supervision of Dr. Laurence Motte. Finally, the work at NeuroSpin was done under the supervision of Dr. Sébastien Mériaux.

## IONP production

- The production and preparation of all magnetosomes used for this PhD work were handled by Sandra Prévéral, Géraldine Adryancyk-Perrier and Michel Péan at the LBC laboratory. The **PhD student** took an active role by giving regular feedbacks on the preparations, in terms of transverse relaxivity and general behavior during *in vivo* experiments, to help improving magnetosomes formulation.
- All NPPEG, NPAC and other IONPs of different sizes (from 2 to 11 *nm*) were synthesized by Sophie Richard and Yoann Lalatonne at the CSPBAT laboratory.

## IONP characterization

- TEM acquisitions to determine magnetosomes size were done by the LBC laboratory.
- All biochemical characterizations of magnetotactic bacteria genetic modification were carried out by the LBC laboratory.
- All magnetic ( $M_S$ , electronic diffraction pattern) and physico-chemical ( $D_h$ , Zeta potential, FTIR) properties of IONPs were characterized by Sophie Richard and Yoann Lalatonne at the CSPBAT. The **PhD student** worked on correlating these parameters with MRI contrasting properties by measuring IONPs relaxivities, prior to discuss the results in comparison with literature.

- All experiments of relaxivity measurements (samples preparation, MRI sequences setting, images acquisition and data post-processing) were performed by the **PhD student**.

### **Antibody against AMB1 magnetosome membrane**

- The specific antibody raised against magnetosomes membrane was produced by the LI2D laboratory.

### **Cell culture and mouse model of glioblastoma**

- The culture of U87 tumor cells was handled by Françoise Geffroy. The **PhD student** helped when needed.
- *In vitro* affinity studies were carried out by Françoise Geffroy. The **PhD student** took part in experiments design and worked on fluorescence images processing to achieve semi-quantitative analyses.
- TEM images of U87 tumor cells samples were acquired by Fabrice Richard (IBDM Institute, Aix-Marseille University, Marseille, France).
- The spheroid culture model was previously developed by Françoise Geffroy, and its use to test magnetosomes affinity has been investigated by the **PhD student** with the help of Françoise Geffroy.
- Induction of U87 mouse model of glioblastoma was carried out by Françoise Geffroy or Erwan Selingue.

### ***In vivo* MRI experiments**

- All *in vivo* MRI experiments were designed by the **PhD student** (mouse model inductions planning, injection protocols and MRI sequences setting).
- All *in vivo* MRI experiments (tumor growth monitoring, brain angiography, molecular imaging study) on the three preclinical scanners were performed by the **PhD student**, with the occasional help of Erwan Selingue (mouse installation in the cradle, intravenous injection of contrast agent).
- Mouse brains were extracted by Françoise Geffroy or Erwan Selingue.
- Immunohistochemical stainings were performed by Françoise Geffroy. The **PhD student** took part in experiments design and worked on fluorescence images processing to achieve semi-quantitative analyses.
- All *in vivo* data post-processings (images reconstruction, brain tumors segmentation, parametric maps and 3D angiograms computation) were carried out by the **PhD student**.





# Appendices



## Protocols for *in vitro* experiments

### A.1 Relaxometry

The measurement of transverse relaxivity  $r_2$  (transverse relaxometry) is performed for each iron-oxide contrast agent tested in this thesis. To compare the obtained results, the experiment is standardized by systematically applying the following protocol. The first step consists in building a phantom containing several tubes filled with different concentrations of the contrast agent, prior to scan it with a parametric sequence dedicated to  $T_2$  measurements (in our case) at the desired magnetic field intensity.

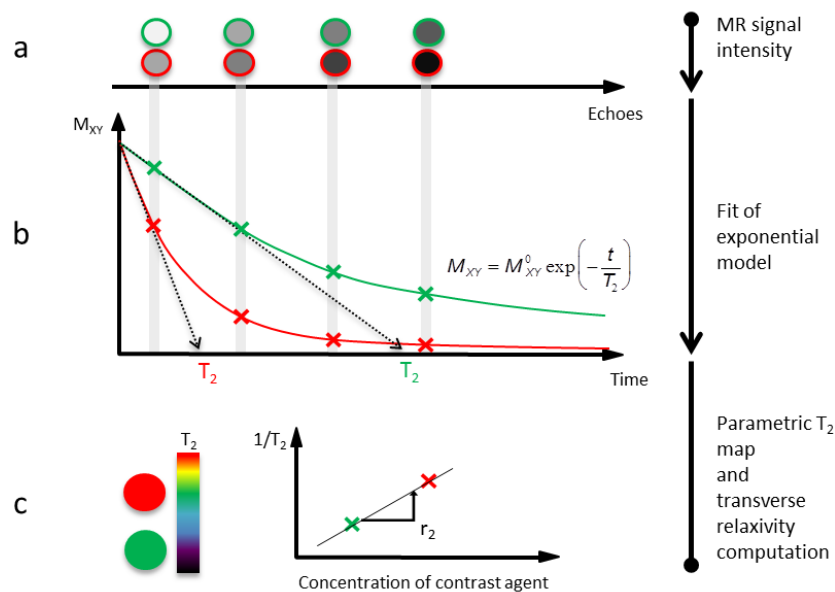


Fig. A.1 – Principle of a transverse relaxometry experiment performed on a phantom containing two tubes filled with a low and a high concentrations of iron-oxide contrast agent. (a) After segmentation and labelization of tubes in the MSME images (here green and red), the MR signal intensity in each tube can be measured along time. (b) Secondly, the measured signal as a function of time is fitted with an exponential model to compute the  $T_2$  value in each voxel. (c) Finally, the transverse relaxivity is estimated as the slope of the linear fit of the mean  $1/T_2$  value in each tube versus contrast agent concentration.

**Principle** A MSME (Multi-Slice Multi-Echo) sequence is used to sample the decay of MR transverse signal thanks to different echo times ( $T_E$ ). It is then possible, by fitting this MR signal decay as a function of time in each voxel, to compute the resulting  $T_2$  value per voxel and obtain a  $T_2$  parametric map. From this map, the transverse relaxivity  $r_2$  can be easily estimated as the slope of the linear fit of the mean  $1/T_2$  value in each tube versus contrast agent concentration. Figure A.1 sums up these different experimental steps.

The different parameters of MSME sequences, used during this PhD thesis for transverse relaxometry experiments at different magnetic field intensities, are listed in Table A.1. In all cases, it is not possible to measure  $T_2$  values smaller than the forth  $T_E$  (in order to guarantee a relevant fit), and higher than the  $T_2$  value of pure water (mean on three magnetic field intensities:  $T_2^{WATER} = 280 \text{ ms}$ ). Finally, it is not possible to distinguish two  $T_2$  values that are too close: for ensuring precise transverse relaxivity estimations, the experiments are designed to measure  $T_2$  values separated from 25  $\text{ms}$  minimum. Therefore, to obtain accurate and separable  $T_2$  values, we need to precisely adjust the range of contrast agent concentrations: this requires to have an idea of  $r_2$  value before measuring it. This is usually done thanks to other studies found in literature. When no prior  $r_2$  value is available, we firstly use a very broad range of concentrations to run a first evaluation, knowing that some tubes might saturate the MRI contrast (either appearing always white or black for all echo times), and afterward, we repeat the measurement with an appropriate range of concentrations.

Experimental parameters		Experimental values		
Magnetic field intensity	$T$	7	11.7	17.2
$T_E$ minimum	$\text{ms}$	7.7	8	8
$\Delta T_E$	$\text{ms}$	7.7	8	8
Nb $T_E$	-	64	64	64
$T_R$	$\text{ms}$	10000	5000	5000
In-plane spatial resolution	$\text{mm} \times \text{mm}$	$0.25 \times 0.25$	$0.25 \times 0.25$	$0.25 \times 0.25$
In-plane field-of-view	$\text{cm} \times \text{cm}$	$3 \times 3$	$3 \times 3$	$3 \times 3$
Nb slices	-	6	6	6
Slice thickness	$\text{mm}$	1.25	1	1
Nb averages	-	4	4	4
Acquisition time	$\text{min}$	80	40	40

Tab. A.1 – Parameters of MSME sequences used for relaxometry experiments at 7, 11.7 and 17.2  $T$ .

**Concentrations range optimization and phantom preparation** The range of contrast agent concentrations is computed in order to measure  $T_2$  values between 30  $\text{ms}$  and 280  $\text{ms}$ , equally spaced by 25  $\text{ms}$ . Once the concentrations range is set, the experimental protocol for phantom fabrication needs to be defined. The MRI phantom is made by diluting the contrast agent in agar, to prevent its sedimentation during MRI experiment, and to mimic biological tissue

environment. All relaxometry experiments are performed with 0.3% agar w/w. In order to avoid heating the contrast agent, 0.6% agar w/w at 50°C is blended 1:1 with contrast agent suspension (at room temperature) two times more concentrated, to finally create the phantom tubes with the desired concentrations. Before sampling from the most concentrated suspension, aliquots were sonicated during 10 *min* and immediately diluted.

Here is a summary of the important steps for phantom preparation:

- Choose the number of tubes in the phantom: for example 6 or 12
- Compute the expected  $T_2$  values, equally spread between 25 *ms* and 280 *ms*
- Use the presumed  $r_2$  value to estimate the contrast agent concentration in each tube
- Optimize these concentration values to facilitate contrast agent dilution
- Compute the successive dilutions leading to the good concentrations range from the initial contrast agent concentration
- Prepare 0.6% agar gel w/w by heating agar powder and distilled water to 100°C under magnetic stirrer, before letting it down to 50°C
- Prepare all contrast agent suspensions, two times more concentrated
- Blend 1:1 agar solution and contrast agent, fill immediately a pre-cut insulin syringe with the mixture, before closing it with two pistons, and repeat this step for the 6 or 12 tubes
- Place all tubes inside a Falcon tube of 50 *mL*, before filling it with distilled water and letting it cool down to room temperature for MRI acquisitions

**MRI data processing** After MRI acquisitions performed on one phantom, data are processed using homemade Matlab routines (MathWorks, Natick, USA), by following these different steps:

- Reconstruct MR image from raw data for each  $T_E$
- Automatically segment and label each tube in the first echo MR image (the one with the highest signal-to-noise ratio), to analyze the MR signal only inside tubes
- Fit an exponential model to estimate the  $T_2$  values in all voxels of each tube, and thus obtain one  $T_2$  parametric map
- Compute the mean  $T_2$  value inside each tube, and rank all these mean  $T_2$  values from the smallest to the greatest
- Associate these sorted increasing values of  $T_2$  with the decreasing concentration values, and compute the linear fit of  $1/T_2$  versus contrast agent concentration, to finally estimate the transverse relaxivity  $r_2$  as the slope of this fit

Warning: It is very important to know the order in which the tubes are placed in the phantom, to control that each computed  $T_2$  value is attributed to the correct tube.

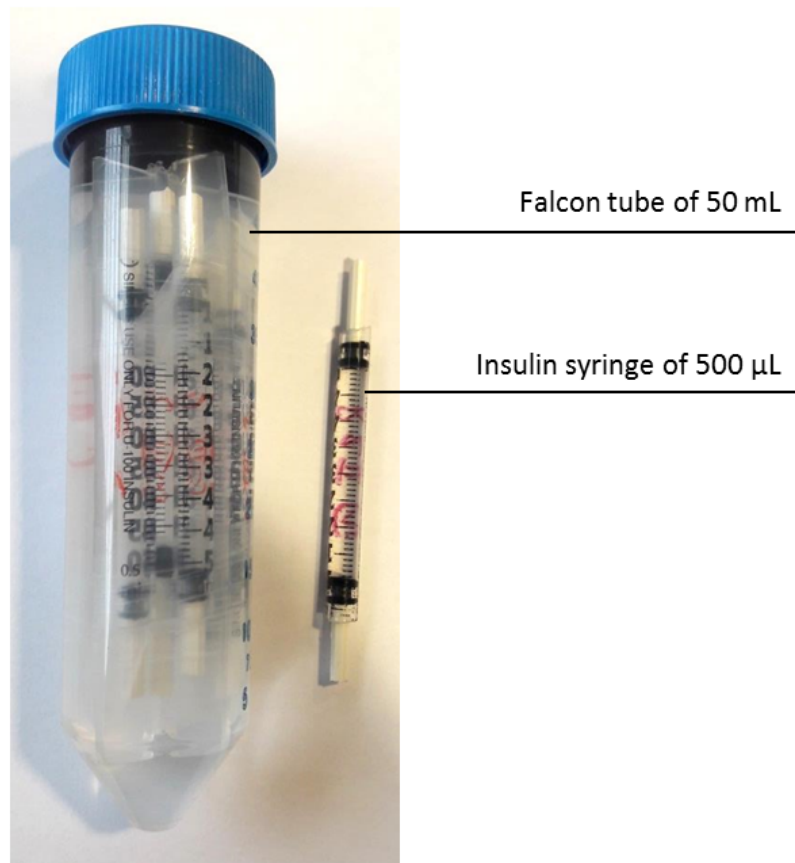


Fig. A.2 – Example of a phantom made of pre-cut insulin syringes, filled with contrast agent diluted in agar, placed inside a Falcon tube of 50 *mL* filled with water.

## A.2 U87 cells culture

U87 cell lines from ATCC<sup>®</sup> (Manassas, USA), issued from human primary glioblastoma, are cultured in DMEM (Dulbecco's Modified Eagle's Medium) without phenol red (Sigma-Aldrich, St. Louis, USA), with 10% of fetal bovine serum (Eurobio, Courtabeuf, France), 1% of glutamine (Lonza, Basel, Switzerland), 1% of pyruvate (Lonza), 1% penicillin/streptomycin (Lonza), and 7  $\mu\text{L}/100\text{ mL}$  of gentamicin (Lonza). U87 cells are grown at 37°C in a humidified atmosphere of 5%  $\text{CO}_2$  for 3 days after seeding in glass bottom plates, for insuring a good level of  $\alpha_v\beta_3$  integrins expression.

## A.3 U87 cells spheroid culture

**Spheroid seed preparation** In one multiwell plate, fill wells with DPBS (Dulbecco's Phosphate-Buffered Saline, GE Healthcare Life Science, Chicago, USA) and place drops of a couple of microliters of U87 cells suspension on the lid, in front of each well. Carefully reverse the lid on wells and incubate at 37°C. Look at cells aggregation with microscope daily. When aggregates are well formed, prepare drops of fresh culture medium on new lid and pool two or three aggregates per culture medium drop. Carefully reverse the lid on wells and incubate at 37°C. When the spheroid approximately reaches 0.5 – 1 *mm* in diameter, change culture mode from

drop to Matrigel<sup>®</sup>.

**Single layer Matrigel<sup>®</sup> culture** This culture mode is appropriate for small spheroids (from 0.5 – 1 mm up to 2.5 mm). Dilute Matrigel<sup>®</sup> at 25% with ice cooled culture medium in pre-cooled tubes. Pour the diluted Matrigel<sup>®</sup> in wells and let it polymerize during 15 min at 37°C. Place the spheroid on Matrigel<sup>®</sup> and let it rest during approximately 5 min at 37°C. Afterward, carefully pour culture medium to cover the spheroid and incubate at 37°C.

**Double layer Matrigel<sup>®</sup> culture** When the spheroid grows above 2.5 mm, it is necessary to include it in a double layer of Matrigel<sup>®</sup> for insuring a spherical growth. Prepare a layer of Matrigel<sup>®</sup> at 25% in well, place the spheroid extracted from a well with single Matrigel<sup>®</sup> layer, carefully pour Matrigel<sup>®</sup> at 15% and incubate at 37°C.

**Spheroid preparation for MRI** Matrigel<sup>®</sup> being a very expensive and very soft gel, another type of gel is needed to hold spheroid during MRI session. Xanthan gel, prepared with PBS containing P/S (penicillin/streptomycin, Lonza), is quite cheap and easy to produce, and enables a good stabilization of spheroid. 1.5 mL Eppendorf tube is filled at 1/3 with this xanthan gel, the spheroid is retrieved with a spoon while keeping the maximum of Matrigel<sup>®</sup> around it, and xanthan gel is added to completely fill the Eppendorf tube. A piston from a 1 mL syringe is used as tight seal before closing the Eppendorf tube. Such sample can be scanned with MRI at room temperature for a couple of hours, after which U87 tumor cells start to suffer and die.

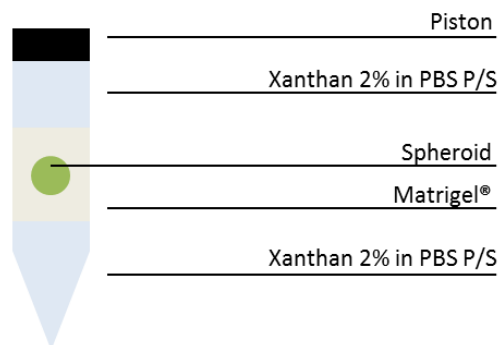


Fig. A.3 – Scheme of spheroid mounted in Eppendorf tube for MRI acquisitions.

## A.4 Immunohistochemical stainings performed on U87 cells

Membranes of U87 cells are stained with Wheat Germ Agglutinin revealed in orange (WGA-Texas Red, Eurobio life science, 1/1000 dilution, 30 min incubation).

Membranes of AMB1 magnetosomes are stained with an anti-AMB1 rabbit antibody revealed in red or green, which has been specifically produced by the LI2D laboratory (1/5000 dilution, 1 h incubation, DK anti-rabbit Alexa647 or DK anti-rabbit Dylight488 revelation).

$\alpha_\nu\beta_3$  integrins are stained with an anti- $\alpha_\nu\beta_3$  mouse antibody revealed in orange (MAB1976H-PE, Millipore, 1/100 dilution, 1 h incubation).

Stained histological slices are mounted on glass plates for fluorescence microscopy with ProLong<sup>®</sup> Gold Antifade Reagent with DAPI (4',6-diamidino-2-phenylindole), DAPI enabling to reveal cell nuclei in blue.

## A.5 Perl's blue staining of U87 cells

U87 cells membrane is permeabilized by incubating in a Triton<sup>®</sup> X-100 (0.2%) bath during 2 *h*, followed by one washout step in ethanol (70%). Then, cells are incubated during 1 *h* with a fresh 1:1 blend of hydrochloric acid solution (1.2 *mM*) and potassium ferrocyanide solution (4%) in order to stain iron ions (the HT20 kit from Sigma-Aldrich, USA, is used to prepare this solution just before using it). After water washout, cells are incubated during 2 *min* with pararosaniline solution (1%, 1/50 dilution, also from HT20 Sigma-Aldrich kit), in order to reveal nuclei. Cells are afterward dehydrated with successive soakings in ethanol solutions (ethanol at 70%, then 96% and 100%, two soakings per solution) and one xylene solution, and stained cells are finally mounted on glass slides with Eukitt<sup>®</sup> medium (Sigma-Aldrich).

## A.6 TEM images of magnetosomes into U87 cells

U87 cells are fixed for 2 *h* in 0.1 *M* cacodylate buffer at  $pH = 7.3$ , containing 2.5% glutaraldehyde and 0.1% tannic acid, then post-fixed with osmium tetroxide for 1 *h* at room temperature. A dehydration is performed by ethanol gradient and acetone bath application. Then, cells are embedded in Epon resin on their coverslip. After 24 *h* of polymerization at 60°C, the coverslip is removed by liquid nitrogen-induced thermal shock. Finally, cells are sectioned with an ultramicrotome (Leica UC7, Germany) and observed with TEM at 200 *kV* (FEI Tecnai G2, USA).





## Protocols for *in vivo* experiments

### B.1 *In vivo* mouse brain imaging

All *in vivo* experiments are conducted in strict accordance with the recommendations of the European Community (86/609/EEC) and the French legislation (decree n°2013-118) for use and care of laboratory animals. The protocol for contrast agent injection is approved by the Comité d'Éthique en Expérimentation Animale du Commissariat à l'Énergie Atomique et aux Énergies Alternatives – Direction des Sciences du Vivant Ile-de-France (CETEA/CEA/DSV IdF) under protocol ID 12-058.

Mice are anesthetized using an air/ $O_2$  mixture (50:50) and isoflurane (3%), before being positioned into dedicated cradle. Respiration rate is continuously monitored and body temperature is kept close to  $37^\circ C$  thanks to a warm water circulation system (on the 11.7  $T$  and 17.2  $T$  scanners), or to a warm air blowing system (on the 7  $T$  scanner). During MRI session, the isoflurane level is adjusted to maintain steady breathing rate and body temperature (isoflurane around 2%).

Contrast agent injections are performed at the mouse tail vein using a 29  $G$  needle (insulin syringe) without removing the animal from the cradle. The caudal vein is dilated using a warm water compress one minute prior to the injection.

### B.2 Mouse brain MRI scans

Here are listed all MRI sequences used during this PhD thesis, with their corresponding parameters.

**RARE**, 7  $T$   $T_2$ -weighted RARE (Rapid Acquisition with Refocused Echoes) sequence:  $T_E/T_R = 30/3000$  ms, in-plane field-of-view =  $1.92 \times 1.68$   $cm^2$ , in-plane spatial resolution =  $150 \times 150$   $\mu m^2$ , 12 slices of 600  $\mu m$  thickness, 18 averages, total acquisition time = 25 min.

**FLASH**, 7  $T$   $T_2^*$ -weighted FLASH (Fast Low Angle SHot) sequence:  $T_E/T_R = 16/485$  ms, in-plane field-of-view =  $1.92 \times 1.68$   $cm^2$ , in-plane spatial resolution =  $160 \times 160$   $\mu m^2$ , 22 slices of 320  $\mu m$  thickness, 48 averages, total acquisition time = 40 min.

**RARE**, 11.7 T  $T_2$ -weighted RARE sequence:  $T_E/T_R = 11/2500$  ms, in-plane field-of-view =  $2 \times 2$  cm<sup>2</sup>, in-plane spatial resolution =  $78 \times 78$   $\mu\text{m}^2$ , 14 slices of 500  $\mu\text{m}$  thickness, 2 averages, total acquisition time = 2 min 40 s.

**FLASH**, 11.7 T  $T_2^*$ -weighted FLASH sequence:  $T_E/T_R = 8/1600$  ms, in-plane field-of-view =  $1.92 \times 1.47$  cm<sup>2</sup>, in-plane spatial resolution =  $75 \times 75$   $\mu\text{m}^2$ , 90 slices of 75  $\mu\text{m}$  thickness, 1 average, total acquisition time = 5 min.

**MGE**, 11.7 T Parametric  $T_2^*$  mapping MGE (Multi Gradient Echo) sequence:  $TE = 3.5/7/10.5/14/17.5/21/24.5/28$  ms,  $TR = 90$  ms, field-of-view =  $1.9 \times 1.42 \times 0.8$  cm<sup>3</sup>, spatial resolution =  $100 \times 100 \times 100$   $\mu\text{m}^3$ , 1 average, total acquisition time = 17 min.

**MGE for *post-mortem* acquisition**, 11.7 T Parametric  $T_2^*$  mapping MGE sequence:  $TE = 4/9/14/19/24/29$  ms,  $TR = 90$  ms, field-of-view =  $1.65 \times 1.44 \times 0.84$  cm<sup>3</sup>, spatial resolution =  $50 \times 50 \times 50$   $\mu\text{m}^3$ , 12 averages, total acquisition time = 14 h 30 min .

**RARE**, 17.2 T  $T_2$ -weighted RARE sequence:  $T_E/T_R = 10/3000$  ms, in-plane field-of-view =  $2.016 \times 2.016$  cm<sup>2</sup>, in-plane spatial resolution =  $90 \times 90$   $\mu\text{m}^2$ , 20 slices of 360  $\mu\text{m}$  thickness, 8 averages, total acquisition time = 22 min 24 s.

**FLASH**, 17.2 T  $T_2^*$ -weighted FLASH sequence:  $T_E/T_R = 8/680$  ms, in-plane field-of-view =  $2.016 \times 2.016$  cm<sup>2</sup>, in-plane spatial resolution =  $90 \times 90$   $\mu\text{m}^2$ , 36 slices of 180  $\mu\text{m}$  thickness, 12 averages, total acquisition time = 30 min.

## B.3 Induction of U87 mouse model of human glioblastoma

U87 cells are cultured as described in Appendix A.2.

Brain tumors are induced by intracerebral injection of U87 cells (120 000 cells in 2  $\mu\text{L}$ ) to 6 weeks old athymic immunodeficient nude mice. For the surgery, mice are anesthetized with an intraperitoneal injection of Ketamine/Xylazine (100/10 mg/kg, 10 mL/kg<sub>BW</sub>) and maintained in a stereotactic frame. A 1 mm hole is drilled in the skull 2 mm right to the bregma, and then U87 cells suspended in PBS are slowly injected with a Hamilton syringe at 3.5 mm depth. Afterward, the syringe is slowly removed and the hole in the skull is filled with bone wax. Finally, the skin is stitched with surgical thread.

Sham surgeries are performed by injecting only PBS instead of U87 cells suspension, while following the exact same procedure.

## B.4 Histology

**Brain preparation** Mice are euthanized with an overdose of Xylazine/Ketamine injected intraperitoneally. Simultaneously, mice are intracardiacally perfused with NaCl 0.9% to remove blood, and then fixed with Paraformaldehyde (PFA) 4%. Mouse brains are extracted, post-fixed during 2 hours in PFA 4%, soaked in sucrose solutions (15% followed by 30%), frozen by

immersion in  $-30^{\circ}\text{C}$  isopentane, to be finally stored at  $-80^{\circ}\text{C}$  for histological analysis. For immunohistochemical stainings and fluorescence microscopy imaging, brain samples are cut into  $20\ \mu\text{m}$  thickness slices with a cryomicrotome, and brain slices are positioned on glass slides.

## B.5 Immunochemical staining

Vessels are stained with an anti-CD31 rat antibody revealed in green (MCA2388, AbD Serotec, 1/50 dilution, 1 *h* incubation, DK anti-rat Alexa488 revelation).

$\alpha_v\beta_3$  integrins are stained with an anti- $\alpha_v\beta_3$  mouse antibody revealed in orange (MAB1976H-PE, Millipore, 1/100 dilution, 1 *h* incubation).

Membranes of AMB1 magnetosomes are stained with an anti-AMB1 rabbit antibody revealed in red, which has been specifically produced by the LI2D laboratory (1/5000 dilution, 1 *h* incubation, DK anti-rabbit Alexa647 revelation).

Macrophages, and especially Kupffer cells, are stained with an anti-CD68 rat antibody revealed in green (MCA1957, AbD Serotec, 1/500 dilution, 1 *h* incubation, DK anti-rat Alexa488 revelation).

Microglia are stained with an anti-Iba1 goat antibody revealed in orange (ab107159, Abcam, 1/250 dilution, 1 *h* incubation, DK antigoat Dylight594 revelation).

Caspase 3 proteins, which are markers of apoptosis, are stained with an anti-Caspase 3 rabbit antibody revealed in green or red (ab13847, Abcam, 1/500 dilution, 1 *h* incubation, DK anti-rabbit Dylight488 or DK anti-rabbit Alexa647 revelation).

Stained histological slices are mounted on glass plates with ProLong<sup>®</sup> Gold Antifade Reagent with DAPI to reveal cell nuclei in blue.



## Data processing protocols

### C.1 Brain angiography using Frangi filter

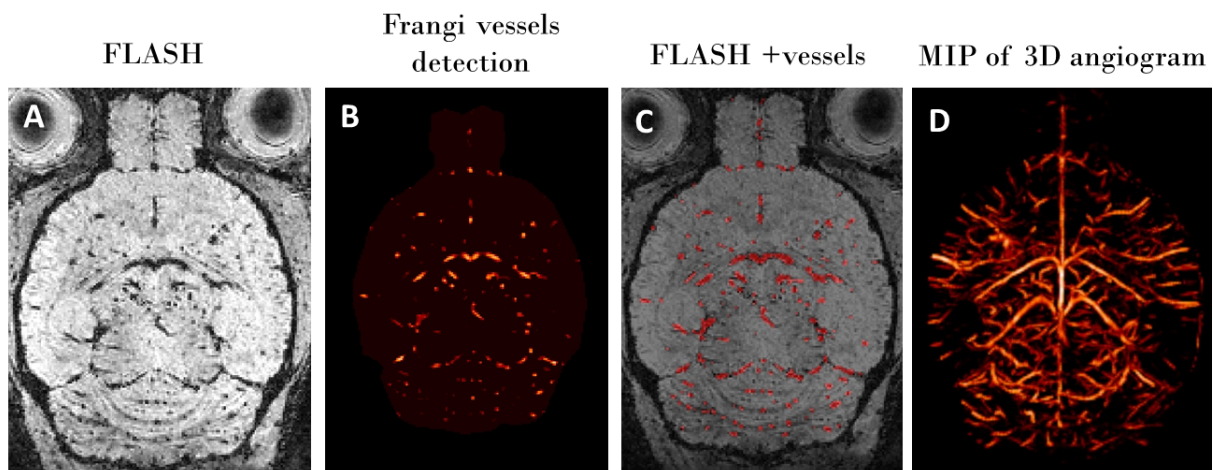


Fig. C.1 – Results of Frangi vessels filtering algorithm. A/ Initial FLASH image of mouse brain. B/ Brain vessels detected with Frangi filter. C/ Overlay of the FLASH image and the detected brain vessels. C/ MIP of 3D brain angiogram.

A filter, based on the multiscale vessel enhancement method proposed by Frangi in 1998 and Manniesing in 2006 (see references in Section 3.3), is applied to non segmented FLASH images (mask brain is applied on the filtered image for visualization). This filter computes in 3D the likelihood of a vessel being present in each voxel, considering the second order gradient values in the surrounding voxels to enhance vasculature and reduce the noise in the image. A Matlab code written by Dirk-Jan Kroon (available on MathWorks file exchange: [Hessian based Frangi Vesselness filter](#)) is optimized for vessels detection on MRI images of mouse brain acquired during this PhD thesis.

3D visualization of vessels enhanced by the Frangi filter is obtained thanks to the volume rendering and Maximum Intensity Projection (MIP) tools provided by Anatomist software ([Brainvisa](#)). Figure C.1 shows one example of mouse brain FLASH image and the resulting 3D angiogram, between which is displayed the result of vessels detection overlaid on the original

FLASH image to appreciate the efficiency of Frangi filter.

The comparison between the 3D pre and post injection angiograms provides an insight on the efficiency of injected IONP as blood pool contrast agent. The values in 3D angiogram computed with Frangi filter seem to be highly dependent on both signal-to-noise ratio (SNR) and image spatial resolution. Based on the pre injection angiogram, a threshold is applied in order to only reveal brain vessels. Then, the same threshold is applied on the post injection image. This threshold appears to be stable when performing the experiments with the same MRI scanner, highlighting that this procedure enabling 3D angiogram reconstruction strongly depends on achievable SNR and spatial resolution.

The *in vivo* efficiency of injected IONP as blood pool contrast agent is assessed by comparing the pre and post thresholded angiograms, and a score  $s$  in percent is computed as follows, to embody the improvement in vessels detection related to IONPs injection:

$$s = 100 \times \frac{N_{POST} - N_{PRE}}{N_{PRE}}$$

where  $N_i$  is the number of voxels above the threshold applied on both pre and post angiograms. This score can be seen as a pseudo-quantitative index of the brain vasculature enhancement due to IONP intravenous injection.

## C.2 Brain angiogram skeletonization and quantification

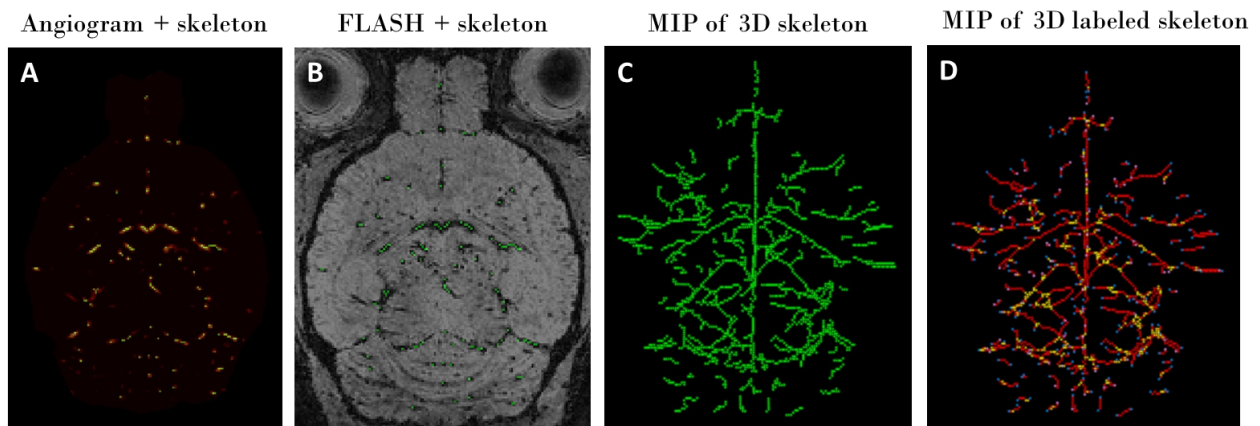


Fig. C.2 – Results of the skeletonization of 3D angiogram. A/ Overlay of a mouse brain angiogram (red colormap) and its skeleton (green). B/ Overlay of the FLASH image (grayscale) and the skeleton (green). C/ MIP of 3D skeleton (green). D/ MIP of 3D color-labeled skeleton: endpoint in blue, slab in red and junction in yellow.

3D angiograms of mouse brain are skeletonized using a Matlab code adapted from the one of Philip Kollmannsberger (available on MathWorks file exchange: [Skeleton3D](#)). Prior to skeletonization, 3D angiograms are thresholded following the same procedure than for the score  $s$  computation. This skeletonization step is only applied on images acquired at 11.7 T (the ones exhibiting the highest spatial resolution), with a threshold set to 1.5 for all images.

One example of 3D skeleton derived from mouse brain angiogram is presented in Figure C.2 (A, B and C). The overlay of the angiogram and its skeleton, but also the one of the original FLASH image and the skeleton, show the efficiency of this skeletonization procedure to detect the center of vessels. The MIP of 3D skeleton is afterward used for quantitative analyses.

The 3D skeletons of mouse brain angiogram are analyzed using the AnalyzeSkeleton plugin of ImageJ software ([Analyze Skeleton](#), written by Ignacio Arganda-Carreras). This plugin automatically calculates the number of branches in the skeleton, their length and the corresponding Euclidean distance, among other features. These measurements are based on the differentiation between slab, junction and endpoint voxels, given the number of neighbors of each voxel. One example of 3D skeleton with labeled voxels is displayed in Figure C.2 D.

### C.3 Analysis of immunohistochemical stainings co-localization

A co-localization algorithm, written in Matlab, is developed for analyzing *in cellulo* and *post-mortem* fluorescence microscopy images. The operating mode of this algorithm is illustrated with the following example of one co-localization study between Venus fluorescence (magnetosomes membrane revealed in green) and WGA one (U87 cell membrane revealed in orange).

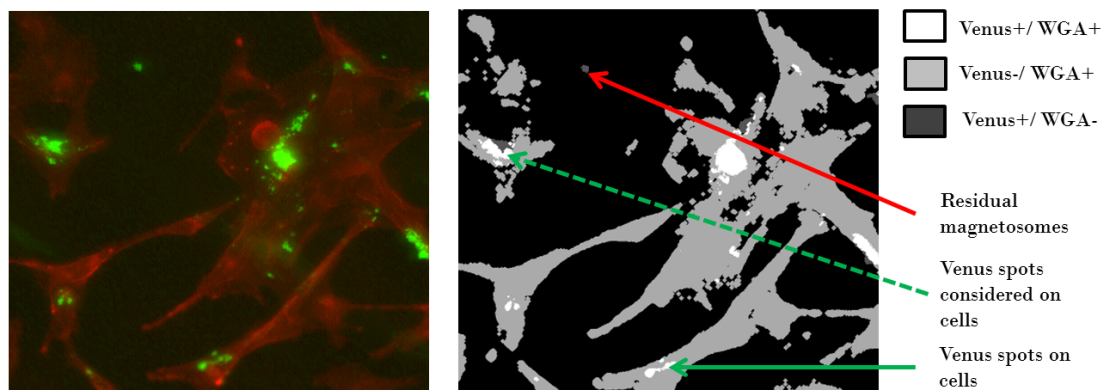


Fig. C.3 – Example of one co-localization study to quantify magnetosomes affinity for U87 cells *in vitro*. Example of a merge between the orange (U87 cell membranes) and green (magnetosome membranes) channels (left), and of a composite image (right) enabling to sort Venus+ clusters into two categories: on cells or out cells. The green dashed arrow shows an example of a cluster partly on cells, the green plain arrow shows a cluster fully on cells and the red one a cluster outside cells.

- The orange channel is used to delineate cells and to sort Venus fluorescence clusters. A thresholding step common to all images is set to retrieve relevant fluorescence from background noise. This step is followed by a simple image dilatation to fill the potential holes in detected clusters.
- The green channel is used to count pixels with positive Venus fluorescence. A thresholding step is also added before pixels counting, to completely eliminate the background noise when detecting both AMB1 V and AMB1 VRGD magnetosomes.
- Finally, a composite image affecting 1 to each pixel [Venus+/WGA-], 2 to each pixel [Venus-/WGA+] and 3 to each pixel [Venus+/WGA+] is created. Each Venus+ cluster

containing at least one pixel [Venus+/WGA+] is considered as a cluster on cells, as illustrated by the green dashed arrow in Figure C.3. Otherwise, the cluster is considered as isolated, as pointed out by the red arrow. This method enables to classify in the 'on cells' category the fluorescence spots which exceed out of cell limits, but whose source is on cells. It also overcomes the problem of imposing a too high threshold, that can limit the extent of fluorescence around big spots but also remove small ones.

- This method was originally developed on native fluorescence images, but it can become very time consuming considering the clustering steps and the extremely high spatial resolution of these images ( $0.323 \mu m$  at x20 magnification). Considering the typical size of detected Venus clusters, the downsampling of input images is possible and can considerably reduce computation time without deteriorating performances. All x20 images are thus downsampled 4 times at the beginning of the pipeline.





# List of Figures

1	Comparaison des propriétés contrastantes <i>in vivo</i> de l'Endorem <sup>®</sup> et des magnétosomes AMB1 . . . . .	XVII
2	Démonstration <i>in vivo</i> de l'affinité des magnétosomes RGD pour le modèle animal de tumeur cérébrale U87. . . . .	XVIII
1.1	Principle of targeting $\alpha_v\beta_3$ integrin <i>in vivo</i> with RGD peptide. . . . .	4
1.2	Principle of using magnetotactic bacteria to produce magnetosomes used as functionalized contrast agent for MRI. . . . .	5
2.1	Magnetic orders described with linear spin lattice from Ashcroft and Mermin. . .	16
2.2	Magnetic domain evolution under applied magnetic field. . . . .	17
2.3	Magnetization loop hysteresis from Estelrich 2015. . . . .	18
2.4	Magnetic regimes of IONP as a function of nanoparticle size from Estelrich 2015. .	19
2.5	Nuclear spin magnetization relaxation after a 90° flip in a Spin-Echo experiment. .	20
2.6	Transverse relaxivity measurement with phantom. . . . .	22
2.7	Simulations of theoretical $R_2$ for a superparamagnetic IONP versus its radius From Vuong 2011. . . . .	24
2.8	Difference between iron oxide core diameter ( $d$ ) and hydrodynamic diameter ( $D_h$ ) of the nanoparticle. . . . .	25
2.9	Improvement of transverse relaxivity through iron-oxide core optimization from Jun 2008, Lee 2007 and Pösel 2012. . . . .	27
2.10	Ferrimagnetic nanoparticle as MRI CA from Lee 2011. . . . .	28
2.11	Influence of PEG chain size on transverse relaxivity from LaConte 2007. . . . .	30
2.12	Magnetosome magnetic structure and magnetotaxis from Dunin-Borkowski 1998 and Bazylinsky 2004. . . . .	32
2.13	Diversity of magnetosomes iron-oxide core from Schuler 2008. . . . .	33
2.14	Importance of magnetosome membrane for functionalization from Ginet 2011 and Lang 2006. . . . .	34
2.15	Magnetic properties of magnetosomes from Li 2010. . . . .	35
2.16	Magnetosome membrane role and its protein content from Lang 2006, AlphanDéry 2011 and Grünberg 2004. . . . .	37
2.17	Example of <i>in vivo</i> magnetic cell tracking from Guzman 2007, Smirnov 2006 and de Vries 2005. . . . .	38
2.18	Example of tissue engineering with magnetic cells, from Fayol 2013 and 2011. . .	39
2.19	Example of hyperthermia therapy with intratumoral injection of extracted magnetosomes from AlphanDéry 2011. . . . .	41

3.1	Magnetosome size analysis to measure mean diameter and shape factor dispersion.	51
3.2	Magnetic properties of MV1 magnetosomes.	52
3.3	Magnetosomes extraction protocol.	53
3.4	Physico-chemical characterization of MV1 magnetosomes membrane from Mériaux 2015.	54
3.5	$T_1$ and $T_2$ mapping using the same phantom of AMB1 magnetosomes at 11.7 T.	56
3.6	IONPs size effect on saturation magnetization and transverse relaxivity.	60
3.7	Graphs of surface area $A$ versus volume $V$ for different shapes.	62
3.8	Schematic representation of the local magnetic field around nanosphere versus nanorods from Mohapatra 2015.	63
3.9	Comparison of <i>in vivo</i> contrasting properties of chemical IONPs.	66
3.10	Comparison of <i>in vivo</i> contrasting properties of magnetosomes.	67
3.11	Anatomical slices from human to mouse.	68
3.12	U87 tumor growth, size and shape analysis.	69
3.13	U87 tumor vessels analysis with <i>in vivo</i> contrast-enhanced MRI.	71
3.14	Iron uptake measurements to U87 tumor bearing mice after injection of NPAC or NPPO-PEG <sub>85</sub> .	73
3.15	Iron uptake measurements in tumor bearing mice after injection of AMB1 magnetosomes.	74
4.1	RGD functionalization of AMB1 magnetosomes	84
4.2	Assessment of successful genetic modification of magnetosomes	85
4.3	Impact of sonication on fluorescence release from functionalized magnetosomes	86
4.4	Transverse relaxivities of functionalized magnetosomes measured at 11.7 T with or without sonication	87
4.5	<i>In vitro</i> qualitative validation of RGD functionalized magnetosomes affinity for U87 cells	88
4.6	<i>In vitro</i> quantification of magnetosomes affinity for U87 cells	89
4.7	<i>In vitro</i> qualitative validation of RGD magnetosomes internalization into U87 cells after binding.	90
4.8	TEM micrographs of U87 cells incubated with magnetosomes	91
4.9	Pictures of U87 spheroids in Matrigel <sup>®</sup>	92
4.10	MRI acquisitions at 7 T on spheroid culture of U87 cells	93
4.11	U87 spheroids grew from cells incubated with AMB1 VRGD magnetosomes	94
4.12	Short term follow-up of MRI contrast enhancement in mouse brain tumor after magnetosomes intravenous injection.	95
4.13	Long term follow-up of MRI contrast enhancement in mouse brain tumor after magnetosomes intravenous injection.	97
4.14	Stained histological slices of AMB1 V or AMB1 VRGD injected mouse brain.	99
4.15	Quantification of AMB1+ pixels in stained histological slices.	101
4.16	<i>Post mortem</i> MRI images acquired 24 h after AMB1 VRGD magnetosomes intravenous injection.	102
4.17	Comparison between high resolution <i>post mortem</i> MR image and histological image.	103
4.18	Stained histological slices of liver from mice injected with AMB1 V or AMB1 VRGD.	104
4.19	Interaction between magnetosomes and microglia.	105

5.1	<i>In vitro</i> kinetics of magnetosomes uptake by U87 cells followed by fluorescence microscopy. . . . .	113
5.2	<i>In vitro</i> kinetics of magnetosomes uptake by U87 cells followed by Perl's blue staining. . . . .	114
5.3	<i>In vitro</i> dose effect on RGD magnetosomes uptake by U87 cells revealed with Perl's blue staining. . . . .	115
5.4	Visual inspection of different preparations of U87 cellsl incubated with AMB1 VRGD versus control. . . . .	116
5.5	MRI signal drop observed for different preparations of U87 cells incubated with AMB1 VRGD. . . . .	117
5.6	Timeline of the single and double injection protocols. . . . .	119
5.7	FLASH images and tumor iron uptake after one simple injection of $200 \mu\text{mol}_{[Fe]}/\text{kg}_{BW}$ versus two injections of $100 \mu\text{mol}_{[Fe]}/\text{kg}_{BW}$ . . . . .	120
5.8	Timeline of the triple injection protocol. . . . .	121
5.9	FLASH images and estimation of tumor iron uptake obtained after three injections of $66 \mu\text{mol}_{[Fe]}/\text{kg}_{BW}$ . . . . .	121
A.1	Measure of the transverse relaxivity. . . . .	137
A.2	Example of a phantom made of pre-cut insulin syringes, filled with contrast agent diluted in agar, placed inside a Falcon tube of 50 mL filled with water. . . . .	140
A.3	Scheme of spheroid mounted in Eppendorf tube for MRI acquisitions . . . . .	141
C.1	Results of Frangi vessels filtering algorithm . . . . .	149
C.2	Results of the skeletonization of 3D angiogram . . . . .	150
C.3	Example of one co-localization study to quantify magnetosomes affinity for U87 cells <i>in vitro</i> . . . . .	151



# List of Tables

1.1	Different type of imaging modalities, adapted from Mahmoudi 2011. . . . .	3
2.1	Different type of coating for IONP adapted from Gupta 2005. . . . .	29
2.2	Measurements of transverse relaxivity of magnetosomes performed by different studies. . . . .	36
3.1	Magnetosomes mean length and mean shape factor. . . . .	51
3.2	Transverse relaxivity measurements of different chemical IONPs. . . . .	57
3.3	Transverse relaxivity values of chemical IONPs with different iron-oxide core diameters but coated with the same PEG chains. . . . .	59
3.4	Transverse relaxivity values of different magnetosomes measured at three magnetic field intensities. . . . .	60
4.1	Co-localization classification for triple immunohistochemical staining: vessels, microglia and magnetosomes. . . . .	106
A.1	Parameters of MSME sequences used for relaxometry experiments at 7, 11.7 and 17.2 <i>T</i> . . . . .	138



# List of acronyms, commonly used symbols and constants

Acronym	Unit	Definition
<i>AMB</i> – 1		<i>Magnetospirillum magneticum</i>
AMB1		Magnetosomes from <i>Magnetospirillum magneticum</i>
AMB1 V		Magnetosomes from <i>Magnetospirillum magneticum</i> genetically modified to harbor Venus protein at its membrane
AMB1 VRGD		Magnetosomes from <i>Magnetospirillum magneticum</i> genetically modified to harbor Venus-RGD protein at its membrane
CA		Contrast Agent
CSPBAT		Chimie, Structures, Propriétés de Biomatériaux et d'Agents Thérapeutiques, Laboratory of Paris 13 University
<i>D</i>		Translational diffusion coefficient of water
<i>D<sub>CR</sub></i>		Critical diameter below which a particle is monodomain
<i>D<sub>H</sub></i>		Hydrodynamic diameter
EPR		Enhanced Permeability and Retention effect
f		Shape factor (width/length)
GBM		Glioblastoma Multiforme
$\gamma$	$rad \cdot s^{-1} \cdot T^{-1}$	Gyromagnetic ratio (for water proton $\gamma = 2.67513 \cdot 10^8 rad \cdot s^{-1} \cdot T^{-1}$ )
IONP		Iron-Oxide NanoParticle
LBC		Laboratoire de Bioénergétique Cellulaire, CEA Cadarache
LI2D		Laboratoire Innovations technologiques pour la Détection et le Diagnostic, CEA Marcoule
PEG		PolyEthylene Glycol
MI		Molecular Imaging
MIDAS		Molecular Imaging and Delivery of Active Substances team, member of UNIRS

Acronym	Unit	Definition
MRI		Magnetic Resonance Imaging
MR		Magnetic Resonance
MTB		Magnetotactic bacteria
<i>MV - 1</i>		<i>Magnetovibrio blakemorei</i>
MV1		Magnetosomes from <i>Magnetovibrio blakemorei</i>
$M_S$	$A \cdot m^2 \cdot kg^{-1}$	Mass saturation magnetisation (often measured in <i>emu/g</i> )
$M_{S,v}$	$A \cdot m^{-1}$	Volumic saturation magnetisation (often measured in <i>Oe</i> )
$\mu_0$	$T \cdot m \cdot A^{-1}$	Magnetic permeability of vacuum ( $\mu_0 = 4\pi 10^{-7} T \cdot m \cdot A^{-1}$ )
NPAC		9 nm maghemite nanoparticle produced in aqueous micelles and coated with caffeic acid.
NPPO-PEG <sub>85</sub>		9 nm maghemite nanoparticle produced in aqueous micelles and coated with PEG chains, 15% of PEG-2100-CH <sub>3</sub> and 85% of PEG-1200-COOH.
RGD		Arginine - Glycine - Aspartic Acid peptide
$r_1$	$mM^{-1} \cdot s^{-1}$	Longitudinal relaxivity
$r_2$	$mM^{-1} \cdot s^{-1}$	Transverse relaxivity
SDS		Sodium Dodecyl Sulfate
SPION		SuperParamagnetic Iron Oxide Nanoparticle
TEM		Transmission Electron Microscopy
$T_1$	$s$	Longitudinal relaxation time
$T_2$	$s$	Transverse relaxation time
$T_E$	$s$	Echo time
$T_R$	$s$	Repetition time
$T_C$	$K$	Curie temperature
$T_N$	$K$	Néel temperature
UNIRS		Unité d'Imagerie par Résonance Magnétique et de Spectroscopie, NeuroSpin, CEA Saclay
WT		Wild Type





# List of Publications

## Peer reviewed journals

- **M. Boucher**, F. Geffroy, N. Ginet, S. Prévéral, L. Bellanger, E. Selingue, G. Adryanczyk-Perrier, M. Péan, C. T. Lefèvre, D. Garcia, D. Pignol and S. Mériaux. Genetically tailored iron-oxide nanoparticles used as MRI probe for *in vivo* molecular imaging of brain tumor. *In preparation*
- S. Richard, **M. Boucher**, A. Saric, A. Herbet, Y. Lalatonne, P. X. Petit, S. Mériaux, D. Boquet, L. Motte; Optimization of pegylated iron oxide nanoplatfoms for Antibody coupling and bio-targeting. *Submitted to ACS Applied Materials & Interfaces*
- S. Richard, A. Saric, **M. Boucher**, F. Geffroy, S. Mériaux, Y. Lalatonne, P. X. Petit, L. Motte; Anti-oxidative theranostic iron oxide nanoparticles towards brain tumors imaging and ROS production. *Submitted to ACS Chemical Biology*
- S. Richard, **M. Boucher**, A. Herbet, Y. Lalatonne, S. Mériaux, D. Boquet, L. Motte; Endothelin B receptors targeted by iron oxide nanoparticles functionalized with a specific antibody: toward immunoimaging of brain tumors. *Journal of Materials Chemistry B*, 3: 2939-2942. doi: [10.1039/C5TB00103J](https://doi.org/10.1039/C5TB00103J)
- S. Mériaux, **M. Boucher**, B. Marty, Y. Lalatonne, S. Prévéral, L. Motte, C.T. Lefèvre, F. Geffroy, F. Lethimonnier, D. Garcia, G. Adryanczyk-Perrier, D. Pignol and N. Ginet; Magnetosomes, Biogenic Magnetic Nanomaterials for Brain Molecular Imaging with 17.2 T MRI Scanner. *Advanced Healthcare Materials*, 4: 1076-1083, 2015. doi: [10.1002/adhm.201400756](https://doi.org/10.1002/adhm.201400756)

## Oral Presentations

Speaker name is underlined.

- **M. Boucher**, F. Geffroy, B. Marty, N. Ginet, C. T. Lefèvre, D. Pignol, and S. Mériaux. *In vitro* and *in vivo* characterization of MV1 magnetosomes as biogenic contrast agents dedicated to high field MRI and first step toward functionalization. *Groupe Thématique de Recherche sur la Vectorisation (now Société Française de Nanomédecine)*, Oral, Orléans - France, December 2013.

- S. Richard, **M. Boucher**, A. Herbet, Y. Lalatonne, S. Mériaux, J. P. Hugnot, D. Boquet, and L. Motte. Superparamagnetic nanoparticles for MRI brain tumors molecular imaging. *Zing Bionanomaterials Conference*, Oral, Nerja - Spain, April 2014.
- S. Richard, A. Herbet, **M. Boucher**, Y. Lalatonne, S. Mériaux, J. P. Hugnot, D. Boquet, and L. Motte. Development of nanoplateform for multimodal imaging of brain tumors. *European Materials Research Society Spring Meeting*, Oral, Lille - France, May 2014.
- J. Bolley, **M. Boucher**, S. Mériaux, N. Pinna, L. Motte, and Y. Lalatonne. Iron oxide nanoparticles size effect on  $T_1$  and  $T_2$  MRI contrast. *European Materials Research Society Spring Meeting*, Oral, Lille - France, May 2014.
- N. Ginet, S. Mériaux, **M. Boucher**, B. Marty, Y. Lalatonne, S. Prévéral, L. Motte, C. T. Lefèvre, F. Geffroy, F. Lethimonnier, M. Péan, D. Garcia, G. Adryanczyk, and D. Pignol. Towards molecular imaging with high-field MRI and biogenic contrast agents. *MagnetoTactic Bacteria*, Oral, Rio de Janeiro - Brazil, September 2014.
- **M. Boucher**, N. Ginet, F. Geffroy, S. Prévéral, G. Adryanczyk-Perrier, M. Péan, C.T. Lefèvre, D. Garcia, D. Pignol, and S. Mériaux. Genetically functionalized magnetosomes as MRI contrast agent for molecular imaging: *in vitro* proof of binding and *in vivo* proof of contrast. *Neuroscience Workshop of Saclay*, Oral, Saclay - France, December 2014.
- **M. Boucher**, N. Ginet, F. Geffroy, S. Prévéral, G. Adryanczyk-Perrier, M. Péan, C. T. Lefèvre, D. Garcia, D. Pignol, and S. Mériaux. Fonctionnalisation par génie génétique de magnétosomes pour l'imagerie moléculaire par IRM de biomarqueurs tumoraux. *Société Française de Résonance Magnétique en Biologie et Médecine*, Oral, Grenoble - France, March 2015.
- **M. Boucher**, N. Ginet, F. Geffroy, S. Prévéral, G. Adryanczyk-Perrier, M. Péan, C. T. Lefèvre, D. Garcia, D. Pignol, and S. Mériaux. Genetically functionalized magnetosomes as MRI contrast agent for molecular imaging: *in vitro* proof of binding and *in vivo* proof of contrast. *International Society of Magnetic Resonance in Medicine*, Oral, Toronto - Canada, May 2015.
- **M. Boucher**, F. Geffroy, E. Selingue, N. Ginet, S. Prévéral, L. Bellanger, G. Adryanczyk-Perrier, M. Péan, C.T. Lefèvre, D. Garcia, D. Pignol, and S. Mériaux. Genetically functionalized magnetosomes used as MRI contrast agent for *in vivo* molecular imaging of brain tumor in U87 mice. *MagnetoTactic Bacteria*, Oral, Marseille - France, September 2016.

## Poster Presentations

Speaker name is underlined.

- **M. Boucher**, N. Ginet, B. Marty, C. T. Lefèvre, D. Garcia, D. Pignol, and S. Mériaux. *In vivo* characterization of MV1-magnetosomes as biogenic contrast agents dedicated to high field MRI: a dose study. *World Molecular Imaging Congress*, Poster, Savannah - USA, September 2013.

- S. Richard, **M. Boucher**, A. Herbet, E. Guénin, Y. Lalatonne, S. Mériaux, J. P. Hugnot, D. Boquet, and L. Motte. Functionalization of nanoplatfrom: toward a new contrast agent specific of brain tumors. *Nanotech*, Poster, Washington - USA, May 2013.
- S. Richard, A. Herbet, **M. Boucher**, Y. Lalatonne, S. Mériaux, J. P. Hugnot, D. Boquet, and L. Motte. Superparamagnetic nanoparticles for immuno imaging of brain tumors by MRI. *European Materials Research Society Spring Meeting*, Poster, Lille - France, May 2013.
- S. Richard, **M. Boucher**, A. Herbet, Y. Lalatonne, S. Mériaux, J. P. Hugnot, D. Boquet, and L. Motte. Nanoplatfrom for immuno imaging of brain tumors by MRI. *Nano Bio Europe*, Poster, Toulouse - France, June 2013.
- **M. Boucher**, N. Ginet, F. Geffroy, S. Prévéral, G. Adryancyk-Perrier, M. Péan, C. T. Lefèvre, D. Garcia, D. Pignol, and S. Mériaux. Genetically functionalized RGD magnetosomes as MRI contrast agent: *in vitro* proof of concept. *World Molecular Imaging Congress*, Poster, Seoul - Korea, September 2014.
- S. Prévéral, G. Adryancyk-Perrier, F. Geffroy, M. Péan, **M. Boucher**, C.T. Lefèvre, D. Garcia, S. Mériaux, D. Pignol, and N. Ginet. RGD-functionalized magnetosomes, a contrast agent with molecular affinity for diagnostic in Magnetic Resonance Imaging. *MagnetoTactic Bacteria*, Poster, Rio de Janeiro - Brazil, September 2014.
- N. Chauffert, P. Weiss, **M. Boucher**, S. Mériaux, and P. Ciuciu. Variable density sampling based on physically plausible gradient waveform: application to 3D MRI angiography. *International Symposium on Biomedical Imaging*, Poster, New-York - USA, April 2015.
- F. Geffroy, **M. Boucher**, N. Ginet, S. Prévéral, L. Bellanger, G. Adryancyk-Perrier, M. Péan, C.T. Lefèvre, D. Garcia, D. Pignol, and S. Mériaux. *In vitro* characterization of AMB1 magnetosomes as biogenic functionalized contrast agents dedicated to molecular MRI. *World Molecular Imaging Congress*, Poster, Honolulu - USA, September 2015.
- **M. Boucher**, F. Geffroy, E. Selingue, N. Ginet, S. Prévéral, L. Bellanger, G. Adryancyk-Perrier, M. Péan, C.T. Lefèvre, D. Garcia, D. Pignol, and S. Mériaux. Genetically functionalized magnetosomes used as MRI probe for molecular imaging of U87 tumor. *European Nanomedecine Meeting and Société Française de Nanomédecine*, Poster, Grenoble - France, December 2015. **Recipient of the best poster award from the British Society of Nanomedicine.**
- **M. Boucher**, F. Geffroy, E. Selingue, N. Ginet, S. Prévéral, G. Adryancyk-Perrier, M. Péan, C.T. Lefèvre, D. Garcia, D. Pignol, and S. Mériaux. Multi-injection of RGD functionalized magnetosomes to improve *in vivo* iron uptake by U87 brain tumor. *World Molecular Imaging Congress*, Poster, New-York - USA, September 2016.
- F. Geffroy, **M. Boucher**, N. Ginet, S. Prévéral, L. Bellanger, G. Adryancyk-Perrier, M. Péan, C.T. Lefèvre, D. Garcia, D. Pignol, and S. Mériaux. *In vitro* multimodal imaging characterization of RGD functionalized magnetosomes accumulation in U87 glioblastoma cells. *World Molecular Imaging Congress*, Poster, New-York - USA, September 2016.
- F. Geffroy, **M. Boucher**, N. Ginet, S. Prévéral, L. Bellanger, G. Adryancyk-Perrier, M. Péan, C.T. Lefèvre, D. Garcia, D. Pignol, and S. Mériaux. *In vitro* multimodal imaging

characterization of RGD functionalized magnetosomes accumulation in U87 glioblastoma cells. *MagnetoTactic Bacteria*, Poster, Marseille - France, September 2016.



**Title: Magnetosomes used as biogenic MRI contrast agent for molecular imaging of glioblastoma model**

This PhD thesis focuses on the study of a new class of contrast agent for MRI, the magnetosomes, which are natural iron-oxide vesicles produced by magnetotactic bacteria. Magnetosomes are naturally coated with a lipid bilayer which content is genetically determined. Lately, researchers have unraveled the proteins content of magnetosome membranes, opening the way to produce genetically functionalized magnetosomes. This PhD work aims at investigating a new alternative path using magnetotactic bacteria to tackle the production of high efficiency MR-based molecular imaging probes. The engineering and production of magnetosomes, carried out by our collaborators from the LBC, the *Laboratoire de Bioénergétique Cellulaire*, are presented and discussed. We firstly characterize wild type magnetosomes as contrast agent for high field MRI, and compare them with chemically produced iron-oxide nanoparticles. Our results confirm that these magnetosomes present very promising contrasting properties *in vitro*, and therefore they can be used *in vivo* as efficient blood pool agent, for vasculature imaging of mouse brain after intravenous injection. Afterward, engineered magnetosomes are tested in a molecular imaging study of a U87 mouse model of glioblastoma. Knowing that  $\alpha_v\beta_3$  integrins over-expressed by tumor cells can be actively targeted by RGD peptide, AMB-1 magnetotactic bacteria are genetically modified to produce RGD functionalized magnetosomes. After verifying their good affinity properties for U87 tumor cells *in vitro*, we demonstrate *in vivo* this specific affinity with MRI acquisitions on a U87 mouse model. Finally, these *in vivo* results are cross-validated with *post mortem* acquisition of histological data.

**Keywords:** Molecular imaging, MRI, iron-oxide nanoparticle, contrast agent, magnetosomes, glioblastoma.

---

**Title: Les magnétosomes utilisés comme agent de contraste produit biologiquement pour l'imagerie moléculaire d'un modèle murin de glioblastome**

Cette thèse porte sur l'étude d'une nouvelle classe d'agent de contraste pour l'IRM, les magnétosomes, qui sont des vésicules d'oxyde de fer produites naturellement par des bactéries magnétotactiques. Les magnétosomes sont naturellement entourés par une membrane bilipidique dont la composition est déterminée génétiquement. Récemment, le contenu protéique de la membrane des magnétosomes a été mis à jour, ouvrant la voie à la production de magnétosomes fonctionnalisés par ingénierie génétique. L'ingénierie et la production des magnétosomes, réalisées le *Laboratoire de Bioénergétique Cellulaire*, sont présentées et discutées. Des magnétosomes sauvages sont caractérisés en tant qu'agents de contraste pour l'IRM, et nos résultats confirment qu'ils présentent des propriétés contrastantes intéressantes pour l'IRM et qu'ils permettent de réaliser l'imagerie de la vascularisation cérébrale chez la souris après une injection intraveineuse. Ensuite, l'étude de faisabilité de la production d'un agent de contraste IRM fonctionnalisé en une seule étape, à l'aide de bactéries magnétotactiques, est réalisée grâce des expériences d'imagerie moléculaire sur un modèle U87 de souris porteuse de glioblastome. Sachant que les cellules tumorales sur-expriment les intégrines  $\alpha_v\beta_3$ , et que ces dernières peuvent être ciblées activement par le peptide RGD, des bactéries magnétotactiques sont génétiquement modifiées pour produire des magnétosomes exprimant le peptide RGD à leur membrane. Après avoir vérifié *in vitro* leur propriétés d'affinité pour les cellules tumorales U87, nous démontrons *in vivo* cette affinité spécifique à l'aide d'acquisitions IRM sur un modèle souris U87. Finalement, ces résultats *in vivo* sont cross-validés par l'acquisition *post mortem* de données histologiques.

**Mots clés :** Imagerie moléculaire, IRM, nanoparticule d'oxyde de fer, agent de contraste, magnétosomes, glioblastome.